Ph.D. thesis

PH.D. THESIS

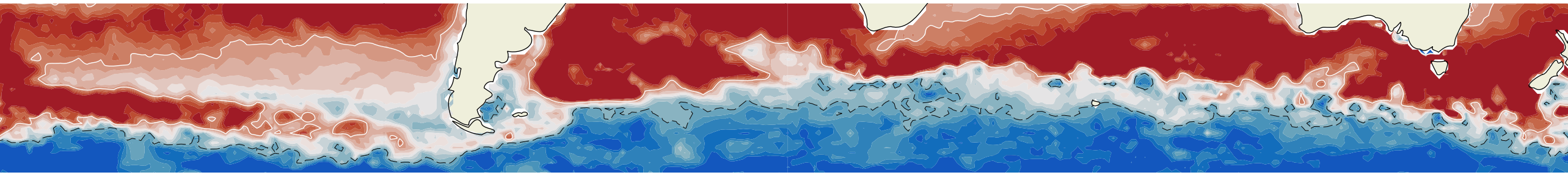

From alpha to beta ocean | Romain Caneill 2023

From alpha to beta ocean

The ocean plays a central role in the climate system by absorbing excess anthropogenic heat and carbon dioxide. Due to the large ocean stratification, vertical exchanges between the ocean interior and the surface are limited. The stratification is controlled by temperature in subtropical regions (alpha oceans) and salinity in polar regions (beta oceans). This thesis investigates the factors influencing the upper ocean stratification. The unique way the thermal expansion coefficient varies with temperature reduces buoyancy fluxes over cold waters. As a result, the contact regions between the ocean interior and the atmosphere are mainly located near the transition between the alpha and beta oceans. This thesis enlightens the central role of the TEC in modulating buoyancy fluxes and thereby controlling the alpha-beta ocean distinction.

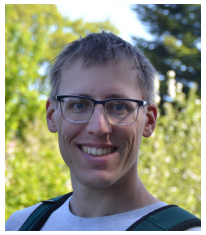

Romain Caneill

ISBN 978-91-8069-555-8 (PRINT)
ISBN 978-91-8069-556-5 (PDF)
Available online: http://hdl.handle.net/2077/79117

From alpha to beta ocean

Exploring the role of surface buoyancy fluxes and seawater thermal expansion in setting the upper ocean stratification

Romain Caneill

DEPARTMENT OF MARINE SCIENCES

UNIVERSITY OF GOTHENBURG

From alpha to beta ocean

Exploring the role of surface buoyancy fluxes and seawater thermal expansion in setting the upper ocean stratification

Romain Caneill

Doctoral thesis

UNIVERSITY OF GOTHENBURG

Department of Marine Sciences
University of Gothenburg
2023

Dissertation for the Degree of Doctor of Philosophy, Ph.D., in Natural Sciences, specialising in Oceanography
University of Gothenburg, 2024

From alpha to beta ocean: Exploring the role of surface buoyancy fluxes and seawater thermal expansion in setting the upper ocean stratification

ISBN 978-91-8069-555-8 (printed)
ISBN 978-91-8069-556-5 (pdf)
Handle http://hdl.handle.net/2077/79117
DOI for the sources of this thesis: 10.5281/zenodo.10203249

This book was typeset by the author using LaTeX.

Contact: romaincaneill.fr
GPG key fingerprint:
70D5 7116 37B2 9335 9088 F124 D0FE 114E BFFD ED7F

Front cover: © Ariane Barba

Back cover photo: The author. Photo credit: © Victoria Caneill

Printed by: Stema Specialtryck AB, Borås, 2023

Keywords: Ocean stratification, Thermal expansion coefficient, Buoyancy fluxes, Transition zone, Alpha – beta ocean

Contents

Abstract

The ocean plays a central role in the climate system by absorbing excess anthropogenic heat and carbon dioxide. Moreover, the ocean circulation distributes heat from the tropics towards the poles. Due to the large ocean stratification, vertical exchanges between the ocean interior and the surface are limited. Subduction links the ocean surface and its interior and occurs in winter at mid- or high-latitudes, where the mixed layers (MLs) are deep. In subtropical regions, temperature and salinity decrease below the ML. Temperature has thus a stabilising effect, while salinity has a destabilising effect, a stratification regime called alpha ocean. Opposite, in polar regions, temperature and salinity increase below the ML, and salinity is the stabilising factor, a regime called beta ocean. In between these two regimes lies the polar transition zone (PTZ), where both temperature and salinity are stabilising. Despite the importance of the alpha-beta distinction, the underlying mechanisms controlling these regimes remain unclear. This thesis investigates the factors influencing the upper ocean stratification and the deep MLs adjacent to the PTZs. From observational profiles, we produce novel climatologies of the upper ocean properties. These climatologies confirm that MLs are deep on the poleward flanks of the alpha oceans. Deep MLs are also present in the beta ocean along the coast of Antarctica. In winter, the transition between the different regimes is abrupt. In summer, both temperature and salinity stratify almost the entire ocean. Based on idealised numerical simulations and observations, we find that the buoyancy fluxes largely determine the position of the PTZ. By stabilising the water column poleward of the PTZ, buoyancy fluxes inhibit convection, permitting beta-ocean formation. The exact position of the PTZ and the adjacent deep MLs are determined by the competition between the winter buoyancy loss and the strength of the existing stratification. Importantly, the impact of heat flux on buoyancy is scaled by the thermal expansion coefficient (TEC). The TEC is a strong function of the temperature, a property unique to water. This diminishes the buoyancy fluxes over cold waters. We find that the local value of the TEC in the subpolar region is of paramount importance in controlling the winter buoyancy loss and stratification, and thus the position of the PTZ. A larger TEC value would cause the alpha ocean to extend poleward, inhibiting beta-ocean formation. Considering the importance of the beta ocean in sea-ice formation, the Earth's climate is influenced by the TEC values, which are directly linked to the ocean surface temperature. In summary, this thesis enlightens the central role of the TEC in modulating buoyancy fluxes and thereby controlling the alpha-beta ocean distinction.

Sammanfattning

Havet spelar en central roll i jordens klimatsystem genom att absorbera en del av överskottet av antropogen värme och koldioxid. Dessutom omfördelar havscirkulationen värme från tropikerna till polerna. På grund av havets starka densitetsskiktning är vertikalt utbyte mellan havets yta och de djupare vattenmassorna begränsat. Subduktion är en process som kopplar havsytan till havets inre, vilket sker under vintern på mellan- och höga latituder, där det översta välblandade skiktet (mixed layer, ML) är djupt. I subtropiska hav minskar temperaturen och salthalten under ML. Temperaturen har därmed en stabiliserande effekt, medan salthalten har en destabiliserande effekt. Denna skiktningsregim kallas alphahav. I motsats till detta har polarhaven ökande salthalt och temperatur under ML, vilket leder till att salthalten är stabiliserande. Denna regim kallas betahav. Mellan alpha- och betaregimerna ligger den polara transitionszonen (PTZ), som är en regim där såväl temperatur som salthalt är stabiliserande. Trots att distinktionen mellan alpha- och betahav är viktig är de underliggande mekanismerna som kontrollerar dessa regimer inte klarlagda. Denna avhandling undersöker faktorerna som påverkar skiktningen i havets översta del och de djupa ML som återfinns i anslutning till PTZ. Vi använder profiler av salthalt och temperatur från observationer för att producera nya klimatologier av de tre regimerna. Dessa klimatologiska data bekräftar att ML är djupt i den del av alphahaven som ligger närmast polerna. Djupa ML återfinns också i betahavet längs Antarktis kust. Under vintern är övergången mellan de olika regimerna abrupt. Under sommaren bidrar både temperatur- och salthaltsfördelning till skiktningen i nästan hela havet. Baserat på idealiserade numeriska simuleringar och observationer av skiktning och flytkraftsflöden, finner vi att flytkraftsflöden till stor del bestämmer positionen för PTZ. Genom att stabilisera vattenpelaren på den sida av PTZ som är närmast polen begränsar flytkraftsflödena konvektiva processer och tillåter därmed att betahav uppstår. Den exakta positionen av PTZ och de närliggande djupa ML bestäms av en balans mellan förlust av flytkraft under vintern och motståndskraften hos den existerande skiktningen. En viktig faktor är att värmeflödets inverkan på flytkraftsflödet ändras med värdet på den termiska expansionskoefficienten (TEC). TEC är starkt beroende av vattnets temperatur – en egenskap som är unik för vatten. Denna egenskap leder till minskade flytkraftsflöden i kallt vatten. Vi finner att det lokala värdet av TEC i den subpolära regionen spelar en mycket viktig roll i att reglera vinterns flytkraftsförlust och stratifiering, och därmed positionen för PTZ. Ett högre värde på TEC skulle orsaka att alphahavet expanderar mot polen och hindrar att betahav bildas. På grund av

betahavets betydelse för bildning av havsis påverkas jordens klimat följaktligen av TEC värdena, som är direkt kopplade till havets yttemperatur. Sammanfattningsvis belyser denna avhandling den centrala roll som TEC spelar i att modulera flytkraftsflöden och därmed i att styra övergången mellan alpha- och betahav.

Acknowledgements

Embarking on this thesis was like navigating the vast and mysterious ocean, following Jules Verne's Captain Nemo in *Vingt mille lieues sous les mers*. Reading this book as a child may have been my first step in earth science. Later, in 2016, my oceanographic expedition set sail in Stockholm with an internship under the guidance of **Fabien Roquet**. **Fabien**, your trust marked the beginning of this adventure. Thank you for not only trusting me during that initial voyage but also inviting me to plunge into the depths once more, this time with greater challenges. I can proudly say that I am an oceanographer now, and this is thanks to you.

Gurvan, your expertise in navigating the NEMO configuration and insightful scientific commentary were like sailing aside a skilled navigator. Thanks, **Jonas**, for all the pertinent comments on manuscripts and all other discussions.

To the crew of friends from Gothenburg University and beyond, thank you. **Etienne**, you showed me the way, and it is always a pleasure to meet you. **Aditya**, **Anne-Sophie**, **Benjamin**, **Birte**, **Blandine**, **Doris**, **Estel**, **Hanna**, **Isabelle**, **James**, **Jan**, **Johan**, **Malin**, **Martin**, **Michaela**, **Milad**, **Paul**, **Rickard**, **Salar**, **Simon**, **Solange**, **Sofia**, **Stina** (thanks for proofreading the "sammanfattning"), **Theo** (big up for the proofreading of this thesis), **Vincent**, **Yvonne**, and everyone I forget, our shared lunches, fikas, games, and discussions formed the ports of refuge. I could not imagine finishing this thesis without your camaraderie, support, and laughter.

My gratitude extends to my friends. **Etienne** and **Damien** for the wave surfing in Brittany. **Olivier**, for the mountaineering. **Tim**, for the support. **Tim**, **Fabien**, and **Vincent** for sharing our passion for music and for the concerts. **Tim** and **Ambroise** for escorting me all the way to my wedding. **Adam** and **Patric** for the climbing and the discovery of Bohuslän's wonderful climbing spots. Many thanks, **Birte**, for the fikas, dinners, games, and for reading my shitty first drafts. Thanks, **Malin**, for the translation of the "sammanfattning". Thanks, **Ariane**, for the cover. Tack så mycket **Yvonne** for your hospitality. Tack **Gunnel** and **Karin** for being so warm and for all the good fikas. You are all lighthouses to me.

In the seas of the PhD, the boat is made of thousands of lines of code. The hull has been crafted under the guidance of **Matthieu**. You shared with me your passion for computer science for more than 15 years. Thanks to the precious gift you offered me, I quickly became a good boat carpenter. Sailing is only possible because many people offered their time to chart the way, so thanks to the developers of **Python**, **numpy**, **xarray**, **xgcm**, **matplotlib**, and **La-**

tex. **Matthieu**, I also thank you for opening my eyes to free software, free as in free speech. Apart from moral considerations, they make my life simpler every day. Thanks also to open-source software programs. So thanks to the crews behind **GNU**, **Linux**, **Debian**, **YunoHost**, **Framasoft**, **Nextcloud**, **Trilium**, and many others; without you, my life as a PhD student and as a human would be a mess. I thank everyone I sailed with in this sea of collaborative effort, particularly **Ryan Abernathey**, **Julius Busecke**, **Andrew Barna**, and **Deepak Cherian**. You and many others are paving the way to open source in science; we need to continue! **CodeRefinery**, thanks also for promoting open science and giving me the opportunity to be an exercise assistant in one of your workshops.

As I sailed through the chapters, the creative winds of **Gee** and **Ploum**'s cartoons and blog posts inspired both my personal and academic lives. The melodies of **Indochine** and **Leprous** served as lifeboats during the stormy writing phase. I extend my gratitude by calling on the crews who accompanied my voyage at sea: **Agent Fresco**, **Balthazar**, **Barclay James Harvest**, **Ben Mazué**, **Bloodhound Gang**, **Edward Elgar**, **Gael Faye**, **Hubert-Félix Thiéfaine**, **Joseph d'Anvers**, **Matmatah**, **Porcupine Tree**, **Supertramp**, **The Alan Parson Project**, and **22**. A journey at sea is not complete without a fair amount of piracy. I hid bottles of Řhum and Ḃeer in this thesis; come find me to get your treasure if you find them! To the pirate lords of metal, **Alestorm**, I raise my bottle of Rhum in gratitude for the good energy. Thanks, **Alexandra Elbakyan**, for the inspiration. Thank you to everyone working to open science and publications. Thanks to the Swedish system for granting me the flexibility to spend valuable time at the harbour during "pappaledig" with my boys. Sweden is one of the few places where it is possible to have children during a PhD without sacrificing family life or the PhD work.

In concluding this acknowledgement, heartfelt thanks to my family. **Maman** et **Papa** I would not be here today without you pushing me and providing wind in my sails. **Matthieu**, **Gaëlle** et **Yann**, you are my anchors.

Victoria, **Balthazar**, et **Olivier**, returning home to you after a day of work is like finding a safe harbour. You, my little boys, made me think of something other than science when I came home, whether I wanted it or not. **Victoria** I cannot be grateful enough to you for all the hard work you put into our family, allowing me to rely on you while working. Our couple forms the rock that allows me to navigate the seas of academia with confidence.

Romain Caneill-Lortal
Gothenburg, November 2023

Funding

This research was supported by the University of Gothenburg and a travel grant from Adlerbertska stiftelsen.

Outline

This thesis is based on four scientific papers referred to in the text by their roman numerals, as listed below.

List of papers

This thesis is based on the following articles:

I Caneill, R., Roquet, F., Madec, G., & Nycander, J. (2022). The Polar Transition from Alpha to Beta Regions Set by a Surface Buoyancy Flux Inversion. *Journal of Physical Oceanography*, *52*(8), 1887–1902. https://doi.org/10.1175/JPO-D-21-0295.1

II Caneill, R., Roquet, F., & Nycander, J. (2023). Southern Ocean deep mixing band emerges from competition between winter buoyancy loss and stratification. *submitted to Ocean Science*. https://doi.org/10.5194/egusphere-2023-2404

III Caneill, R., & Roquet, F. (2023). Temperature versus salinity: Distribution of stratification control in the global ocean. *in preparation for Ocean Science*

IV Roquet, F., Ferreira, D., Caneill, R., Schlesinger, D., & Madec, G. (2022). Unique thermal expansion properties of water key to the formation of sea ice on Earth. *Science Advances*, *8*(46). https://doi.org/10.1126/sciadv.abq0793

Romain Caneill's contribution

In **Paper I** RC designed the model setup with the help of FR and GM. RC ran all experiments, developed and conducted all analyses. RC was the main contributor for writing the manuscript.

In **Paper II**, RC and all co-authors participated in the design of the study. RC produced all the climatologies and initiated most of the analyses. RC was the main contributor to writing the manuscript.

In **Paper III**, RC produced all climatologies and initiated most of the analyses.

In **Papers I, II, and III**, RC designed and implemented all workflows, allowing for these studies to be reproducible.

In **Paper IV**, RC carried out the analysis of the Estimating the Circulation and Climate of the Ocean (ECCO) product and contributed to the final manuscript.

Other works not included in this thesis:

xgcm xgcm is a Python package that allows for analysis of staggered grid data sets (e.g., model outputs). RC wrote the documentation for using xgcm with the NEMO ocean model. Before this work, no example of using xgcm with NEMO was available.

xnemogcm RC wrote the Python package xnemogcm alone until version 0.4.1 (the latest version is 0.4.2). This package opens NEMO output data and processes them to be used as input for xgcm.

gsw-xarray gsw-xarray is a wrapper around GSW-python for xarray. It adds Climate and Forecast (CF) conventions when existing and adds units to the output. It is also able to convert input variables into the proper unit, if necessary. This project is shared between RC and Andrew Barna (Scripps Institution of Oceanography, UC San Diego).

List of abbreviations

AAIW Antarctic Intermediate Water
ACC Antarctic Circumpolar Current

CB columnar buoyancy
CMIP Coupled Model Intercomparison Project
CO_2 carbon dioxide
CS cooling season

DMB deep mixing band

ECCO Estimating the Circulation and Climate of the Ocean
EOS equation of state

GPCP Global Precipitation Climatology Project

HCC haline contraction coefficient

ISCCP-FH MPF third generation International Satellite Cloud Climatology Project monthly means

MIMOC Monthly Isopycnal & Mixed-layer Ocean Climatology
ML mixed layer
MLD mixed layer depth

NEMO Nucleus for European Modelling of the Ocean

OAflux Objectively Analyzed Air-Sea Fluxes
OGCM ocean general circulation model

PF Polar Front
PTZ polar transition zone

RBF radial basis function

SAF Subantarctic Front
SAMW Subantarctic Mode Water
SB Southern Boundary
SCI stratification control index
SO Southern Ocean
SSH sea surface height
SST sea surface temperature

TEC thermal expansion coefficient
TKE turbulent kinetic energy

WOCE World Ocean Circulation Experiment

Chapter 1

Introduction

More than 50 years ago, pioneering work conducted by Manabe and Wetherald (1967) paved the way to showing the dominant role of carbon dioxide (CO_2) in setting the climate temperature. An increase in CO_2 leads to an increase in the temperature of the atmosphere at the surface of the Earth (Manabe & Wetherald, 1975). This result was found using atmospheric models without any ocean heat transport. However, because of its large heat capacity, the ocean is able to absorb part of the excess heat of the atmosphere (Oeschger et al., 1975; Cess & Goldenberg, 1981). Furthermore, the ocean mitigates atmospheric climate change by absorbing part of the anthropogenic CO_2 (Sabine et al., 2004), concurrently leading to acidification of the ocean (Doney et al., 2009). Moreover, the ocean provides a massive heat and moisture reservoir to the atmosphere, and the oceanic circulation plays a key role in the climate system (Rhines et al., 2008). The exact heat and carbon pathways in the ocean are still not fully understood (Ridge & McKinley, 2021; Gruber et al., 2023).

The global ocean circulation and the vertical fluxes in the ocean are intrinsically linked to the vertical variations of seawater density with depth. The stratification strength is measured by the vertical derivative of density; thus, homogeneous water is unstratified. At the surface, a homogeneous layer called the mixed layer (ML) lies over the pycnocline, where density increases rapidly with depth. By contrast, the deep ocean is weakly stratified. Through its large stratification, the pycnocline blocks vertical mixing, and the result is that the deep ocean is isolated from the atmosphere (Sprintall & Cronin, 2009).

Stratification changes if the density of one layer changes, which can happen by surface buoyancy fluxes, mixing, advection, or diffusion of temperature or salinity (pure "warming" or "freshening"; Bindoff & McDougall, 1994). Another way to change stratification is when isopycnal depth changes without the thermohaline properties changing ("heaving" of isopycnals; Bindoff & McDougall, 1994). Ekman pumping and suction are the processes of water downwelling and upwelling induced by the curl of the wind stress. These adiabatic effects can thus change the upper ocean stratification by heaving.

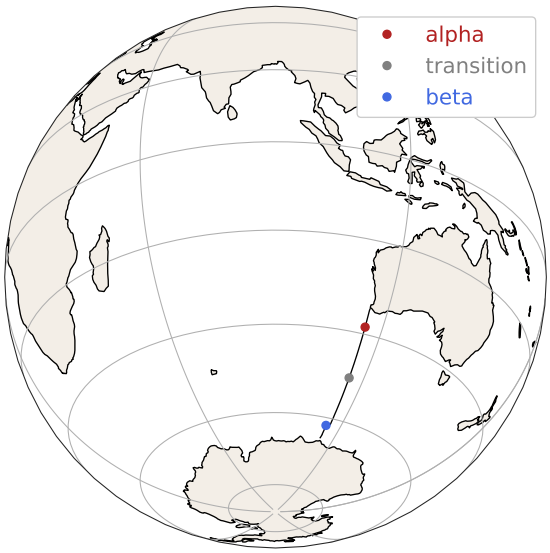

Figure 1.1: Location of the WOCE IO9S transect in the Southern Ocean. The three dots are the location of the profiles in Fig. 1.3. Figure adapted from Caneill and Roquet (2023).

1.1 Alpha – beta oceans

Temperature and salinity in the ocean vary horizontally and vertically. When looking at a transect of temperature and salinity between Australia and Antarctica along the IO9S section defined by the World Ocean Circulation Experiment (WOCE) (Fig. 1.1), two very different regimes are visible (Figs. 1.2 and 1.3). In the subtropical region, close to Australia, the surface temperature is warm (approximately 18 °C) and decreases with depth to about 10 °C at 400 m deep. Opposite, in the polar region, the near-surface temperature is −1 °C and increases with depth to 2 °C at 400 m. The transect of Figs. 1.2 and 1.3 has been measured in the summer, so a shallow warm layer occupies the upper 100 meters. The variation of temperature with depth thus follows an opposing pattern in subtropical regions (temperature decreases with depth) compared to polar regions (temperature increases with depth below the winter layer). Salinity follows a similar pattern as temperature: salinity decreases with depth in the subtropics, while in the polar region it increases with depth. These two opposite thermohaline structures have been called alpha and beta oceans by Carmack (2007), representative of subtropical and polar regions, respectively.

The density of seawater decreases with temperature and increases with salinity. Light water always lies above denser water in stable conditions. Thus, when temperature decreases with depth or salinity increases with depth, they contribute to stabilising the water column. Conversely, when temperature increases with depth or salinity decreases with depth, they decrease the stability of the water column. In an alpha ocean, temperature is thus the stabilising component, while salinity tends to decrease stability. It is the opposite in the beta ocean, where salinity is the stratifying component. In between the alpha and beta oceans lies a transition zone, which is usually quite narrow. Here, both temperature and salinity contribute to stability. The progression from al-

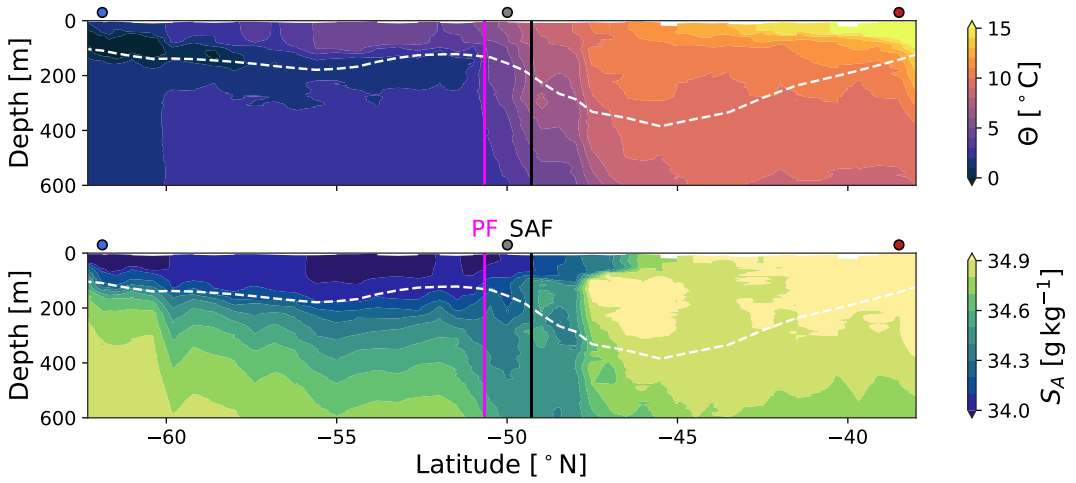

Figure 1.2: Temperature and salinity sections along the IO9S transect. Data are from the hydrographic cruise 09AR20120105 (CCHDO Hydrographic Data Office, 2023). The vertical lines mark the boundaries of, from north to south, alpha ocean, transition zone, and beta ocean. These boundaries are determined by the Subantarctic Front (SAF, black line) and the Polar Front (PF, purple line). The white and dashed line represents the climatological winter mixed layer depth (from de Boyer Montégut (2023)). Figure adapted from Caneill and Roquet (2023).

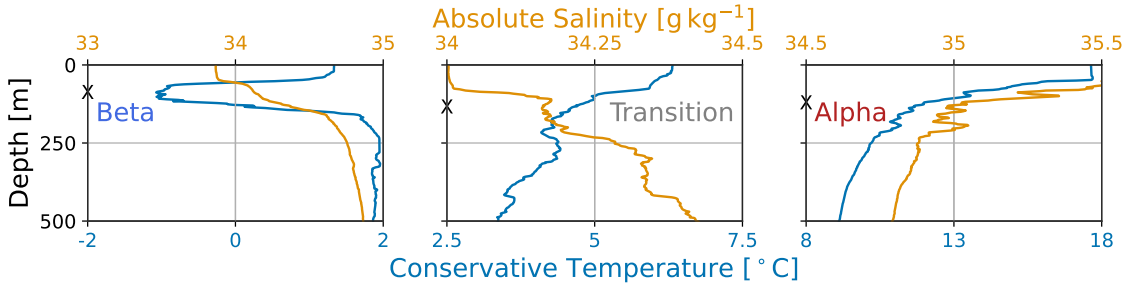

Figure 1.3: Profiles of temperature (blue) and salinity (orange). The three panels correspond to the three dots in Fig. 1.1. The black crosses on the left vertical axes represent the climatological winter mixed layer depth. Figure adapted from Caneill and Roquet (2023).

pha ocean to transition zone to beta ocean, from subtropical to polar regions is a remarkable feature found in the North Atlantic Ocean, the North Pacific Ocean, and the Southern Ocean (SO) (Pollard et al., 2002; You, 2002; Carmack, 2007; Stewart & Haine, 2016). Figure 1.4 presents the distribution of the different zones (adapted from Roquet et al. (2022)).

The alpha – beta distinction has multiple implications. Sea ice can only form if a strong halocline prevents heat-loss-driven convection, a condition found in the beta oceans (Carmack, 2007). At the same time, in the beta oceans, the reservoir of heat located at depth can limit sea-ice growth if the ML reaches this reservoir (Polyakov et al., 2013; Wilson et al., 2019). Sea ice increases the albedo of the ocean and creates feedback on the climate, so a decrease of sea ice in a warmer climate causes a general decrease of the ocean albedo and thus an increase in heat absorption (Curry et al., 1995). Antarctic and

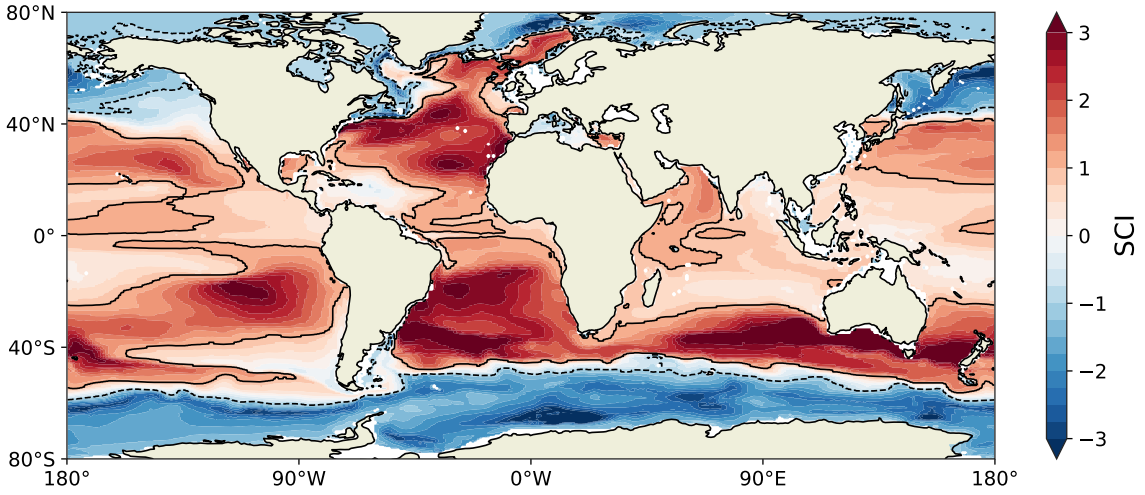

Figure 1.4: Distribution of the alpha oceans (red), beta oceans (blue), and transition zones (light colours). The solid (dashed) lines separate alpha (beta) oceans from transition zones. The zones are determined using the stratification control index below the mixed layer (defined in Chapter 2.4). Figure adapted from Roquet et al. (2022).

Arctic sea-ice extent and properties are changing, and so is the albedo (Perovich & Polashenski, 2012). A decrease in the beta oceans' extent could amplify the decrease in sea ice and, furthermore, amplify the response on the climate system.

The Nordic Seas are situated in a transition zone between the alpha and beta oceans, in which currents and deep water formation are largely impacted by freshwater fluxes (Lambert et al., 2018). Winter MLs are generally deeper in regions stabilised by temperature than when salinity stratifies, which makes the beta ocean able to re-stratify faster (Carmack, 2007). The Barents Sea encounters an increase in heat content induced by the advection of warm water from the Atlantic Ocean, which drives the decrease of sea ice (Årthun et al., 2012; Onarheim et al., 2015). In the Barents Sea, alpha and beta oceans are separated by the Polar Front, which, even if constrained by topography, has intensified since 2005 (Barton et al., 2018). In the global oceans, the transition zones seem to be key places highly sensitive to changes in climate and ocean circulation.

In alpha and beta oceans, when temperature and salinity effects on stratification partially compensate, the water column is subject to double diffusion, a process that contributes to interior mixing (Stern, 1960; Schmitt, 1994; You, 2002). In the transition zone, both temperature and salinity increase the stability; consequently, double diffusion does not occur there.

The permanent halocline characteristic of beta oceans is formed as polar regions encounter more precipitation than evaporation (Carmack et al., 2016; Pellichero et al., 2018). Added to this freshwater excess, the high-latitude ocean loses heat, so the surface temperature becomes cold. The opposite happens in the subtropics, where the ocean evaporates and gains heat, promoting the formation of the thermocline and high surface salinity. Carmack (2007) hypothesised that the thermodynamics of seawater could also play a major role

in the alpha – beta distinction. Yet, the mechanisms behind the alpha – beta distinction remain to be properly described.

1.2 Thermodynamics of seawater

Surface temperature and salinity vary because of, e.g., solar warming, evaporation, sea-ice formation or melt, precipitation, river runoff, and the exchange of heat with the atmosphere. In regions where water sinks to depth and loses contact with the atmosphere, the water masses keep their properties. As the mixing in the ocean interior is reduced compared to the changes induced by surface forcing, these properties are mostly conserved along the way. There are exceptions, such as close to the seafloor, where dissipation of internal waves enhances vertical mixing and thus the consumption of dense, deep water.

At the surface, the combined effects of temperature and salinity set the density of water. At depth, the pressure also impacts the density: while being almost incompressible, seawater density still increases with depth as the pressure becomes very large in the ocean interior. The function giving density from temperature, salinity, and pressure is called the equation of state (EOS). The EOS is a nonlinear relationship. The main nonlinearities arise from the dependence on temperature and pressure.

The temperature-induced nonlinearity makes the thermal expansion coefficient (TEC) vary with temperature and produces the following effect: a variation of 1 °C in temperature produces a different variation in density depending on the original temperature. In cold water, the density almost does not change with temperature changes, while it changes a lot in warm temperatures. At low salinities, water can even contract upon warming near the freezing point. Through this effect, when two water parcels with the same density but different compensating temperatures and salinities mix, the resulting water parcel becomes necessarily denser. This effect is called “contraction under mixing”, or cabbeling. The nonlinearity in pressure arises as the effect of temperature on density depends on the pressure (it can also be seen the other way around: the effect of pressure on density depends on temperature). The resulting effect, called thermobaricity, implies that two water parcels having the same density at a certain depth (but different temperature and salinity) will not have the same density as each other when the pressure changes.

Cabbeling and thermobaricity have been recognised as important contributions to interior water mass transformation in the ocean (Garrett & Horne, 1978; McDougall & You, 1990; Iudicone et al., 2008; Klocker & McDougall, 2010; Stewart & Haine, 2016; Groeskamp et al., 2016; Thomas & Shakespeare, 2015). Numerical simulations with modified equations of states have shown that the global circulation and properties are dependent on the used EOS and its nonlinearities (de Boer et al., 2007; Roquet et al., 2015b; Nycander et al., 2015). Rooth (1982), Bryan (1986), and Aagaard and Carmack (1989) pointed out that the decrease in thermal expansion in cold water is likely to enhance the role of salinity in polar regions. While looking at the effect of the EOS on global circulation, this thesis does, however, not focus on cabbeling and

thermobaricity, which are interior mixing processes, but rather on the surface forcing and how it might depend on the TEC.

1.3 Buoyancy fluxes, wind, and overturning

Density of water changes at the surface due to heat and freshwater fluxes. The change in density is quantified by the buoyancy fluxes, which have thermal and haline components coming from heat and freshwater fluxes, respectively. At the surface, for seawater with salinity above $25\,\mathrm{g\,kg^{-1}}$, the maximum density is always found at the freezing point ($\theta = -1.9\,^{\circ}\mathrm{C}$). This means that heat and freshwater gain decrease density (positive buoyancy fluxes). In contrast, heat and freshwater loss increase density (negative buoyancy fluxes). Heat and freshwater fluxes are often compensating as cooling regions tend to receive excess precipitations and vice versa. As a consequence, the buoyancy fluxes are the result of the competition between them (Schmitt et al., 1989).

The ocean is forced at its surface by buoyancy fluxes, which set density, and wind stress, that provides momentum and energy for mixing. The horizontal circulations in the gyres are mainly driven by the curl of wind stress induced by the so-called Sverdrup balance (Sverdrup, 1947; Stommel, 1948; Munk, 1950). However, by changing the density and thus the pressure field, buoyancy fluxes alone can also generate horizontal currents in geostrophic balance (e.g., de Verdière, 1988).

For a long time, buoyancy fluxes along with interior mixing were considered responsible for the overturning circulation in the ocean. Dense waters are formed at high latitudes sink and are consumed by vertical mixing in the interior (Stommel, 1958; Stommel & Arons, 1959; Stommel, 1961; Munk, 1966). However, measurements of vertical diffusivity in the ocean interior were one order of magnitude smaller than the one estimated to consume enough water and produce the observed overturning. Large vertical mixing is enhanced over rough topography and low elsewhere (Polzin et al., 1997).

Later, wind stress driving northward Ekman transport and upward Ekman suction in the SO has been recognised as the driver of an adiabatic overturning cell. The upwelling of water from the ocean interior towards the surface results in the steepening of isopycnals. Mesoscale eddies tend to flatten the isopycnals and counteract the effect of wind. Wind is thus considered the main driver of the upper cell of the overturning circulation (e.g., Toggweiler & Samuels, 1998; Wolfe & Cessi, 2010; Cessi, 2019). However, on the complete opposite view, numerical experiments have shown that in the presence of a reentrant channel, buoyancy fluxes alone could drive overturning and deep stratification (Barkan et al., 2013; Sohail et al., 2019; Klocker et al., 2023b).

In all cases, the SO is a central place for setting the general circulation. The next section describes this ocean.

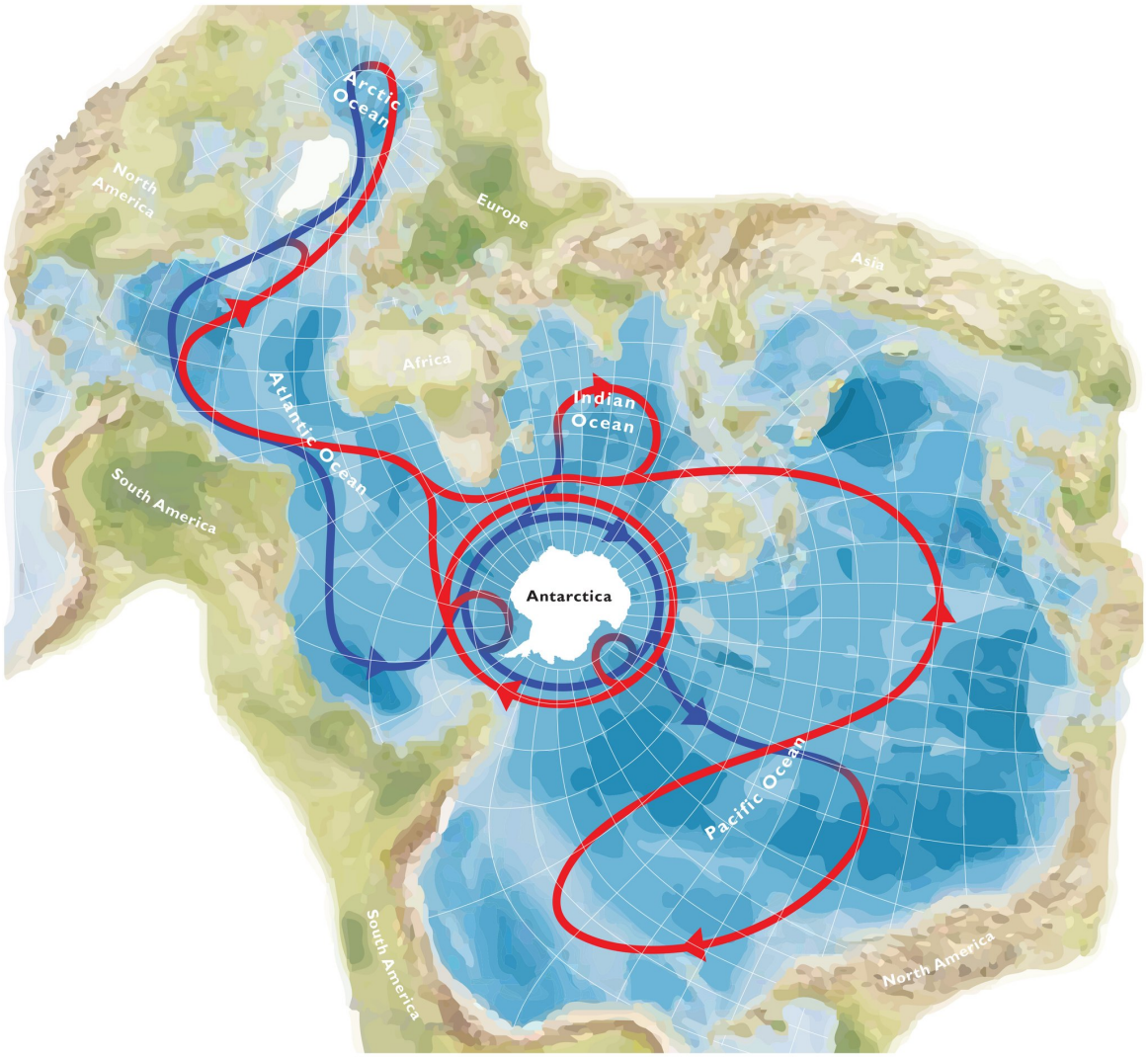

Figure 1.5: Splihaus projection of the world oceans. The arrows represent a highly simplified view of the global overturning circulation, with surface currents in red and deep currents in blue. The Southern Ocean appears to connect the Atlantic, Pacific, and Indian basins. Figure from Meredith (2019).

1.4 The Southern Ocean: a central point of the global circulation

The SO connects the three major basins of the global ocean: the Atlantic, Indian, and Pacific Oceans. This connection is best seen in the Spilhaus projection of the Earth's oceans, where it appears that all oceans are large water pools connected through the SO (Fig. 1.5, from Meredith (2019)). Each ocean has its own thermohaline properties, so these properties become linked through the SO.

The SO hosts the Antarctic Circumpolar Current (ACC), the world's largest oceanic current. The ACC flows without a meridional boundary blocking it and has a transport of about 135 Sv at the Drake passage (Cunningham et al., 2003). The ACC is zonally organised into fronts. These fronts have been historically

defined based on hydrographic properties (e.g., Emery, 1977; Whitworth, 1980), such as the geographical position of a certain isotherm at a certain depth (Belkin & Gordon, 1996). These fronts are thus defined as the boundaries of different water masses. Other definitions exist; instead of using a property, one can use a gradient, refining the idea of a boundary between water masses. With the era of satellite observations of sea surface height (SSH), other definitions arose, where fronts are defined as dynamical fronts, i.e., they correspond to the location of the jets that form the ACC. Indeed, horizontal gradients of SSH are directly linked to surface velocities through geostrophy. The two main fronts of interest in this thesis are the Subantarctic Front (SAF) and the Polar Front (PF). The SAF is closely linked to the northern boundary of the ACC, although its definition varies among the authors that define dynamic fronts. North of the SAF, deep MLs are found in winter, where the Subantarctic Mode Water (SAMW) originates. South of the SAF, a salinity minimum is found at depth, a marker specific for the Antarctic Intermediate Water (AAIW). The PF marks the northern extent of the cold Antarctic Surface Water. The SAF and PF indicate the boundary between alpha – transition and transition – beta, respectively (Pollard et al., 2002; Pauthenet et al., 2017).

The SO not only hosts a vigorous horizontal current but is also a key area of formation of intermediate and deep water, playing an important role in the global overturning circulation. Antarctic Bottom Water is mostly produced close to the coast of Antarctica, where sea ice is formed, producing dense, cold, and salty water that flows down to the bottom of the ocean. Intermediate waters consist of SAMW and AAIW and form the upper limb of the overturning circulation. These waters are formed north of the SAF and between the SAF and PF, respectively. MLs that are deeper than 250 m north of the SAF form the deep mixing band (DMB) (Dong et al., 2008; DuVivier et al., 2018). In winter, intense heat loss and the Ekman transport of cold water deepen the ML (Naveira Garabato et al., 2009; Holte et al., 2012; Rintoul & England, 2002). The SAMW originates from these deep MLs and reaches the permanent pycnocline through lateral advection (Belkin & Gordon, 1996; Speer et al., 2000; Hanawa & Talley, 2001; Sallée et al., 2010; Klocker et al., 2023a).

1.5 This thesis

We have seen that the boundaries between subtropical and subpolar regions, particularly in the SO, are central to the global circulation in the oceans and the climate. As the EOS is nonlinear, the effect of temperature on stratification and the effect of heat fluxes on buoyancy fluxes are not the same depending on the water temperature and, thus, depending on the region. The type of stratification is similar in all the polar regions, and the transition between alpha and beta is linked to intermediate water formation. The aim of this thesis is to assert the role of the local value of the TEC in modulating buoyancy fluxes and stratification strength, and thus to understand how this intrinsic property of seawater controls part of the large-scale state of the oceans. This thesis also contributes to the understanding and description of the SO fronts from

the perspective of stratification regimes. Finally, this thesis provides a general description of the alpha, beta, and transition zones in the global ocean.

We use a combination of numerical simulations in which we modify the EOS to assess the role of the TEC and how changing the buoyancy fluxes of thermal stratification modify the circulation and state of the ocean. We also combine observational data to produce climatologies of stratification (strength and regime) and buoyancy fluxes, which allows us to describe the processes from which the DMB and transition zones are arising.

Chapter 2 briefly describes the data and methods used in this thesis; more detailed descriptions are found in the attached papers. Based on **Papers I and II**, Chapter 3 presents how the interplay between buoyancy fluxes and summer stratification sets the winter stratification. Chapter 4 provides a summary of the major role of the local value of the TEC in shaping the ocean state, using **Papers I, II, and IV**. The global description of the stratification regimes is done in Chapter 5 (**Paper III**). Finally, conclusions and perspectives are given in Chapter 6.

Chapter 2

Data and methods

2.1 NEMO BASIN (Paper I)

This section presents the numerical model configuration used in **Paper I**. The reader is referred to the paper for all details. The Nucleus for European Modelling of the Ocean (NEMO) (Madec, 2019) ocean general circulation model (OGCM) is used to assess the role of surface buoyancy fluxes on the type of stratification of the subpolar regions.

The configuration represents an idealised basin with a size of 40° of longitude and 60° of latitude, with its southern boundary at the equator. A 1° longitude Mercator grid is used, and the topography is defined as slopes (Fig. 2.1a). To better represent the western boundary currents, we use a terrain following coordinate with 36 vertical levels, which allows the currents to adjust their vorticity by going up or down the boundary slope. The topography is flattened around the equator to minimise ageostrophic currents induced by the numerical schemes. No wall is present at the equator, but a no-meridional flux condition is applied. The turbulent kinetic energy (TKE) closure is used, with a background diffusivity of $10^{-4}\,\mathrm{m^2\,s^{-1}}$.

Heat and freshwater fluxes are represented using relaxation laws, so that analytical functions for the restoring values of temperature and salinity are provided. The heat flux is split into penetrative (solar) and non-penetrative components. The wind stress is zonally constant, with no meridional component. These forcing fields are inspired by Lévy et al. (2010) and Wolfe and Cessi (2014) and represent zonal averages over the ocean (Fig. 2.1).

Due to the low resolution of the configuration, it can be run for 2000 years until equilibrium is reached. The last 50 years are used for the analyses, either as global time averages or monthly averages.

A novelty of these simulations is the use of the simplified equation of state (EOS) proposed by Roquet et al. (2015b) (Eq. (2.1)). The thermal expansion coefficient (TEC), α, is linearly dependent on temperature and pressure (Eq. (2.2)), while the haline contraction coefficient (HCC), β, is constant (Eq. (2.3)).

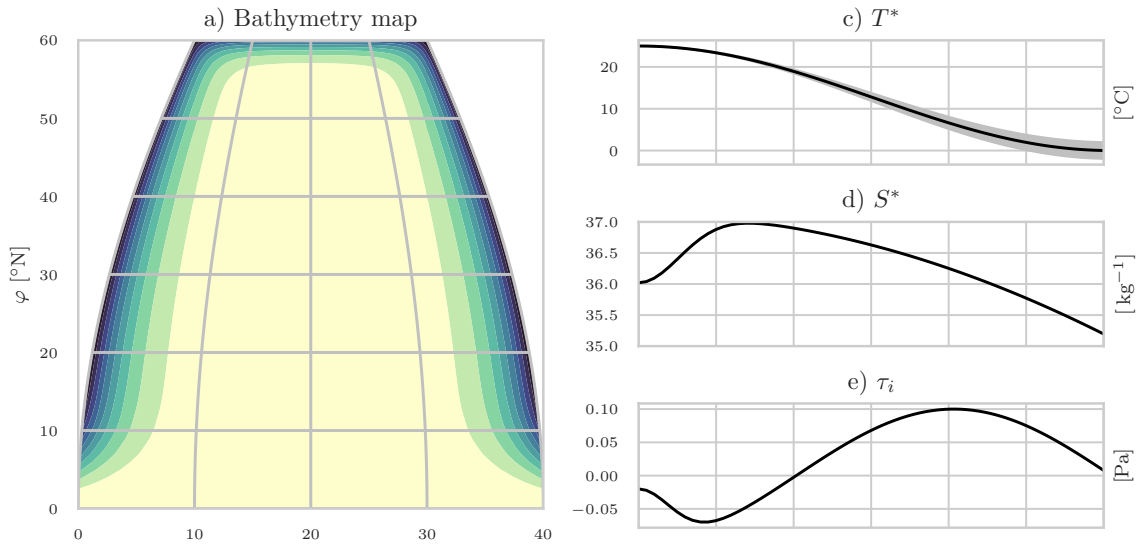

Figure 2.1: Bathymetry of the basin in a) and b). Forcing fields used by the model, with c) the restoring temperature, d) the restoring salinity, e) the zonal wind stress. The average values are plotted in black. For panels c), the gray zone represents the seasonal variations. Figure adapted from Caneill et al. (2022).

Coefficient	Value	Description
a_0	$1.65 \times 10^{-1}\,°\mathrm{C}^{-1}\,\mathrm{kg\,m}^{-3}$	linear thermal expansion coefficient
b_0	$7.6554 \times 10^{-1}(\mathrm{g/kg})^{-1}\mathrm{kg\,m}^{-3}$	linear haline expansion coefficient
C_b	$9.9 \times 10^{-3}\,°\mathrm{C}^{-2}\,\mathrm{kg\,m}^{-3}$	cabbeling coefficient
T_h	$2.4775 \times 10^{-5}\,°\mathrm{C}^{-1}\,\mathrm{dbar}^{-1}\,\mathrm{kg\,m}^{-3}$	thermobaric coefficient

Table 2.1: Default value of the simplified equation of state coefficients.

This allows us to adjust buoyancy fluxes and stratification by changing the parameters of the TEC, a_0 and C_b:

$$\rho(\Theta, S_A, p) = \rho_0 - \left(a_0 + \frac{1}{2}C_b\Theta_a + T_h p\right)\Theta_a + b_0 S_a \tag{2.1}$$

$$\alpha = \frac{1}{\rho_0}(a_0 + C_b\Theta_a + T_h p) \tag{2.2}$$

$$\beta = \frac{b_0}{\rho_0} \tag{2.3}$$

with $\Theta_a = \Theta - 10\,°\mathrm{C}$, $S_a = S_A - 35\,\mathrm{g\,kg}^{-1}$, and p the pressure.

Five combinations of parameters are used to test the sensitivity of stratification to annual buoyancy fluxes (Table 2.2).

Name	a_0 in $^\circ\mathrm{C}^{-1}\,\mathrm{kg\,m}^{-3}$	C_b in $^\circ\mathrm{C}^{-2}\,\mathrm{kg\,m}^{-3}$
ref	1.65×10^{-1}	9.9×10^{-3}
A	1.65×10^{-1}	13.2×10^{-3}
B	1.45×10^{-1}	8.7×10^{-3}
C	1.85×10^{-1}	11.1×10^{-3}
D	1.65×10^{-1}	6.6×10^{-3}

Table 2.2: The five combinations of parameters.

2.2 Buoyancy fluxes and Ekman transport of buoyancy (Papers I and II)

Surface buoyancy fluxes are an essential component of global circulation, as they modify water density. Thus, they are calculated both for the model simulations and from observations. They are derived from heat and freshwater fluxes (e.g., Gill & Adrian, 1982):

$$\mathcal{B}^{surf} = \underbrace{\frac{g\alpha}{\rho_0 C_p} Q_{tot}}_{\mathcal{B}_\Theta^{surf}} \underbrace{- \frac{g\beta S}{\rho_0}(E - P - R)}_{\mathcal{B}_S^{surf}} \tag{2.4}$$

where g is the gravitational acceleration, $C_p \simeq 3997\,\mathrm{J\,kg}^{-1}\,\mathrm{K}^{-1}$ the heat capacity of seawater, Q_{tot} the total heat flux in $\mathrm{W\,m}^{-2}$, E the evaporation, P the precipitation, R the river runoff all in $\mathrm{kg\,m}^{-2}\,\mathrm{s}^{-1}$, and S the surface salinity. The buoyancy fluxes $\mathcal{B}^{Surf}$ are in $\mathrm{m}^2\,\mathrm{s}^{-3}$. Buoyancy fluxes are heat and freshwater fluxes scaled by α and β, respectively.

In **Paper I**, heat and freshwater fluxes are outputs of the NEMO simulations. In **Paper II**, we used observations based on a mixture of different products to compute the heat and freshwater fluxes in the Southern Ocean (SO). The Objectively Analyzed Air-Sea Fluxes (OAflux) 1-degree dataset (Yu & Weller, 2007) provides turbulent heat fluxes and evaporation. The third generation International Satellite Cloud Climatology Project monthly means (ISCCP-FH MPF) provides radiative fluxes (Schiffer & Rossow, 1983; Rossow & Schiffer, 1999). The Global Precipitation Climatology Project (GPCP) Version 2.3 provides precipitation (Adler et al., 2018). We used river runoff from Estimating the Circulation and Climate of the Ocean (ECCO) Version 4, Release 4 (Forget et al., 2015). The reader is referred to **Paper II** for a more detailed description of the datasets used. Due to the difficulties of computing turbulent fluxes, following Schanze and Schmitt (2013), we removed the global average (time, longitude, and latitude) of the heat and freshwater fluxes to get a balance. We then define a cooling season (CS) from April to September in the SO for estimating the buoyancy loss.

The Ekman transport advects cold and fresh water northward in the SO; this

effect is taken into account by calculating the Ekman transport of buoyancy:

$$\mathcal{B}_\Theta^{Ek} = -\frac{g\alpha}{\rho_0 f}\left(\tau^y \frac{\partial \Theta}{\partial x} - \tau^x \frac{\partial \Theta}{\partial y}\right) \tag{2.5}$$

$$\mathcal{B}_S^{Ek} = \frac{g\beta}{\rho_0 f}\left(\tau^y \frac{\partial S}{\partial x} - \tau^x \frac{\partial S}{\partial y}\right) \tag{2.6}$$

with τ^x and τ^y the eastward and northward wind stress, respectively, and f the Coriolis parameter. The fluxes $\mathcal{B}_\Theta^{Ek}$ and $\mathcal{B}_S^{Ek}$ are contained within the Ekman layer. When making the commonly used assumption that the Ekman layer is entirely contained within the mixed layer (ML), the total buoyancy flux, $\mathcal{B} = \mathcal{B}^{Ek} + \mathcal{B}^{surf}$, is the buoyancy flux to the ML. We used daily averages from the CMEMS "Global Ocean Wind L4 Reprocessed 6 Hourly Observations" for wind stress and ARMOR3D weekly product (Guinehut et al., 2012) for computing temperature and salinity gradients.

2.3 Columnar buoyancy (Paper II)

We use columnar buoyancy (CB) as an indicator of stratification strength (Lascaratos & Nittis, 1998; Herrmann et al., 2008):

$$CB(Z) = \int_Z^0 -zN^2(z)\mathrm{d}z \tag{2.7}$$

with the z-axis oriented upward, Z the depth at which the CB is computed, and $N^2(z) = -\frac{g}{\widetilde{\rho_\theta}}\frac{\partial \widetilde{\rho_\theta}}{\partial z}$ the squared buoyancy frequency. $\widetilde{\rho_\theta}$ is the locally referenced potential density (Vallis, 2017). In our case, using potential density reference at the surface instead of locally referenced potential density to compute $N^2(z)$ leads to negligible differences. This way, the formula can be expressed by using density profiles instead of doing two numerical operations (differentiation followed by summation). Integration by parts of Eq. (2.7) then gives:

$$CB(Z) \simeq \frac{g}{\rho_0}\int_Z^0 \left[\rho_\theta(Z) - \rho_\theta(z)\right]\mathrm{d}z \tag{2.8}$$

The CB is positive in a stable stratification. It represents the amount of buoyancy that must be lost to produce a ML of depth Z and of potential density $\rho_\theta(Z)$. Dividing it by a time gives the buoyancy flux that must be applied during this time to form this ML, called B_Z (Faure & Kawai, 2015). We only consider B_Z to the depth of 250 m (i.e., B_{250}), which is the threshold for defining deep ML used by DuVivier et al. (2018):

$$B_{250} = \frac{-CB(-250)}{\Delta t} \tag{2.9}$$

The ocean loses buoyancy during six months of the year, so to allow a direct comparison between the mean buoyancy loss and stratification, we took six months for Δt.

B_{250} can be split into the thermal and haline components to quantify their individual effects:

$$B_{250} = \underbrace{\frac{g}{\Delta t}\int_{-250}^{0}\alpha(z)\frac{\partial\Theta}{\partial z}z\mathrm{d}z}_{B_{250}^{\Theta}} \underbrace{-\frac{g}{\Delta t}\int_{-250}^{0}\beta(z)\frac{\partial S}{\partial z}z\mathrm{d}z}_{B_{250}^{S}} \tag{2.10}$$

In **Paper II**, B_{250} is computed using the Monthly Isopycnal & Mixed-layer Ocean Climatology (MIMOC) in depth coordinates produced by Schmidtko et al. (2013).

2.4 Stratification Control Index (Papers I, III, and IV)

To compare the relative impact of temperature and salinity on stratification strength, we define the stratification control index (SCI):

$$SCI = \frac{N_\Theta^2 - N_S^2}{N_\Theta^2 + N_S^2} \tag{2.11}$$

$$N^2 = -\frac{g}{\rho_0}\frac{\partial\rho_\Theta}{\partial z} = N_\Theta^2 + N_S^2 \tag{2.12}$$

$$N_\Theta^2 = g\alpha\frac{\partial\Theta}{\partial z} \tag{2.13}$$

$$N_S^2 = -g\beta\frac{\partial S_A}{\partial z}\,. \tag{2.14}$$

N_Θ^2 and N_S^2 are the thermal and haline components of the squared buoyancy frequency N^2. A negative value of N_Θ^2 (N_S^2) means that temperature (salinity) has a destabilising effect. We only consider stable stratification ($N^2 > 0$), so if temperature or salinity has a destabilising effect, it means that the other property compensates and has a larger stratifying effect. The SCI is the tangent of the Turner angle ($SCI = \tan(Tu)$) (Ruddick, 1983).

The SCI catches states of no temperature or no salinity stratification:

$$N_\Theta^2 = 0 \implies SCI = -1 \tag{2.15}$$

$$N_S^2 = 0 \implies SCI = 1 \tag{2.16}$$

Thus, temperature has a stratifying effect when $SCI > -1$. Salinity follows a symmetrical pattern and stratifies when $SCI < 1$. We can define three zones bounded by $SCI = \pm 1$ and characterised by different thermohaline stratification regimes. We use these three zones for the definition of alpha ocean, transition zone, and beta ocean:

- *alpha ocean* when $1 < SCI$,
- *transition zone* when $-1 \leq SCI \leq 1$,
- *beta ocean* when $SCI < -1$.

The SCI can be computed at any depth below the ML, but as we mainly focus on the permanent pycnocline, we compute the SCI just below the winter ML. In the definition that Carmack (2007) proposed, alpha (beta) means that temperature (salinity) stratifies. According to this definition, the $-1 \leq SCI \leq 1$ region would thus be both alpha and beta. Stewart and Haine (2016) proposed a definition of the transition zone based on the Turner angle at each location and date. Their transition zones are defined as where the stratification seasonally evolves between being mainly stratified by temperature and being mainly stratified by salinity. "Transition" is thus to be understood as "alternating" for them, while in our definition, "transition" means "doubly stratified", in contrast to the alpha and beta oceans where a partial compensation occurs between temperature and salinity.

In **Papers I and IV** the SCI has been computed from the models' monthly outputs (NEMO BASIN and ECCO) and in **Paper III** it has been computed on each individual profile of the EN4 database (Sect. 2.5).

2.5 EN4 and radial basis function interpolation (Paper II)

Paper III uses the EN.4.2.2 (Good et al., 2013) ensemble members using Gouretski and Cheng (2020) MBT and Gouretski and Reseghetti (2010) XBT corrections. To remove spikes prior to computing the vertical gradient, the profiles have been smoothed and re-sampled to a regular vertical grid (Johnson et al., 2002) (more details are given in **Paper III**).

The mixed layer depth (MLD) is computed using a density threshold criteria of $0.03\,\mathrm{kg\,m^{-3}}$ referenced to 10 m depth (de Boyer Montégut, 2004). The SCI is then computed using the temperature and salinity values at 10 m and 30 m under the ML. The MLD and SCI are then gridded onto a regular longitude – latitude grid for each month using a radial basis function (RBF) interpolation. The class *scipy.interpolate.RBFInterpolator* from the Python *scipy* library is used (Virtanen et al., 2020).

To account for the anisotropy between the longitude and latitude scale factors, the latitude (φ) is transformed by a Mercator projection, using the following formula:

$$\varphi' = \ln\Big(\tan\Big(\frac{\varphi}{2}\frac{\pi}{180} + \frac{\pi}{4}\Big)\Big) \cdot \frac{180}{\pi} \tag{2.17}$$

This will virtually increase the difference in latitude between two points located in polar regions, so that longitude and latitude become isotropic.

To find a balance between accuracy and computation efficiency, the closest 300 points around each grid point are selected for the interpolation using the distance d:

$$d^2 = \left[\frac{\Delta\lambda}{L_\lambda}\right]^2 + \left[\frac{\Delta\varphi'}{L_{\varphi'}}\right]^2 + \left[\frac{\Delta t}{L_t}\right]^2 \tag{2.18}$$

with $\Delta\lambda$ the difference of longitude between the grid point and the measurement point, $\Delta\varphi'$ the difference of modified latitude, and Δt the number of days of difference between the measurement and the interpolation date. The three Ls express the decorrelation scales for longitude (L_λ), modified latitude ($L_{\varphi'}$) and

time (L_t). The three decorrelation scales have been chosen as: $L_\lambda = L_{\varphi'} = 3.3°$, and $L_t = 45\,\mathrm{d}$, similar to the coefficient used to produce the MIMOC database (Schmidtko et al., 2013). We used a Gaussian function for the interpolation kernel.

Chapter 3

The interplay of buoyancy fluxes and upper ocean stratification key to formation of deep mixed layers (Papers I and II)

3.1 Context

At the surface of the ocean, fluxes of heat and freshwater induce a change in density, and they can thus be converted into buoyancy fluxes. Winter surface buoyancy loss due to heat produces dense water in the Nordic Seas (Isachsen et al., 2007; Petit et al., 2020) and deepens the mixed layer (ML) in the Southern Ocean (SO), producing Subantarctic Mode Water (SAMW), a process further enhanced by Ekman transport of cold water (Naveira Garabato et al., 2009; Holte et al., 2012; Rintoul & England, 2002). On the other hand, an increase in freshwater fluxes can dampen the formation of intermediate or deep water, as in the Labrador Sea (Lazier, 1980).

Buoyancy fluxes impact the transformation of water masses (Walin, 1982; Speer et al., 2000; Kuhlbrodt et al., 2007; Cessi, 2019), as well as the rate of formation of deep water in the North Atlantic basin (Mauritzen & Häkkinen, 1999). Water mass transformations can arise from surface buoyancy fluxes but also from diffusive or advective fluxes. In subpolar to polar regions, heat is lost in winter and freshwater is gained from precipitations. This is thus a balance between these two components that sets the final buoyancy fluxes (Schmitt et al., 1989). Moreover, both haline and thermal components of buoyancy fluxes must be studied separately in water mass transformation studies (Speer et al., 1995; Karstensen & Lorbacher, 2011).

3.2 The deep mixing band and its ventilation role

In winter in the SO, a belt of MLs deeper than 250 m is located north of the Subantarctic Front (SAF) (Fig. 3.1 and Dong et al. (2008)). The belt

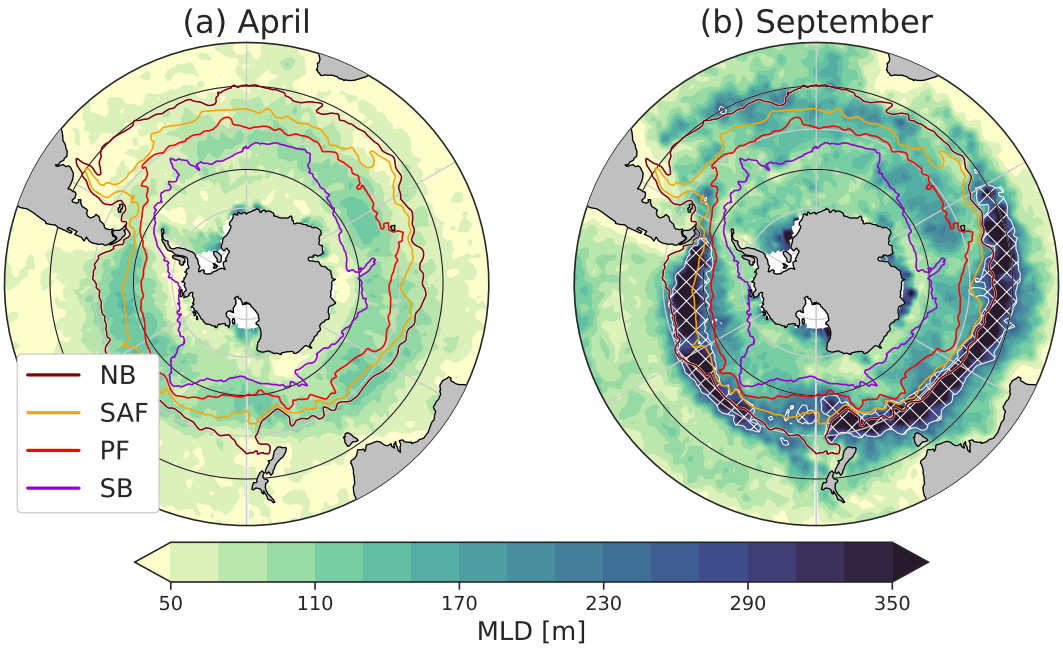

Figure 3.1: Climatology of the mixed layer depth in the Southern Ocean in (a) April and (b) September. The area hashed in white represents the deep mixing band, where the mixed layers are deeper than 250 m. The main fronts of the Southern Ocean are also plotted. The mixed layer depths are from de Boyer Montégut (2023) and the fronts from Park et al. (2019). Figure adapted from Caneill et al. (2023).

is referred to as the deep mixing band (DMB) (DuVivier et al., 2018). The DMB is important for the global stratification structure of the ocean, as the SAMW is formed when water escapes the DMB by lateral induction (Belkin & Gordon, 1996; Speer et al., 2000; Hanawa & Talley, 2001; Klocker et al., 2023a). SAMW is thus formed through a mixture of air-sea fluxes and Ekman transport (Sloyan & Rintoul, 2001). SAMW takes up a large amount of anthropogenic carbon dioxide (CO_2) (Sabine et al., 2004), so it is important to understand the processes of its formation. SAMW constitutes a significant part of the upper limb of the global overturning circulation and thus is able to transport its properties (CO_2, heat, etc) to depth (Sloyan & Rintoul, 2001). The DMB is found in the Indian and Pacific sectors of the SO. It has been found that winter heat loss is the main driver of ML deepening within the DMB and that the transport of cold water by Ekman transport intensifies buoyancy loss (Naveira Garabato et al., 2009; Holte et al., 2012; Rintoul & England, 2002). However, the question of why it is so narrow is still not fully answered, and any unique component of surface forcing is not able to explain it (e.g., wind stress, wind stress curl, buoyancy flux, or mesoscale eddy activity) (DuVivier et al., 2018).

3.3 Annual buoyancy fluxes set the position of the polar transition zone (Paper I)

In **Paper I**, our idealised simulations (Chapter 2.1) are able to reproduce an ocean with two different stratification types: alpha in the subtropics and beta in the polar region. The alpha – beta boundary is oriented along a north-east diagonal (**Paper I**, Fig. 5c) and is similar to the North Atlantic polar transition zone (PTZ). A single region of convection is present, as only one hemisphere was represented. This region of deep MLs is located on the northern flank of the alpha ocean and contains the densest surface water. The deepest MLs reach the bottom, as no denser water is present. As these dense waters are formed between the subtropical and subpolar gyres, they are equivalent to the mode and intermediate waters of the SO. In the beta ocean, the winter ML is shallower than 200 m due to the large stratification induced by freshwater.

Deep MLs are formed in a region of annual buoyancy loss, and the beta ocean is encountering annual buoyancy gain. This buoyancy gain comes from positive freshwater fluxes having a greater effect than heat loss on buoyancy fluxes. By changing the equation of state (EOS) as a way to change the relative importance of freshwater and heat on buoyancy fluxes, we show that the transition between the alpha and beta oceans is located close to the position where the sign of the annual buoyancy fluxes changes. Moreover, convection occurs systematically on the northern flank of the alpha ocean and is thus bounded to the north by the PTZ. A schematic view of the process leading to the formation of the transition is drawn in Figure 3.2. After leaving the subtropics, surface water that flows poleward within the western boundary current enters a region of annual buoyancy loss driven by intense heat loss. Along its way, the ML deepens until the water enters a region of annual buoyancy gain. In this region, the ML becomes shallower, and a freshwater cap is able to build up, preventing convection from occurring. The intermediate water formed in the deep ML region is then advected equatorward, although it is also associated with a cyclonic flow in the north before flowing equatorward at the western boundary at depth.

The buoyancy gain in beta ocean is driven by positive freshwater fluxes, while the thermal component of buoyancy fluxes becomes small. The thermal component becomes small not because of a reduction of heat fluxes but, on the contrary, because of the decrease in the thermal expansion coefficient (TEC) in cold water. Chapter 4 describes our findings on the impact of TEC variations on global ocean circulation and climate.

The wind forcing was identical in each experiment, and similar results were obtained when using a linear EOS or when removing seasonal variations of the forcing fields. This paper demonstrates the role of buoyancy forcing in setting the ocean's large-scale stratification and the region of intermediate water formation.

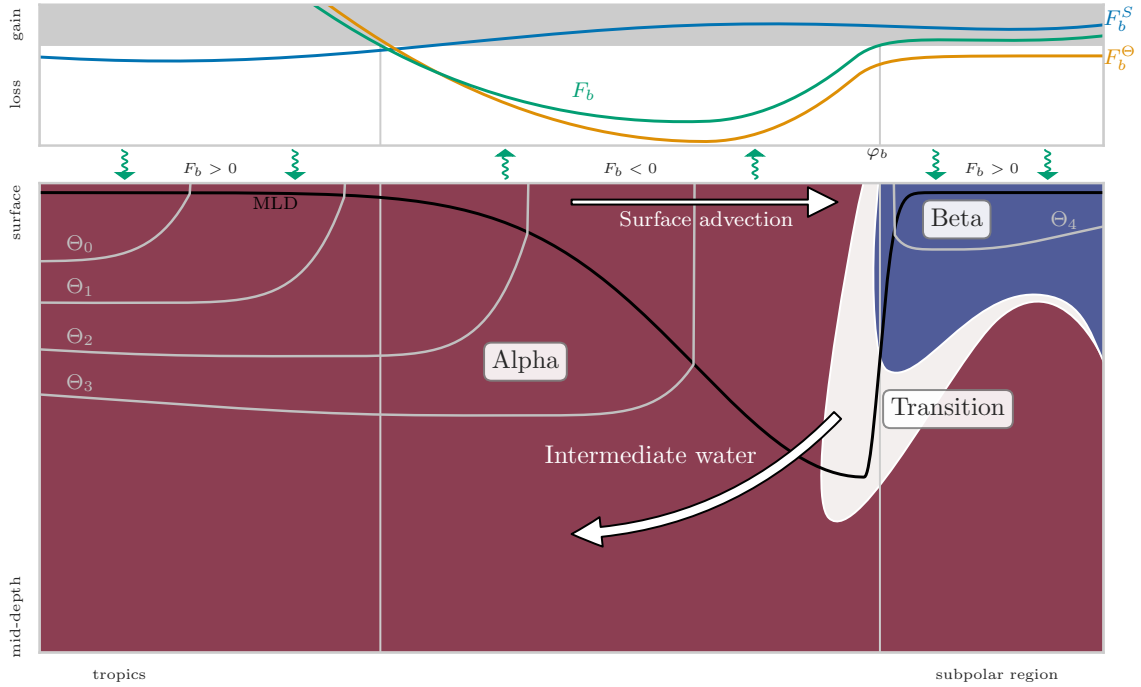

Figure 3.2: Conceptual view of the ocean. The upper panel represents annual buoyancy fluxes (F_b, green line) and its thermal (F_b^Θ, orange line) and haline (F_b^S, blue line) components. The green wavy arrows go upward when the ocean is losing buoyancy and they go upward when it is gaining it. In the bottom panel, the black line represents the mixed layer depth, red colours are for alpha ocean, white colours for transition zone, and blue colours for beta ocean. Figure from Caneill et al. (2022)

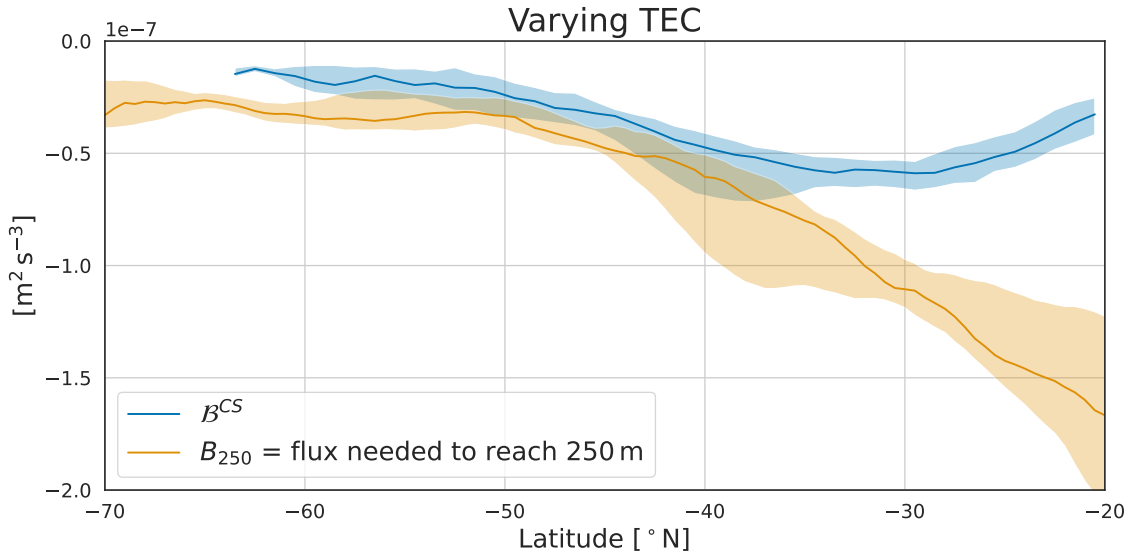

Figure 3.3: Buoyancy loss during the cooling season ($\mathcal{B}^{CS}$, blue line) and stratification strength (B_{250}, orange line). The lines are zonal medians and the shadings are the first and third quartiles. The deep mixing band can occur where the two shaded curves cross. Figure adapted from Caneill et al. (2023).

3.4 Balance between seasonal buoyancy loss and stratification sets the deep mixing band (Paper II)

Processes of the SO, e.g., the Antarctic Circumpolar Current (ACC), large eddy activity, and sea ice, are not represented in the idealised basin model used in **Paper I**. We thus asked whether the existence and position of the DMB present in the SO could still be directly linked to buoyancy fluxes. For this, we computed climatologies of buoyancy fluxes and stratification based on observations (Chapters 2.2 and 2.3). A good correlation is found between annual surface buoyancy fluxes and the position of the DMB (Fig. 3c of **Paper II**). When adding Ekman buoyancy fluxes (Fig. 3i of **Paper II**), the DMB is located in the region of continuous buoyancy loss. South of it, the ocean is either positive or alternating between positive and negative in a patchy way. However, annual buoyancy loss in a region does not necessarily imply deep MLs in this region.

To fully explain the position of the DMB, one needs to take both the cooling season (CS) buoyancy loss and the summer stratification into account. Indeed, all the CS buoyancy loss erodes the summer stratification to produce the ML deepening. We found that the DMB is not necessarily located in areas of maximum CS buoyancy loss nor at the minimums of stratification (Fig. 3.3 and Fig. 3.4a and b). However, the DMB is systematically located where the CS buoyancy loss exceeds the stratification quantified by B_{250} (Fig. 3.4c). It results in a narrow band where the buoyancy loss can overcome the stratification. North of the DMB, the stratification is too large, and south of it, despite a small stratification, the buoyancy loss is too small. As in **Paper I**, we show here that the buoyancy loss is small because of the decrease in the TEC (Chapter 4) and not a decrease in heat loss. In regions of large advection of tropical water, as e.g., in the Agulhas Current, highly stratified water is continuously advected. Despite large heat losses, this blocks the formation of deep MLs.

3.5 Summary

Based on idealised numerical simulations and observations, this chapter explores the strong influence that buoyancy fluxes exert on the upper ocean stratification, summarised here:

- The deep MLs are found in regions of annual buoyancy loss at mid-latitudes. Poleward of these regions, the buoyancy flux is positive, and the oceans are losing heat and gaining freshwater. This allows for the formation of the halocline constituent of the beta oceans.
- The wind is found to not be of primary importance in setting the different stratification regimes. Wind stress forces the large-scale gyre circulation, but buoyancy fluxes directly impact the density and the stratification.
- The buoyancy loss during the CS fights against the summer stratification to deepen the ML. It is the balance between these two processes that,

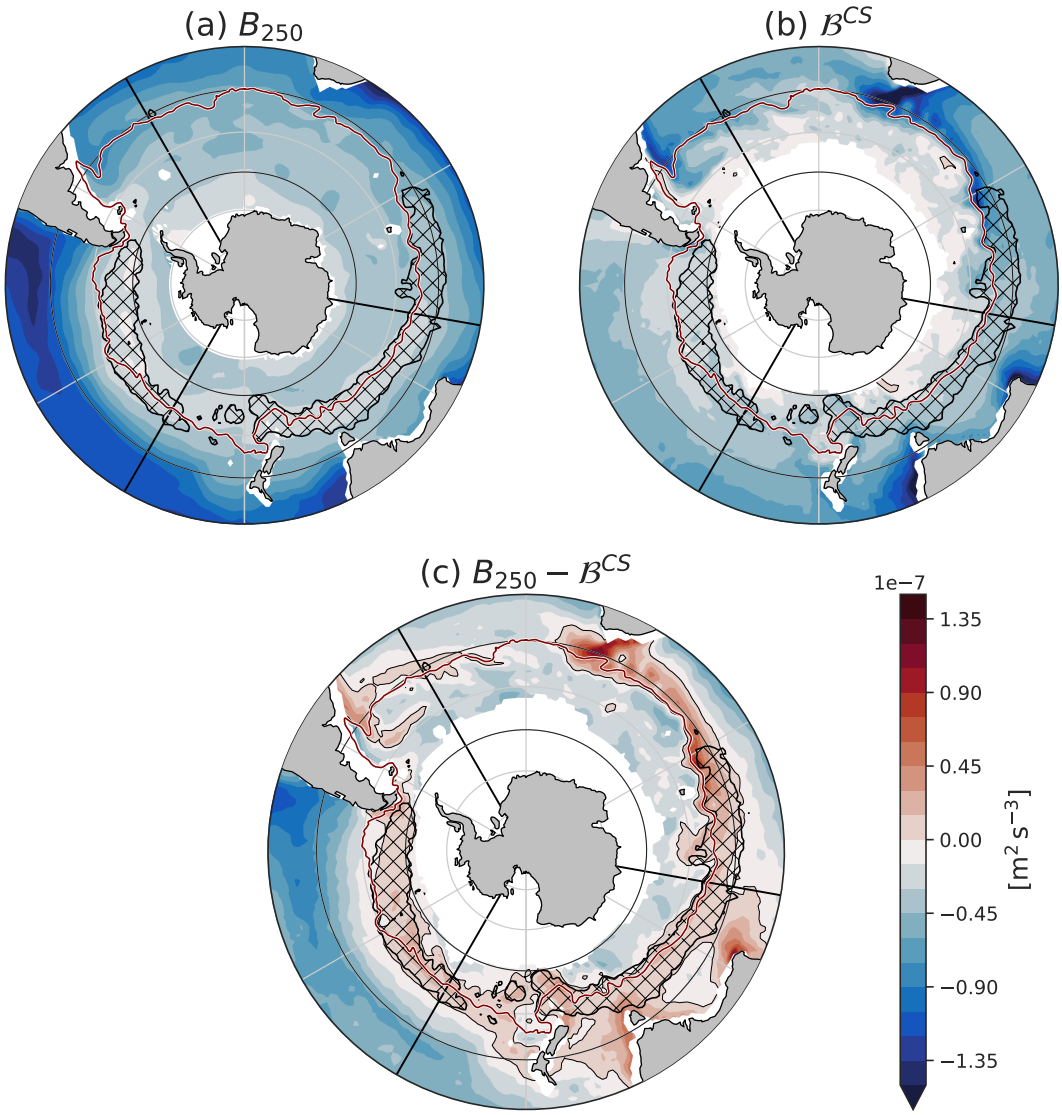

Figure 3.4: Climatology of (a) stratification strength, (b) buoyancy loss during the cooling season, and (c) the difference between them. The area hatched in black represent the observed deep mixing band. Figure adapted from Caneill et al. (2023).

eventually, sets the position of the deep MLs and ventilation regions. However, this balance is only valid away from regions where the western boundary currents advect highly stratified subtropical water and block the deepening of the ML.

- On the whole, buoyancy fluxes strongly constrain the possible regions of formation of deep MLs and, at the same time, control the upper ocean stratification regimes.

Chapter 4

The effects of the variable thermal expansion coefficient (Papers I, II, and IV)

4.1 Context

The thermal expansion coefficient (TEC), α, quantifies the relative change of density associated with a change of temperature:

$$\alpha(\Theta, S_A, p) = -\frac{1}{\rho} \left.\frac{\partial \rho}{\partial \Theta}\right|_{S_A,p} \tag{4.1}$$

where ρ is the water density, Θ the Conservative Temperature, S_A the Absolute Salinity, and p the pressure (Roquet et al., 2015a; IOC et al., 2015).

Freshwater temperature has the rare property that its density is maximal around 4 °C at a pressure of 0 dbar. This implies that the TEC is negative below 4 °C for freshwater (Fig. 4.1). A direct implication of this property is that dimictic lakes have a bottom temperature of 4 °C all year long. However, the salinity of water in the oceans is greater than $30\,\mathrm{g\,kg^{-1}}$, except in some small regions, e.g., the Baltic Sea. The effect of salinity on the TEC is to increase it, so in the oceans, the TEC is always positive (Fig. 4.1). Despite being positive, the TEC varies on the surface of the oceans, following an almost linear relationship with the sea surface temperature (SST), and is about ten times smaller at −2 °C than at 30 °C (Figs. 4.1 and 4.2). The variation of the TEC with temperature is the origin of the so-called cabbeling effect (described as "contraction under mixing") (McDougall, 1987). The TEC is a function of pressure, which leads to an effect called thermobaricity. Isopycnal diffusion leads to diapycnal advection because of cabbeling and thermobaricity, which in turn impacts water mass transformation (Garrett & Horne, 1978; McDougall & You, 1990; Iudicone et al., 2008; Klocker & McDougall, 2010; Thomas & Shakespeare, 2015; Stewart & Haine, 2016; Groeskamp et al., 2016).

The temperature dependence of the TEC is not only a scientific curiosity, as it makes polar water density less sensitive to temperature changes than warm

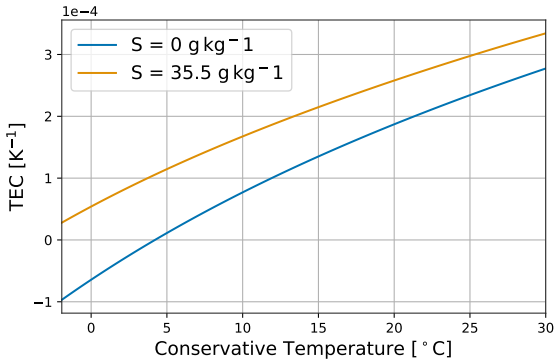

Figure 4.1: Thermal expansion coefficient function of Conservative Temperature at a pressure of $0\,\mathrm{dbar}$. To highlight the role of salinity, two constant values for the Absolute Salinity are used: $0\,\mathrm{g\,kg^{-1}}$ (blue line) and $0\,\mathrm{g\,kg^{-1}}$ (orange line). Figure adapted from Caneill et al. (2023).

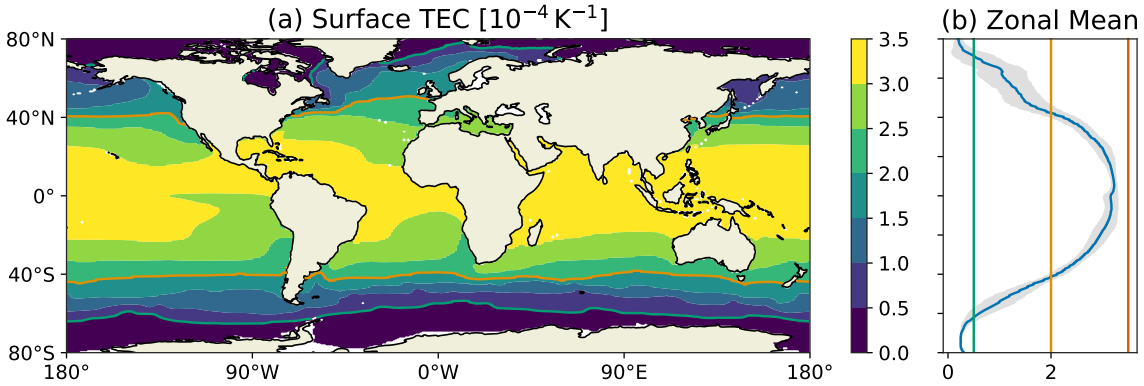

Figure 4.2: Map of the surface thermal expansion coefficient (a) and its zonal mean (b). The thermal expansion coefficient value is highly correlated with the sea surface temperature and shows almost an order of magnitude of variation in the oceans. The figures are based on ECCO. Figure adapted from Roquet et al. (2022).

water. As a result, salinity becomes more important in setting stratification in polar regions, and the importance of heat fluxes in buoyancy fluxes within polar regions is reduced (Rooth, 1982; Bryan, 1986; Aagaard & Carmack, 1989; Roquet et al., 2015b). Changes in the TEC value and variations impact the global circulation of the ocean (Roquet et al., 2015b; Nycander et al., 2015). The ocean gains heat in warm regions, and loses heat in cold regions, thus gaining more buoyancy (due to a large value of the TEC in warm water) than it loses (due to a small value of the TEC in cold water). With a balanced heat flux, this implies that the global buoyancy budget is positive (Garrett et al., 1993; Zahariev & Garrett, 1997; Hieronymus & Nycander, 2013). In a steady state, this positive budget of buoyancy fluxes thus balances the interior consumption of buoyancy by cabbeling. At a seasonal scale, variations of the TEC modulate the impact of summer and winter heat fluxes, so seasonal variations in the TEC increase the global buoyancy flux by 35% (Schanze & Schmitt, 2013).

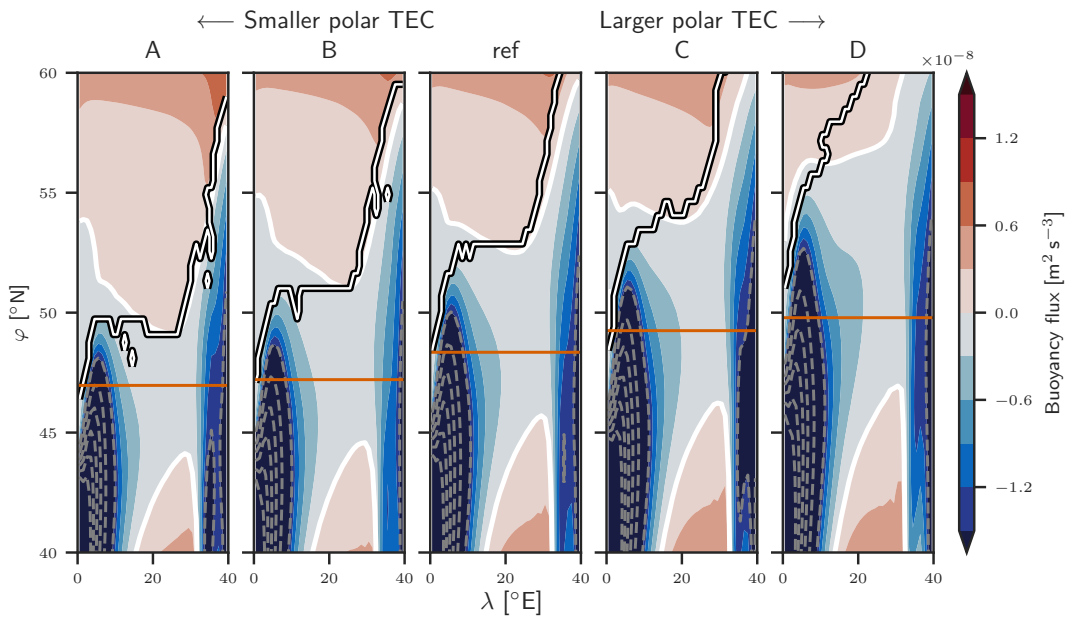

Figure 4.3: Annual buoyancy flux for every model run, ordered from lower to larger polar thermal expansion coefficient value. The white line with black contour represents the boundary between the alpha and beta oceans. Figure from Caneill et al. (2022).

4.2 The thermal expansion coefficient dampens the effect of heat fluxes in polar region (Papers I and II)

With the set of numerical experiments in **Paper I**, we were able to modify the value of the TEC in the subpolar region, thus subsequently changing the contribution of heat fluxes to buoyancy fluxes. As noted in earlier studies, the small polar value of the TEC is likely to weaken the contribution of heat fluxes (Rooth, 1982; Bryan, 1986; Aagaard & Carmack, 1989; Cerovečki et al., 2011), but this effect had not been intrinsically studied before. While keeping the same restoring conditions, an increased value of the TEC in the subpolar region of our basin led to a shrinking of the region of buoyancy loss towards the north. The buoyancy loss is driven by heat loss and counterbalanced by freshwater gain. When more importance is given to heat loss (through increased TEC), the polar area where buoyancy is gained decreases in size. This is what is observed in the basin runs (Fig. 4.3). When the buoyancy flux inversion gets pushed northward, the position of the polar transition zone (PTZ) follows.

In **Paper II**, based on heat flux products derived from observations, we computed the buoyancy fluxes of the cooling season (CS) in the SO, both with the varying TEC and with α_0, a constant TEC representative of 40°S (Fig. 4.4a and b). Intense winter heat loss is driving the CS buoyancy loss in the Southern Ocean (SO). Taking the constant TEC increases the contribution of heat fluxes in the total buoyancy fluxes south of 40°S, where the surface water is colder than the reference value and hence the TEC is smaller. Opposite, north of 40°S, the constant TEC is smaller than what it should be, reducing the contribution of heat fluxes. The actual CS buoyancy loss using the varying TEC has a maximum intensity at 30°S and becomes abruptly close to zero south of it

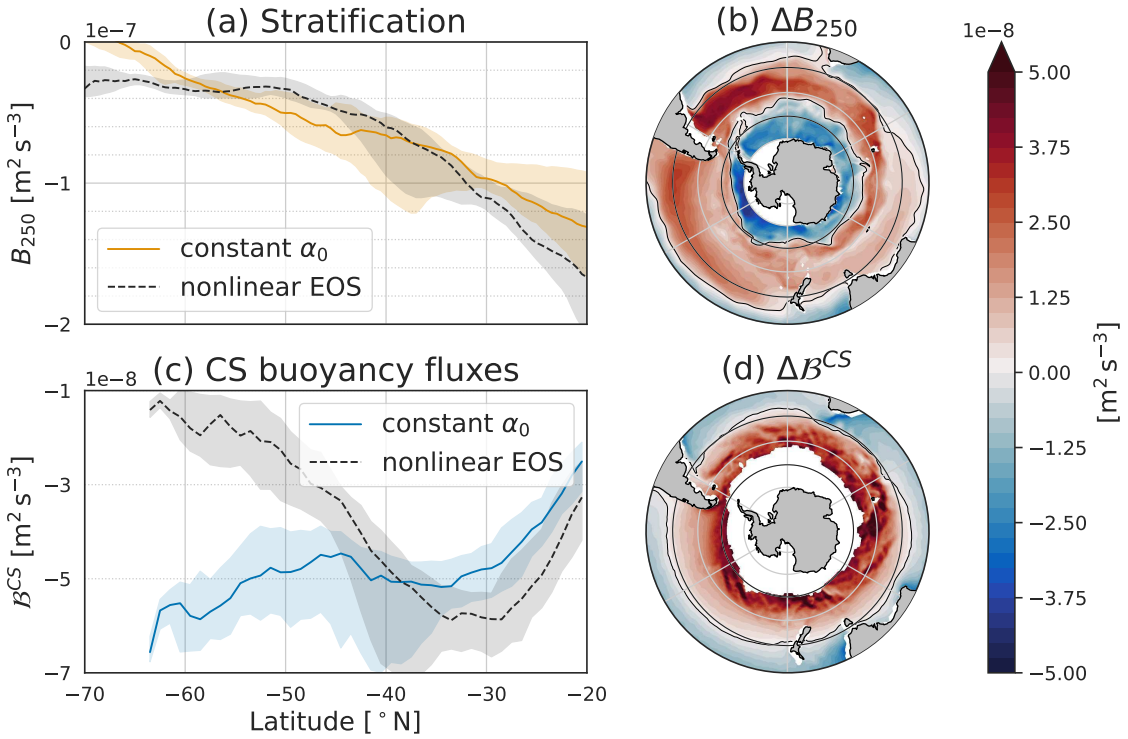

Figure 4.4: Stratification and buoyancy fluxes computed using either the varying thermal expansion coefficient or the constant α_0. In panels (a) and (c), black dashed lines represent results with the varying thermal expansion coefficient, while blue or orange continuous lines represent results with the constant α_0. The light shadings correspond to the 25th and 75th percentiles. Panels (b) and (d) are the differences between using the varying thermal expansion coefficient and the constant α_0, for B_{250} and $\mathcal{B}^{CS}$, respectively. Figure from Caneill et al. (2023).

(Fig. 4.4a, black dashed line). In contrast, when using the constant TEC, the buoyancy loss becomes increasingly important southwards, meaning that heat loss is not reduced southwards (Fig. 4.4a and b). The observed reduction of the winter buoyancy loss south of 40°S arises only because of the decrease in the TEC value and not because of a reduction in heat loss.

These two studies emphasise the substantial impact of the local value of the TEC in setting both annual and seasonal buoyancy fluxes.

4.3 The thermal expansion coefficient scales the effect of temperature on stratification (Papers I, II, and IV)

Paper I focuses on the role of buoyancy fluxes in setting the position of the transition zone. However, the effect of the TEC variations on the stratification is indirectly seen. Indeed, the northward migration of the PTZ (whose average latitude is called φ_β in the paper) is more significant than the one of the buoyancy flux inversion (whose latitude is called φ_b) when the polar vale of the TEC increases (evolution of φ_β and φ_b, Fig. 10 a and b of **Paper I**). This presumably comes from the fact that when the TEC increases in the beta ocean, stratifi-

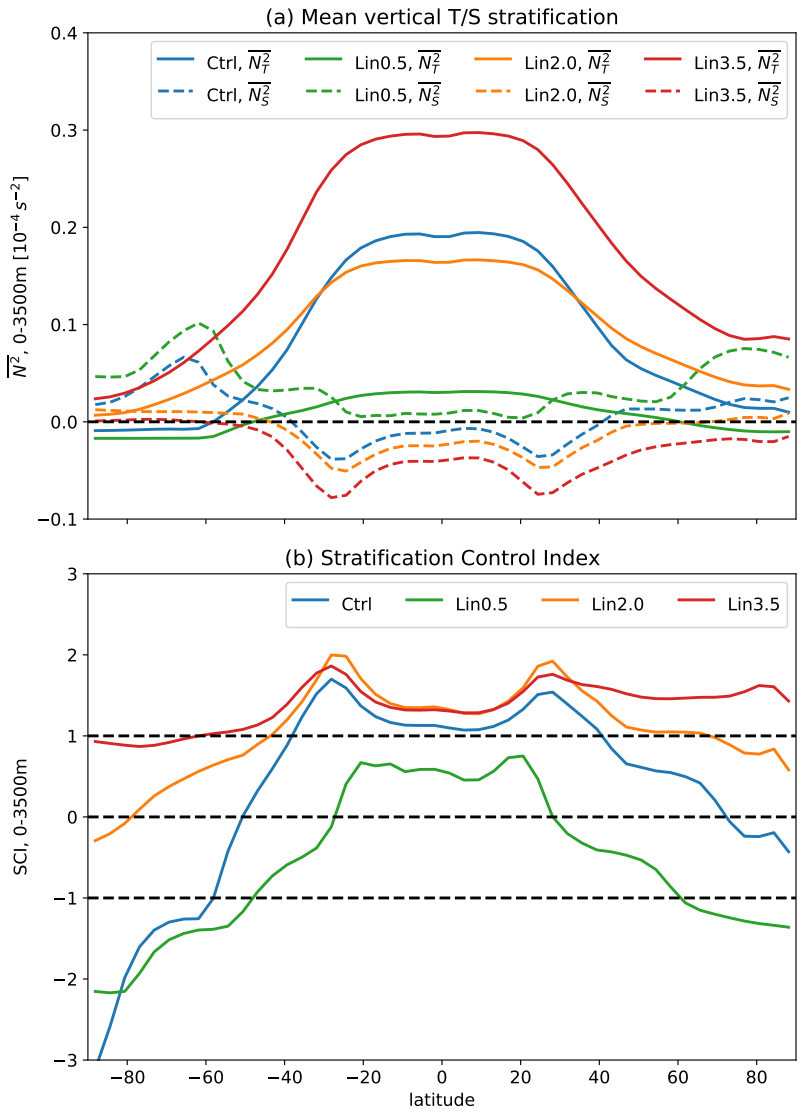

Figure 4.5: Zonal averages of (a) the temperature and salinity components of stratification and (b) the stratification control index for the aquaplanet model runs. The different colours represent different values of the thermal expansion coefficient used in these runs. Figure from Roquet et al. (2022).

cation decreases due to the temperature inversion. This effect alone shifts the PTZ northward. The effect of the buoyancy flux inversion is thus amplified.

In **Paper II**, using an observation-based climatology, we computed the stratification derived from the columnar buoyancy using either the local value of the TEC or the value representative of 40°S, α_0. The difference between the two results corresponds to the effect of the variations of the TEC on stratification (Fig. 4.4c and d). North of 40°S, α_0 is smaller than the local value of the TEC, and the upper ocean is stratified by temperature. Thus, the stratification decreases when using α_0. Between 40°S and 55°S, the local value of the TEC is smaller than α_0 while keeping a stratifying effect of temperature: using α_0 the constant TEC increases stratification. South of 55°S, the water column encounters a temperature inversion, and using α_0 enhances the destabilising effect of temperature, hence reducing stratification. We conclude that

a portion of the large subtropical stratification comes from the fact that the (varying) TEC is large. The decrease in stratification in the subpolar region is partly because of the decrease in TEC. Finally, the very low values of the TEC in the polar beta ocean stop the decrease in stratification that the temperature inversion would cause with larger TEC values.

Paper IV uses an ocean – atmosphere coupled numerical model on an idealised global configuration (an aquaplanet with two ridges representing the continents). A reference run (*Ctrl*) uses the full equation of state (EOS) and thus a varying TEC. Six runs with constant TEC are implemented (*LinX* with X in 0.5, 1.0, 1.25, 1.5, and 3.5 in units of $10^{-4}\,^{\circ}\mathrm{C}^{-1}$ the constant TEC). The differences between the circulation for each run thus arise from the direct impact of the value of the TEC and the indirect feedback. One main result of this study is that if the TEC is too large in the polar regions, the heat loss induces a large buoyancy loss that itself creates convection. This convection in the polar regions makes it impossible for sea ice to form; as soon as water is cold enough to freeze, it convects. Another result is that the stratification at one place using the varying TEC (nonlinear EOS) resembles the stratification at the same place, obtained with a constant value of the TEC close to the local value of the varying TEC (Fig. 4.5). Thus, the stratification control index (SCI) of the whole water column with a constant low value of the TEC (*Lin0.5*, green curves, Fig. 4.5) is close to the SCI resulting from the nonlinear EOS (*Ctrl*, blue curves) in polar regions. In contrast, *Lin0.5* is the run that produces the largest difference in stratification in tropical regions, where the difference between the values of the TEC between *Ctrl* and *Lin0.5* is the largest. A similar effect applies for *Lin2.0* and *Lin3.5*: they represent well the tropical stratification, but very poorly the polar stratification, to the point that no beta ocean exists any more.

4.4 Combined effect of the thermal expansion coefficient: application to the deep mixing band (Paper II)

Taking the balance between buoyancy loss during the CS and stratification strength allows predicting the location and width of the deep mixing band (DMB) (Chapter 3.4). Using the same balance but α_0 the constant TEC in calculation, we determined the combined effect of the TEC on buoyancy fluxes and on stratification (**Paper II**). Where buoyancy fluxes are more negative than stratification measured by B_{250}, the mixed layer (ML) induced by buoyancy loss reaches 250 m or goes deeper. The DMB is present between 35°S and 50°S, but contrary to reality in this case, it even extends to Antarctica (Fig. 4.6). South of 50°S, the mixed layer depths (MLDs) are deeper than 250 m. With a constant TEC, the DMB would not be a "band" any more but would maybe be called "deep mixing Southern Ocean". A constant TEC would produce deep MLs everywhere in the SO, but in reality, they are only observed in the narrow DMB. This is thus the decrease of the TEC at low temperatures that sets the southern extent of the DMB. In reality, the low value of the TEC south of the DMB induces a reduction in buoyancy loss during the CS. This small buoyancy

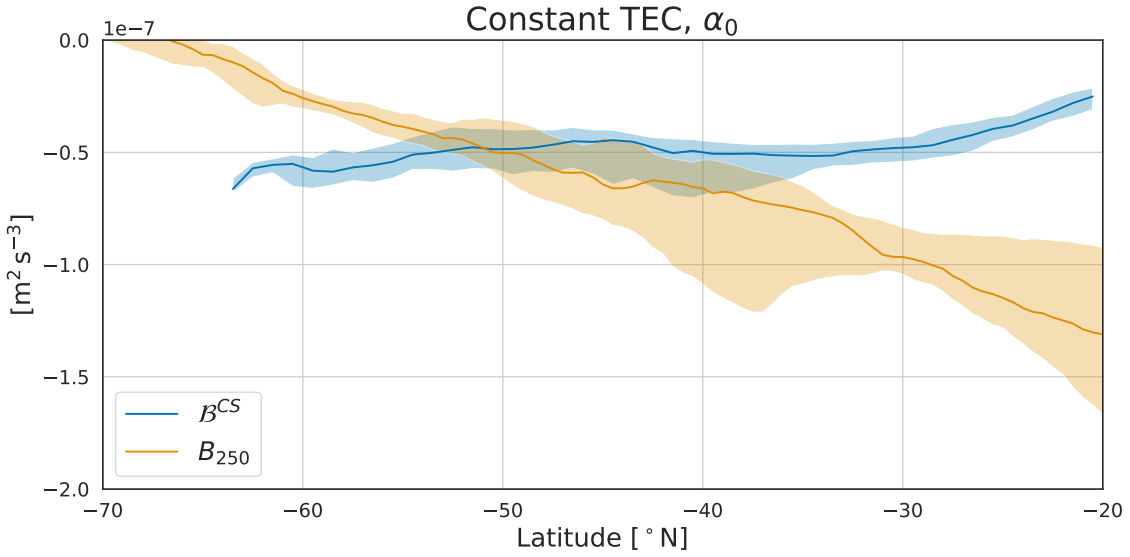

Figure 4.6: Buoyancy loss during the CS ($\mathcal{B}^{CS}$, blue line) and stratification strength (B_{250}, orange line), using the constant thermal expansion coefficient, α_0, for the calculations. The lines are zonal medians and the shadings are the first and third quartiles. The DMD could occur where $\mathcal{B}^{CS}$ becomes more negative than B_{250}. Figure adapted from Caneill et al. (2023).

loss is not able to destroy the stratification and produce deep MLs, despite a decrease in the stratification strength induced by the low values of the TEC.

4.5 Can we distinguish the effect of the thermal expansion coefficient on buoyancy fluxes and on stratification?

The effects of the TEC on upper ocean stratification and on buoyancy fluxes are not easily distinguishable, particularly in model runs where both effects are linked. When the ocean loses (gains) heat, its upper density increases (decreases) more or less depending on the value of the TEC. The buoyancy fluxes quantify this change. If the water column were to uniformly gain heat at every depth, the vertical temperature gradient would stay constant. However, due to the change in temperature, the TEC would change, changing the stratification strength at the same time. There are thus two distinguished roles of the TEC: one in scaling heat fluxes and the other in scaling temperature stratification.

In parts of the ocean, these two effects partly compensate for each other, slightly decreasing the importance of the value of the TEC in these regions. This is, for example, what happens in the subtropic (subpolar region), where using a smaller (larger) value of the TEC decreases (increases) stratification but also decreases (increases) the buoyancy loss during the CS (Figs. 4.4a and 4.4c north of 55°S). In the polar beta oceans, however, as they are regions of winter heat loss where temperature has a destabilising effect, an increase in the TEC value increases the buoyancy loss while decreasing the stratification. Beta oceans are thus regions where the value of the TEC is of primary importance in controlling the upper stratification.

4.6 Summary of the effects of the thermal expansion coefficient variations on global scale

The three papers described in this chapter provide an overview of the effect of TEC values on a global scale. I conclude this chapter by summarising these effects:

- Large TEC values in the subtropics are producing a large upper ocean stratification. This effect is dampened by the fact that the large value of the TEC also enhances the winter buoyancy loss induced by heat fluxes.
- In the subantarctic zone (between 55°S and 40°S), the TEC has a relatively small value, which decreases the stratification (induced by temperature). At the same time, this small value damps the effect of heat fluxes on buoyancy fluxes. The effect of the damping of heat fluxes is to limit the southward extent of the DMB.
- In the beta ocean, the TEC is the smallest, thus making the temperature inversion possible. It also makes heat fluxes very inefficient at changing density. This is the region where the role of the TEC is most important. Opposite to the subtropics and subantarctic zone, the effect of the small value of the TEC is to increase stratification, both directly by reducing the impact of the temperature inversion on stratification and indirectly by making the winter buoyancy loss very small.
- Overall, it is the fact that the TEC becomes small in cold water that allows the formation of beta oceans. The halocline present in beta oceans limits the deepening of the MLs and allows for sea-ice formation.

Chapter 5

Characterising alpha and beta oceans from observations (Paper III)

5.1 Context

Previous studies have discussed a relation between ocean stratification and the horizontal zonation of the ocean. In the Southern Ocean (SO), Pollard et al. (2002) proposed to relate the Subantarctic Front (SAF) and Polar Front (PF) to boundaries between different regimes of thermohaline stratification. Carmack (2007) proposed the terms "alpha" and "beta" oceans to distinguish the effects of temperature and salinity on stratification. These two studies were, however, only based on a few hydrographic transects. On a global scale, You (2002), Helber et al. (2012), Stewart and Haine (2016), and Clément et al. (2020) produced maps to quantify the role of temperature and salinity in setting the stratification. Here we aim at mapping more accurately the different regimes and revealing an underlying relationship with the MLD distribution. As we focus on the stratification control index (SCI) below the mixed layer (ML), our approach is slightly different from the cited studies. Moreover, we use the EN4 database of temperature and salinity profiles from 2004 to 2021 to produce our mixed layer depth (MLD) and SCI climatologies, which extends the time period compared to previous studies. Further, computing the SCI directly on the profiles increases the accuracy of the results.

5.2 Climatologies of the stratification control index

In winter, the tropical regions around the equator have a SCI between -1 and 1 and are thus classified as transition zones (Figs. 5.1 and 5.2). They are regions gaining heat at the surface and, at the same time, gaining a substantial amount of freshwater through rain. These two fluxes are creating a warm, fresh, and highly stratified layer with a MLD around 50 m. Poleward of the tropical regions are found alpha oceans, with a winter $SCI > 1$. The MLD

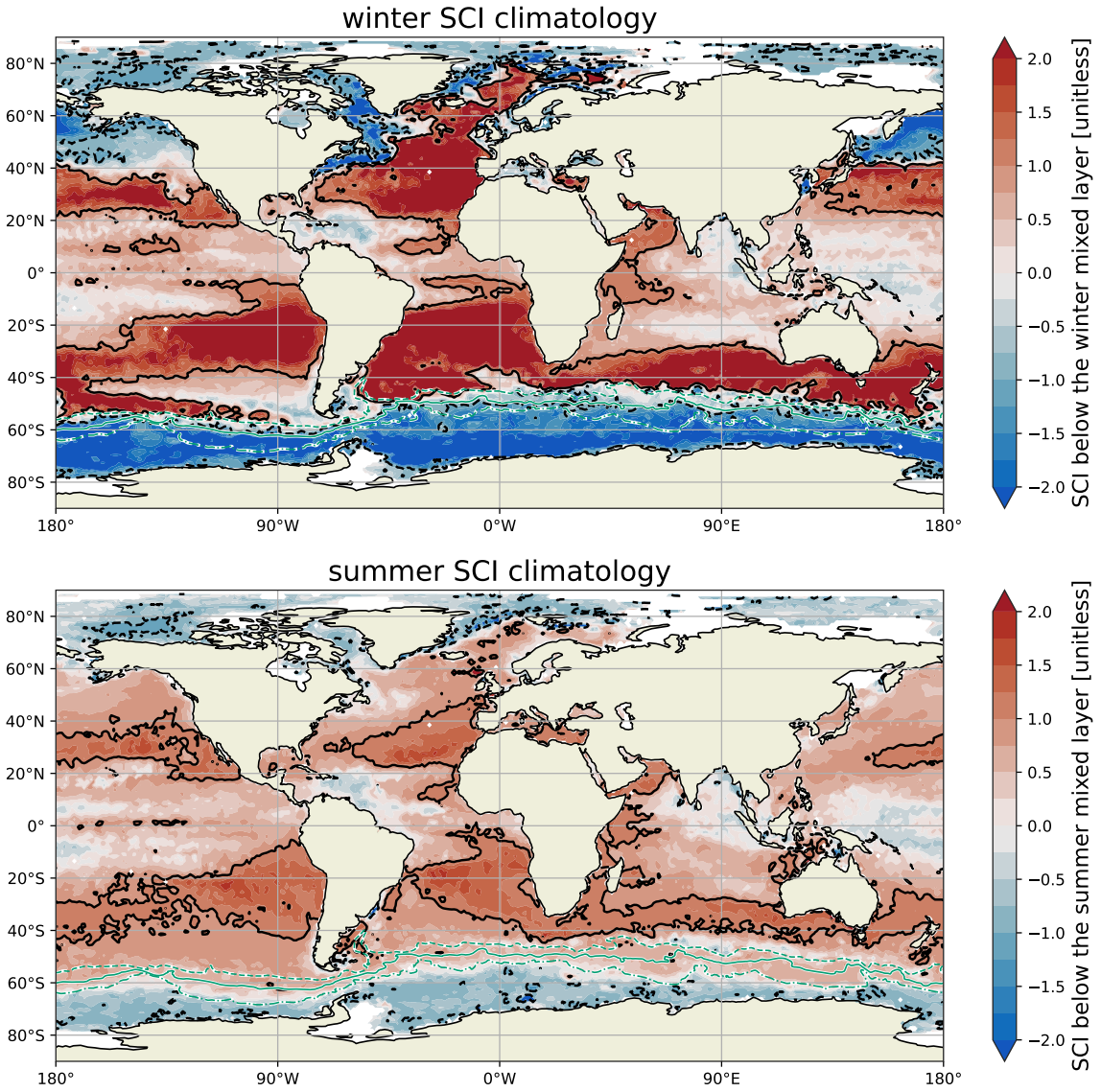

Figure 5.1: Stratification control index below the winter mixed layer (upper panel) and below the summer mixed layer (lower panel). The colours are saturated at $SCI = \pm 2$. The ocean is red where temperature predominantly stratifies, and blue where salinity predominantly stratifies. The continuous (dashed) black lines mark $SCI = 1$ ($SCI = -1$). Figure adapted from Caneill and Roquet (2023).

varies in these alpha oceans, from less than 100 m on the equator side to more than 300 m in the SO deep mixing band (DMB) and in the North Atlantic (**Paper III**). In the North Atlantic, there is a large interannual variability; for example, in the Irminger Sea, where deep convection occurs, MLDs of 400 m in 2014 were followed the next year by MLDs of 1200 m. Interannual variability is also found in the DMB but is less extreme.

A narrow polar transition zone (PTZ) is present in the SO and North Atlantic basin between the alpha and beta oceans, below the winter ML. In the North Pacific Ocean, the PTZ is only narrow on the western side and gets wider towards the east, becoming 20 degrees wide in latitude. In the South Pacific Ocean, a tongue of transition zone also exists. A main difference be-

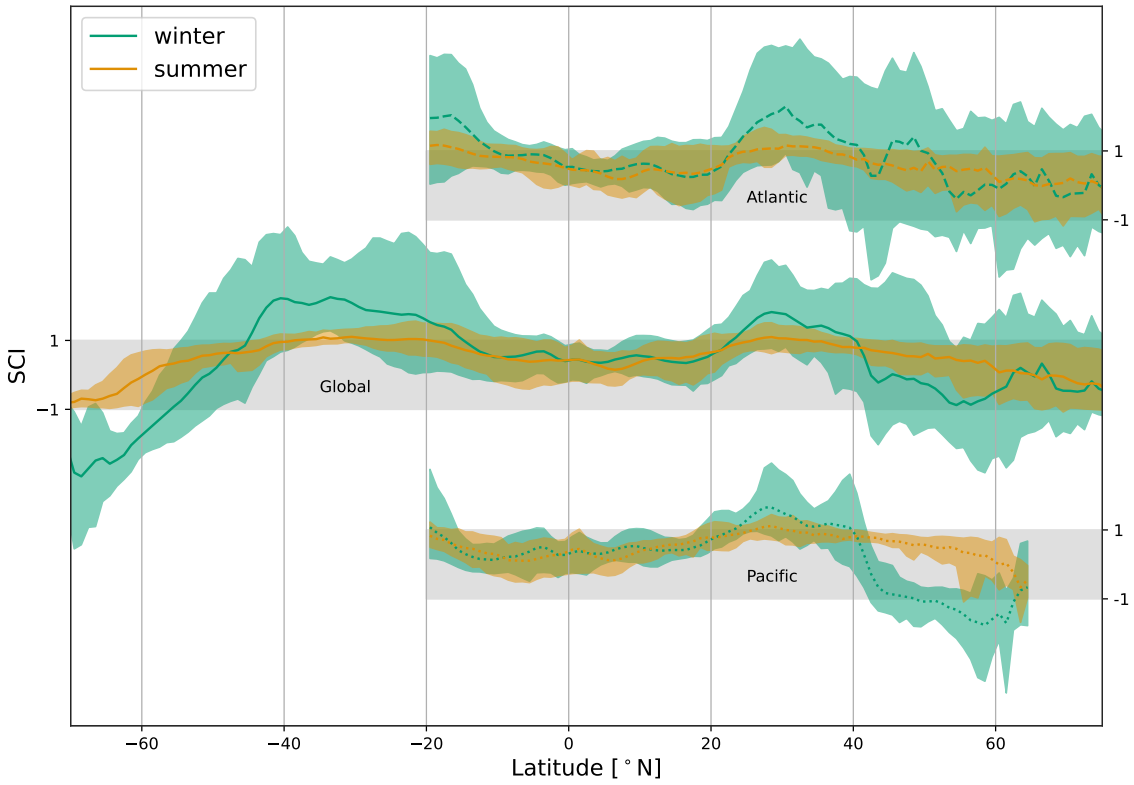

Figure 5.2: Zonal climatology of winter (green) and summer (orange) stratification control index below the mixed layer. The lines are the zonal means, and the shadings are the 10th and 90th percentiles. The middle lines are the global zonal means. The upper and lower lines, starting at 20°S, separate the Pacific basin, where the stratification control index is approximately zonally constant, from the Atlantic basin, where the stratification control index encounters large longitudinal variations. The Atlantic and Pacific zonal means have been shifted vertically for clarity, and they refer to their own axis on the right. The gray bands represent $-1 < SCI < 1$. Figure adapted from Caneill and Roquet (2023).

tween the South and North Pacific transition zones is that the south tongue is surrounded by alpha ocean before merging with the PTZ west of Drake Passage. In the North Pacific Ocean, the separation between the alpha and beta oceans follows an almost east-west direction. On the other hand, in the North Atlantic basin, the alpha ocean stretches northward along the European coast, while the beta ocean extends southward along the eastern coast of Greenland and the American coast. The separation thus follows a north-east diagonal.

The summer picture looks quite different (Fig. 5.1, lower panel, and Fig. 5.2). The SCI is generally smaller (in absolute value) during the summer than in the winter. It is larger than -1 everywhere and exceeds 1 only in parts of the subtropical regions. The SCI of the PTZ in the North Pacific basin shifts from a negative value in winter to a positive value in summer (visible between 40°N and 60°N, Fig. 5.2) and is almost the only region where the SCI changes sign between winter and summer. The main tendency is that the SCI value gets dampened during the summer while keeping its sign.

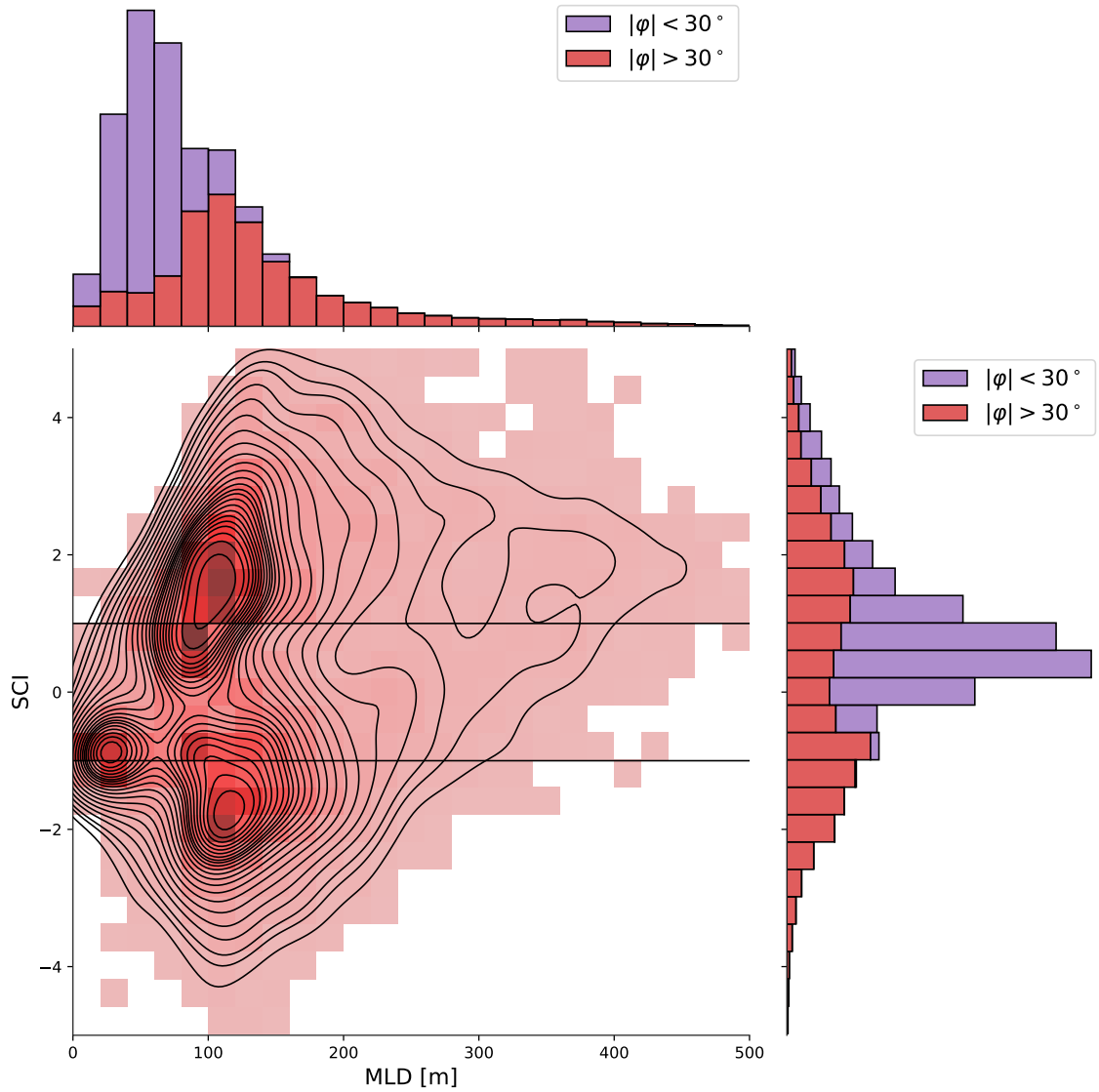

Figure 5.3: Stratification control index versus mixed layer depth in winter. The centre figure represents a 2 dimensions histogram (colours), with a kernel density estimation (contour lines) superimposed. For the centre figure, only data with a latitude $|\varphi| > 30°$ are shown. The histograms on the sides are split into the tropical regions ($|\varphi| < 30°$) in purple, and the rest of the ocean ($|\varphi| > 30°$) in red. The upper histogram is for the mixed layer depth, and the histogram on the right is for the stratification control index. Data are taken from the winter $1°$ climatology. Each data point is weighted by the area of its corresponding cell of the $1°$ grid. Figure adapted from Caneill and Roquet (2023).

5.3 On the link with the mixed layer depth

Deep MLs seem to occur more often in alpha oceans than in beta oceans or transition zones (**Paper III**, compare maps of the MLD and the SCI, Figs. 3 and 7). This impression is confirmed when plotting the SCI versus the MLD (Fig. 5.3). MLs deeper than 250 m are mostly found in the alpha oceans (larger values of the two-dimensional histogram, Fig. 5.3). Deep MLs are also found in oceans classified as transition zones and are almost absent in beta oceans. Indi-

vidual profiles in the beta oceans show deep MLs along the coast of Antarctica, but they represent a small area and are thus not seen in this figure.

Tropical regions (defined here with an absolute value of the latitude less than 30°) are only plotted on the top and right histograms. They represent a large area with shallow MLs (less than 100 m) and are classified almost exclusively as transition zones.

For higher latitudes ($|\varphi| \geq 30°$), the ML distribution exhibits a peak at 120 m. The SCI distribution poleward of 30° is bimodal, centred around ± 1.5. The oceans thus encounter partial compensation between temperature and salinity more often than when temperature and salinity both stabilise. Poleward of 30°, the shallowest MLs are found in regions where salinity dominates the stratification ($SCI < 0$), either in transition zones or beta oceans. Regions that encounter large density compensation (large $|SCI|$) do not present shallow ML.

5.4 Summary

This chapter provides new insights on the zonation of the oceans between the alpha, transition, and beta regimes, and its propensity to encounter density compensation between temperature and salinity. To sum up, here is a summary:

- We confirm the zonation of alpha oceans at mid-latitudes, beta oceans at high latitudes, and the PTZs in between. However, **Paper III** reveals large differences in the structure between the North Atlantic and North Pacific basins. The North Pacific PTZ is almost zonal and becomes very wide eastward. Opposite, the North Atlantic PTZ is very narrow and follows a diagonal into the northwest.

- Except for the tropical oceans, the distribution of the SCI is bimodal, with the modes centred around $SCI = \pm 1.5$. The ocean in general tends to go towards temperature and salinity compensation rather than being doubly stabilised.

- Both in the North Atlantic basin and in the SO, deep MLs occur in the alpha ocean, near the boundary with the PTZ.

- Overall, the climatology of the winter SCI provides a global view of the oceans, where the regimes of stratification are highlighted. This allows for a precise determination of the role of temperature and salinity in setting the stratification.

Chapter 6

Conclusions and Outlook

In this thesis, we examined the mechanisms governing the zonation of the upper ocean stratification into different regimes, and specifically: Why and where is there a shift from alpha to beta oceans? For this, we studied the link between buoyancy fluxes and stratification. Using an idealised basin-like numerical model in **Paper I**, we found that the transition was located close to the sign inversion of the annual buoyancy fluxes. Buoyancy gain driven by positive freshwater fluxes in the northernmost part of the basin was creating a strong halocline, which was acting as a strong freshwater cap, preventing convection from occurring there. In **Paper II**, we used observational data to compare the autumn – winter buoyancy loss with the stratification strength of the upper ocean at the end of summer. We found that the simple balance between them is sufficient to explain the formation and shape of the DMB. Close to the strong western boundary currents (e.g., the Agulhas Current or the East Australian Current), highly stratified water is advected and the balance does not hold any more, thus no deep ML is formed despite strong buoyancy loss in winter. South of the DMB, the drop in the value of the TEC makes winter heat loss inefficient to increase density, limiting the southern extent of the DMB.

The type of stratification, quantified by the stratification control index (SCI), is linked to the position of the Subantarctic Front (SAF) and Polar Front (PF) in the Southern Ocean (SO) (**Paper III**). Defining circumpolar fronts using the SCI may not be very practical, as the SAF is surrounded by winter transition zones in the southeast Pacific Ocean while being at the boundary between the alpha ocean and transition zone elsewhere. However, a broad consistency is revealed, as well as large structural disparities around the SO. In summer, the entire SO is stratified by temperature below the mixed layer (ML) ($\mathrm{SCI} \geq -1$), south of the Southern Boundary (SB) front, $\mathrm{SCI} \geq 0$ which means that salinity is the dominant stratifying agent. The SB, defined with a dynamic definition, thus matches a stratification front. The stratification front may partly arise from the path of the water masses and advection. Globally, the absolute value of the SCI is larger in winter than in summer. This indicates that large density compensations occur between temperature and salinity

below the winter ML. Moreover, the summer SCI is between -1 and 1 everywhere, meaning that both temperature and salinity increase stratification below the summer ML. One exception is in the centre of the subtropical gyres, where $SCI > 1$.

Deep winter MLs are found in the alpha oceans, mainly in the deep mixing band (DMB) and in the Nordic Seas. In these regions, winter heat loss is the key component of convection. Opposite, close to the Antarctic coast, the surface temperature is at freezing point, so water cannot cool more to change density. Moreover, the value of the thermal expansion coefficient (TEC) makes any temperature change negligible for stratification. However, winter heat loss makes seawater freeze, increasing salinity through brine rejection and leading to convection. The driver of convection is thus different in alpha and beta oceans.

One key hypothesis of this thesis was that the origin of the transition between alpha and beta lies in the equation of state (EOS) and, more specifically, in the fact that the local value of the TEC is not the same everywhere on Earth. Artificially increasing the value of the TEC in the subpolar region leads to a decrease in the area of the beta ocean (**Paper I**). Further, it also increased the winter buoyancy loss, thus pushing the convective zone poleward and reducing the area available for the beta ocean. The local value of the TEC also scales the effect of temperature on stratification. Thus, a large value of the TEC in the polar regions makes it impossible to maintain a temperature inversion (**Paper IV**), making it impossible for sea ice to form. In **Paper II**, we found that the low value of the TEC south of the SAF damps a lot the winter heat loss effect on buoyancy, and despite a small stratification, no deep ML is formed. The decrease in the TEC is thus the origin of the southern boundary of the DMB. In both **Paper I** and **Paper IV**, we concluded that the cabbeling effect (defined as "contraction under mixing") is not necessary to explain the alpha – beta transition in the ocean. On the contrary, it is the *local* value of the TEC that sets the stratification.

The work conducted in this thesis contributes to the understanding of the role of the intrinsic properties of seawater in large-scale circulation. We showed that the local value of the TEC scales both the effect of temperature on stratification, and of heat fluxes on buoyancy. This scaling is obvious when looking at the equations, but the effect of this scaling on the global circulation and stratification of the ocean remained to be investigated. To the question "Why is there a shift from alpha to beta oceans?" my answer is: "The shift occurs because at high latitudes the formation of beta oceans is forced by the small value of the TEC in cold water". The zonation between the different regimes is mainly a consequence of the surface buoyancy fluxes over the oceans.

This thesis answers some questions but, at the same time, opens new horizons. Here are some future perspectives that I would like to see investigated in the future:

- Computing the SCI at the bottom of the ML is an efficient way to produce a global view of the upper ocean stratification. It can thus be used to compare and validate the different simulations that form the Coupled

Model Intercomparison Project (CMIP). The ocean is warming, so we can hypothesise that temperature will increase its control of the stratification, though the increase in the TEC. An increase in the TEC could also increase the buoyancy loss during winter. Deep MLs would shift poleward, and the surface of the beta oceans would decrease at the same time. Precise inspection of the CMIP outputs is necessary to verify the validity of these hypotheses.

- We concluded that cabbeling is not necessary to produce the polar transition zone (PTZ) between the alpha and beta oceans, but it would be useful to find a way to quantify its effect. There is, however, no easy way to do it because, as long as one uses a nonlinear EOS, the local values of the TEC will largely control the circulation. A possible way to have a varying TEC but no cabbeling would be to first run numerical simulations with the full EOS and to compute the buoyancy sink due to cabbeling. Then one could rerun the model with an extra term of buoyancy that would counterbalance the sink. This method would probably require a lot of changes in the model code, and closing the energy budget would probably be quite hard.

- Going beyond idealised simulation is an extra step that I would be happy to see achieved in the future. de Boer et al. (2007), Roquet et al. (2015b), and Nycander et al. (2015) have, for example, seen that the global circulation is sensitive to the EOS in realistic ocean simulations. Adding a fully coupled atmosphere could permit to gain more knowledge on the role of the TEC.

- By subducting heat and carbon, deep and intermediate waters mitigate the warming of the atmosphere. The DMB and the Nordic Seas convection are located in the alpha ocean, at the boundary of the transition zone. In a warming ocean, the value of the TEC increases, as does the role of temperature, both in stratification and buoyancy fluxes, directly impacting stratification. Changes in the stratification of these regions may directly impact the global climate. Global atmosphere – ocean coupled numerical simulations could be used to quantify the shift in the position of the transition zones and the feedback on the climate system.

- As water gets advected in the ML, it can encounter variations in the surface buoyancy flux due to the spatial variability of heat and freshwater fluxes. Following the water column from a Lagrangian perspective would tackle the issue that regions with large advection are forecasting deep MLs in **Paper II**, but they are not observed. Indeed, the Eulerian simple model of **Paper II** does not take the advection of stratified water into account. It would be possible to include this advection as an extra term in the model or compute the buoyancy fluxes along the trajectory using the Lagrangian frame. While not critical for the results of **Paper II**, using one of these two solutions would allow us to refine the analyses and study the interannual variability of the DMB, for example.

The climate would be very different if water had different physical and chemical properties. It is the remarkably large heat capacity and large latent heat of water that makes the ocean a very efficient heat conveyor. Among the specificities of the chemistry of water, we have focused in this thesis on the unique way the TEC varies with temperature. Owing to the large TEC values, the temperature easily stratifies the warm *alpha oceans*. However, at low temperatures, the TEC drops to near-zero values, letting salinity take control of the stratification and forming the cold *beta oceans*. It is interesting to notice that the observed heat and freshwater fluxes lead to comparable *surface buoyancy fluxes*. A uniform *seawater thermal expansion* coefficient would disrupt this delicate balance; temperature's effect would be too large or too small. Only the unique variations in the TEC allow both temperature and salinity to shape the *upper ocean stratification* in the way it is observed. The limited number of points of contact between the interior of the ocean and the atmosphere and the scarcity of vertical exchanges in the ocean generate the memory of the climate. Long-term climate change is therefore regulated by ocean breathing, which itself results from the subtle interplay between the thermodynamics of seawater and interactions with the atmosphere.

« En outre, j'ai surpris ces courants de haut en bas et de bas en haut, qui forment la vraie respiration de l'Océan. »
« What's more, I've detected those falling and rising currents that make up the ocean's true breathing. »

Capitaine Nemo, *Vingt mille lieues sous les mers*
Jules Verne, 1870

Bibliography

Aagaard, K., & Carmack, E. C. (1989). The role of sea ice and other fresh water in the Arctic circulation. *Journal of Geophysical Research*, *94*(C10), 14485. https://doi.org/10.1029/JC094iC10p14485

Adler, R., Sapiano, M., Huffman, G., Wang, J.-J., Gu, G., Bolvin, D., Chiu, L., Schneider, U., Becker, A., Nelkin, E., Xie, P., Ferraro, R., & Shin, D.-B. (2018). The Global Precipitation Climatology Project (GPCP) Monthly Analysis (New Version 2.3) and a Review of 2017 Global Precipitation. *Atmosphere*, *9*(4), 138. https://doi.org/10.3390/atmos9040138

Årthun, M., Eldevik, T., Smedsrud, L. H., Skagseth, Ø., & Ingvaldsen, R. B. (2012). Quantifying the Influence of Atlantic Heat on Barents Sea Ice Variability and Retreat*. *Journal of Climate*, *25*(13), 4736–4743. https://doi.org/10.1175/JCLI-D-11-00466.1

Barkan, R., Winters, K. B., & Llewellyn Smith, S. G. (2013). Rotating horizontal convection. *Journal of Fluid Mechanics*, *723*, 556–586. https://doi.org/10.1017/jfm.2013.136

Barton, B. I., Lenn, Y.-D., & Lique, C. (2018). Observed Atlantification of the Barents Sea Causes the Polar Front to Limit the Expansion of Winter Sea Ice. *Journal of Physical Oceanography*, *48*(8), 1849–1866. https://doi.org/10.1175/JPO-D-18-0003.1

Belkin, I. M., & Gordon, A. L. (1996). Southern Ocean fronts from the Greenwich meridian to Tasmania. *Journal of Geophysical Research: Oceans*, *101*(C2), 3675–3696. https://doi.org/10.1029/95JC02750

Bindoff, N. L., & McDougall, T. J. (1994). Diagnosing Climate Change and Ocean Ventilation Using Hydrographic Data. *Journal of Physical Oceanography*, *24*(6), 1137–1152. https://doi.org/10.1175/1520-0485(1994)024<1137:DCCAOV>2.0.CO;2

Bryan, F. (1986). High-latitude salinity effects and interhemispheric thermohaline circulations. *Nature*, *323*(6086), 301–304. https://doi.org/10.1038/323301a0

Caneill, R., & Roquet, F. (2023). Temperature versus salinity: Distribution of stratification control in the global ocean. *in preparation for Ocean Science*.

Caneill, R., Roquet, F., Madec, G., & Nycander, J. (2022). The Polar Transition from Alpha to Beta Regions Set by a Surface Buoyancy Flux Inversion. *Journal of Physical Oceanography*, *52*(8), 1887–1902. https://doi.org/10.1175/JPO-D-21-0295.1

Caneill, R., Roquet, F., & Nycander, J. (2023). Southern Ocean deep mixing band emerges from competition between winter buoyancy loss and stratification. *submitted to Ocean Science*. https://doi.org/10.5194/egusphere-2023-2404

Carmack, E. C., Yamamoto-Kawai, M., Haine, T. W. N., Bacon, S., Bluhm, B. A., Lique, C., Melling, H., Polyakov, I. V., Straneo, F., Timmermans, M.-L., &

Williams, W. J. (2016). Freshwater and its role in the Arctic Marine System: Sources, disposition, storage, export, and physical and biogeochemical consequences in the Arctic and global oceans. *Journal of Geophysical Research: Biogeosciences*, *121*(3), 675–717. https://doi.org/10.1002/2015JG003140

Carmack, E. C. (2007). The alpha/beta ocean distinction: A perspective on freshwater fluxes, convection, nutrients and productivity in high-latitude seas. *Deep Sea Research Part II: Topical Studies in Oceanography*, *54*(23-26), 2578–2598. https://doi.org/10.1016/j.dsr2.2007.08.018

CCHDO Hydrographic Data Office. (2023). CCHDO Hydrographic Data Archive, Version 2023-11-21 [In CCHDO Hydrographic Data Archive]. https://doi.org/10.6075/J0CCHAM8

Cerovečki, I., Talley, L. D., & Mazloff, M. R. (2011). A Comparison of Southern Ocean Air–Sea Buoyancy Flux from an Ocean State Estimate with Five Other Products. *Journal of Climate*, *24*(24), 6283–6306. https://doi.org/10.1175/2011JCLI3858.1

Cess, R. D., & Goldenberg, S. D. (1981). The effect of ocean heat capacity upon global warming due to increasing atmospheric carbon dioxide. *Journal of Geophysical Research: Oceans*, *86*(C1), 498–502. https://doi.org/10.1029/JC086iC01p00498

Cessi, P. (2019). The Global Overturning Circulation. *Annual Review of Marine Science*, *11*(1), 249–270. https://doi.org/10.1146/annurev-marine-010318-095241

Clément, L., McDonagh, E. L., Marzocchi, A., & Nurser, A. J. G. (2020). Signature of Ocean Warming at the Mixed Layer Ḃase. *Geophysical Research Letters*, *47*(1). https://doi.org/10.1029/2019GL086269

Cunningham, S. A., Alderson, S. G., King, B. A., & Brandon, M. A. (2003). Transport and variability of the Antarctic Circumpolar Current in Drake Passage. *Journal of Geophysical Research: Oceans*, *108*(C5), 2001JC001147. https://doi.org/10.1029/2001JC001147

Curry, J. A., Schramm, J. L., & Ebert, E. E. (1995). Sea Ice-Albedo Climate Feedback Mechanism. *Journal of Climate*, *8*(2), 240–247. https://doi.org/10.1175/1520-0442(1995)008<0240:SIACFM>2.0.CO;2

de Boer, A. M., Sigman, D. M., Toggweiler, J. R., & Russell, J. L. (2007). Effect of global ocean temperature change on deep ocean ventilation. *Paleoceanography*, *22*(2). https://doi.org/10.1029/2005PA001242

de Boyer Montégut, C. (2004). Mixed layer depth over the global ocean: An examination of profile data and a profile-based climatology. *Journal of Geophysical Research*, *109*(C12), C12003. https://doi.org/10.1029/2004JC002378

de Boyer Montégut, C. (2023). Mixed layer depth climatology computed with a density threshold criterion of 0.03kg/m3 from 10 m depth value. https://doi.org/10.17882/91774

de Verdière, C. A. (1988). Buoyancy driven planetary flows. *Journal of Marine Research*, *46*(2), 215–265. https://doi.org/10.1357/002224088785113667

Doney, S. C., Fabry, V. J., Feely, R. A., & Kleypas, J. A. (2009). Ocean Acidification: The Other CO $_2$ Problem. *Annual Review of Marine Science*, *1*(1), 169–192. https://doi.org/10.1146/annurev.marine.010908.163834

Dong, S., Sprintall, J., Gille, S. T., & Talley, L. (2008). Southern Ocean mixed-layer depth from Argo float profiles. *Journal of Geophysical Research*, *113*(C6), C06013. https://doi.org/10.1029/2006JC004051

DuVivier, A. K., Large, W. G., & Small, R. J. (2018). Argo Observations of the Deep Mixing Band in the Southern Ocean: A Salinity Modeling Challenge. *Journal of Geophysical Research: Oceans*, *123*(10), 7599–7617. https://doi.org/10.1029/2018JC014275

Emery, W. J. (1977). Antarctic Polar Frontal Zone from Australia to the Drake Passage. *Journal of Physical Oceanography*, *7*(6), 811–822. https://doi.org/10.1175/1520-0485(1977)007<0811:APFZFA>2.0.CO;2

Faure, V., & Kawai, Y. (2015). Heat and salt budgets of the mixed layer around the Subarctic Front of the North Pacific Ocean. *Journal of Oceanography*, *71*(5), 527–539. https://doi.org/10.1007/s10872-015-0318-0

Forget, G., Campin, J.-M., Heimbach, P., Hill, C. N., Ponte, R. M., & Wunsch, C. (2015). Ecco version 4: An integrated framework for non-linear inverse modeling and global ocean state estimation. *Geoscientific Model Development*, *8*(10), 3071–3104. https://doi.org/10.5194/gmd-8-3071-2015

Garrett, C., Outerbridge, R., & Thompson, K. (1993). Interannual Variability in Meterrancan Heat and Buoyancy Fluxes. *Journal of Climate*, *6*(5), 900–910. https://doi.org/10.1175/1520-0442(1993)006<0900:IVIMHA>2.0.CO;2

Garrett, C., & Horne, E. (1978). Frontal circulation due to cabbeling and double diffusion. *Journal of Geophysical Research*, *83*(C9), 4651. https://doi.org/10.1029/JC083iC09p04651

Gill, A. E., & Adrian, E. (1982). *Atmosphere-ocean dynamics* (Vol. 30). Academic press.

Good, S. A., Martin, M. J., & Rayner, N. A. (2013). EN4: Quality controlled ocean temperature and salinity profiles and monthly objective analyses with uncertainty estimates. *Journal of Geophysical Research: Oceans*, *118*(12), 6704–6716. https://doi.org/10.1002/2013JC009067

Gouretski, V., & Cheng, L. (2020). Correction for systematic errors in the global dataset of temperature profiles from mechanical bathythermographs. *Journal of Atmospheric and Oceanic Technology*, *37*(5), 841–855.

Gouretski, V., & Reseghetti, F. (2010). On depth and temperature biases in bathythermograph data: Development of a new correction scheme based on analysis of a global ocean database. *Deep Sea Research Part I: Oceanographic Research Papers*, *57*(6), 812–833.

Groeskamp, S., Abernathey, R. P., & Klocker, A. (2016). Water mass transformation by cabbeling and thermobaricity. *Geophysical Research Letters*, *43*(20), 10, 835–10, 845. https://doi.org/10.1002/2016GL070860

Gruber, N., Bakker, D. C. E., DeVries, T., Gregor, L., Hauck, J., Landschützer, P., McKinley, G. A., & Müller, J. D. (2023). Trends and variability in the ocean carbon sink. *Nature Reviews Earth & Environment*, *4*(2), 119–134. https://doi.org/10.1038/s43017-022-00381-x

Guinehut, S., Dhomps, A.-L., Larnicol, G., & Le Traon, P.-Y. (2012). High resolution 3-D temperature and salinity fields derived from in situ and satellite observations. *Ocean Science*, *8*(5), 845–857. https://doi.org/10.5194/os-8-845-2012

Hanawa, K., & Talley, L. D. (2001). Chapter 5.4 Mode waters [ISSN: 0074-6142]. In G. Siedler, J. Church, & J. Gould (Eds.), *Ocean Circulation and Climate* (pp. 373–386). Academic Press. https://doi.org/https://doi.org/10.1016/S0074-6142(01)80129-7

Helber, R. W., Kara, A. B., Richman, J. G., Carnes, M. R., Barron, C. N., Hurlburt, H. E., & Boyer, T. (2012). Temperature versus salinity gradients below the ocean mixed layer. *Journal of Geophysical Research: Oceans*, *117*(C5), n/a–n/a. https://doi.org/10.1029/2011JC007382

Herrmann, M., Somot, S., Sevault, F., Estournel, C., & Déqué, M. (2008). Modeling the deep convection in the northwestern Mediterranean Sea using an eddy-permitting and an eddy-resolving model: Case study of winter 1986–1987. *Journal of Geophysical Research*, *113*(C4), C04011. https://doi.org/10.1029/2006JC003991

Hieronymus, M., & Nycander, J. (2013). The Buoyancy Budget with a Nonlinear Equation of State. *Journal of Physical Oceanography*, *43*(1), 176–186. https://doi.org/10.1175/JPO-D-12-063.1

Holte, J. W., Talley, L. D., Chereskin, T. K., & Sloyan, B. M. (2012). The role of air-sea fluxes in Subantarctic Mode Water formation. *Journal of Geophysical Research: Oceans*, *117*(C3). https://doi.org/10.1029/2011JC007798

IOC, SCOR, & IAPSO. (2015). The International thermodynamic equation of seawater–2010: Calculation and use of thermodynamic properties.[includes corrections up to 31st October 2015]. *Intergovernmental Oceanographic Commission, Manuals and Guides*, *56*, 220. http://teos-10.org/pubs/TEOS-10_Manual.pdf

Isachsen, P. E., Mauritzen, C., & Svendsen, H. (2007). Dense water formation in the Nordic Seas diagnosed from sea surface buoyancy fluxes. *Deep Sea Research Part I: Oceanographic Research Papers*, *54*(1), 22–41. https://doi.org/10.1016/j.dsr.2006.09.008

Iudicone, D., Madec, G., Blanke, B., & Speich, S. (2008). The Role of Southern Ocean Surface Forcings and Mixing in the Global Conveyor. *Journal of Physical Oceanography*, *38*(7), 1377–1400. https://doi.org/10.1175/2008JPO3519.1

Johnson, G. C., Kunze, E., McTaggart, K. E., & Moore, D. W. (2002). Temporal and Spatial Structure of the Equatorial Deep Jets in the Pacific Ocean*. *Journal of Physical Oceanography*, *32*(12), 3396–3407. https://doi.org/10.1175/1520-0485(2002)032<3396:TASSOT>2.0.CO;2

Karstensen, J., & Lorbacher, K. (2011). A practical indicator for surface ocean heat and freshwater buoyancy fluxes and its application to the NCEP reanalysis data. *Tellus A: Dynamic Meteorology and Oceanography*, *63*(2), 338–347. https://doi.org/10.1111/j.1600-0870.2011.00510.x

Klocker, A., Naveira Garabato, A. C., Roquet, F., De Lavergne, C., & Rintoul, S. R. (2023a). Generation of the Internal Pycnocline in the Subpolar Southern Ocean by Wintertime Sea Ice Melting. *Journal of Geophysical Research: Oceans*, *128*(3), e2022JC019113. https://doi.org/10.1029/2022JC019113

Klocker, A., & McDougall, T. J. (2010). Influence of the Nonlinear Equation of State on Global Estimates of Dianeutral Advection and Diffusion. *Journal of Physical Oceanography*, *40*(8), 1690–1709. https://doi.org/10.1175/2010JPO4303.1

Klocker, A., Munday, D., Gayen, B., Roquet, F., & LaCasce, J. (2023b). Deep-reaching global ocean overturning circulation generated by surface buoyancy forcing [Accepted for publication]. *Tellus*.

Kuhlbrodt, T., Griesel, A., Montoya, M., Levermann, A., Hofmann, M., & Rahmstorf, S. (2007). On the driving processes of the Atlantic meridional overturning circulation. *Reviews of Geophysics*, *45*(2). https://doi.org/10.1029/2004RG000166

Lambert, E., Eldevik, T., & Spall, M. A. (2018). On the Dynamics and Water Mass Transformation of a Boundary Current Connecting Alpha and Beta Oceans. *Journal of Physical Oceanography*, *48*(10), 2457–2475. https://doi.org/10.1175/JPO-D-17-0186.1

Lascaratos, A., & Nittis, K. (1998). A high-resolution three-dimensional numerical study of intermediate water formation in the Levantine Sea. *Journal of Geophysical Research: Oceans*, *103*(C9), 18497–18511. https://doi.org/10.1029/98JC01196

Lazier, J. R. (1980). Oceanographic conditions at Ocean Weather Ship Bravo, 1964–1974. *Atmosphere-Ocean*, *18*(3), 227–238. https://doi.org/10.1080/07055900.1980.9649089

Lévy, M., Klein, P., Tréguier, A.-M., Iovino, D., Madec, G., Masson, S., & Takahashi, K. (2010). Modifications of gyre circulation by sub-mesoscale physics. *Ocean Modelling*, *34*(1-2), 1–15. https://doi.org/10.1016/j.ocemod.2010.04.001

Madec, T., Gurvan and NEMO System. (2019). NEMO ocean engine. https://doi.org/10.5281/ZENODO.1464816

Manabe, S., & Wetherald, R. T. (1967). Thermal Ĕquilibrium of the Atmosphere with a Given Distribution of Relative Humidity. *Journal of the Atmospheric Sciences*, *24*(3), 241–259. https://doi.org/10.1175/1520-0469(1967)024<0241:TEOTAW>2.0.CO;2

Manabe, S., & Wetherald, R. T. (1975). The effects of doubling the co 2 concentration on the climate of a general circulation model. *Journal of Atmospheric Sciences*, *32*(1), 3–15.

Mauritzen, C., & Häkkinen, S. (1999). On the relationship between dense water formation and the "Meridional Overturning Cell" in the North Atlantic Ocean. *Deep Sea Research Part I: Oceanographic Research Papers*, *46*(5), 877–894. https://doi.org/10.1016/S0967-0637(98)00094-6

McDougall, T. J. (1987). Thermobaricity, cabbeling, and water-mass conversion. *Journal of Geophysical Research*, *92*(C5), 5448. https://doi.org/10.1029/JC092iC05p05448

McDougall, T. J., & You, Y. (1990). Implications of the nonlinear equation of state for upwelling in the ocean interior. *Journal of Geophysical Research*, *95*(C8), 13263. https://doi.org/10.1029/JC095iC08p13263

Meredith, M. (2019). The global importance of the southern ocean and the key role of its freshwater cycle. *Ocean Challenge*, *23*.

Munk, W. H. (1950). On the wind-driven ocean circulation. *Journal of Meteorology*, *7*(2), 80–93. https://doi.org/10.1175/1520-0469(1950)007<0080:OTWDOC>2.0.CO;2

Munk, W. H. (1966). Abyssal recipes. *Deep Sea Research and Oceanographic Abstracts*, *13*(4), 707–730. https://doi.org/10.1016/0011-7471(66)90602-4

Naveira Garabato, A. C., Jullion, L., Stevens, D. P., Heywood, K. J., & King, B. A. (2009). Variability of Subantarctic Mode Water and Antarctic Intermediate Water in the Drake Passage during the Late-Twentieth and Early-Twenty-First Centuries. *Journal of Climate*, *22*(13), 3661–3688. https://doi.org/10.1175/2009JCLI2621.1

Nycander, J., Hieronymus, M., & Roquet, F. (2015). The nonlinear equation of state of sea water and the global water mass distribution: Global Water Mass Dis-

tribution. *Geophysical Research Letters*, *42*(18), 7714–7721. https://doi.org/10.1002/2015GL065525

Oeschger, H., Siegenthaler, U., Schotterer, U., & Gugelmann, A. (1975). A box diffusion model to study the carbon dioxide exchange in nature. *Tellus*, *27*(2), 168–192. https://doi.org/10.1111/j.2153-3490.1975.tb01671.x

Onarheim, I. H., Eldevik, T., Årthun, M., Ingvaldsen, R. B., & Smedsrud, L. H. (2015). Skillful prediction of Barents Sea ice cover. *Geophysical Research Letters*, *42*(13), 5364–5371. https://doi.org/10.1002/2015GL064359

Park, Y.-H., Park, T., Kim, T.-W., Lee, S.-H., Hong, C.-S., Lee, J.-H., Rio, M.-H., Pujol, M.-I., Ballarotta, M., Durand, I., & Provost, C. (2019). Observations of the Antarctic Circumpolar Current Over the Udintsev Fracture Zone, the Narrowest Choke Point in the Southern Ocean. *Journal of Geophysical Research: Oceans*, *124*(7), 4511–4528. https://doi.org/10.1029/2019JC015024

Pauthenet, E., Roquet, F., Madec, G., & Nerini, D. (2017). A Linear Decomposition of the Southern Ocean Thermohaline Structure. *Journal of Physical Oceanography*, *47*(1), 29–47. https://doi.org/10.1175/JPO-D-16-0083.1

Pellichero, V., Sallée, J.-B., Chapman, C. C., & Downes, S. M. (2018). The southern ocean meridional overturning in the sea-ice sector is driven by freshwater fluxes. *Nature Communications*, *9*(1), 1789. https://doi.org/10.1038/s41467-018-04101-2

Perovich, D. K., & Polashenski, C. (2012). Albedo evolution of seasonal Arctic sea ice. *Geophysical Research Letters*, *39*(8), 2012GL051432. https://doi.org/10.1029/2012GL051432

Petit, T., Lozier, M. S., Josey, S. A., & Cunningham, S. A. (2020). Atlantic Deep Water Formation Occurs Primarily in the Iceland Basin and Irminger Sea by Local Buoyancy Forcing. *Geophysical Research Letters*, *47*(22). https://doi.org/10.1029/2020GL091028

Pollard, R., Lucas, M., & Read, J. (2002). Physical controls on biogeochemical zonation in the Southern Ocean. *Deep Sea Research Part II: Topical Studies in Oceanography*, *49*(16), 3289–3305. https://doi.org/10.1016/S0967-0645(02)00084-X

Polyakov, I. V., Pnyushkov, A. V., Rember, R., Padman, L., Carmack, E. C., & Jackson, J. M. (2013). Winter Convection Transports Atlantic Water Heat to the Surface Layer in the Eastern Arctic Ocean*. *Journal of Physical Oceanography*, *43*(10), 2142–2155. https://doi.org/10.1175/JPO-D-12-0169.1

Polzin, K. L., Toole, J. M., Ledwell, J. R., & Schmitt, R. W. (1997). Spatial Variability of Turbulent Mixing in the Abyssal Ocean. *Science*, *276*(5309), 93–96. https://doi.org/10.1126/science.276.5309.93

Rhines, P., Häkkinen, S., & Josey, S. A. (2008). Is Oceanic Heat Transport Significant in the Climate System? In R. R. Dickson, J. Meincke, & P. Rhines (Eds.), *Arctic–Subarctic Ocean Fluxes* (pp. 87–109). Springer Netherlands. https://doi.org/10.1007/978-1-4020-6774-7_5

Ridge, S. M., & McKinley, G. A. (2021). Ocean carbon uptake under aggressive emission mitigation. *Biogeosciences*, *18*(8), 2711–2725. https://doi.org/10.5194/bg-18-2711-2021

Rintoul, S. R., & England, M. H. (2002). Ekman Transport Dominates Local Air–Sea Fluxes in Driving Variability of Subantarctic Mode Water. *Journal of Physical*

Oceanography, *32*(5), 1308–1321. https://doi.org/10.1175/1520-0485(2002)032<1308:ETDLAS>2.0.CO;2

Rooth, C. (1982). Hydrology and ocean circulation. *Progress in Oceanography*, *11*(2), 131–149. https://doi.org/10.1016/0079-6611(82)90006-4

Roquet, F., Madec, G., McDougall, T. J., & Barker, P. M. (2015a). Accurate polynomial expressions for the density and specific volume of seawater using the TEOS-10 standard. *Ocean Modelling*, *90*, 29–43. https://doi.org/10.1016/j.ocemod.2015.04.002

Roquet, F., Ferreira, D., Caneill, R., Schlesinger, D., & Madec, G. (2022). Unique thermal expansion properties of water key to the formation of sea ice on Earth. *Science Advances*, *8*(46). https://doi.org/10.1126/sciadv.abq0793

Roquet, F., Madec, G., Brodeau, L., & Nycander, J. (2015b). Defining a Simplified Yet "Realistic" Equation of State for Seawater. *Journal of Physical Oceanography*, *45*(10), 2564–2579. https://doi.org/10.1175/JPO-D-15-0080.1

Rossow, W. B., & Schiffer, R. A. (1999). Advances in Understanding Clouds from ISCCP. *Bulletin of the American Meteorological Society*, *80*(11), 2261–2287. https://doi.org/10.1175/1520-0477(1999)080<2261:AIUCFI>2.0.CO;2

Ruddick, B. (1983). A practical indicator of the stability of the water column to double-diffusive activity. *Deep Sea Research Part A. Oceanographic Research Papers*, *30*(10), 1105–1107. https://doi.org/10.1016/0198-0149(83)90063-8

Sabine, C. L., Feely, R. A., Gruber, N., Key, R. M., Lee, K., Bullister, J. L., Wanninkhof, R., Wong, C. S., Wallace, D. W. R., Tilbrook, B., Millero, F. J., Peng, T.-H., Kozyr, A., Ono, T., & Rios, A. F. (2004). The Oceanic Sink for Anthropogenic CO $_2$. *Science*, *305*(5682), 367–371. https://doi.org/10.1126/science.1097403

Sallée, J.-B., Speer, K., Rintoul, S., & Wijffels, S. (2010). Southern Ocean Thermocline Ventilation. *Journal of Physical Oceanography*, *40*(3), 509–529. https://doi.org/10.1175/2009JPO4291.1

Schanze, J. J., & Schmitt, R. W. (2013). Estimates of Cabbeling in the Global Ocean. *Journal of Physical Oceanography*, *43*(4), 698–705. https://doi.org/10.1175/JPO-D-12-0119.1

Schiffer, R. A., & Rossow, W. B. (1983). The international satellite cloud climatology project (isccp): The first project of the world climate research programme. *Bull. Amer. Meteorol. Soc.*, *64*, 779–784.

Schmidtko, S., Johnson, G. C., & Lyman, J. M. (2013). MIMOC: A global monthly isopycnal upper-ocean climatology with mixed layers: MIMOC. *Journal of Geophysical Research: Oceans*, *118*(4), 1658–1672. https://doi.org/10.1002/jgrc.20122

Schmitt, R. W. (1994). Double Diffusion in Oceanography. *Annual Review of Fluid Mechanics*, *26*(1), 255–285. https://doi.org/10.1146/annurev.fl.26.010194.001351

Schmitt, R. W., Bogden, P. S., & Dorman, C. E. (1989). Evaporation Minus Precipitation and Density Fluxes for the North Atlantic. *Journal of Physical Oceanography*, *19*(9), 1208–1221. https://doi.org/10.1175/1520-0485(1989)019<1208:EMPADF>2.0.CO;2

Sloyan, B. M., & Rintoul, S. R. (2001). Circulation, Řenewal, and Modification of Antarctic Mode and Intermediate Water. *Journal of Physical Oceanography*,

31(4), 1005–1030. https://doi.org/10.1175/1520-0485(2001)031<1005:CRAMOA>2.0.CO;2

Sohail, T., Vreugdenhil, C. A., Gayen, B., & Hogg, A. M. (2019). The Impact of Turbulence and Convection on Transport in the Southern Ocean. *Journal of Geophysical Research: Oceans*, *124*(6), 4208–4221. https://doi.org/10.1029/2018JC014883

Speer, K., Isemer, H.-J., & Biastoch, A. (1995). Water Mass Formation from Revised COADS Data. *Journal of Physical Oceanography*, *25*(10), 2444–2457. https://doi.org/10.1175/1520-0485(1995)025<2444:WMFFRC>2.0.CO;2

Speer, K., Rintoul, S. R., & Sloyan, B. (2000). The Diabatic Deacon Cell. *Journal of Physical Oceanography*, *30*(12), 3212–3222. https://doi.org/10.1175/1520-0485(2000)030<3212:TDDC>2.0.CO;2

Sprintall, J., & Cronin, M. F. (2009). Upper Ocean Vertical Structure. In J. H. Steele (Ed.), *Encyclopedia of Ocean Sciences (Second Edition)* (Second Edition, pp. 217–224). Academic Press. https://doi.org/https://doi.org/10.1016/B978-012374473-9.00627-5

Stern, M. E. (1960). The "Salt-Fountain" and Thermohaline Convection. *Tellus*, *12*(2), 172–175. https://doi.org/10.3402/tellusa.v12i2.9378

Stewart, K. D., & Haine, T. W. N. (2016). Thermobaricity in the Transition Zones between Alpha and Beta Oceans. *Journal of Physical Oceanography*, *46*(6), 1805–1821. https://doi.org/10.1175/JPO-D-16-0017.1

Stommel, H. (1948). The westward intensification of wind-driven ocean currents. *Eos, Transactions American Geophysical Union*, *29*(2), 202–206.

Stommel, H. (1958). The abyssal circulation. *Deep Sea Research (1953)*, *5*(1), 80–82. https://doi.org/10.1016/S0146-6291(58)80014-4

Stommel, H. (1961). Thermohaline Convection with Two Stable Regimes of Flow. *Tellus*, *13*(2), 224–230. https://doi.org/10.1111/j.2153-3490.1961.tb00079.x

Stommel, H., & Arons, A. (1959). On the abyssal circulation of the world ocean—I. Stationary planetary flow patterns on a sphere. *Deep Sea Research (1953)*, *6*, 140–154. https://doi.org/10.1016/0146-6313(59)90065-6

Sverdrup, H. U. (1947). Wind-Driven Currents in a Baroclinic Ocean; with Application to the Equatorial Currents of the Eastern Pacific. *Proceedings of the National Academy of Sciences*, *33*(11), 318–326. https://doi.org/10.1073/pnas.33.11.318

Thomas, L. N., & Shakespeare, C. J. (2015). A New Mechanism for Mode Water Formation involving Cabbeling and Frontogenetic Strain at Thermohaline Fronts. *Journal of Physical Oceanography*, *45*(9), 2444–2456. https://doi.org/10.1175/JPO-D-15-0007.1

Toggweiler, J. R., & Samuels, B. (1998). On the Ocean's Large-Scale Circulation near the Limit of No Vertical Mixing. *Journal of Physical Oceanography*, *28*(9), 1832–1852. https://doi.org/10.1175/1520-0485(1998)028<1832:OTOSLS>2.0.CO;2

Vallis, G. K. (2017). *Atmospheric and oceanic fluid dynamics*. Cambridge University Press.

Virtanen, P., Gommers, R., Oliphant, T. E., Haberland, M., Reddy, T., Cournapeau, D., Burovski, E., Peterson, P., Weckesser, W., Bright, J., van der Walt, S. J., Brett, M., Wilson, J., Millman, K. J., Mayorov, N., Nelson, A. R. J., Jones, E., Kern, R., Larson, E., ... SciPy 1.0 Contributors. (2020). SciPy 1.0: Fun-

damental Algorithms for Scientific Computing in Python. *Nature Methods*, *17*, 261–272. https://doi.org/10.1038/s41592-019-0686-2

Walin, G. (1982). On the relation between sea-surface heat flow and thermal circulation in the ocean. *Tellus*, *34*(2), 187–195. https://doi.org/10.1111/j.2153-3490.1982.tb01806.x

Whitworth, T. (1980). Zonation and geostrophic flow of the Antarctic circumpolar current at Drake Passage. *Deep Sea Research Part A. Oceanographic Research Papers*, *27*(7), 497–507. https://doi.org/10.1016/0198-0149(80)90036-9

Wilson, E. A., Riser, S. C., Campbell, E. C., & Wong, A. P. S. (2019). Winter Upper-Ocean Stability and Ice–Ocean Feedbacks in the Sea Ice–Covered Southern Ocean. *Journal of Physical Oceanography*, *49*(4), 1099–1117. https://doi.org/10.1175/JPO-D-18-0184.1

Wolfe, C. L., & Cessi, P. (2010). What Sets the Strength of the Middepth Stratification and Overturning Circulation in Eddying Ocean Models? *Journal of Physical Oceanography*, *40*(7), 1520–1538. https://doi.org/10.1175/2010JPO4393.1

Wolfe, C. L., & Cessi, P. (2014). Salt Feedback in the Adiabatic Overturning Circulation. *Journal of Physical Oceanography*, *44*(4), 1175–1194. https://doi.org/10.1175/JPO-D-13-0154.1

You, Y. (2002). A global ocean climatological atlas of the Turner angle: Implications for double-diffusion and water-mass structure. *Deep Sea Research Part I: Oceanographic Research Papers*, *49*(11), 2075–2093. https://doi.org/10.1016/S0967-0637(02)00099-7

Yu, L., & Weller, R. A. (2007). Objectively Analyzed Air–Sea Heat Fluxes for the Global Ice-Free Oceans (1981–2005). *Bulletin of the American Meteorological Society*, *88*(4), 527–540. https://doi.org/10.1175/BAMS-88-4-527

Zahariev, K., & Garrett, C. (1997). An Apparent Surface Buoyancy Flux Associated with the Nonlinearity of the Equation of State. *Journal of Physical Oceanography*, *27*(2), 362–368. https://doi.org/10.1175/1520-0485(1997)027<0362:AASBFA>2.0.CO;2

Paper I

The Polar Transition from Alpha to Beta Regions Set by a Surface Buoyancy Flux Inversion

ROMAIN CANEILL,[a] FABIEN ROQUET,[a] GURVAN MADEC,[b] AND JONAS NYCANDER[c]

[a] *Department of Marine Sciences, University of Gothenburg, Gothenburg, Sweden*
[b] *LOCEAN Laboratory, Sorbonne Université-CNRS-IRD-MNHN, Paris, France*
[c] *Department of Meteorology, Stockholm University, Stockholm, Sweden*

(Manuscript received 2 December 2021, in final form 9 March 2022)

ABSTRACT: The stratification is primarily controlled by temperature in subtropical regions (alpha ocean) and by salinity in subpolar regions (beta ocean). Between these two regions lies a transition zone, often characterized by deep mixed layers in winter and responsible for the ventilation of intermediate or deep layers. While of primary interest, no consensus on what controls its position exists yet. Among the potential candidates, we find the wind distribution, air–sea fluxes, or the nonlinear cabbeling effect. Using an ocean general circulation model in an idealized basin configuration, a sensitivity analysis is performed testing different equations of state. More precisely, the thermal expansion coefficient (TEC) temperature dependence is explored, changing the impact of heat fluxes on buoyancy fluxes in a series of experiments. The polar transition zone is found to be located at the position where the sign of the surface buoyancy flux reverses to become positive, in the subpolar region, while wind or cabbeling are likely of secondary importance. This inversion becomes possible because the TEC is reducing at low temperature, enhancing in return the relative impact of freshwater fluxes on the buoyancy forcing at high latitudes. When the TEC is made artificially larger at low temperature, the freshwater flux required to produce a positive buoyancy flux increases and the polar transition moves poleward. These experimets demonstrate the important role of competing heat and freshwater fluxes in setting the position of the transition zone. This competition is primarily influenced by the spatial variations of the TEC linked to meridional variations of the surface temperature.

KEYWORDS: Buoyancy; Intermediate waters; Surface fluxes

1. Introduction

The transition between warm saline subtropical waters and cold fresh subpolar waters is usually very abrupt and has similar structures on the North Atlantic Ocean, the North Pacific Ocean, and the Southern Ocean, suggesting that the same processes lead to these transitions. Not only do the surface temperature and salinity change, but also the way they vary with depth. Subtropical regions are characterized by a decrease of the temperature with depth together with a decrease of salinity: temperature has a stratifying effect while salinity has a destabilizing one. On the contrary, surface temperature is colder than subsurface temperature in polar regions, so temperature destratifies the water column and salinity controls the stable stratification. These two opposite stratification types are referred to as alpha (temperature control) and beta (salinity control) and are representative of middle and high latitudes, respectively, with the beta ocean halocline being essential for the formation of sea ice (Carmack 2007). In between these alpha and beta regions lies a transition zone. Its exact definition varies among authors, but it can often be associated with a surface density maximum (Roden 1970). It contains a weak stratification, making it an ideal place for connecting surface and intermediate water and for increased mixing (Stewart and Haine 2016).

In the Southern Ocean, the transition between alpha and beta ocean is achieved by a succession of fronts closely related to the stratification of the water column and impacting the biological production (Pollard et al. 2002; Pauthenet et al. 2017). These frontal areas are the place of formation of Antarctic Intermediate Water (AAIW) and Subantarctic Mode Water (SAMW). The mixed layer (ML) is deep in winter, and the water escapes the seasonal thermocline to reach the permanent one through lateral subduction (Piola and Georgi 1982; Marsh et al. 2000; Holte et al. 2012; Sallée et al. 2010). A similar ventilation process occurs in the North Atlantic (Woods 1985).

The ventilation of the thermocline in the subtropical gyres is primarily induced by Ekman downwelling (Marshall et al. 1993; Karstensen and Quadfasel 2002). However, in the transition zones of the Southern and North Atlantic oceans, the Ekman vertical velocity is oriented upward, so wind can hardly explain the local downwelling (McCartney 1982; Sallée et al. 2010; Nycander et al. 2015).

The water masses that are exported below the mixed layer must be associated with buoyancy fluxes, whether they come from surface fluxes, diffusive fluxes, advection, or mixing, before taking part of the global overturning circulation (Walin 1982; Speer et al. 2000; Kuhlbrodt et al. 2007; Cessi 2019). The production of AAIW and SAMW results from both horizontal advection induced by wind stress and eddies and from the surface buoyancy fluxes (Sloyan and Rintoul 2001). The surface buoyancy loss during winter produces dense deep

Denotes content that is immediately available upon publication as open access.

Corresponding author: Romain Caneill, romain.caneill@gu.se

DOI: 10.1175/JPO-D-21-0295.1

water in the Nordic seas and surrounding basins (Isachsen et al. 2007; Petit et al. 2020), and their rate of formation is directly impacted by the buoyancy forcing (Mauritzen and Häkkinen 1999). Moreover, buoyancy fluxes and particularly freshwater inputs can damp the creation of deep water in the Labrador seas (Lazier 1980).

The surface heat loss contributes strongly to deepening the mixed layer in the subpolar regions; however, the positive surface freshwater flux present at high latitudes counterbalances the heat loss. Schmitt et al. (1989) studied the relative importance of buoyancy flux due to heat and salt and suggested the idea of a balance between these two effects, but while having high uncertainties due to their flux estimates. The distinction between thermal and haline buoyancy forcing is important for water mass transformation (Speer et al. 1995; Karstensen and Lorbacher 2011). The effect of heat and freshwater fluxes on the buoyancy fluxes needs to be studied carefully as the equation of state (EOS) for seawater is nonlinear.

The buoyancy is a function of the active tracers, temperature, and salinity through the equation of state for seawater. The contribution of temperature and salinity to buoyancy are scaled by the thermal expansion coefficient (TEC) and the haline contraction coefficient (HCC), respectively (Roquet et al. 2015). These coefficients describe how much the density changes when temperature or salinity changes. While the HCC varies by less than 10% in the ocean, the TEC is highly dependent on temperature and pressure. It increases almost linearly with temperature and is about 9 times smaller in polar regions than in the tropics. Variations of the TEC are responsible for the two main nonlinearities in the EOS: cabbeling (variation with temperature) and thermobaricity (variation with pressure). It is known that these nonlinearities have a nonnegligible impact on water mass transformations, as they can cause diapycnal advection from isopycnal diffusion (e.g., Garrett and Horne 1978; McDougall and You 1990; Iudicone et al. 2008; Klocker and McDougall 2010; Stewart and Haine 2016; Thomas and Shakespeare 2015). The overall result of cabbeling is that at steady state, when the time- and spaced-averaged surface heat and freshwater fluxes vanish, the average surface buoyancy flux is positive, compensating the interior buoyancy sink due to cabbeling (Hieronymus and Nycander 2013).

Another implication of the TEC variation is that the buoyancy loss associated with a heat loss depends on the value of the TEC, itself a strong function of temperature. As the surface buoyancy flux in subpolar regions results from a competition between its thermal and haline components, it is likely that the decrease of the TEC at low temperature increases the relative haline influence, as pointed out by Rooth (1982), Bryan (1986), and Aagaard and Carmack (1989). The nonlinearities are found to be important in the global circulation and to contribute to setting the global ocean properties. A difference of mean salinity and temperature along with differences of circulation are found when using a linear EOS on a realistic ocean global circulation model compared to a realistic EOS (Roquet et al. 2015; Nycander et al. 2015). However, the buoyancy fluxes have not been accurately studied in the cited studies.

This study aims to investigate how the location of the polar transition (between alpha and beta ocean) and of the intermediate water location are influenced by the surface buoyancy flux, and especially by its latitudinal change of sign. As the buoyancy flux is strongly linked to the TEC in the polar area, modifying the parameters for the EOS in a numerical model study is used here as an effective method to modulate the relative impact of heat and freshwater on the surface buoyancy flux. The stratification is also impacted, while keeping similar surface temperature and salinity fields and the same wind forcing between the experiments. For the numerical experiments, an idealized configuration of the NEMO (Nucleus for European Modeling of the Ocean; Madec et al. 2019) ocean general circulation model (OGCM) has then been developed, using a simplified EOS allowing for a full control of its nonlinearities (Roquet et al. 2015).

This paper is organized as follow. The equation of state for seawater, its properties, and the stratification control index are presented in section 2. The model configurations are then described in section 3, followed by the description and analysis of the reference run (section 4). A comparison of the different parameter is then discussed (section 5) and further discussions and conclusions are given in section 6.

2. The equation of state for seawater

a. General properties

The EOS for seawater gives the density as a function of temperature, salinity, and pressure. Under the Boussinesq approximation, the thermal expansion coefficient α and the haline contraction coefficient β are defined as

$$\alpha = -\frac{1}{\rho_0}\frac{\partial \rho}{\partial \Theta}\bigg|_{S_A,p}, \tag{1}$$

$$\beta = \frac{1}{\rho_0}\frac{\partial \rho}{\partial S_A}\bigg|_{\Theta,p}. \tag{2}$$

We use here the Conservative Temperature Θ and Absolute Salinity S_A following the TEOS-10 standard (McDougall 2003; IOC et al. 2015), but for simplicity we will call them temperature and salinity in the rest of the paper.

The surface buoyancy fluxes are related to the fluxes of heat and freshwater, weighted by the TEC and HCC, and can be decomposed into their respective contributions:

$$F_b = \underbrace{\frac{g\alpha}{\rho_0 C_p} Q_{\text{tot}}}_{F_b^\Theta} + \underbrace{\frac{-g\beta}{\rho_0} f_S}_{F_b^S}, \tag{3}$$

where g is the gravity acceleration, $C_p \simeq 3991.86$ J kg^{-1} K^{-1} the heat capacity, Q the total heat flux (W m^{-2}), and $f_S = S_{\text{surf}}(E - P)$ the equivalent salt flux in (g kg^{-1}) kg m^{-2} s^{-1}, linked to the evaporation E and precipitation P (both in kg m^{-2} s^{-1}), through the surface salinity S_{surf}. The term F_b^Θ is the heat contribution, F_b^S the salt contribution, and F_b the total surface buoyancy flux (m^2 s^{-3}). We define the buoyancy flux using a

TABLE 1. Default value of the simplified equation of state coefficients.

Coefficient	Value	Description
a_0	1.65×10^{-1} °C^{-1} kg m^{-3}	Linear thermal expansion coefficient
b_0	7.6554×10^{-1} (g kg^{-1})$^{-1}$ kg m^{-3}	Linear haline expansion coefficient
C_b	9.9×10^{-3} °C^{-2} kg m^{-3}	Cabbeling coefficient
T_h	2.4775×10^{-5} °C^{-1} dbar^{-1} kg^{-3}	Thermobaric coefficient

salt flux and not a freshwater flux as salinity restoring conditions creating a salt flux are used in the model configuration.

b. The simplified equation of state

Roquet et al. (2015) proposed a simplified version of the EOS that retains the main nonlinearity of the EOS while being analytically tractable, so that the TEC is linearly dependent on the temperature and the pressure and the HCC is constant. This simplified version of the nonlinear EOS produces realistic ocean properties when applied on OGCMs, in contrast to a linear EOS where both the TEC and HCC are constant (Nycander et al. 2015). Were we use this simplified equation of state, i.e.,

$$\rho(\Theta, S_A, p) = \rho_0 - \left(a_0 + \frac{1}{2} C_b \Theta_a + T_h p\right)\Theta_a + b_0 S_a, \quad (4)$$

with $\Theta_a = \Theta - 10$°C, $S_a = S_A - 35$ g kg^{-1}, and p the pressure. Table 1 gives the standard values and description of the coefficients of the EOS. The T_h term sets the thermobaricity dependence and is kept for realistic representation of the deep circulation, but is kept constant in all the experiments. The dependence of the TEC on the temperature and the constant value of the HCC are evident using this simplified EOS, as they become

$$\alpha = \frac{1}{\rho_0}(a_0 + C_b \Theta_a + T_h p), \quad (5)$$

$$\beta = \frac{b_0}{\rho_0}. \quad (6)$$

This simplified equation is used to compute the density and buoyancy flux in the different runs of the circulation model used in this study.

c. The stratification control index

Changes in Θ or S_A lead to changes of the density that affect the circulation and stratification. The stratification control index (SCI) is defined such as to compare the relative effect of temperature and salinity on the stratification:

$$\mathrm{SCI} = \frac{N_\Theta^2 - N_S^2}{N_\Theta^2 + N_S^2}, \quad (7)$$

$$N^2 = -\frac{g}{\rho_0}\frac{\partial \rho_\Theta}{\partial z} = N_\Theta^2 + N_S^2, \quad (8)$$

TABLE 2. The different parameters of the simplified EOS for the five runs. The other parameters are kept constant and equal to the default values.

Name	a_0 (°C^{-1} kg m^{-3})	C_b (°C^{-2} kg m^{-3})
Ref	1.65×10^{-1}	9.9×10^{-3}
A	1.65×10^{-1}	13.2×10^{-3}
B	1.45×10^{-1}	8.7×10^{-3}
C	1.85×10^{-1}	11.1×10^{-3}
D	1.65×10^{-1}	6.6×10^{-3}

$$N_\Theta^2 = g\alpha \frac{\partial \Theta}{\partial z}, \quad (9)$$

$$N_S^2 = -g\beta \frac{\partial S_A}{\partial z}. \quad (10)$$

Two critical transitions occur, when SCI = 1 (no salinity stratification) and SCI = −1 (no temperature stratification). This means that three states of the stratification can be expected:

1) SCI ≥ 1, an *alpha ocean* stratified by temperature and destratified by salinity,
2) SCI ≤ -1, a *beta ocean* stratified by salinity and destratified by temperature,
3) $-1 <$ SCI < 1, a *transition zone* doubly stratified by both temperature and salinity.

Note that the SCI has not been defined previously in the literature to our knowledge. However, it can be directly linked to standard indexes, such as the Turner angle [SCI = tan(Tu)] or the density ratio, $R_\rho = -N_\Theta^2/N_S^2$ (Ruddick 1983). For stable stratifications ($N^2 > 0$), the SCI is uniquely defined over the real numbers and has the advantage to treat symmetrically the effect of salinity and temperature and avoid singularities, contrary to the density ratio. We therefore chose to focus on this new index here.

The SCI will be computed 10 m below the mixed layer, from monthly mean values. For every longitude–latitude point the SCI at the time of deepest mixed layer will be retained for the ocean classification. Thus, we classify the ocean based on the permanent thermocline, and not on the seasonal one. Note that our definition of the alpha, beta and transition zones differ slightly from previous ones (Carmack 2007; Stewart and Haine 2016). We retain our definition to get a unique decomposition between the three ocean types.

3. The model configurations

In a series of sensitivity experiments, the parameters that control the surface TEC dependance on temperature, a_0 and C_b, are modified between each run. A total of five different parameter combinations are used (Table 2).

a. Description of the model

The NEMO (Madec et al. 2019) OGCM is used for the simulation. The configuration represents an idealized basin on the sphere, 40° of longitude wide, and from 0° to about 60°N,

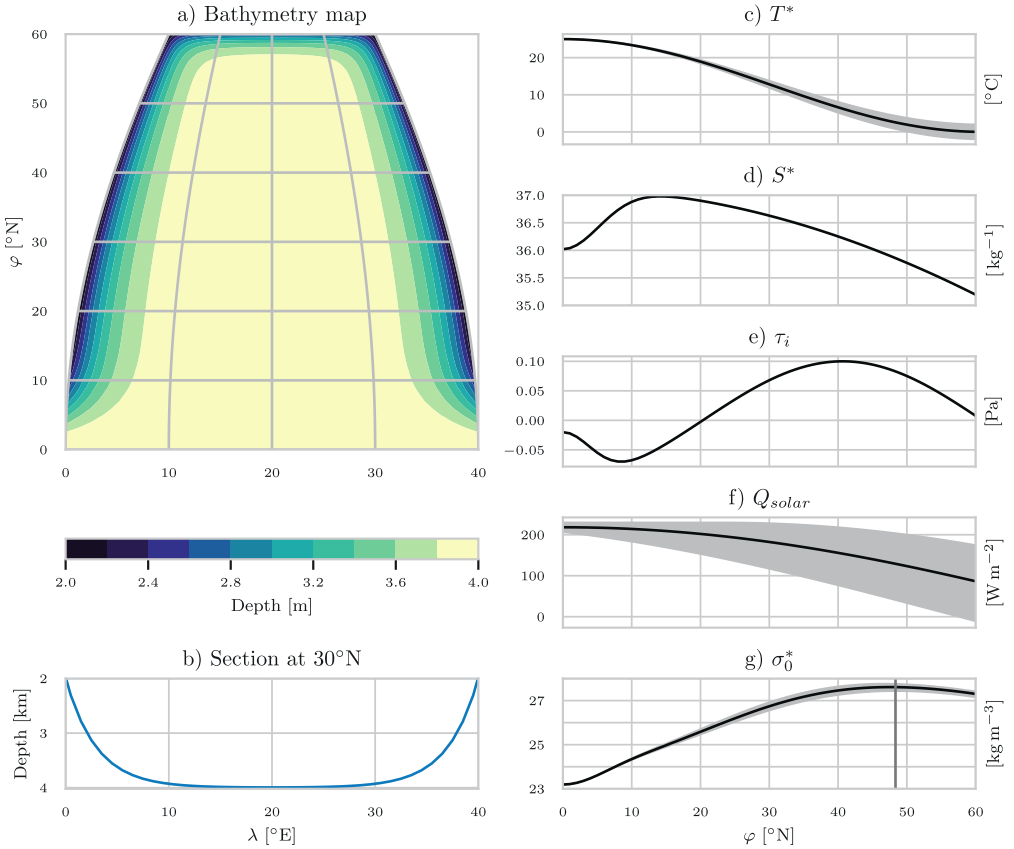

FIG. 1. (a),(b) Bathymetry of the basin. Forcing fields used by the model, with (c) the restoring temperature, (d) the restoring salinity, (e) the zonal wind stress, (f) the solar heat flux, and (g) the restoring density anomaly. The average values are plotted in black. For (c), (f), and (g), the gray zone represents the seasonal variation range. The vertical line in (e) represents φ_M, the latitude of the winter maximum restoring density.

similar to the one of Lazar et al. (1999). The width of the basin (in meters) decreases with latitude, and the Coriolis parameter is computed as $f = 2\Omega \sin(\varphi)$. A 1° longitude Mercator grid is used so the resolution (in meters) scales as cos(latitude), the number of grid points is 42 in longitude and 79 in latitude. The topography in meters is represented by an exponential slope with a length scale of 3°:

$$h(\lambda) = 4000 - 2000\left[\exp\left(-\frac{\lambda}{3}\right) + \exp\left(\frac{\lambda - 40}{3}\right)\right], \qquad (11)$$

with λ the longitude. A similar topography applies at the northern boundary, using the latitude coordinate. The bathymetry along the coast is 2000 m and reaches 4000 m in the central basin (Figs. 1a,b). A nonlinear free surface is used. The time step is 45 min. A terrain following coordinate is used, where the five upper levels have a constant thickness of 10 m, and the thickness then increases to 440 m at the bottom of the deepest parts, for a total of 36 vertical levels. To minimize the ageostrophic current due to the error on the pressure gradient caused by the terrain following coordinates close to the equator, the topography is flattened around the equator at the depth of 4000 m. Symmetric boundary conditions are used at the equator, with a no meridional fluxes condition applied. This symmetrical condition is equivalent to having a two hemispheres model forced with the same forcing, and only retain the Northern Hemisphere, while only computing the northern one.

The effect of unresolved eddies is parameterized using the Gent and McWilliams (1990) formulation, and lateral mixing is done along the neutral plane. A turbulent kinetic energy (TKE) closure is used to compute the vertical viscosity and diffusivity coefficients, with background values set to 10^{-4} m^2 s^{-1}. This high vertical diffusivity value allows a high consumption of bottom water through vertical turbulent diffusion and thus a sufficiently strong overturning circulation.

b. *Forcing fields*

The model is forced by analytical fields that represent the zonal wind stress, the heat, and haline fluxes. The analytical functions have been inspired and adapted from Lévy et al. (2010) and Wolfe and Cessi (2014), chosen to represent zonal

averages over the ocean. The thermal and haline forcing are both represented by a relaxation law so the surface fluxes are proportional to the difference between a restoring value and the ocean surface value:

$$Q_{\text{tot}} = A_\Theta(T^* - \text{SST}), \tag{12}$$

$$f_S = A_S(S^* - \text{SSS}), \tag{13}$$

with $A_S = 3.858 \times 10^{-3}$ kg m^{-2} s^{-1} the haline restoring coefficient, $A_\Theta = 40$ W m^{-2} °C^{-1} the temperature restoring coefficient, and SST (SSS) the sea surface temperature (salinity). The restoring fields are defined by the following equations:

$$T^* = [T_{\text{eq}} - T_N(d)]\cos^2\left(\frac{\pi\varphi}{2L}\right) + T_N(d), \tag{14}$$

$$T_N(d) = \Delta T \cos\left(\pi\,\frac{d + 159}{180}\right), \tag{15}$$

$$S^* = S_0 \exp\left[-\left(\frac{\varphi}{260}\right)^2\right] - S_1 \exp\left[-\left(\frac{\varphi}{7.5}\right)^2\right], \tag{16}$$

where $T_N(d)$ represents the seasonal variation of T^* with the respect of the day of the year d and φ the latitude in degrees. $T_{\text{eq}} = 25$°C is the temperature at the equator, $\Delta T = 2$°C, $L = 61$°C is the approximate latitudinal basin extension, $S_0 = 37.12$ g kg^{-1}, and $S_1 = 1.1$ g kg^{-1}.

The heat flux is split into a shortwave (solar) part and the nonsolar remainder:

$$Q_{\text{solar}}(\varphi, d) = 230 \cos\left[\pi\,\frac{\varphi - 23.5\cos\left(\pi\,\dfrac{d + 189}{180}\right)}{0.9 \times 180}\right], \tag{17}$$

$$Q_{\text{non solar}} = Q_{\text{tot}} - Q_{\text{solar}}. \tag{18}$$

The solar part is applied with a day/night cycle and is split into two bands with e-folding depths of 23 m (fraction 42%) and 0.35 m (fraction 58%) (Madec et al. 2019). The seasonal variation of the heat forcing induces a thermal restratification in summer, while the penetrative heat flux helps to reduce the upper stratification and limits the minimum mixed layer depth in tropical regions. We emphasize, however, that the results of our study are not sensitive to these details.

From the restoring fields, it is possible to define a restoring density anomaly σ_0^*, defined as the density anomaly of water at the surface, with a temperature T^* and a salinity S^*, along with the latitude φ_M where this forcing density is maximum:

$$\sigma_0^* = \rho(T^*, S^*, 0) - 1000 \quad \text{and} \quad \sigma_0^*(\varphi_M) = \max(\sigma_0^*). \tag{19}$$

For the reference run, this latitude is equal to 48.3°N.

The zonal wind stress follows the equation

$$\tau_\lambda = 0.1\left[-\cos\left(\frac{3\pi\varphi}{2L}\right) + 0.8\exp\left(-\frac{\varphi^2}{5.77^2}\right)\right]. \tag{20}$$

These fields are plotted in Fig. 1. The restoring temperature decreases from 25°C at the equator to 0°C on average at 60°N (−2°C in winter and 2°C in summer). The winter also corresponds to the period with less solar flux, which encounters a higher seasonality at high latitude than at the equator.

Several critical processes are missing here to obtain a realistic forcing, including the absence of interactive atmosphere and of sea ice, as the restoring temperature is too high to allow the formation of sea ice. We return to the potential limitations of not including sea ice formation in our configuration in section 6.

The model is run 2000 years for each simulation until equilibrium with level averages of temperature and salinity trends below 0.1°C and 0.01 g kg^{-1} per millennium, respectively. Fifty-year mean fields are used for all the subsequent analyzes, except for the SCI and for the mixed layer depth, where monthly averages are used.

4. Reference run

a. General description

The reference run uses the reference parameters for the EOS defined in Table 1 and is labeled as ref. The wind stress is kept constant between the different runs. As the barotropic streamfunction depends to first order on the wind stress, it is very similar for all the runs. It is shown in Fig. 2 along with the theoretical Ekman vertical velocities at the bottom of the Ekman column. The three expected gyres are present: an equatorial gyre from 0° to 10°N, a subtropical gyre from 10° to ~40°N, and a subpolar gyre from ~40° to 60°N. The theoretical Ekman vertical velocity w_{Ek} shows downwelling south of 34.8°N and upwelling north of this latitude. The w_{Ek} is computed using the following formula in spherical coordinates (Pedlosky 1996, chapter 1):

$$w_{\text{Ek}} = -\frac{1}{\rho_0}\,\frac{1}{R\cos\varphi}\,\frac{\partial}{\partial\varphi}\left(\frac{\tau_\lambda\cos\varphi}{\rho_0 f}\right), \tag{21}$$

where R is Earth's radius.

Figure 3 shows the overturning streamfunctions in density coordinates. The reference depth used for the potential density does not have a major impact on the results, thus σ_0 referenced at the surface is used. The surface circulation induced by the wind is visible at low latitude. A deeper cell corresponds to the deep circulation induced by the surface buoyancy forcing. This circulation is weak but oriented toward the equator.

Figure 4 shows the mean SST, SSS, and surface density anomaly (σ_0) of the reference run. The main features expected to be produced by the model are present: a strong western boundary current visible in the SST and the SSS, advecting warm and salty water between about 10° and 45°N, an equatorial upwelling at the eastern side, high salinity forced by net evaporation in the subtropics and low salinity (precipitation zones) close to the equator and in the subpolar region, while a cold freshwater pool is found on the northwest part of the basin.

The lowest densities are found in the western tropics, where the warmest SST are found. By contrast, the densest surface waters are not found at the coldest SST, due to the compensating

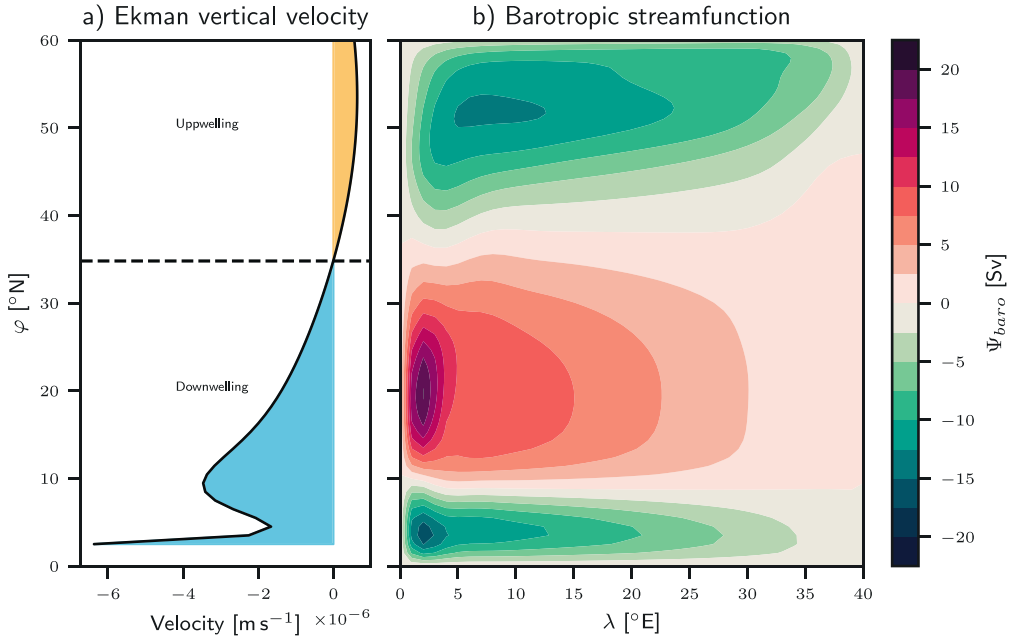

FIG. 2. Wind induced circulation: (a) theoretical Ekman vertical velocity and (b) barotropic response for the reference run. The Ekman velocity is not shown south of 2°N, as it diverges to $-\infty$.

effect of salt. They are located in the northeast area of the basin, while the coldest water is in the northwest, in a very fresh area. The maximum surface density anomaly is smaller than the maximum of σ_0^*. However, in similar runs without seasonality in the forcing fields, the surface maximum density anomaly is larger than the maximum of σ_0^*, due to advection of salty water in a cold region (figure not shown).

The western boundary current is visible on the sea surface height (SSH; Fig. 5a). An eastern boundary current is also visible in the eastern side, north of 30°N. These two currents advect warm and salty water in direction of the pole, and under the restoring condition these water masses will lose both heat and salinity.

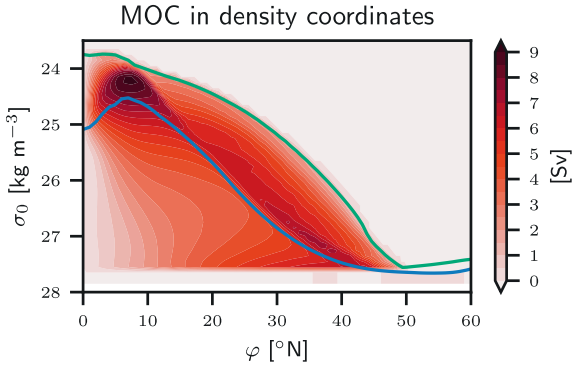

FIG. 3. Meridional overturning streamfunction computed in density coordinates. The green and blue lines represent the zonal minimum and maximum surface densities, respectively. Following standard conventions, the circulation is clockwise around maximum streamfunction values.

The annual maximum of the mixed layer depth (MLD) is shown in Fig. 5b. We use a density criterion with a threshold of 0.01 kg m^{-3} (de Boyer Montégut 2004). Because of the seasonality of the heat forcing, the mixed layer gets shallower in summer and deepens in winter, especially in the northern part of the basin where the temperature seasonality is the most important. Looking at the annual maximum reveals the deep convective area, which is situated in the northeast part of the basin. The fresh and cold pool visible on the SST and SSS maps appears to be very stratified and to have a shallow MLD of less than 200 m, compared to more than 3000 m on the eastern side at the same latitude. The SCI at the bottom of the winter ML (Fig. 5c), defined by Eq. (7), shows a sharp demarcation between the alpha (in red) and beta ocean (in blue) around 50°N. The northwest fresh pool is a beta ocean, implying that the salinity increases with depth (stabilizing effect), but that the temperature also increases (destabilizing effect). This means that deep water is saltier and warmer than the water in the mixed layer, implying that this deep water has been formed in a warmer area. A very narrow transition zone (surrounded by the white contour in the figure) lies between the alpha and beta ocean.

The alpha–beta front matches closely the northern limit of the deep ML region. Indeed, the beta region arises from the fact that fresh and cold water lies over saltier and warmer water. This deeper water comes from the deep ML region where it convects and is then advected into the northwest pool.

Figure 6 presents two sections of the SCI, at the end of the winter, when the mixed layer is the deepest, and at the end of

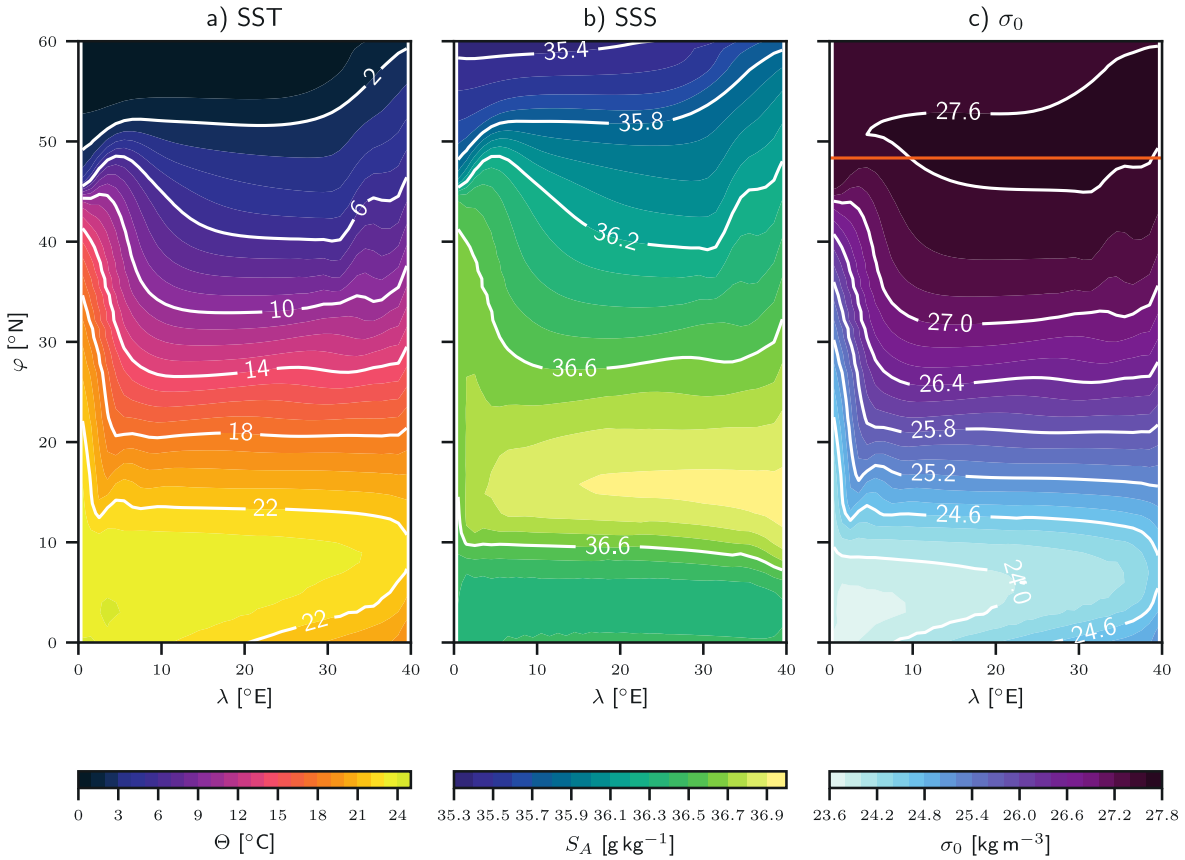

FIG. 4. (a) SST, (b) SSS, and (c) surface density anomaly for reference run. The horizontal orange line in (c) indicates φ_M.

the summer when the surface layers are the most stratified. The shallow fresh pool is visible north of 50°N, where the ocean is stratified by the salinity in the upper 100 m, particularly in the section 1 (at λ = 14.5°E). Apart from this small area, the majority of the ocean is classified as alpha ocean and a transition zone area exists between 40° and 50°N, close to the surface, and in the tropical region, and below 2000 m alpha ocean prevails. Due to the annual cycle of the thermal forcing, restratifying thermally the ocean in summer, the beta region is limited in its depth. On both sections it is seen that this shallow layer of beta ocean acts as a lid that prevents convection in winter. A control run conducted without the annual cycle shows deeper beta region in the north (not shown).

b. *Buoyancy forcing and response*

Following Eq. (3), Fig. 7 presents the surface buoyancy flux and its decomposition into the thermal and haline components. The annual-mean surface buoyancy flux sets the surface density change induced by the external forcing; we thus use the yearly averages of the surface buoyancy flux. The southern part of the basin gains heat while the northern part loses it. The fluxes are small around 10°N, where the surface velocity is zonal and the mixed layer shallow, leaving enough time for the water to thermally equilibriate with the forcing. The most negative buoyancy fluxes due to heat are found in the vicinity of the western boundary current, where warm water is advected northward.

The maximum values of F_b^Θ are roughly 10 times larger than the maximum values of F_b^S. However, as F_b^Θ is small in the northern part of the basin, these two components are comparable there. Around 55°N, the buoyancy forcing changes sign and becomes positive northward due to the freshening flux. This inversion of the surface flux is possible because 1) the heat flux becomes small in the north and 2) the TEC decreases at low temperature. The effect of this second point is that the influence of the heat flux on the buoyancy flux decreases in the polar regions. The densest surface water must be located in an area of buoyancy loss, so the surface buoyancy flux inversion marks a northern limit for the surface densest water. Moreover, this densest surface water is located where the mixed layer is deepest, i.e., in the convective zone.

5. Comparison with different parameters in the EOS

In the reference run the position where the surface buoyancy flux changes sign in the north is well correlated with the position of the alpha–beta front. This front also corresponds to the northern boundary of the deep ML area and the southern

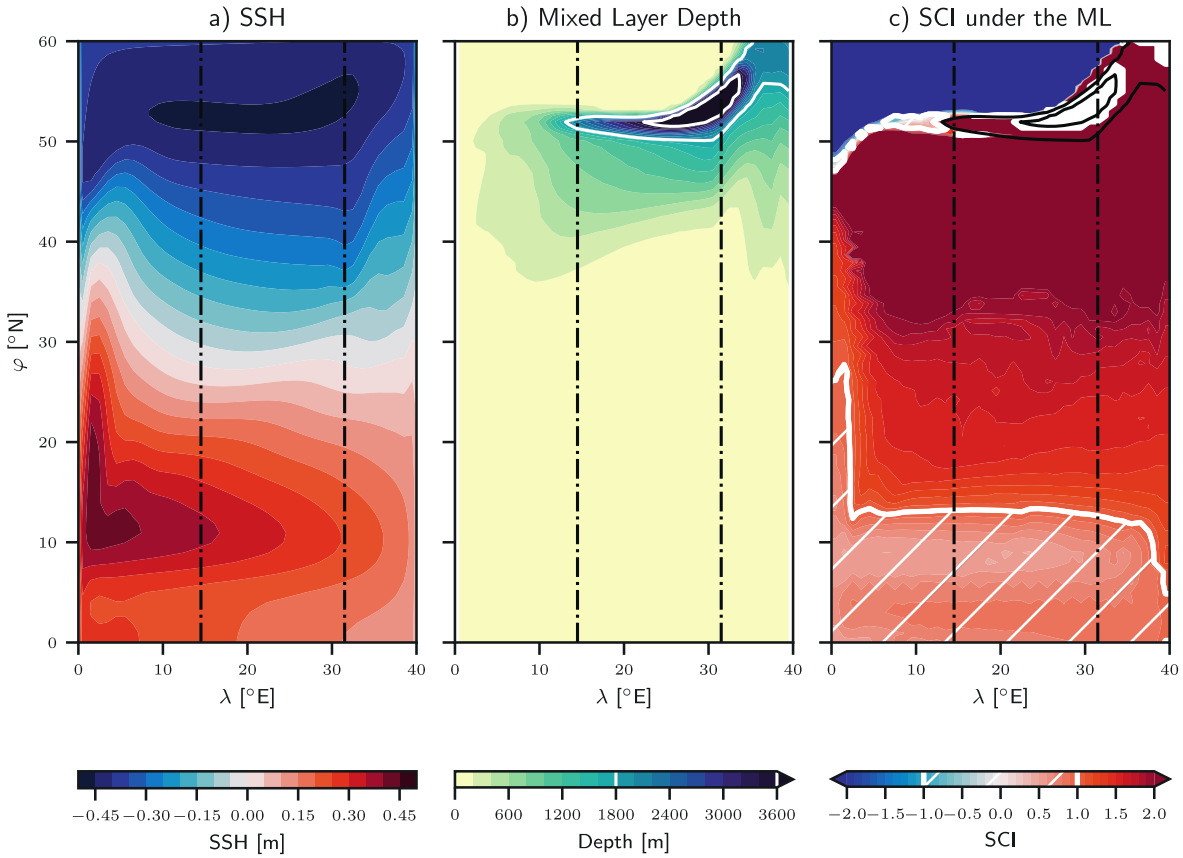

FIG. 5. (a) Sea surface height, (b) annual deepest mixed layer depth, and (c) stratification control index under the mixed layer for the reference run, taken in each point at the time of the year when the mixed layer is the deepest. The white contour in (c) indicates the transition zone, i.e., $-1 < \mathrm{SCI} < 1$, while the two black contours emphasize the 1800- and 3600-m MLD [these contours correspond to the two white contours of (b)]. When the mixed layer reaches the bottom cell, no value is used for the SCI (white areas). The black dashed lines represent the location of the sections presented in Fig. 6.

boundary of the northwest fresh pool. This section studies the causality hidden behind this correlation. Added to the reference experiment, four sensitivity runs have been conducted, with changes of the EOS parameters (Fig. 8a), resulting in different variations of the TEC with temperature. The wind is kept unchanged between the different runs.

Figure 9 shows the total surface buoyancy flux for the five experiments, along with the position of the beta boundary (SCI = −1) (the white line with a black contour). The runs are ordered with increasing polar TEC value from left to right (Fig. 8b). In this way, the experiments are organized with a relative decrease (increase) of the salinity (temperature) effect from left to right. Even if not exactly located at the same place, the positions of the polar transition zone and the buoyancy flux inversion are very close and follow a similar evolution between the runs. For higher values of the TEC (lower relative salinity impact) the transition zone is pushed to the north of the basin, where the salt fluxes eventually take control of the buoyancy flux. On the contrary, if the TEC is small, the heat flux will have a smaller impact on the buoyancy flux (as it is scaled by it) and the salinity control arises more to the south. The more the alpha–beta boundary is pushed to the north, the more it becomes affected by the subpolar gyre, and loses its zonality to become more meridional. The beta ocean is associated with shallow MLD, and a deep ML is found just south of the beta boundary (Fig. A1, appendix A).

The locations of the polar transition zone and of the buoyancy flux inversion are not perfectly zonal due to the effect of the subpolar gyre. However, it is possible to compute an equivalent average latitude, which corresponds to the southern latitude of a zonally uniform ocean, sharing the same integrated area that the area of interest (either the area $\mathrm{SCI} < -1$ or of buoyancy gain in the subpolar region). The detail of the calculation is given in appendix B. The φ_b is the equivalent latitude of the buoyancy flux inversion and φ_β the southern latitude of the fresh beta area. We use φ_β as a proxy for the latitude of the polar transition, as its latitudinal extension is very narrow in our experiments.

These two latitudes increase when φ_M increases, emphasizing the role of the buoyancy forcing (Fig. 10a). When buoyancy

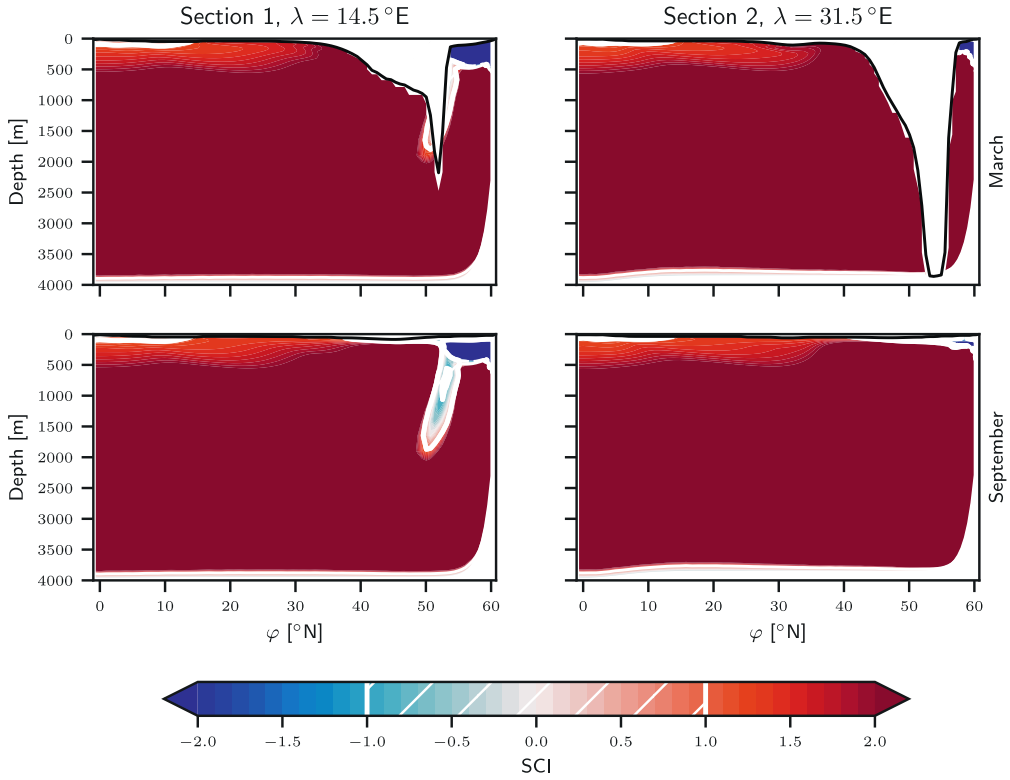

FIG. 6. Sections of the SCI in March and September for the longitudes 14.5° and 31.5°E. The mixed layer reaches the bottom in March at 31.5°E, and below 2000 m all the ocean has a SCI greater than 2.

flux inversion latitude increases, this pushes the beta ocean further north, as shown in Fig. 10b. As the wind is unchanged between the five experiments, the effect of the Ekman pumping cannot be the direct driving effect of the change of latitude of the transition zone. In contrast, the buoyancy forcing is modified at leading order. More specifically, as heat and salt play opposite roles for the buoyancy flux in the northern region, the location where they exactly balance and where the buoyancy flux has an inversion is not only function of their amplitude but also function of the variable TEC. So if the TEC value in the polar region increases, the latitude of the buoyancy inversion increases as well (Fig. 10c). In contrast, the latitude of both buoyancy inversion and polar transition are not monotonically varying with C_b (Fig. 10d).

Changing the TEC and the position of the deep-water creation also changes the properties of the abyssal water (Figs. 10e,f). When the buoyancy inversion is moved northward, the bottom water becomes consequently colder and fresher. As a result, the basin average of both salinity and temperature decrease, with a value of about 0.2 g kg^{-1} and 2°C, respectively, for the range of the experiments.

6. Discussions and conclusions

We have studied here the control of the position of the polar transition zone by the air–sea buoyancy fluxes, particularly by the competition between opposing heat and freshwater surface fluxes. We used an idealized configuration of the OGCM NEMO to verify the hypothesis that the wind or the cabbeling effect are not the main driver of the alpha–beta transition, and that they are not setting the position of the convergence zone and subduction, but on the contrary that the buoyancy fluxes are leading the control. As the relative effect of the heat and freshwater fluxes on the buoyancy fluxes is scaled by the TEC, we modified the equation of state for seawater while restoring the surface temperature and salinity toward the same fields to change the magnitude of these fluxes. When the value of the TEC was artificially increased in the subpolar region, the effect of temperature on stratification and buoyancy flux was made stronger, decreasing the relative impact of salinity fluxes.

The reference run uses a simplified nonlinear EOS with parameters that best fit the TEOS-10 standard (Roquet et al. 2015). The resulting circulation is close to the expected one for a closed basin with three gyres. A striking point is that the convective zone is located immediately south of the beta region. It is easily understood why deep convection cannot occur in the beta region. Since the stratification near the surface is there controlled by the salinity, the winter cooling cannot destabilize the water column. In other words, the capping layer of freshwater prevents convection in the beta region.

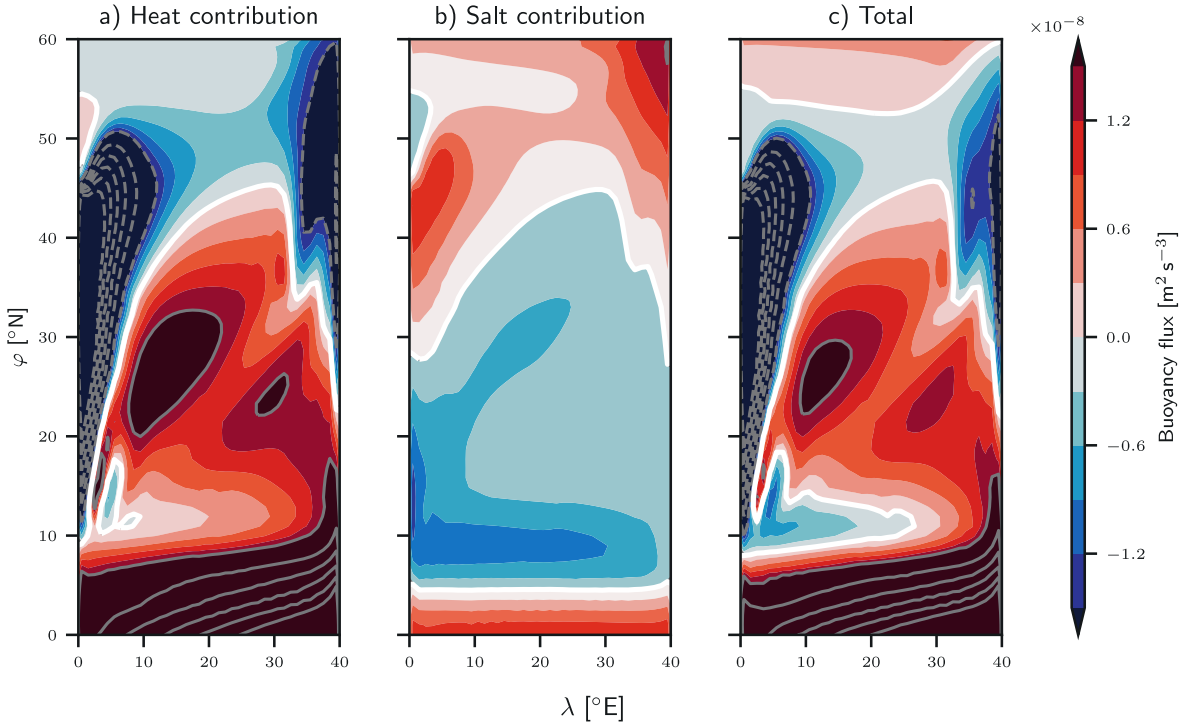

FIG. 7. Buoyancy fluxes: (a) the heat contribution, (b) the salt contribution, and (c) the total flux. The colors are saturated at $\pm 1.5 \times 10^{-8}$ m^2 s^{-3} so that the variations of the salt contribution are visible. The gray lines are separated by 1.5×10^{-8} m^2 s^{-3}, and the white line here underlines the 0 m^2 s^{-3} contour.

The maximum surface densities occur in the convective zone. It has been noted in the past that the transition zones in the Northern Hemisphere are indeed located in areas of local maximum density and low stratification (Roden 1970; Stewart and Haine 2016). If the surface water is denser than the water below the mixed layer, the column becomes unstable and the mixed layer deepens. This dense water may escape the seasonal thermocline and ventilate the permanent thermocline through lateral advection, a process reminiscent of the formation of North Atlantic Deep Water in the North Atlantic basin. Due to the large seasonality of the thermal forcing, the convective region is likely to become stratified by temperature in summer. The densification of surface water happens where surface buoyancy fluxes are negative. If dense water is advected into a region of positive surface buoyancy fluxes, it becomes lighter and thus contributes to making the mixed

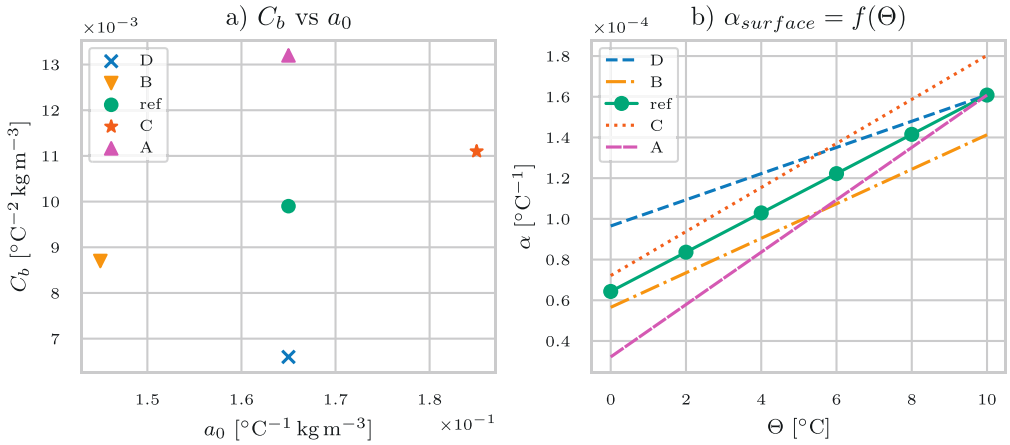

FIG. 8. (a) C_b vs a_0 scatterplot, and (b) variation of the TEC with respect of the temperature for the five experiments.

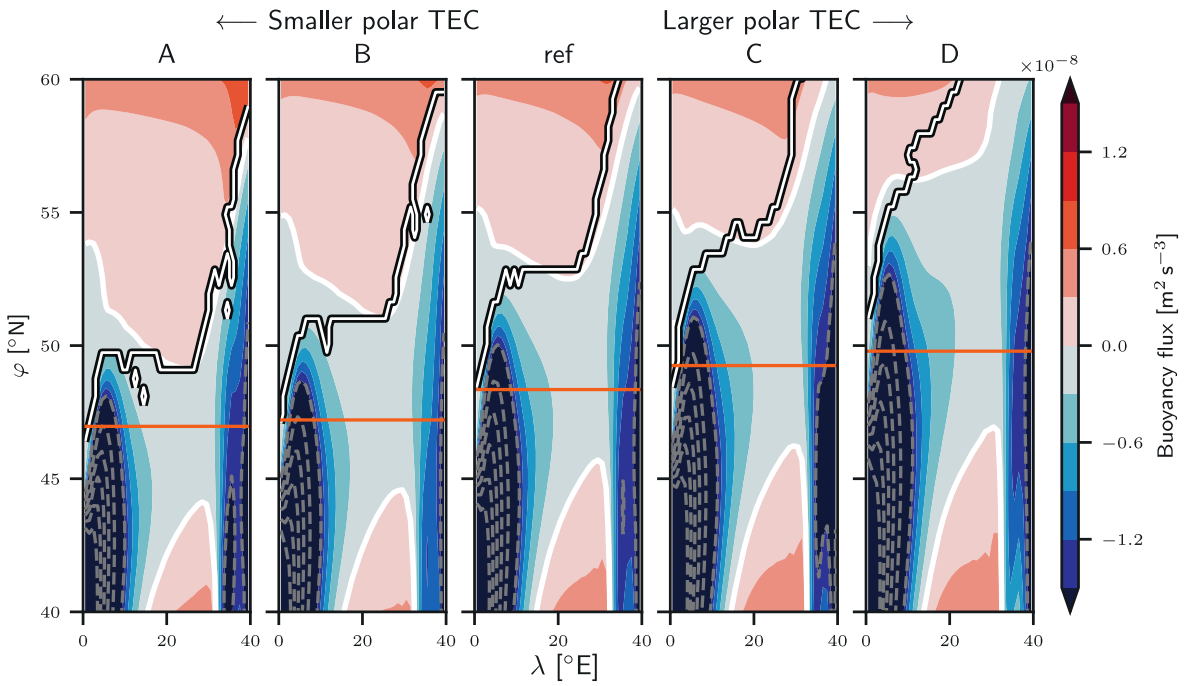

FIG. 9. Net buoyancy flux for every run. No major difference is visible south of 40°N so the figures have been cropped. The white line with black contour represents the −1 value of the SCI under the ML. As the polar transition zone is very narrow between the alpha and beta oceans, this line corresponds very well to the transition between the alpha and beta oceans. The orange line represents the latitude of φ_M, the latitude of maximum value of σ_0^*.

layer shallower. This simple mechanism highlights the importance of the position where the sign of the surface buoyancy flux changes, which itself results from a competition between heat and freshwater fluxes.

Figure 11 presents a conceptual view of the buoyancy flux control on the stratification, and on the intermediate water formation. Three regions result from the competition between F_b^Θ and F_b^S: a region a buoyancy loss surrounded by two regions of buoyancy gain. At the surface, water is advected poleward in the region of buoyancy loss (in the eastern part of the basin). This loss leads to an increase of the mixed layer depth, until the surface layer reaches the subpolar region, where the buoyancy fluxes become positive again. A fresh layer stratified by salinity is formed that prevents convection in this region. At depth, the water formed in the deep mixed layer area leaves the winter mixed layer by lateral induction to form the intermediate (or deep) water. This induction is directed equatorward on average, although it is associated with a cyclonic flow in the north before reaching the western slope to form a deep boundary current.

The polar transition zone corresponds to the boundary between the alpha and beta zones. In our experiments, the transition zone is very narrow and it matches the position where the surface buoyancy flux changes sign, becoming positive toward the north. The surface buoyancy flux changes sign when the negative heat flux becomes overridden by the positive freshwater flux. Importantly, this inversion is not driven by an intensification of the freshwater flux, but rather by the dropping value of the TEC associated with decreasing surface temperatures. If the TEC value is increased at low temperature in the model, the relative effect of salinity on the stratification is decreased and the convective zone is shifted poleward. In the extreme case where the TEC value is made very large for low temperatures (e.g., for a linear EOS with a value of the TEC close to the ocean average value of 2×10^{-4} °C^{-1}), the freshwater flux cannot overcome the large buoyancy loss due to heat fluxes anywhere. The result is a disappearance of the beta ocean in those simulations (not shown). In this study, the wind forcing has been kept unchanged. The large migration of the polar transition zone despite constant wind demonstrates that it is the buoyancy forcing that controls its position rather than the wind. However, the wind forcing can modify the buoyancy forcing through generation of meridional Ekman fluxes and by modulating the strength and structure of basin-scale gyres, indirectly affecting the position of the polar transition. We leave the task of assessing how the wind forcing affects the polar transition for a future work.

There are of course important limitations due to the nature of the single hemisphere basin configuration used in this study. The absence of a reentrant channel complicates the analogy with the Southern Ocean, although it is widely recognized that the general stratification depends critically on the presence of the Southern Ocean to produce a deep reaching circumpolar current and deepen the permanent pycnocline (Gnanadesikan 1999; Wolfe and Cessi 2011). The coarse

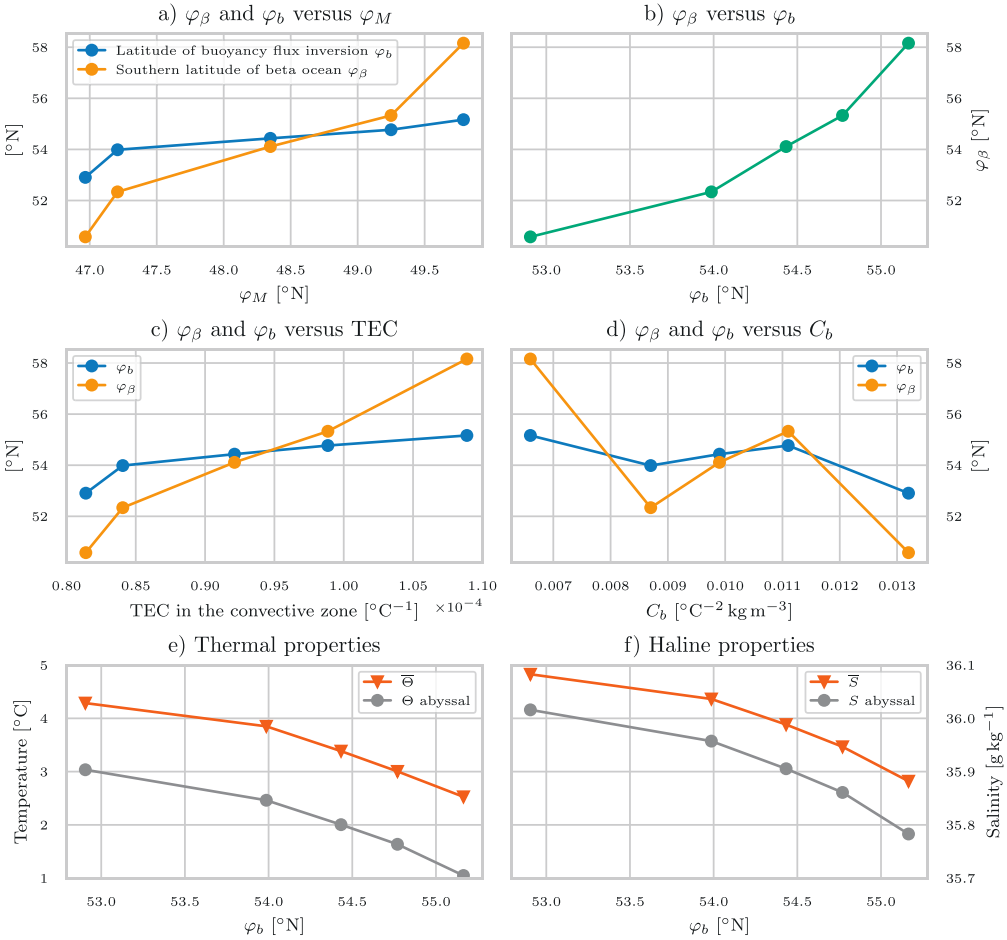

FIG. 10. (a) Latitude of the southern boundary of the beta ocean φ_β and latitude of the buoyancy front φ_b vs φ_M the latitude of maximum σ_0^*, (b) φ_β vs φ_b, (c) φ_b function of the value of the TEC in the convective area, (d) φ_β and φ_b vs cabbeling parameter C_b. Evolution of the basin average and abyssal (e) temperature and (f) salinity as a function of the front latitude. The abyssal properties are computed as latitude–longitude averages over the bottom cell of the ocean.

resolution used here also means mesoscale variability is not explicitly resolved, which would otherwise significantly complicate the structure and variability of the transition zone. As sea ice and brine rejection are not represented in the present idealized model, convection does not occur in the beta region resulting in the absence of a bottom stratification between deep and bottom waters. Sea ice modifies the freshwater forcing, through brine rejection or melting, modulating air–sea fluxes in the polar region. If the added freshwater is transported away from the sea ice formation area, e.g., by Ekman transport, the polar transition may consequently be shifted equatorward and convection in the transition zone may become hindered. Investigation would be needed to determine the contribution of sea ice melting to the freshwater budget around the transition zones. However, our results depend mainly on fluxes into the sea, so we expect the role of TEC variations on the surface buoyancy fluxes to be a robust feature directly applicable to the real ocean. As the transition zone in all basins is characterized by rapid changes in the type of stratification control (Pollard et al. 2002; Carmack 2007; Pauthenet et al. 2019), it is likely that the position of these fronts will remain primarily influenced by the surface buoyancy fluxes.

The mean ocean temperature, through its associated influence on the TEC value, is known to have an impact on the overturning circulation by the induced change of stratification (e.g., de Boer et al. 2007; Schloesser 2020). What has been less discussed is the potential migration of the deep-water formation area. As TEC is primarily a function of surface temperature (Roquet et al. 2015), a change of the TEC driven by surface warming will also impact the relative influence of the heat and freshwater fluxes. This change can be expected to influence in return the global circulation and the deep ocean thermohaline properties. We did not find

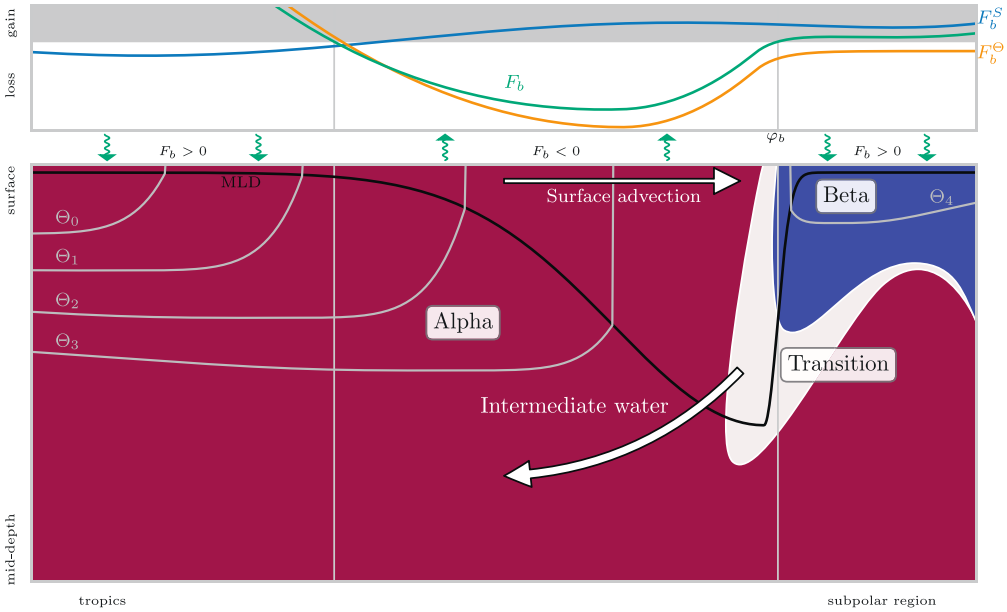

FIG. 11. Zonal conceptual view of the ocean. (top) The surface buoyancy fluxes, where the gray background is for positive fluxes and the white one for negative fluxes. The green wavy arrows represent the surface buoyancy flux: they are oriented downward for buoyancy gain, and upward for buoyancy loss. The two latitudes of buoyancy flux inversion are indicated by the vertical gray lines. (bottom) The zonal view of the ocean is shown. The red color is used for the alpha ocean, blue color for the beta ocean, and white for the transition zone. The mixed layer depth is represented by the black line, and the five gray lines represent five isotherms named by Θ_n with n between 0 and 5.

any indication that the cabbeling effect may be of leading order in setting the position of the polar transition and convective area, as similar locations and structures of the polar transition zone were found for model runs with vastly different cabbeling parameters but similar TEC in the polar area (runs not shown, C_b varying between 0 and 35×10^{-3} °C^{-2} kg m^{-3}). This does not mean, of course, that cabbeling has no effect in the transition zone, as it has been estimated that a significant densification of water masses is generated by cabbeling in transition zones (e.g., Groeskamp et al. 2016); however, this implies that the position and overall structure of the transition zone is probably not determined by the cabbeling effect.

This study highlights the primary importance of surface buoyancy fluxes in setting the general structure of the ocean stratification and the associated meridional overturning. It also documents one key way the thermodynamic properties of seawater have a global impact on the ocean circulation, namely, through the effect of geographic variations of the TEC on the distribution and sign of the surface buoyancy fluxes.

Acknowledgments. The computations were enabled by resources provided by the Swedish National Infrastructure for Computing (SNIC) at Tetralith partially funded by the Swedish Research Council through Grant Agreement 2018-05973. The authors appreciate the helpful reviews from two anonymous reviewers.

Data availability statement. The model data (output) can be found on Zenodo: https://doi.org/10.5281/zenodo.5607673. The scripts for the analyzes are hosted on GitHub, along with the model configuration source files: https://doi.org/10.5281/zenodo.6340730. All the runs and the analyze are reproducible within a few steps.

APPENDIX A

Comparison of MLD

Figure A1 compares the MLD for the five runs, along with the position of the beta ocean boundary. As expected, the beta ocean has a shallow ML, and the deepest ML are found immediately south of the polar transition zone. A clear correlation between the latitude of the maximum MLD, latitude of φ_M and polar TEC value can be seen, indicating that increasing the value of the TEC at low temperature is accompanied with a poleward migration of the polar transition zone.

APPENDIX B

Equivalent Latitude Calculation

This appendix gives the detail of the equivalent latitude calculation for the buoyancy flux inversion. First the area A of the ocean poleward of 48°N that gains buoyancy is

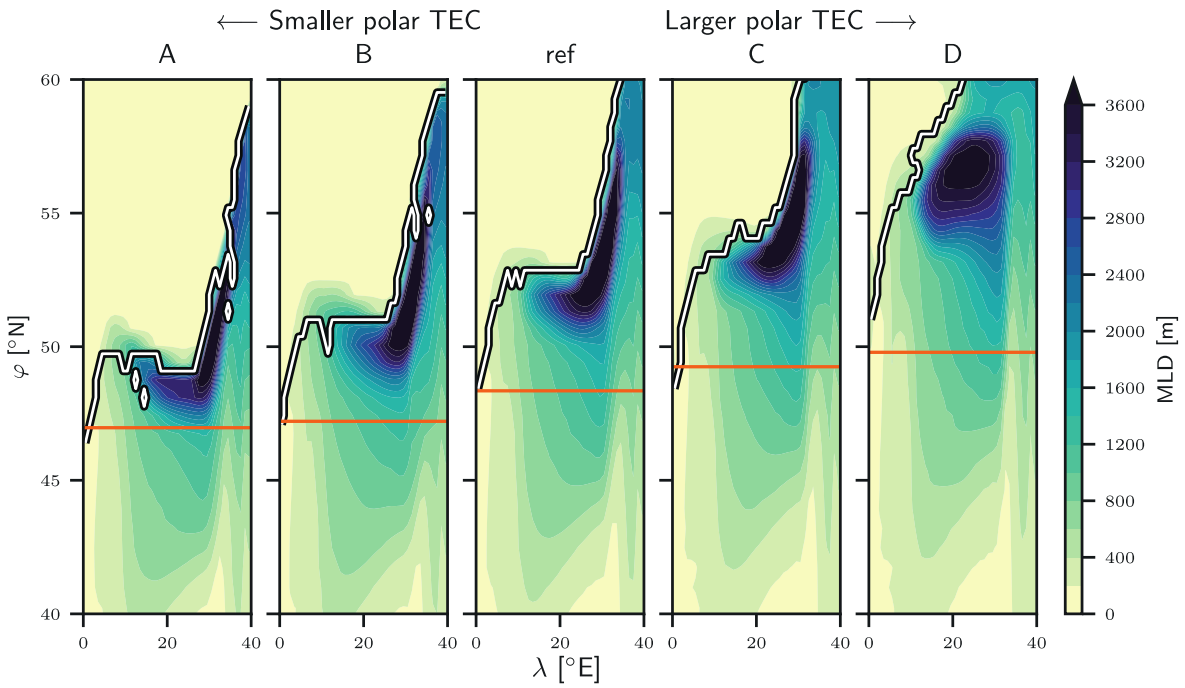

FIG. A1. Annual maximum of MLD for every runs. The white line with black contour represents the −1 value of the SCI under the ML. As the transition zone is very narrow between the alpha and beta oceans, this line corresponds very well to the transition between the alpha and beta oceans. The orange line represents the latitude of φ_M, the latitude of maximum value of σ_0^*.

computed. The area A_{eq} of a zonally uniform ocean bounded by the southern latitude φ_b is calculated as

$$A_{\text{eq}} = A = \int_{\lambda_W}^{\lambda_W} \int_{\varphi_b}^{\varphi_N} a^2 \cos\left(\varphi \frac{\pi}{180}\right) \varphi\lambda, \tag{B1}$$

where $\lambda_W = 0°\text{E}$ ($\lambda_E = 40°\text{E}$) is the western (eastern) coast, $\varphi_N \simeq 60.5°\text{N}$ is the northern boundary of the basin, and $a \simeq 111\,198$ km the length of 1° at the equator. Inverting this equation gives

$$\varphi_b = \arcsin\left[\sin(\varphi_N) - \frac{A}{a^2(\lambda_W - \lambda_E)}\right]. \tag{B2}$$

The same method is used for the area where SCI < -1 to compute the southern boundary of the latitude of the fresh beta area.

REFERENCES

Aagaard, K., and E. C. Carmack, 1989: The role of sea ice and other fresh water in the Arctic circulation. *J. Geophys. Res.*, **94**, 14 485–14 498, https://doi.org/10.1029/JC094iC10p14485.

Bryan, F., 1986: High-latitude salinity effects and interhemispheric thermohaline circulations. *Nature*, **323**, 301–304, https://doi.org/10.1038/323301a0.

Carmack, E. C., 2007: The alpha/beta ocean distinction: A perspective on freshwater fluxes, convection, nutrients and productivity in high-latitude seas. *Deep-Sea Res. II*, **54**, 2578–2598, https://doi.org/10.1016/j.dsr2.2007.08.018.

Cessi, P., 2019: The global overturning circulation. *Annu. Rev. Mar. Sci.*, **11**, 249–270, https://doi.org/10.1146/annurev-marine-010318-095241.

de Boer, A. M., D. M. Sigman, J. R. Toggweiler, and J. L. Russell, 2007: Effect of global ocean temperature change on deep ocean ventilation. *Paleoceanography*, **22**, PA2210, https://doi.org/10.1029/2005PA001242.

de Boyer Montégut, C., 2004: Mixed layer depth over the global ocean: An examination of profile data and a profile-based climatology. *J. Geophys. Res.*, **109**, C12003, https://doi.org/10.1029/2004JC002378.

Garrett, C., and E. Horne, 1978: Frontal circulation due to cabbeling and double diffusion. *J. Geophys. Res.*, **83**, 4651, https://doi.org/10.1029/JC083iC09p04651.

Gent, P. R., and J. C. McWilliams, 1990: Isopycnal mixing in ocean circulation models. *J. Phys. Oceanogr.*, **20**, 150–155, https://doi.org/10.1175/1520-0485(1990)020<0150:IMIOCM>2.0.CO;2.

Gnanadesikan, A., 1999: A simple predictive model for the structure of the oceanic pycnocline. *Science*, **283**, 2077–2079, https://doi.org/10.1126/science.283.5410.2077.

Groeskamp, S., R. P. Abernathey, and A. Klocker, 2016: Water mass transformation by cabbeling and thermobaricity. *Geophys. Res. Lett.*, **43**, 10 835–10 845, https://doi.org/10.1002/2016GL070860.

Hieronymus, M., and J. Nycander, 2013: The buoyancy budget with a nonlinear equation of state. *J. Phys. Oceanogr.*, **43**, 176–186, https://doi.org/10.1175/JPO-D-12-063.1.

Holte, J. W., L. D. Talley, T. K. Chereskin, and B. M. Sloyan, 2012: The role of air-sea fluxes in Subantarctic Mode Water

formation. *J. Geophys. Res.*, **117**, C03040, https://doi.org/10.1029/2011JC007798.

IOC, SCOR, and IAPSO, 2015: The International Thermodynamic Equation of Seawater—2010: Calculation and use of thermodynamic properties. Intergovernmental Oceanographic Commission, Manuals and Guides 56, 220 pp., http://www.teos-10.org/pubs/TEOS-10_Manual.pdf.

Isachsen, P. E., C. Mauritzen, and H. Svendsen, 2007: Dense water formation in the Nordic Seas diagnosed from sea surface buoyancy fluxes. *Deep-Sea Res. I*, **54**, 22–41, https://doi.org/10.1016/j.dsr.2006.09.008.

Iudicone, D., G. Madec, B. Blanke, and S. Speich, 2008: The role of Southern Ocean surface forcings and mixing in the global conveyor. *J. Phys. Oceanogr.*, **38**, 1377–1400, https://doi.org/10.1175/2008JPO3519.1.

Karstensen, J., and D. Quadfasel, 2002: Formation of Southern Hemisphere thermocline waters: Water mass conversion and subduction. *J. Phys. Oceanogr.*, **32**, 3020–3038, https://doi.org/10.1175/1520-0485(2002)032<3020:FOSHTW>2.0.CO;2.

——, and K. Lorbacher, 2011: A practical indicator for surface ocean heat and freshwater buoyancy fluxes and its application to the NCEP reanalysis data. *Tellus*, **63A**, 338–347, https://doi.org/10.1111/j.1600-0870.2011.00510.x.

Klocker, A., and T. J. McDougall, 2010: Influence of the nonlinear equation of state on global estimates of dianeutral advection and diffusion. *J. Phys. Oceanogr.*, **40**, 1690–1709, https://doi.org/10.1175/2010JPO4303.1.

Kuhlbrodt, T., A. Griesel, M. Montoya, A. Levermann, M. Hofmann, and S. Rahmstorf, 2007: On the driving processes of the Atlantic meridional overturning circulation. *Rev. Geophys.*, **45**, RG2001, https://doi.org/10.1029/2004RG000166.

Lazar, A., G. Madec, and P. Delecluse, 1999: The deep interior downwelling, the Veronis effect, and mesoscale tracer transport parameterizations in an OGCM. *J. Phys. Oceanogr.*, **29**, 2945–2961, https://doi.org/10.1175/1520-0485(1999)029<2945:TDIDTV>2.0.CO;2.

Lazier, J. R., 1980: Oceanographic conditions at Ocean Weather Ship Bravo, 1964–1974. *Atmos.–Ocean*, **18**, 227–238, https://doi.org/10.1080/07055900.1980.9649089.

Lévy, M., P. Klein, A.-M. Tréguier, D. Iovino, G. Madec, S. Masson, and K. Takahashi, 2010: Modifications of gyre circulation by sub-mesoscale physics. *Ocean Model.*, **34**, 1–15, https://doi.org/10.1016/j.ocemod.2010.04.001.

Madec, G., and Coauthors, 2019: NEMO ocean engine. Notes du Pôle de modélisation de l'Institut Pierre-Simon Laplace 27, Zenodo, https://doi.org/10.5281/ZENODO.1464816.

Marsh, R., A. J. G. Nurser, A. P. Megann, and A. L. New, 2000: Water mass transformation in the Southern Ocean of a global isopycnal coordinate GCM. *J. Phys. Oceanogr.*, **30**, 1013–1045, https://doi.org/10.1175/1520-0485(2000)030<1013:WMTITS>2.0.CO;2.

Marshall, J. C., R. G. Williams, and A. J. G. Nurser, 1993: Inferring the subduction rate and period over the North Atlantic. *J. Phys. Oceanogr.*, **23**, 1315–1329, https://doi.org/10.1175/1520-0485(1993)023<1315:ITSRAP>2.0.CO;2.

Mauritzen, C., and S. Häkkinen, 1999: On the relationship between dense water formation and the "Meridional Overturning Cell" in the North Atlantic Ocean. *Deep-Sea Res. I*, **46**, 877–894, https://doi.org/10.1016/S0967-0637(98)00094-6.

McCartney, M. S., 1982: The subtropical recirculation of mode-waters. *J. Mar. Res.*, **40**, 64.

McDougall, T. J., 2003: Potential enthalpy: A conservative oceanic variable for evaluating heat content and heat fluxes. *J. Phys. Oceanogr.*, **33**, 945–963, https://doi.org/10.1175/1520-0485(2003)033<0945:PEACOV>2.0.CO;2.

——, and Y. You, 1990: Implications of the nonlinear equation of state for upwelling in the ocean interior. *J. Geophys. Res.*, **95**, 13 263–13 276, https://doi.org/10.1029/JC095iC08p13263.

Nycander, J., M. Hieronymus, and F. Roquet, 2015: The nonlinear equation of state of sea water and the global water mass distribution. *Geophys. Res. Lett.*, **42**, 7714–7721, https://doi.org/10.1002/2015GL065525.

Pauthenet, E., F. Roquet, G. Madec, and D. Nerini, 2017: A linear decomposition of the Southern Ocean thermohaline structure. *J. Phys. Oceanogr.*, **47**, 29–47, https://doi.org/10.1175/JPO-D-16-0083.1.

——, ——, ——, J.-B. Sallée, and D. Nerini, 2019: The thermohaline modes of the global ocean. *J. Phys. Oceanogr.*, **49**, 2535–2552, https://doi.org/10.1175/JPO-D-19-0120.1.

Pedlosky, J., 1996: *Ocean Circulation Theory*. Springer, 467 pp., https://doi.org/10.1007/978-3-662-03204-6.

Petit, T., M. S. Lozier, S. A. Josey, and S. A. Cunningham, 2020: Atlantic deep water formation occurs primarily in the Iceland Basin and Irminger Sea by local buoyancy forcing. *Geophys. Res. Lett.*, **47**, e2020GL091028, https://doi.org/10.1029/2020GL091028.

Piola, A. R., and D. T. Georgi, 1982: Circumpolar properties of Antarctic intermediate water and Subantarctic Mode Water. *Deep-Sea Res.*, **29A**, 687–711, https://doi.org/10.1016/0198-0149(82)90002-4.

Pollard, R., M. Lucas, and J. Read, 2002: Physical controls on biogeochemical zonation in the Southern Ocean. *Deep-Sea Res. II*, **49**, 3289–3305, https://doi.org/10.1016/S0967-0645(02)00084-X.

Roden, G. I., 1970: Aspects of the mid-pacific transition zone. *J. Geophys. Res.*, **75**, 1097–1109, https://doi.org/10.1029/JC075i006p01097.

Rooth, C., 1982: Hydrology and ocean circulation. *Prog. Oceanogr.*, **11**, 131–149, https://doi.org/10.1016/0079-6611(82)90006-4.

Roquet, F., G. Madec, L. Brodeau, and J. Nycander, 2015: Defining a simplified yet "realistic" equation of state for seawater. *J. Phys. Oceanogr.*, **45**, 2564–2579, https://doi.org/10.1175/JPO-D-15-0080.1.

Ruddick, B., 1983: A practical indicator of the stability of the water column to double-diffusive activity. *Deep-Sea Res.*, **30A**, 1105–1107, https://doi.org/10.1016/0198-0149(83)90063-8.

Sallée, J.-B., K. Speer, S. Rintoul, and S. Wijffels, 2010: Southern Ocean thermocline ventilation. *J. Phys. Oceanogr.*, **40**, 509–529, https://doi.org/10.1175/2009JPO4291.1.

Schloesser, F., 2020: The Atlantic meridional overturning circulation and the cabbeling effect. *J. Phys. Oceanogr.*, **50**, 2561–2572, https://doi.org/10.1175/JPO-D-20-0085.1.

Schmitt, R. W., P. S. Bogden, and C. E. Dorman, 1989: Evaporation minus precipitation and density fluxes for the North Atlantic. *J. Phys. Oceanogr.*, **19**, 1208–1221, https://doi.org/10.1175/1520-0485(1989)019<1208:EMPADF>2.0.CO;2.

Sloyan, B. M., and S. R. Rintoul, 2001: Circulation, renewal, and modification of Antarctic mode and intermediate water. *J. Phys. Oceanogr.*, **31**, 1005–1030, https://doi.org/10.1175/1520-0485(2001)031<1005:CRAMOA>2.0.CO;2.

Speer, K., S. R. Rintoul, and B. Sloyan, 2000: The diabatic Deacon cell. *J. Phys. Oceanogr.*, **30**, 3212–3222, https://doi.org/10.1175/1520-0485(2000)030<3212:TDDC>2.0.CO;2.

Speer, K. G., H.-J. Isemer, and A. Biastoch, 1995: Water mass formation from revised COADS data. *J. Phys. Oceanogr.*, **25**, 2444–2457, https://doi.org/10.1175/1520-0485(1995)025<2444:WMFFRC>2.0.CO;2.

Stewart, K. D., and T. W. N. Haine, 2016: Thermobaricity in the transition zones between alpha and beta oceans. *J. Phys. Oceanogr.*, **46**, 1805–1821, https://doi.org/10.1175/JPO-D-16-0017.1.

Thomas, L. N., and C. J. Shakespeare, 2015: A new mechanism for mode water formation involving cabbeling and frontogenetic strain at thermohaline fronts. *J. Phys. Oceanogr.*, **45**, 2444–2456, https://doi.org/10.1175/JPO-D-15-0007.1.

Walin, G., 1982: On the relation between sea-surface heat flow and thermal circulation in the ocean. *Tellus*, **34**, 187–195, https://doi.org/10.3402/tellusa.v34i2.10801.

Wolfe, C. L., and P. Cessi, 2011: The adiabatic pole-to-pole overturning circulation. *J. Phys. Oceanogr.*, **41**, 1795–1810, https://doi.org/10.1175/2011JPO4570.1.

——, and ——, 2014: Salt feedback in the adiabatic overturning circulation. *J. Phys. Oceanogr.*, **44**, 1175–1194, https://doi.org/10.1175/JPO-D-13-0154.1.

Woods, J. D., 1985: The physics of thermocline ventilation. *Coupled Ocean-Atmosphere Modelling*, J. C. J. Nihoul, Ed., Elsevier Oceanography Series, Vol. 40, Elsevier, 543–590, https://doi.org/10.1016/S0422-9894(08)70730-X.

Paper II

https://doi.org/10.5194/egusphere-2023-2404
Preprint. Discussion started: 19 October 2023

Southern Ocean deep mixing band emerges from a competition between winter buoyancy loss and upper stratification strength

Romain Caneill[1], Fabien Roquet[1], and Jonas Nycander[2]

[1]Department of Marine Sciences, University of Gothenburg, Göteborg, Sweden
[2]Department of Meteorology, Stockholm University, Stockholm, Sweden

Correspondence: Romain Caneill (romain.caneill@gu.se)

Abstract. The Southern Ocean hosts a winter deep mixing band (DMB) near the Antarctic Circumpolar Current's (ACC) northern boundary, playing a pivotal role in Subantarctic Mode Water formation. Here, we investigate what controls the presence and geographical extent of the DMB. Using observational data, we construct seasonal climatologies of surface buoyancy fluxes, Ekman buoyancy transport, and upper stratification. The strength of the upper ocean stratification is determined using the columnar buoyancy index, defined as the buoyancy input necessary to produce a 250 m deep mixed layer. It is found that the DMB lies precisely where the autumn – winter buoyancy loss exceeds the columnar buoyancy found in late summer. The buoyancy loss decreases towards the south, while in the north, the stratification is too strong to produce deep mixed layers. Although this threshold is also crossed in the Agulhas current and East Australian current regions, advection of buoyancy is able to stabilise the stratification. The Ekman buoyancy transport has a secondary impact on the DMB extent due to the compensating effects of temperature and salinity transports on buoyancy. Changes in surface temperature drive spatial variations of the thermal expansion coefficient (TEC). These TEC variations are necessary to explain the limited meridional extent of the DMB. We demonstrate this by comparing buoyancy budgets derived using varying TEC values with those derived using a constant TEC value. Reduced TEC in colder waters leads to decreased winter buoyancy loss south of the DMB, yet substantial heat loss persists. Lower TEC values also weaken the effect of temperature stratification, partially compensating for the effect of buoyancy loss damping. TEC modulation impacts both the DMB characteristics and its meridional extent.

1 Introduction

The Southern Ocean (SO) plays a crucial role in global climate dynamics (Rintoul, 2018). The Antarctic Circumpolar Current (ACC), a defining feature, is demarcated by key fronts (Fig. 1): the Northern Boundary (NB), the Subantarctic Front (SAF), the Polar Front (PF), the Southern Antarctic Circumpolar Current Front (SACCF), and the Southern Boundary (SB) (Orsi et al., 1995). These fronts mark distinct regions of water masses with varying properties and stratification (Pauthenet et al., 2017). Temperature is the stratifying agent north of the SAF in the Atlantic and Indian sectors of the SO (Pollard et al., 2002), a regime known as the alpha ocean (Carmack, 2007). Between the SAF and the PF, both temperature and salinity increase stratification in the so-called polar transition zone (Caneill et al., 2022). Finally, salinity is the only stratifying agent in the beta ocean south of the PF.

https://doi.org/10.5194/egusphere-2023-2404
Preprint. Discussion started: 19 October 2023

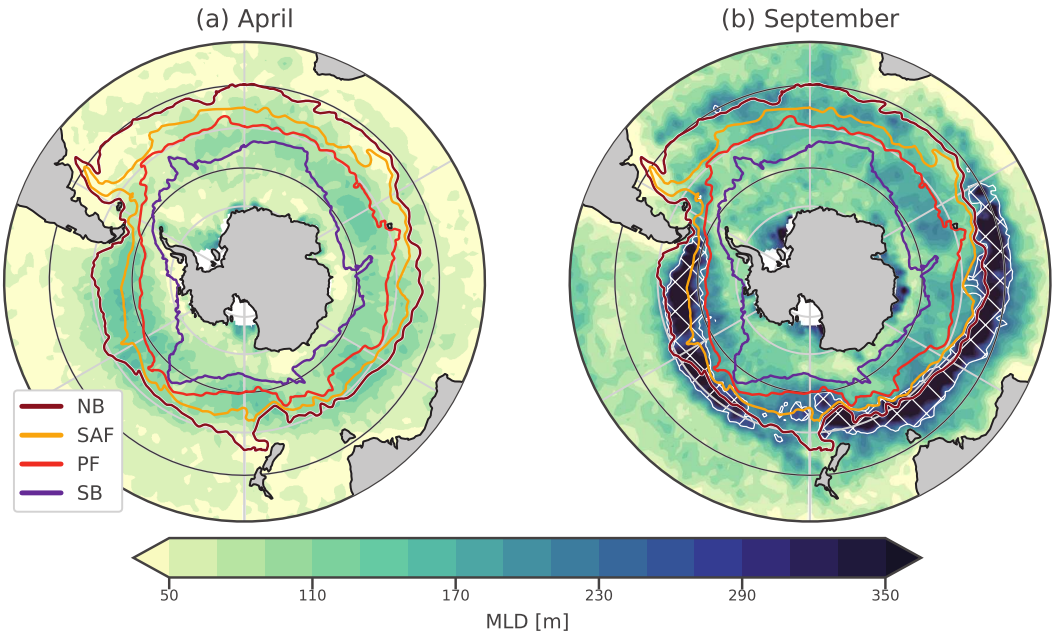

Figure 1. Mixed layer depth climatology in the SO with the major ACC fronts in (a) April and (b) September. From north to south, the NB (maroon colour), SAF (yellow), PF (red), and SB (purple) fronts from Park et al. (2019) are plotted. The MLD are from de Boyer Montégut (2023). Hatches and white contour represent the DMB. For these maps, and for the following maps of this paper, the northern boundary is at 30 °S. In latitude, grid lines are spaced every 10 degrees, with black lines at 40 °S and 60 °S.

A striking phenomenon known as the deep mixing band (DMB) emerges during winter in the SO (DuVivier et al., 2018). Situated mostly north of the SAF (Fig. 1 and Dong et al. (2008)), this narrow band of intense vertical mixing is of paramount importance in shaping the ocean's thermal and dynamic structure. The DMB is characterised by mixed layers (MLs) deeper than 250 m in winter. Intense buoyancy loss due to winter heat release deepens the ML, and the Ekman transport of cold water intensifies it (Naveira Garabato et al., 2009; Holte et al., 2012; Rintoul and England, 2002). This distinctive feature is found in both the Indian and Pacific sectors of the SO and underpins the formation of the Subantarctic Mode Water (SAMW) (Belkin and Gordon, 1996; Speer et al., 2000; Hanawa and Talley, 2001; Klocker et al., 2023). The SAMW, a conduit for heat and carbon exchange, exerts significant influence on the global oceanic circulation and climate processes as it forms a major component of the upper limb of the global overturning circulation (Sloyan and Rintoul, 2001). By its capacity to take up anthropogenic CO_2 it is a key component of the Earth's climate (Sabine et al., 2004).

The DMB is a major site for the uptake of anthropogenic heat and carbon from the surface to the interior (Roemmich et al., 2015; Gruber et al., 2019), however the physics controlling both its location and latitudinal extent remains insufficiently un-

https://doi.org/10.5194/egusphere-2023-2404
Preprint. Discussion started: 19 October 2023

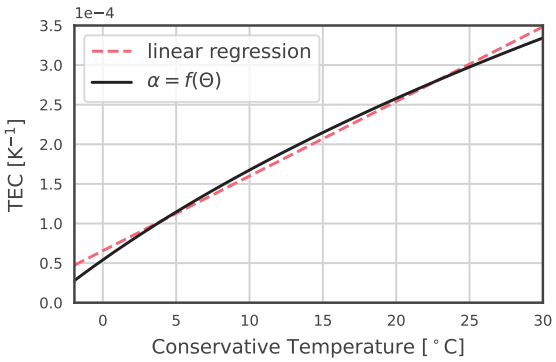

Figure 2. Thermal Expansion Coefficient function of Conservative Temperature. The pressure is $0\,\mathrm{dbar}$ and the Absolute Salinity $35.5\,\mathrm{g\,kg^{-1}}$. The graph stops at $-1.9\,^{\circ}\mathrm{C}$, the freezing point.

derstood (DuVivier et al., 2018; Fernández Castro et al., 2022). Holte et al. (2012) argued that the strength of the summer stratification determines the potential of the water column to form a deep ML in the following winter. The stratification in summer is decreased by enhanced vertical mixing (Sloyan et al., 2010), eddy-driven jet scale overturning circulation (Li and Lee, 2017), and wind stress curl induced upwelling (Dong et al., 2008). Downstream of the Agulhas Retroflection and downstream of the Campbell Plateau, eddy diffusion of heat has a tendency to stabilise the mixed layer (Sallée et al., 2006, 2008), and the spring and summer heat gain contributes to increase stratification. The geostrophic flow is roughly oriented along the isotherms and does not induce any large horizontal heat fluxes in the SO, away from western boundary currents (Dong et al., 2007). In contrast, a subsurface salinity maximum advected from subtropical water is present in most of the SO in summer, decreasing stratification below it (DuVivier et al., 2018). This salinity-driven weakening of stratification could be compensated by temperature stratification.

Another effect relates to the nonlinear nature of the equation of state for seawater, known to play a role for the formation of Antarctic Intermediate Water (Nycander et al., 2015). The density change induced by temperature is scaled by the thermal expansion coefficient (TEC, α), defined as:

$$\alpha = -\frac{1}{\rho}\frac{\partial \rho}{\partial \Theta}\bigg|_{S_{\mathrm{A}},p} \tag{1}$$

using Conservative Temperature Θ and Absolute Salinity S_{A} (IOC et al., 2015). The TEC also scales the contribution of heat fluxes to buoyancy fluxes. The TEC is a function of temperature and pressure and follows a quasi-linear relationship with temperature at the surface (Fig. 2). It is about 10 times smaller at $-1.8\,^{\circ}\mathrm{C}$ than at $30\,^{\circ}\mathrm{C}$. This effect makes the density of cold water less sensitive to temperature changes than that of warm water, enhancing the role of salinity and minimising the influence of heat fluxes on buoyancy fluxes in polar regions (Bryan, 1986; Aagaard and Carmack, 1989; Roquet et al., 2015). Variations in the TEC value also imply that winter heat fluxes have less impact on density than summer heat fluxes. Schanze and Schmitt (2013) showed that variations in the TEC increase the global buoyancy flux by 35% due to seasonal effects. The variations in

https://doi.org/10.5194/egusphere-2023-2404
Preprint. Discussion started: 19 October 2023

the value of the TEC allow for a total non-zero buoyancy flux while having a zero net heat flux (Garrett et al., 1993; Zahariev and Garrett, 1997; Hieronymus and Nycander, 2013). The global stratification distribution is very sensitive to changes in the TEC value (Roquet et al., 2015; Nycander et al., 2015). Its low value in the polar regions is the fundamental mechanism that allows the maintenance of a halocline under large cooling conditions and thus strongly promotes sea ice formation (Roquet et al., 2022).

Using numerical simulations of an idealised closed basin, Caneill et al. (2022) studied the impact of buoyancy fluxes in setting the position of the deep MLs, the equivalent of a DMB in their simulations. In their closed basin study, they determined that the inversion of the sign of annual buoyancy fluxes primarily drives the poleward extent of the deep mixed layers. These buoyancy fluxes resulted from a competition between heat loss and freshwater gain. The inversion was, however, not driven by either an increase in freshwater fluxes or a decrease in heat loss. Rather, it was driven by the decrease in the TEC value in cold water, which strongly reduced the heat flux contribution to buoyancy fluxes towards the pole. The competition between heat and freshwater fluxes is thus unequal in polar regions. It is not clear whether a simple link between the DMB position and buoyancy fluxes still holds in the SO and if the variations of the TEC are sufficient to constrain the poleward extent of the DMB. In fact, the position of the DMB is not correlated with a unique component of the surface forcing, which includes wind stress, wind stress curl, buoyancy flux, and mesoscale eddy activity (DuVivier et al., 2018).

Here, we aim to characterise the dominant control of the position of the DMB in the SO by the interplay of buoyancy fluxes and stratification. For this, we create climatologies of buoyancy fluxes and stratification and compare their respective intensities. The effect of the Ekman transport is added as an extra term in the buoyancy fluxes. Measuring surface buoyancy fluxes presents challenges, entailing significant uncertainties within the SO (Cerovečki et al., 2011; Swart et al., 2019), so we focus on the climatological state of the ocean. Both seasonal and annual fluxes are taken into account, and the focus for stratification is late summer, after preconditioning has occurred, just before the ML starts to deepen. Additionally, we also aim at characterising the impact of the variations in the TEC value on the width of the DMB. For this, we compare the climatologies computed with modified TEC values.

This paper is organised as follows: First, we present the data used in this study; we then describe the equations that govern buoyancy fluxes, the Ekman transport, and stratification intensity. We continue by describing the results and we end with a discussion and conclusions.

2 Data and methodology

Here, we describe how we constructed the climatologies for buoyancy fluxes and stratification (both its strength and thermohaline components). The general methodology consists in computing monthly components of the buoyancy fluxes for each year before averaging to produce monthly climatologies. We used the years 2005 to 2016 for all fluxes, as this is the record period of the ISCCP-FH MPF product (providing short and long wave heat fluxes). The stratification is computed using the Monthly Isopycnal & Mixed-layer Ocean Climatology (MIMOC) (Schmidtko et al., 2013).

https://doi.org/10.5194/egusphere-2023-2404
Preprint. Discussion started: 19 October 2023

2.1 Buoyancy fluxes

2.1.1 Surface buoyancy fluxes

Surface buoyancy fluxes are defined from heat and freshwater fluxes (e.g. Gill and Adrian, 1982):

$$\mathcal{B}^{surf} = \underbrace{\frac{g\alpha}{\rho_0 C_p} Q_{tot}}_{\mathcal{B}^{surf}_\Theta} \underbrace{- \frac{g\beta S}{\rho_0}(E - P - R)}_{\mathcal{B}^{surf}_S} \tag{2}$$

where g is the gravity acceleration, $C_p \simeq 3997\,\mathrm{J\,kg^{-1}\,K^{-1}}$ the heat capacity, Q_{tot} the total heat flux in $\mathrm{W\,m^{-2}}$, E the evaporation, P the precipitation, R the river runoff both in $\mathrm{kg\,m^{-2}\,s^{-1}}$, and S the surface salinity. $\mathcal{B}^{surf}_\Theta$ is the heat contribution, $\mathcal{B}^{surf}_S$ the salt contribution, and $\mathcal{B}^{surf}$ the total surface buoyancy flux in $\mathrm{m^2\,s^{-3}}$.

Q_{tot} is divided into 4 components: net long wave radiation (Q_{LW}), net short wave radiation (Q_{SW}), latent heat (Q_{LH}), and sensible heat (Q_{SH}). Monthly latent and sensible heat fluxes are taken from the monthly means Objectively Analyzed Air–Sea Fluxes 1 degree dataset (OAflux; Yu and Weller, 2007) (these fluxes are only provided for oceans free of ice) and ISCCP-FH MPF (monthly means) for the short and long waves (Schiffer and Rossow, 1983; Rossow and Schiffer, 1999). The TEC is computed using the SST provided by OAflux, and the surface salinity is taken from Estimating the Circulation and Climate of the Ocean (ECCO) Version 4, Release 4 (Forget et al., 2015). ECCO monthly outputs have been bilinearly interpolated from the tiles onto a 1-degree longitude–latitude grid using the SciPy Python library (Virtanen et al., 2020).

Due to the difficulties in computing the turbulent fluxes, the total heat budget is not closed. Following Schanze and Schmitt (2013), we remove the global average (time, longitude, and latitude) of the heat and freshwater fluxes to balance them. Before adjustment, the average of the heat fluxes is $24.49\,\mathrm{W\,m^{-2}}$, and the average integrated freshwater imbalance is $-0.2\,\mathrm{Sv}$. Compared to the heat and buoyancy fluxes derived from ECCO, it is found that the patterns of heat and buoyancy gain or loss are better represented after correction (Appendix A).

Freshwater fluxes combine OAflux for evaporation, Global Precipitation Climatology Project (GPCP) Version 2.3 for precipitation (Adler et al., 2018), and ECCO for river runoff.

Two seasonal components are necessary to complement the annual mean of the fluxes: buoyancy loss and buoyancy gain. We split the annual buoyancy flux into its negative and positive components: the "cooling season" (CS) and the "warming season" (WS). CS is defined by the months April to September (included) and WS by the months October to March (included). This gives $\mathcal{B}^{CS}$ and $\mathcal{B}^{WS}$. This division captures an overview of buoyancy loss and gain throughout the seasons.

Sea ice formation and melting are associated with freshwater fluxes at the surface of the ocean. In the Southern Ocean, sea ice mostly forms close to the Antarctic coast and melts more uniformly after being exported away by wind and oceanic currents (Holland and Kwok, 2012). In the sea ice covered area, winter heat fluxes are small, and brine rejection when sea-ice is forming is the main component of buoyancy fluxes (Klocker et al., 2023). In summer, buoyancy fluxes are positive as sea ice melts and the ocean warms up (Pellichero et al., 2018). In this study, we focus on the DMB located north of and within the ACC, which is ice-free all year. Therefore, we will not take sea ice formation or melting into account in our buoyancy flux calculations.

https://doi.org/10.5194/egusphere-2023-2404
Preprint. Discussion started: 19 October 2023

2.1.2 Ekman buoyancy fluxes

The Ekman transport advects heat and salt, which leads to lateral buoyancy fluxes. As is commonly done, we assume that the Ekman depth is contained within the ML (e.g. Qiu and Kelly, 1993; Sallée et al., 2006; Dong et al., 2007), so Ekman transport acts to modulate the buoyancy forcing seen at the bottom of the ML.

Associating the Ekman depth with the MLD comes from the fact that the turbulent viscosity should be large in the ML and small below. However, this is not obvious; studies do not always agree, depending on the region and method. Lenn and Chereskin (2009) found that viscosity decreased from approximately $0.1\,\mathrm{m^2\,s^{-1}}$ at 26 m depth to near zero at 90 m in the Drake passage using ADCP measurement of velocity. In contrast, Roach et al. (2015) found that a model with a vertically uniform viscosity between $0.05\,\mathrm{m^2\,s^{-1}}$ and $0.25\,\mathrm{m^2\,s^{-1}}$ represented the observed spirals well. Nevertheless, despite the lack of observations of the Ekman depth in the SO, Dong et al. (2007) found that using the MLD as the Ekman depth was giving accurate results in the mixed layer heat budget.

To compute buoyancy fluxes, one needs to compute the Ekman horizontal transport (e.g. Qiu and Kelly, 1993; Yang, 2006):

$$-fV_{\mathrm{Ek}} = \frac{\tau^x}{\rho} \quad \text{and} \quad fU_{\mathrm{Ek}} = \frac{\tau^y}{\rho} \tag{3}$$

Using the heat and freshwater fluxes due to horizontal Ekman advection,

$$Q_{Ek} = \rho_0 C_p \boldsymbol{U_{Ek}} \cdot \boldsymbol{\nabla} \Theta \tag{4}$$

$$FW_{Ek} = \frac{\rho_0}{S} \boldsymbol{U_{Ek}} \cdot \boldsymbol{\nabla} S \tag{5}$$

the Ekman transport is derived from wind stress using (3), leading to:

$$\mathcal{B}_\Theta^{Ek} = -\frac{g\alpha}{\rho_0 f}\left(\tau^y \frac{\partial \Theta}{\partial x} - \tau^x \frac{\partial \Theta}{\partial y}\right) \tag{6}$$

$$\mathcal{B}_S^{Ek} = \frac{g\beta}{\rho_0 f}\left(\tau^y \frac{\partial S}{\partial x} - \tau^x \frac{\partial S}{\partial y}\right) \tag{7}$$

$\mathcal{B}^{Ek}$ are fluxes within the Ekman layer. Under the assumption that the Ekman layer is contained within the ML, $\mathcal{B}$, the sum of $\mathcal{B}^{Ek}$ and $\mathcal{B}^{surf}$, corresponds to the buoyancy flux taken at the base of the ML.

We computed daily averages of wind stress from the CMEMS "Global Ocean Wind L4 Reprocessed 6 Hourly Observations". To compute horizontal gradients of temperature and salinity, we used the ARMOR3D weekly product (Guinehut et al., 2012). We took the average of the three upper levels (0 m, 5 m, and 10 m) and then did a linear interpolation in time to get daily data.

2.2 Stratification from columnar buoyancy

We quantify the stratification using the columnar buoyancy (Lascaratos and Nittis, 1998; Herrmann et al., 2008):

$$CB(Z) = \int_Z^0 -zN^2(z)\mathrm{d}z \tag{8}$$

https://doi.org/10.5194/egusphere-2023-2404
Preprint. Discussion started: 19 October 2023

with the z-axis oriented upward. $N^2(z)$ is calculated using the locally referenced potential density. For shallow depths, an approximation using the potential density referenced at the surface is applicable. By integrating Eq. (8) with this approximation, a formula directly using potential density profiles is obtained:

$$CB(Z) \simeq \frac{g}{\rho_0} \int_Z^0 [\rho_\theta(Z) - \rho_\theta(z)] \, \mathrm{d}z \tag{9}$$

The columnar buoyancy, positive under stable stratification, quantifies the vertically integrated amount of buoyancy that must be lost to create a ML of depth Z. We compute this index in April, which corresponds to the most stratified water column before it is eroded during the cooling season. Dividing $-CB$ by a time Δt gives the buoyancy fluxes necessary to deepen the ML to Z during Δt (Faure and Kawai, 2015). Following DuVivier et al. (2018), we use the depth of 250 m as the deep mixed layer threshold:

$$B_{250} = \frac{-CB(-250)}{\Delta t} \tag{10}$$

We used $\Delta t = 6$ months to allow comparison with the mean buoyancy loss of the cooling season (Sect. 2.1.1).

The influence of temperature and salinity alone on stratification is done by separating their effects, as is similarly done by Sterl and De Jong (2022). B_{250} can thus be split using the decomposition of the buoyancy frequency into the thermal and haline components:

$$B_{250} = \underbrace{\frac{g}{\Delta t} \int_{-250}^0 \alpha(z) \frac{\partial \Theta}{\partial z} z \mathrm{d}z}_{B_{250}^\Theta} \underbrace{- \frac{g}{\Delta t} \int_{-250}^0 \beta(z) \frac{\partial S}{\partial z} z \mathrm{d}z}_{B_{250}^S} \tag{11}$$

We expect B_{250}^Θ to be positive north of the PF and negative south of it, while B_{250}^S should be negative north of the SAF and positive south of it.

The columnar buoyancy is computed using Monthly Isopycnal & Mixed-layer Ocean Climatology (MIMOC) in depth coordinates (Schmidtko et al., 2013).

2.3 Effect of the variations of the TEC

The TEC scales the effect of heat fluxes on buoyancy fluxes and determines the importance of temperature for stratification. To investigate how the TEC variations affect stratification and buoyancy fluxes, we computed them using α_0, a constant TEC characteristic of the waters in the DMB. This replacement is made in Eqs. (2), (6), and (11). It will be explicitly mentioned when the constant TEC is used and the results are presented in Sect. 4.

To compute the value of α_0, we used the average temperature of surface water located at $40\,^\circ\mathrm{S}$ ($\Theta \simeq 14.7\,^\circ\mathrm{C}$), a salinity of $35.5\,\mathrm{g\,kg^{-1}}$, and a pressure of $0\,\mathrm{dbar}$. The result is $\alpha_0 \simeq 2.1 \times 10^{-4}\,\mathrm{K^{-1}}$. The latitude $40\,^\circ\mathrm{S}$ has been chosen as it roughly corresponds to the latitude located just north of the DMB.

https://doi.org/10.5194/egusphere-2023-2404
Preprint. Discussion started: 19 October 2023

3 Results

3.1 Annual buoyancy fluxes

Annual surface buoyancy fluxes induced by heat fluxes ($\mathcal{B}_\Theta^{surf}$) tend to be negative (cooling) north of $50\,^\circ$S and positive south of it, but the pattern shows large regional disparities (Fig. 3 (a)). The DMB is associated with a net annual cooling; in the Indian and Pacific sectors, it is surrounded by regions of net annual warming. The heat loss is located north of the ACC in the Atlantic and Indian sectors, while the heat loss in the east Pacific sector is located within the ACC. Except for this large region of loss in the Pacific sector, even if the heat fluxes look patchy, heat is mostly gained within the ACC. This is due to large radiative heat fluxes compared to small sensible heat fluxes (Czaja and Marshall, 2015). Thus, heat fluxes are not zonally constant in the ACC (Song, 2020; Josey et al., 2023). Overall, in both the Indian and Pacific sectors of the SO, the DMB is surrounded by annual heat gain in the north and south. We note that the regions with the largest annual surface heat loss are colocated with the western boundary currents, due to the advection of warm water (Fig. 3 (a)).

In contrast to the patchiness and geographical variability of $\mathcal{B}_\Theta^{surf}$, the distribution of the haline component of the surface buoyancy fluxes, $\mathcal{B}_S^{surf}$, is much smoother. Precipitation in the south and evaporation in the subtropical gyres are responsible for the global pattern of freshwater fluxes (Fig. 3 (b)). $\mathcal{B}_S^{surf}$ is mainly positive within the DMB and positive everywhere south of it. This illustrates the fact that freshwater forcing depends little on ocean conditions, contrary to heat flux.

The sum of these two surface components, $\mathcal{B}^{surf}$, is similar to $\mathcal{B}_\Theta^{surf}$ north of the ACC (Fig. 3 (c)). Within and south of the ACC, it is positive everywhere except in the Pacific sector, where the DMB occurs: a narrow band of buoyancy loss is present with a large tongue of buoyancy gain north of it. Overall, a circumpolar band of buoyancy loss is present in the SO, surrounded by buoyancy gain, particularly in the Indian and Pacific sectors. Caneill et al. (2022) found that the poleward boundary of the deep MLs region was located at the inversion of the annual buoyancy fluxes in a coarse-resolution idealised closed basin study. The circulation in the SO differs from the one in a closed basin as considered in Caneill et al. (2022); the path of the ACC is more or less zonal, while the closed basin circulation has an important meridional upper ocean transport. Moreover, the ACC interacts with the bathymetry and presents a large eddy activity, two phenomena not really represented in the idealised basin of Caneill et al. (2022). Despite these differences, their conclusion that deep MLs (the DMB in the SO) are bounded poleward by the inversion of the annual buoyancy fluxes still holds in the SO. Additionally, the DMB is also bounded equatorward by tongues of annual buoyancy gain, so that the DMB coincides with a narrow band of annual buoyancy loss surrounded by buoyancy gain.

3.2 Effect of the Ekman transport

The Ekman transport brings cold water northward south of about $30\,^\circ$S and thus creates a negative buoyancy flux at the base of the Ekman layer (Fig. 4 (a)). The largest negative values are found around the NB of the ACC in the Indian Ocean. The SAF has a large SST meridional gradient (Kostianoy et al., 2004), which enhances the meridional advection of cold water and thus creates a large negative buoyancy flux. The Ekman salt component presents large positive values close to the NB (Fig. 4 (b)). Summed together, the buoyancy fluxes induced by the Ekman transport are negative in the SO and positive in the southern part

https://doi.org/10.5194/egusphere-2023-2404
Preprint. Discussion started: 19 October 2023

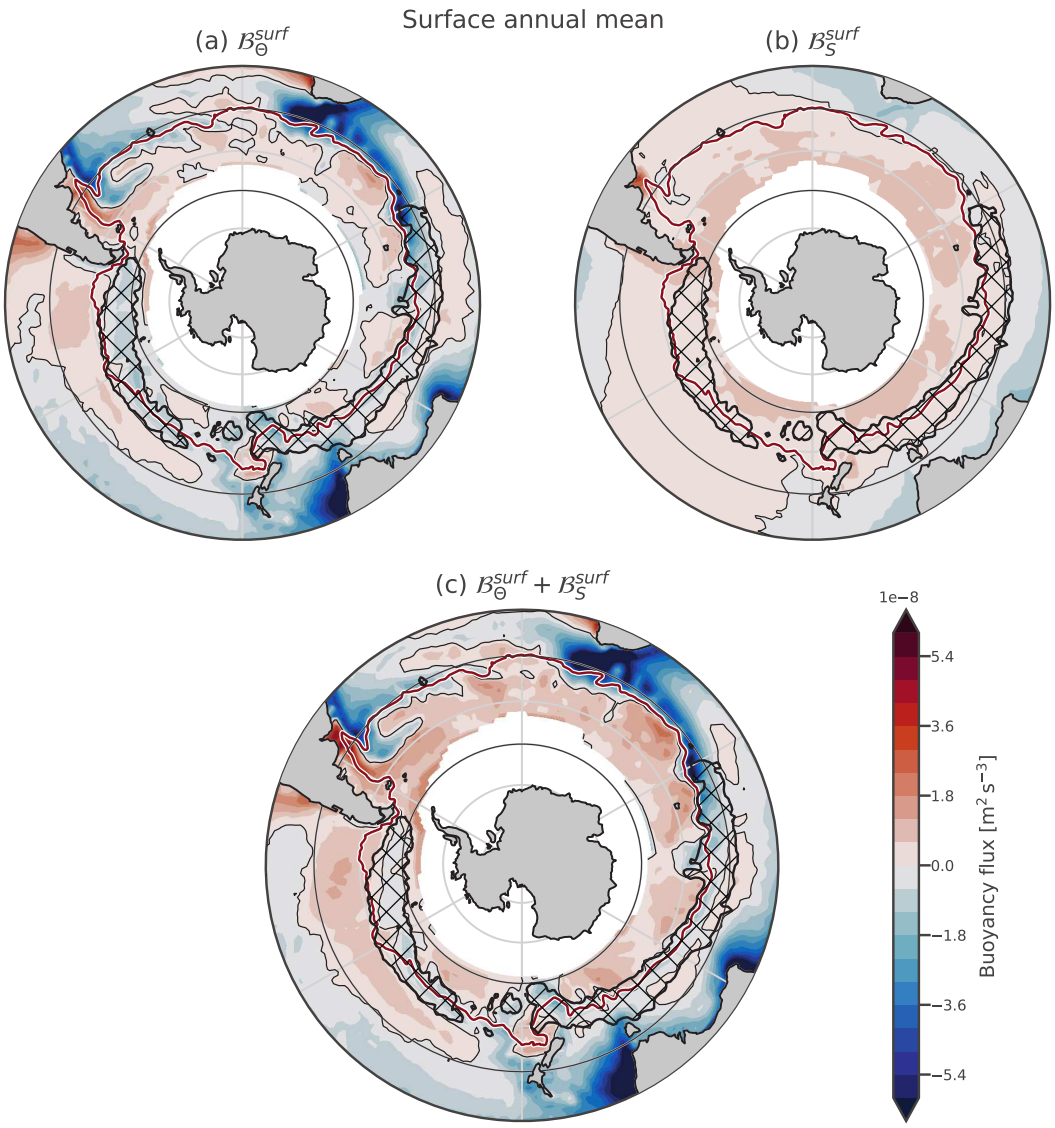

Figure 3. Climatology of the annual components of the surface buoyancy fluxes. The heat component (a), haline component (b), and their sum (c) are plotted. On every plot, the thin black lines represent the 0 of the fluxes, and the maroon line is the northern boundary of the ACC, defined as the northernmost closed contour of Mean Dynamic Topography, as defined by Park et al. (2019). Hatches represent the DMB. The northern boundary is at 30 °S. In latitude, grid lines are spaced every 10 degrees, with black lines at 40 °S and 60 °S.

https://doi.org/10.5194/egusphere-2023-2404
Preprint. Discussion started: 19 October 2023

of the subtropical gyres (Fig. 4 (c)). The negative temperature anomaly in the ocean induced by the Ekman transport creates a positive anomaly in surface heat fluxes. As a result, Ekman and atmospheric heat fluxes likely partially compensate for each other. Such partial compensation can be seen when comparing Fig. 3 (a) and Fig. 4 (a) and (d), e.g., in the south-east Pacific Ocean, north of the ACC. When the Ekman contribution is included, almost all the SO south of $30\,^{\circ}\mathrm{S}$ is losing buoyancy due to heat on the annual mean.

Regions within the ACC that gain heat from the atmosphere encounter compensation from Ekman transport and are thus also losing heat on the annual mean (Fig. 4 (d)). Although $\mathcal{B}_{\Theta}^{surf}$ is overall positive south of the NB of ACC, when the Ekman heat component is included, $\mathcal{B}_{\Theta}^{tot}$ becomes negative almost everywhere in the SO (Fig. 4 (d)). The Ekman heat transport thus has a destabilising effect that counteracts the surface heat gain. The total salt component resembles its atmospheric part while being slightly modulated by Ekman transport. $\mathcal{B}$ is negative between the ACC and $25\,^{\circ}\mathrm{S}$, and south of the DMB, it alternates between regions of positive and negative values (Fig. 4 (f) and Fig. 5 (b)). It is continuously negative within the northern part of the ACC in the Pacific sector.

In short, the Ekman transport generates important fluxes of both temperature and salinity but the net effect on the buoyancy at the bottom on the ML remains limited overall, with a few regional exceptions such as around the Kerguelen Plateau.

https://doi.org/10.5194/egusphere-2023-2404
Preprint. Discussion started: 19 October 2023

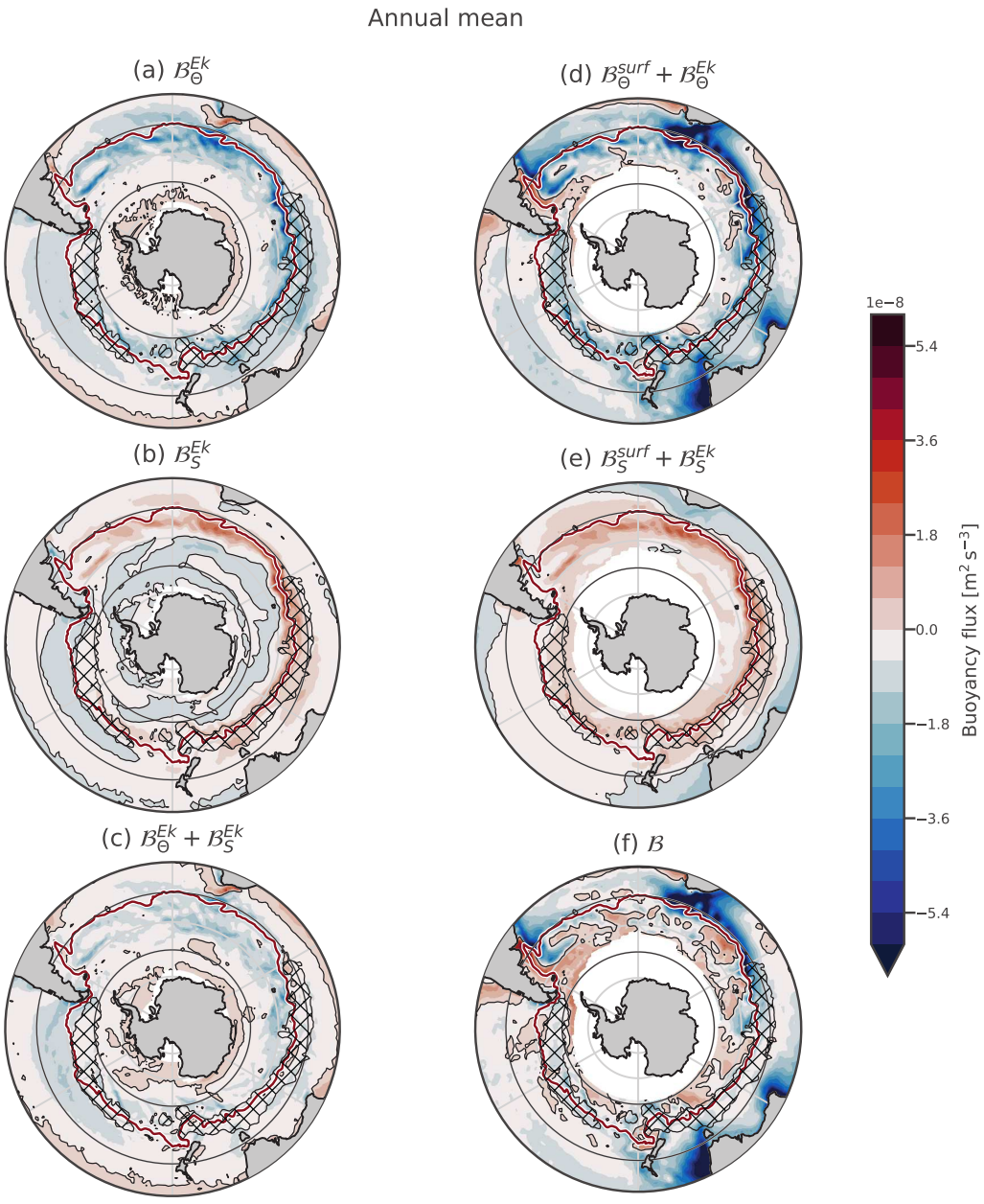

Figure 4. Climatology of the annual components of the Ekman induced buoyancy fluxes, and the sum with the surface fluxes. The subplots are organized as follows: the columns show the Ekman fluxes and the sum of Ekman and surface. The rows show the thermal component, haline component, and their sum.

https://doi.org/10.5194/egusphere-2023-2404
Preprint. Discussion started: 19 October 2023

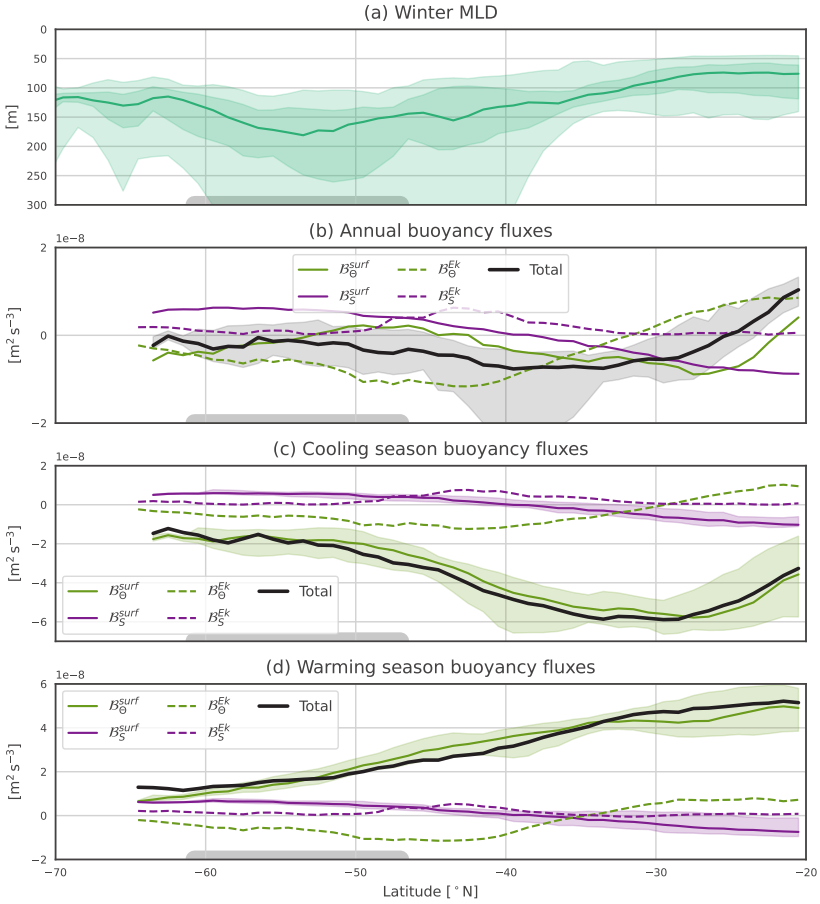

Figure 5. (a) Winter MLD. The shading represents respectively the 5th – 95th, and 25th – 75th percentiles, and the solid line is the zonal median. Mixed layers deeper than 250 m are found between 40 °S and 60 °S depending on the SO sector. (b) annual mean of the buoyancy flux components, (c) cooling season means, and (d) warming season means. The black line is $\mathcal{B}$ the sum of surface and Ekman fluxes. The vertical grid spacing is constant between panels. The black, green, and purple shading represents the region between the 25th and 75th percentiles for the total, heat surface, and salt surface components. The majority of the zonal differences arise from the surface heat component. The gray box in the bottom represents a median position of the ACC.

https://doi.org/10.5194/egusphere-2023-2404
Preprint. Discussion started: 19 October 2023

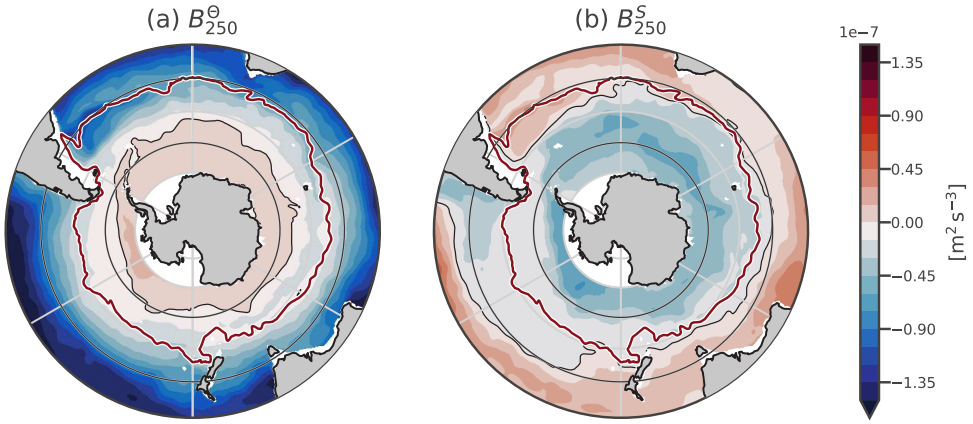

Figure 6. Climatology of (a) the thermal and (b) haline components of B_{250}.

3.3 Upper ocean stratification and seasonal cycle of buoyancy fluxes

The strength of the stratification is studied using the columnar buoyancy B_{250} (computed in April, before the cooling season), i.e. the equivalent buoyancy flux necessary to erode the summer stratification and form a 250 m deep mixed layer. The subtropical and subpolar SO are thermally stratified ($B^{\Theta}_{250} < 0$), while in the polar region, the temperature component of stratification is negative (Fig. 6 (a)). The haline stratification follows an opposite pattern, with the salinity component of stratification decreasing stratification in the subtropical regions ($B^{S}_{250} > 0$) and increasing it in the polar regions (Fig. 6 (b)). We note that the transition from salinity destabilisation to stabilisation is located northward of the temperature inversion. The exact location of these stratification changes depends on the reference depth taken (250 m here), but the global pattern is a robust feature of the stratification from subtropical to polar environments (Carmack, 2007; Roquet et al., 2022).

In the DMB, as well as everywhere except close to Antarctica, the temperature stratifies on average in the upper 250 m in summer (Fig. 6 (a)). The role of salinity is to stabilise the DMB in the Pacific Ocean; in the Indian Ocean, the DMB is located at the boundary between the salinity-stabilising and destabilising regimes. The presence of a salinity maximum advected from Agulhas water around 150 m deep in the region north of the ACC helps to decrease the summer stratification in the Indian Ocean (Wang et al., 2014; Small et al., 2021; Fernández Castro et al., 2022).

The stratification is the weakest in the southern part of the SO (Fig. 7 (a), Fig. 8, and Fig. 9 (a)). The strongest stratifications are found in the subtropics (dark blue colours representative of the most negative value of B_{250}, Fig. 7 (a)). At 20 °S, it reaches a value more than five times larger than in the polar region. A band of stratification minimums exists around the DMB. Part of

https://doi.org/10.5194/egusphere-2023-2404
Preprint. Discussion started: 19 October 2023

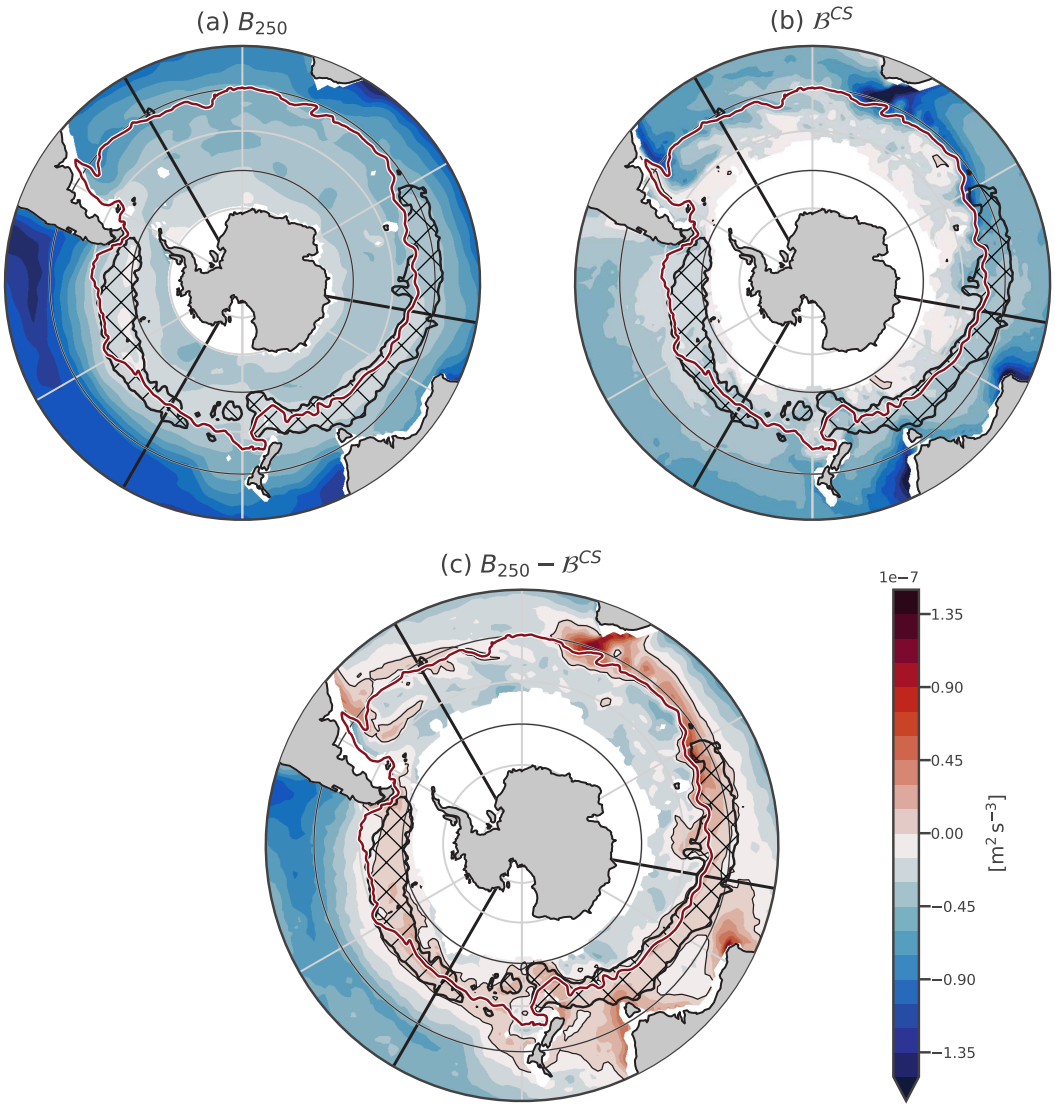

Figure 7. Climatology of (a) the CS buoyancy fluxes, (b) the intensity of late summer stratification characterized by B_{250}, and (c) the difference $B_{250} - \mathcal{B}^{CS}$. The hatches surrounded by the black contour represent the DMB. The three black lines represent the transects plotted in Fig. 8.

the existence of this minimum can be attributed to the fact that B_{250} includes the effect of the seasonal cycle of the stratification. Outside the DMB, B_{250} captures more permanent stratification than within the DMB. Weak stratification is also found outside

https://doi.org/10.5194/egusphere-2023-2404
Preprint. Discussion started: 19 October 2023

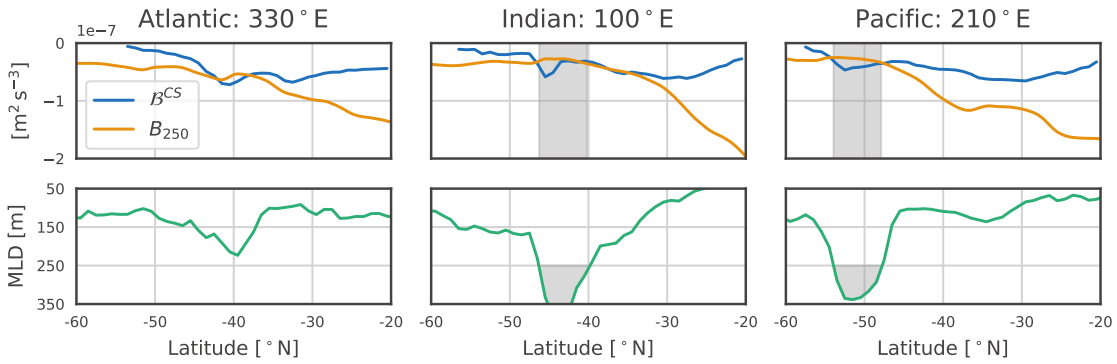

Figure 8. B_{250} (orange curves) and $\mathcal{B}^{CS}$ (blue curves) (upper row), and observed winter MLD (green curve in lower row), for 3 different transects in the Atlantic, Indian, and Pacific sectors of the SO. The gray box represent the DMB.

the DMB, and the stratification minimum is not very pronounced. The general trend is that the stratification decreases from the subtropics to the polar region.

The annual mean of $\mathcal{B}_\Theta^{surf}$ hides a large seasonal cycle with a large winter buoyancy loss and a large summer buoyancy gain (Fig. B1 in Appendix B). In contrast, the other components have a very small seasonal cycle compared to $\mathcal{B}_\Theta^{surf}$ (Fig. 5 (c) and (d)). To go beyond annual buoyancy fluxes, one can compare the seasonal fluxes with the position of the DMB (Fig. 5 (a)). One striking point is that the DMB (with MLDs deeper than 250 m) is not located in regions of the largest annual or winter buoyancy loss but south of them. The largest CS buoyancy loss of about $-6 \times 10^{-8}\,\mathrm{m^2\,s^{-3}}$ is located around 30 °S, where the winter MLD barely exceeds 100 m. The winter buoyancy loss is three times lower at 50 °S, a region where deep MLs are formed. Therefore, a large winter buoyancy loss itself is not sufficient to produce deep winter ML. This is because the poleward advection of stratified water from the subtropics limits the ML deepening. Therefore, stratification strength also needs to be taken into account when studying deep ML formation.

Regions where $\mathcal{B}^{CS}$ is more negative than B_{250} have a large probability of forming a ML deeper than 250 m, unless another process not taken into account makes the water column more stable. The CS buoyancy loss driven by heat fluxes is the most intense around 30 °S ((Fig. 7 (b)), a region where the gain in summer buoyancy is also very large. Apart from the summer buoyancy gain, this is also a region where subtropical stratified water is advected. South of it, the winter buoyancy loss becomes smaller, so it has less potential to form a deep mixed layer. The general pattern is that the buoyancy loss becomes smaller from 30 °S poleward.

Both the buoyancy loss and the stratification decrease poleward. To assert how the balance between these two opposite effects shapes the DMB, we compare the position of the DMB with the residual $B_{250} - \mathcal{B}^{CS}$ (Fig. 7 (c)). MLD larger than 250 m are only found where $B_{250} > \mathcal{B}^{CS}$, but not vice versa. The largest mismatch is located south of Africa, in the Agulhas Retroflection region. Our analysis does not include the direct effect of advection by the geostrophic flow. However, our results strongly point to its restoring effect on the stratification in the regions of large western boundary currents such as the Agulhas

https://doi.org/10.5194/egusphere-2023-2404
Preprint. Discussion started: 19 October 2023

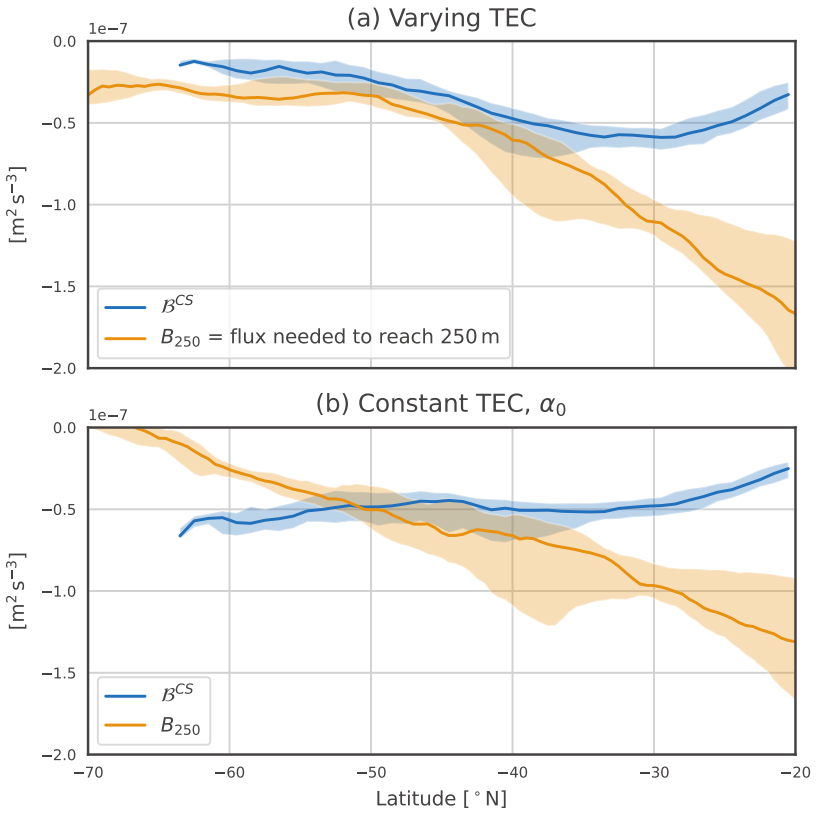

Figure 9. CS buoyancy fluxes (blue) and B_{250}, the buoyancy fluxes needed to produce a 250 m deep mixed layer (orange). (a) is computed using the realistic varying TEC and (b) is computed with α_0. Shaded areas correspond to the 1st and 3rd quartiles, and the solid lines are the zonal medians. The blue line corresponds to the black line of Fig. 5 (c). This plot extends to 20 °S to highlight the increase of stratification towards the tropics, and the maximum buoyancy loss located around 30 °S.

Retroflection or the East Australian current. Overall, the simple balance between B_{250} and $\mathcal{B}^{CS}$ as main drivers of deep ML formation does not hold at the western boundary currents but otherwise predicts with good accuracy the location of the DMB.

265 The zonal sections and the zonal median show the competition between the winter buoyancy loss and the existing summer stratification (Fig. 8 and Fig. 9 (a)). Sections in the middle of the Atlantic, Indian, and Pacific sectors of the SO are plotted. In the transect of the Atlantic sector, the MLD does not reach 250 m, but the location where buoyancy fluxes are more negative than stratification still corresponds to the position of the deepest MLD of the transect. It becomes clear that only in a few locations does the winter buoyancy loss become sufficient to erode the stratification.

https://doi.org/10.5194/egusphere-2023-2404
Preprint. Discussion started: 19 October 2023

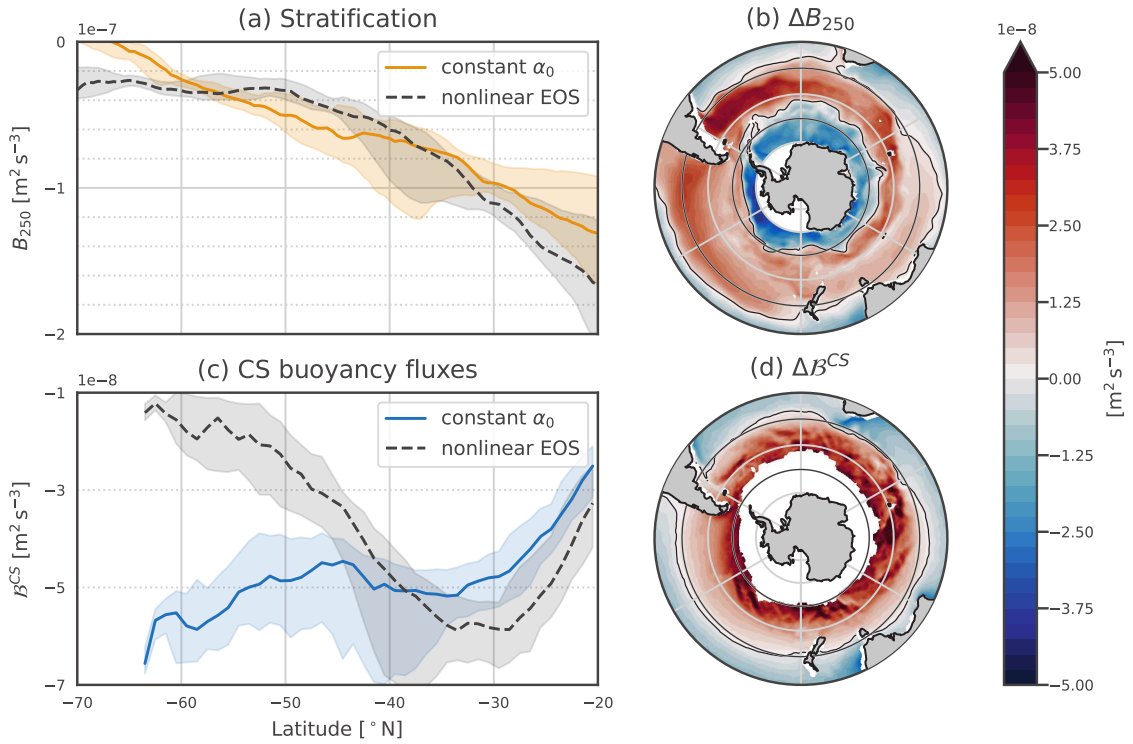

Figure 10. Stratification and buoyancy fluxes and computed using the nonlinear EOS or a constant α_0. In panels (a) and (c), black dashed lines are for the nonlinear EOS, and blue or orange continuous lines are with constant α_0. The spacing between the horizontal dotted gray line is the same in these two panels and equal to 2×10^{-8} m^2 s^{-3} The light shadings correspond to the 25th and 75th percentiles. Panels (b) and (d) are the difference between using the varying TEC and the constant α_0, for B_{250} and $\mathcal{B}^{CS}$ respectively.

Despite a weak stratification south of 50 °S in the Atlantic and Indian sectors, no deep ML is observed as the winter buoyancy loss is smaller there. As seen previously, the heat component of the buoyancy fluxes is scaled by the TEC, itself a function of temperature. We will now explore the importance of this mechanism.

4 Effect of the local value of the TEC

To understand how variations in the TEC value affect the SO stratification, we computed the buoyancy fluxes and the columnar buoyancy using a constant value α_0, representative of 40 °S. We use the residual of buoyancy loss and stratification to predict the geographical extent that the DMB would have in this case.

Heat fluxes are negative in winter, so south of 40 °S, where α_0 is larger than the real value of the TEC, the buoyancy fluxes become more negative (blue line in Fig. 9 (b) and Fig. 10 (b) and (c)). On the contrary, the buoyancy fluxes become smaller

https://doi.org/10.5194/egusphere-2023-2404
Preprint. Discussion started: 19 October 2023

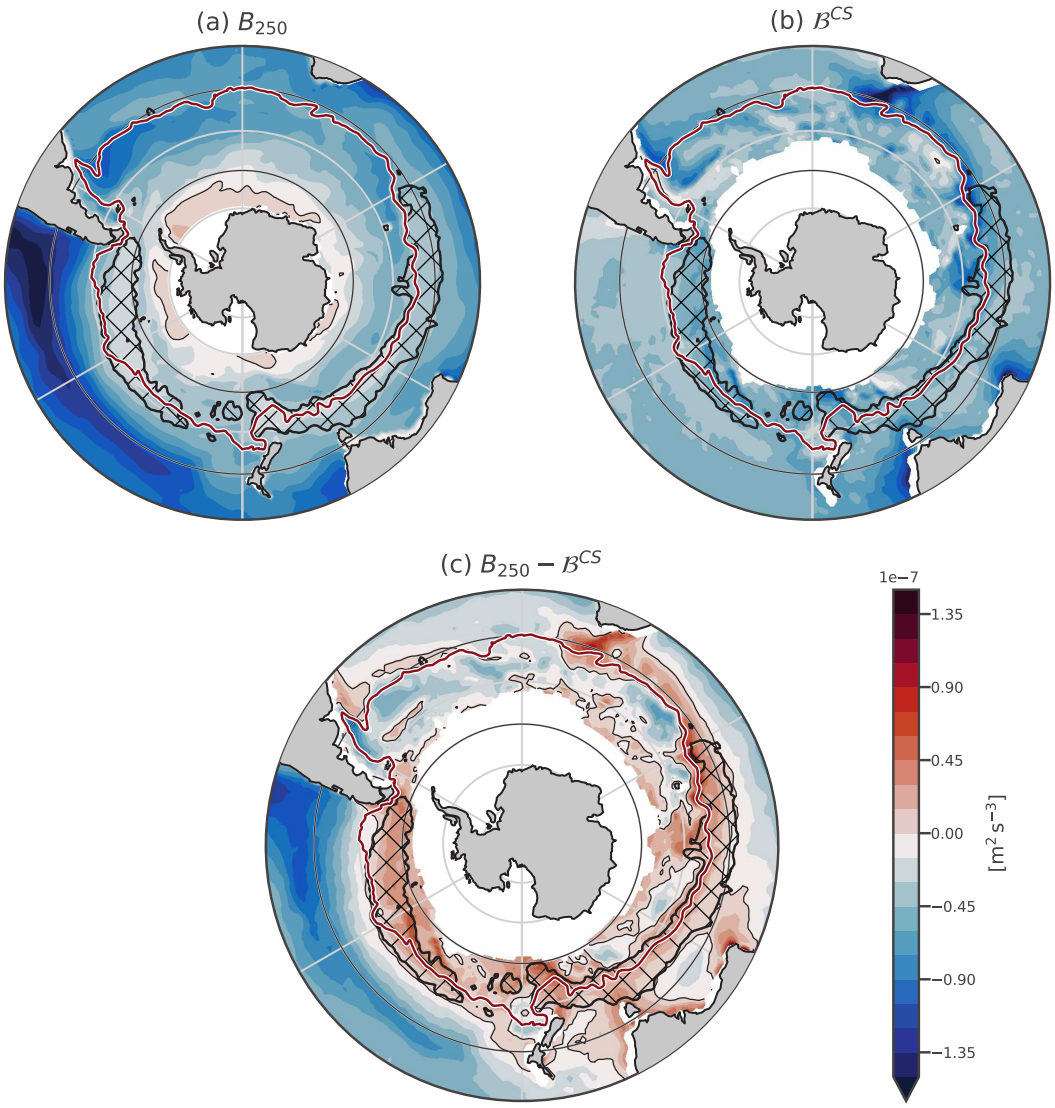

Figure 11. Same as Fig. 7 but using α_0 in computations. Hence, (c) represents where the ocean could form the DMB if the TEC was constant. The hatches represent the observed DMB. The region with sea-ice around Antarctica is masked in white.

https://doi.org/10.5194/egusphere-2023-2404
Preprint. Discussion started: 19 October 2023

north of $40\,^{\circ}\mathrm{S}$. This implies that the poleward extent of the DMB is primarily determined by the decrease in TEC value, which significantly damps heat fluxes impact on buoyancy fluxes. It is not constrained by a decrease in winter heat loss to the south.

The TEC modulates the effect of temperature on stratification. North of $40\,^{\circ}\mathrm{S}$, the temperature stratifies and the TEC value is larger than α_0, so using α_0 implies a weaker stratification (orange line in Fig. 9 (b) and Fig. 10 (a)). $\Delta B_2 50$, the difference between the columnar buoyancy computed with the varying TEC and the constant TEC is thus negative (Fig. 10 (b)). In contrast, between $40\,^{\circ}\mathrm{S}$ and the PF, where temperature still decreases with depth and the TEC value is smaller than α_0, stratification is strengthened. South of the temperature inversion, where colder water lies above warmer water, an increased TEC value decreases or even destabilises the stratification. Such regions are found where $\Delta B_{250} < 0$, close to Antarctica, as seen in Fig. 10. The effect of the TEC on stratification is thus not constant over all the SO, but it is its small value that allows the typical temperature inversion of polar regions while having a stable water column.

Where $\mathcal{B}^{CS}$ is more negative than B_{250}, deep MLs would be produced (Fig. 9 (b) and Fig. 11). The global pattern of stratification strength changes slightly with the constant TEC (Fig. 11 (a)). The stratification is weakening continuously from the subtropics towards Antarctica, until it eventually becomes negative and thus unstable. The winter buoyancy loss is intense everywhere within the SO and does not decrease poleward (Fig. 11 (b)).

In the Indian Ocean, a second region where $B_{250} - \mathcal{B}^{CS} > 0$ appears south of the DMB (the red region close to the sea ice edge). North of this second band, around $50\,^{\circ}\mathrm{S}$, even if $\mathcal{B}^{CS}$ becomes very negative due to the large value of α_0, the stratification is also slightly stronger, which counterbalances for the larger buoyancy loss. In the Pacific Ocean, where stratification is smaller, the predicted DMB extends all the way to the sea ice edge. As the reference value for the TEC is $40\,^{\circ}\mathrm{S}$, the northern boundary of the DMB does not change much.

The overall effect of using the constant TEC is that the southern boundary of the predicted DMB is shifted southward, up to the edge of the sea ice. The DMB formed in an ocean with a constant α_0 would overlap with the observed DMB (Fig. 11 (c)). In the Indian Ocean, two DMBs are formed: one with the same position as the observed one, and one within the ACC, close to the actual sea-ice edge. In the Pacific Ocean, these two DMBs are merged into a wide one. It is likely that such deep MLs would be formed, as mean advection is more or less zonal and does not bring highly stratified waters within the ACC. The narrowness of the DMB thus arises from the decrease of the TEC, that itself induces a decrease in winter buoyancy loss.

https://doi.org/10.5194/egusphere-2023-2404
Preprint. Discussion started: 19 October 2023

5 Discussion and conclusions

In this study, our goal was to determine if the position of the Southern Ocean DMB and its narrowness can be explained only by the balance between the buoyancy loss of the cooling season and the stratification intensity. We find that this balance is sufficient to predict the DMB away from western boundary currents. The narrowness of the DMB emerges because, south of it, despite a weakly stratified ocean, the buoyancy fluxes are small. This small buoyancy loss results from the decrease of the TEC in cold water and not from a decrease in winter heat loss towards the pole.

A perfect prediction of the DMB spatial extent is not realistic, as other processes such as wind-induced turbulence contribute to deepening the ML (Holte et al., 2012). Our study, however, highlights the first-order role of the competition between winter buoyancy loss and existing stratification in forming the DMB. North of $40\,^{\circ}\mathrm{S}$, despite the largest CS buoyancy loss, no deep ML is produced because the stratification of the water column induced by temperature is also very strong. In contrast, within the ACC (except in the East Pacific sector), the water column is only weakly stratified, but the CS buoyancy loss is small. Hence, it is only in a narrow band that both winter buoyancy loss is large enough and stratification is weak enough to significantly deepen the ML.

The buoyancy fluxes follow a strong seasonal cycle, mainly driven by surface heat fluxes. South of $30\,^{\circ}\mathrm{S}$, the Ekman transport advects cold water northward, which produces a negative heat flux. It is likely that this flux itself induces a positive heat flux from the atmosphere on an annual scale. This could explain why the negative Ekman heat flux can counterbalance the surface heat gain (Tamsitt et al., 2016). Ekman transport must therefore be taken into account when computing buoyancy fluxes in the mixed layer. Because of the variability of the wind stress, it drives a large part of the inter-annual variability of the SAMW temperature and salinity (Rintoul and England, 2002).

We have included the effect of the Ekman transport in the buoyancy fluxes. If the Ekman depth is below the MLD, a part of the buoyancy flux that we estimate will be brought below the ML. However, previous studies have found only minor differences in the ML heat budget if taking the MLD as Ekman depth, or 1.5 times the MLD (Dong et al., 2007). Furthermore, the ageostrophic velocities within the Ekman layer decrease with depth, so most of the transport occurs closer to the surface than to the bottom of the Ekman layer. Thus, if the Ekman depth is slightly larger than the MLD, the transport within the ML will only be slightly overestimated.

Even if the annual buoyancy fluxes are a small residual compared to the seasonal fluxes, they will impact the buoyancy budget of the water column along its path. The region within the ACC in the Pacific Ocean tends to lose buoyancy on an annual scale (Fig. 3 (f)) and stratification is smallest in the East Pacific sector (Fig. 7 (a)). This decrease in stratification could be partially attributed to the annual loss of buoyancy. In the Southeast Pacific sector, the low stratification of the upper ocean during summer is also linked to enhanced vertical diffusivity in the upper ocean (Sloyan et al., 2010).

The decrease of the TEC in cold water damps the effect of the heat component of the buoyancy fluxes. This also decreases the contribution of temperature to stratification. Using a constant TEC for the calculation of buoyancy fluxes, we have shown that the region of large buoyancy loss would be located further poleward, while the stratification induced by temperature would increase if the TEC was constant. As a result of these two opposite effects, the DMB's southern boundary would be located

https://doi.org/10.5194/egusphere-2023-2404
Preprint. Discussion started: 19 October 2023

further poleward. This theoretical result has previously been observed in idealised model runs with various values for the polar TEC (Caneill et al., 2022). In line with Roquet et al. (2022), we find that by restraining the deepening of the ML, the variations of the TEC strongly limit the rates of exchange between the surface and the ocean interior. South of the ACC, the impact of temperature is to decrease stratification beneath the winter mixed layer (Pollard et al., 2002). A higher TEC would amplify this effect, resulting in reduced stratification. Furthermore, a higher value of the TEC would enhance the impact of heat loss on buoyancy loss. Thus, climate change and an increase in the (sub)polar ocean temperature may lead to a further southward extent of the DMB.

A direct implication of our study is that one should not convert buoyancy and freshwater fluxes into heat fluxes. It is important to retain the scaling effect of the TEC on the heat component of the buoyancy fluxes. Taking the annual heat flux and converting it to buoyancy flux using the mean TEC or taking the mean buoyancy flux is not equivalent, as described by Schanze and Schmitt (2013). Thus, when studying stratification, heat and freshwater fluxes need to be converted into buoyancy or density fluxes to accurately quantify their effects on density.

In summary, this study provides a global view of the formation of the deep mixing band in the Southern Ocean. The balance between 1) stratification at the end of summer and 2) buoyancy loss during the cooling season is sufficient to explain the formation of the DMB, its position, and its width. The reduction of the thermal expansion coefficient value in cold water limits the influence of heat fluxes on buoyancy fluxes. Consequently, despite the large loss of heat in winter, stratification cannot be significantly eroded south of the actual DMB. The small stratification of the Southeast Pacific sector of the ACC is easily eroded, and despite the small winter buoyancy loss in this region, deep MLs are formed in winter.

Code and data availability. ECCO has been downloaded from https://ecco.jpl.nasa.gov/drive (ECCO Consortium et al., 15-03-2022, 2021).
OAflux has be downloaded from ftp://ftp.whoi.edu/pub/science/oaflux/data_v3/monthly/ (accessed on 2022-02-24)
ISCCP-FH MPF has been downloaded from https://isccp.giss.nasa.gov/pub/flux-fh/tar-nc4_MPF/ (accessed on 2022-03-01).
GPCP has been downloaded from https://www.ncei.noaa.gov/data/global-precipitation-climatology-project-gpcp-monthly/access (accessed on 2022-03-01).
The "Global Ocean Wind L492 Reprocessed 6 hourly Observations" has been replaced on November 2022 by the Global Ocean Hourly Reprocessed Sea Surface Wind and Stress from Scatterometer and Model, E.U Copernicus Marine Service Information (CMEMS), Marine Data Store (MDS), DOI: 10.48670/moi-00185. The data have been downloaded from https://data-cersat.ifremer.fr/data/ocean-wind/mwf/mwf-blended/reprocessing/v6/ (accessed on 2023-10-02).
ARMOR3D with DOI: 10.48670/moi-00052 (accessed on 2022-06-23) has been downloaded from ftp://nrt.cmems-du.eu/Core/MULTIOBS_GLO_PHY_TSUV_3D_MYNRT_015_012/dataset-armor-3d-rep-weekly
MIMOC has been downloaded from http://www.pmel.noaa.gov/mimoc (accessed on 2021-12-09).
The MLD from de Boyer Montégut (2023) based on the work of de Boyer Montégut (2004) has been downloaded from https://www.seanoe.org/data/00806/91774/data/103667.tar (accessed on 2023-08-01).
The climatologies produced in this paper will be shared on Zenodo after the review process. During the review process, they are available upon request to the contact author. The scripts used to make the figures will be shared via Github and a Zenodo DOI after the review process.

https://doi.org/10.5194/egusphere-2023-2404
Preprint. Discussion started: 19 October 2023

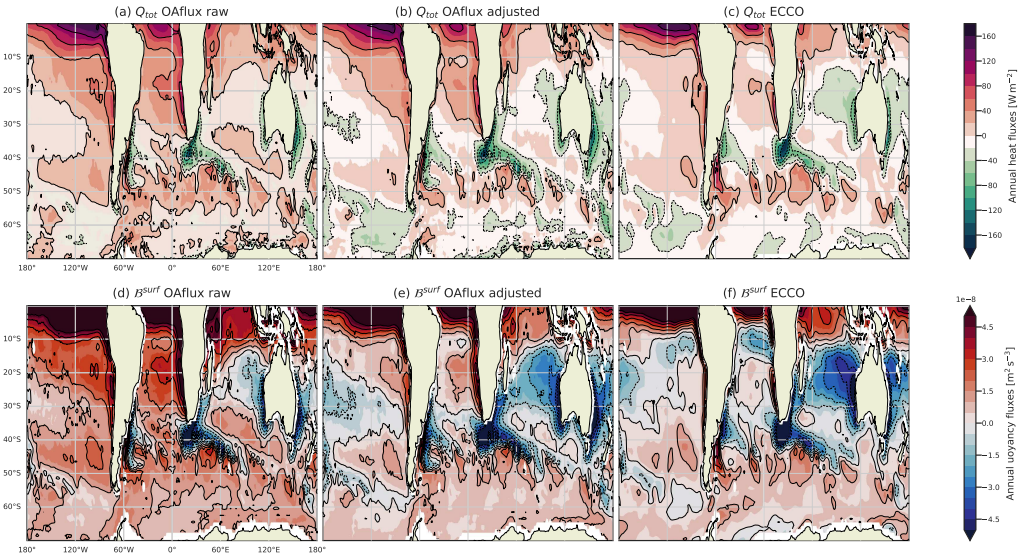

Figure A1. Heat fluxes (first row) and surface buoyancy fluxes (second row) are presented. The first column is the climatology annual mean without any correction, the second column is with our adjustment, and the 3rd column has been computed with the fluxes from ECCO.

During the review process, source code is available upon request to the contact author. All the analyses and figures are reproducible within a few steps.

Appendix A: Correction of heat fluxes

This appendix assesses the validity of the correction on heat fluxes we have applied. Due to the heat imbalance of OAflux, without correction the ocean gains too much heat compared to ECCO (Fig. A1). This is particularly visible in the SO: without correction, almost all the SO gains heat on average, whereas ECCO and our adjusted product show more patchiness and variability. This excess of heat gain is also visible in the buoyancy fluxes (Fig. A1 second row). For example, without the heat correction all Pacific sector of SO gains heat, while in ECCO and after correction a small band of buoyancy loss is present. The comparison of the adjusted product with ECCO allows us to have confidence that our computations represent well the climatological state of the SO.

https://doi.org/10.5194/egusphere-2023-2404
Preprint. Discussion started: 19 October 2023

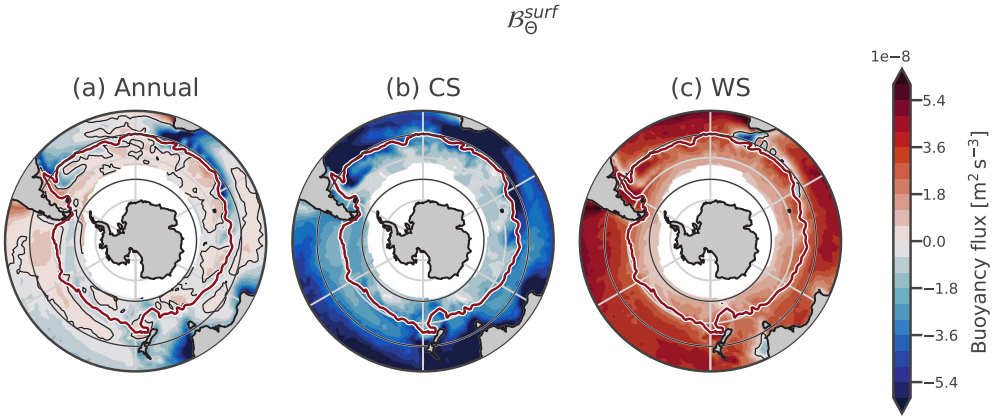

Figure B1. Climatology of the annual, Cooling Season, and Warming Season surface heat component of the buoyancy flux.

Appendix B: Extra maps of buoyancy fluxes

https://doi.org/10.5194/egusphere-2023-2404
Preprint. Discussion started: 19 October 2023

Author contributions. All authors contributed to the study conception. RC conducted analyses. RC prepared the manuscript with contributions from all co-authors.

Competing interests. The authors declare that they have no conflict of interest.

Acknowledgements. The analyses that lead to this publication are based on snakemake (Mölder et al., 2021), xarray (Hoyer and Hamman, 2017; Hoyer et al., 2023), xgcm (Abernathey et al., 2022), cf-xarray (Cherian et al., 2023), and thermodynamic computations were made using gsw-xarray, the xarray wrapper around GSW-Python (McDougall and Barker, 2011; Caneill and Barna, 2023).

This publication is based upon the WHOI OAFlux datasets supported by the NOAA's Global Ocean Monitoring and Observing (GOMO) Program and NASA's Making Earth System Data Records for Use in Research Environments (MEaSUREs) Program.

https://doi.org/10.5194/egusphere-2023-2404
Preprint. Discussion started: 19 October 2023

References

Aagaard, K. and Carmack, E. C.: The role of sea ice and other fresh water in the Arctic circulation, Journal of Geophysical Research, 94, 14 485, https://doi.org/10.1029/JC094iC10p14485, 1989.

Abernathey, R. P., Busecke, J. J. M., Smith, T. A., Deauna, J. D., Banihirwe, A., Nicholas, T., Fernandes, F., James, B., Dussin, R., Cherian, D. A., Caneill, R., Sinha, A., Uieda, L., Rath, W., Balwada, D., Constantinou, N. C., Ponte, A., Zhou, Y., Uchida, T., and Thielen, J.: xgcm, https://doi.org/10.5281/zenodo.7348619, 2022.

Adler, R., Sapiano, M., Huffman, G., Wang, J.-J., Gu, G., Bolvin, D., Chiu, L., Schneider, U., Becker, A., Nelkin, E., Xie, P., Ferraro, R., and Shin, D.-B.: The Global Precipitation Climatology Project (GPCP) Monthly Analysis (New Version 2.3) and a Review of 2017 Global Precipitation, Atmosphere, 9, 138, https://doi.org/10.3390/atmos9040138, 2018.

Belkin, I. M. and Gordon, A. L.: Southern Ocean fronts from the Greenwich meridian to Tasmania, Journal of Geophysical Research: Oceans, 101, 3675–3696, https://doi.org/10.1029/95JC02750, 1996.

Bryan, F.: High-latitude salinity effects and interhemispheric thermohaline circulations, Nature, 323, 301–304, https://doi.org/10.1038/323301a0, 1986.

Caneill, R. and Barna, A.: gsw-xarray, https://doi.org/10.5281/zenodo.8297619, 2023.

Caneill, R., Roquet, F., Madec, G., and Nycander, J.: The Polar Transition from Alpha to Beta Regions Set by a Surface Buoyancy Flux Inversion, Journal of Physical Oceanography, 52, 1887–1902, https://doi.org/10.1175/JPO-D-21-0295.1, 2022.

Carmack, E. C.: The alpha/beta ocean distinction: A perspective on freshwater fluxes, convection, nutrients and productivity in high-latitude seas, Deep Sea Research Part II: Topical Studies in Oceanography, 54, 2578–2598, https://doi.org/10.1016/j.dsr2.2007.08.018, 2007.

Cerovečki, I., Talley, L. D., and Mazloff, M. R.: A Comparison of Southern Ocean Air–Sea Buoyancy Flux from an Ocean State Estimate with Five Other Products, Journal of Climate, 24, 6283–6306, https://doi.org/10.1175/2011JCLI3858.1, 2011.

Cherian, D., Almansi, M., Bourgault, P., Thyng, K., Thielen, J., Magin, J., Aoun, A., Buntemeyer, L., Caneill, R., Davis, L., Fernandes, F., Hauser, M., Heerdegen, A., Kent, J., Mankoff, K., Müller, S., Schupfner, M., Vo, T., and Haëck, C.: cf_xarray, https://doi.org/10.5281/zenodo.8152257, If you use this software, please cite it using these metadata., 2023.

Czaja, A. and Marshall, J.: Why is there net surface heating over the Antarctic Circumpolar Current?, Ocean Dynamics, 65, 751–760, https://doi.org/10.1007/s10236-015-0830-1, 2015.

de Boyer Montégut, C.: Mixed layer depth over the global ocean: An examination of profile data and a profile-based climatology, Journal of Geophysical Research, 109, C12 003, https://doi.org/10.1029/2004JC002378, 2004.

de Boyer Montégut, C.: Mixed layer depth climatology computed with a density threshold criterion of 0.03kg/m3 from 10 m depth value, https://doi.org/10.17882/91774, 2023.

Dong, S., Gille, S. T., and Sprintall, J.: An Assessment of the Southern Ocean Mixed Layer Heat Budget, Journal of Climate, 20, 4425–4442, https://doi.org/10.1175/JCLI4259.1, 2007.

Dong, S., Sprintall, J., Gille, S. T., and Talley, L.: Southern Ocean mixed-layer depth from Argo float profiles, Journal of Geophysical Research, 113, C06 013, https://doi.org/10.1029/2006JC004051, 2008.

DuVivier, A. K., Large, W. G., and Small, R. J.: Argo Observations of the Deep Mixing Band in the Southern Ocean: A Salinity Modeling Challenge, Journal of Geophysical Research: Oceans, 123, 7599–7617, https://doi.org/10.1029/2018JC014275, 2018.

ECCO Consortium, Fukumori, I., Wang, O., Fenty, I., Forget, G., Heimbach, P., and Ponte, R. M.: ECCO Central Estimate (Version 4 Release 4), Retrieved from https://ecco.jpl.nasa.gov/drive, 15-03-2022.

https://doi.org/10.5194/egusphere-2023-2404
Preprint. Discussion started: 19 October 2023

ECCO Consortium, Fukumori, I., Wang, O., Fenty, I., Forget, G., Heimbach, P., Ponte, R., et al.: Synopsis of the ECCO central production global ocean and sea-ice state estimate (version 4 release 4), https://doi.org/10.5281/zenodo.4533349, 2021.

Faure, V. and Kawai, Y.: Heat and salt budgets of the mixed layer around the Subarctic Front of the North Pacific Ocean, Journal of Oceanography, 71, 527–539, https://doi.org/10.1007/s10872-015-0318-0, 2015.

Fernández Castro, B., Mazloff, M., Williams, R. G., and Naveira Garabato, A. C.: Subtropical Contribution to Sub-Antarctic Mode Waters, Geophysical Research Letters, 49, https://doi.org/10.1029/2021GL097560, 2022.

Forget, G., Campin, J.-M., Heimbach, P., Hill, C. N., Ponte, R. M., and Wunsch, C.: ECCO version 4: an integrated framework for non-linear inverse modeling and global ocean state estimation, Geoscientific Model Development, 8, 3071–3104, https://doi.org/10.5194/gmd-8-3071-2015, 2015.

Garrett, C., Outerbridge, R., and Thompson, K.: Interannual Variability in Meterrancan Heat and Buoyancy Fluxes, Journal of Climate, 6, 900–910, https://doi.org/10.1175/1520-0442(1993)006<0900:IVIMHA>2.0.CO;2, 1993.

Gill, A. E. and Adrian, E.: Atmosphere-ocean dynamics, vol. 30, Academic press, 1982.

Gruber, N., Clement, D., Carter, B. R., Feely, R. A., Van Heuven, S., Hoppema, M., Ishii, M., Key, R. M., Kozyr, A., Lauvset, S. K., Lo Monaco, C., Mathis, J. T., Murata, A., Olsen, A., Perez, F. F., Sabine, C. L., Tanhua, T., and Wanninkhof, R.: The oceanic sink for anthropogenic CO_2 from 1994 to 2007, Science, 363, 1193–1199, https://doi.org/10.1126/science.aau5153, 2019.

Guinehut, S., Dhomps, A.-L., Larnicol, G., and Le Traon, P.-Y.: High resolution 3-D temperature and salinity fields derived from in situ and satellite observations, Ocean Science, 8, 845–857, https://doi.org/10.5194/os-8-845-2012, 2012.

Hanawa, K. and Talley, L. D.: Chapter 5.4 Mode waters, in: Ocean Circulation and Climate, edited by Siedler, G., Church, J., and Gould, J., vol. 77 of *International Geophysics*, pp. 373–386, Academic Press, https://doi.org/https://doi.org/10.1016/S0074-6142(01)80129-7, iSSN: 0074-6142, 2001.

Herrmann, M., Somot, S., Sevault, F., Estournel, C., and Déqué, M.: Modeling the deep convection in the northwestern Mediterranean Sea using an eddy-permitting and an eddy-resolving model: Case study of winter 1986–1987, Journal of Geophysical Research, 113, C04 011, https://doi.org/10.1029/2006JC003991, 2008.

Hieronymus, M. and Nycander, J.: The Buoyancy Budget with a Nonlinear Equation of State, Journal of Physical Oceanography, 43, 176–186, https://doi.org/10.1175/JPO-D-12-063.1, 2013.

Holland, P. R. and Kwok, R.: Wind-driven trends in Antarctic sea-ice drift, Nature Geoscience, 5, 872–875, https://doi.org/10.1038/ngeo1627, 2012.

Holte, J. W., Talley, L. D., Chereskin, T. K., and Sloyan, B. M.: The role of air-sea fluxes in Subantarctic Mode Water formation: SAMW FORMATION, Journal of Geophysical Research: Oceans, 117, n/a–n/a, https://doi.org/10.1029/2011JC007798, 2012.

Hoyer, S. and Hamman, J.: xarray: N-D labeled arrays and datasets in Python, Journal of Open Research Software, 5, https://doi.org/10.5334/jors.148, 2017.

Hoyer, S., Roos, M., Joseph, H., Magin, J., Cherian, D., Fitzgerald, C., Hauser, M., Fujii, K., Maussion, F., Imperiale, G., Clark, S., Kleeman, A., Nicholas, T., Kluyver, T., Westling, J., Munroe, J., Amici, A., Barghini, A., Banihirwe, A., Bell, R., Hatfield-Dodds, Z., Abernathey, R., Bovy, B., Omotani, J., Mühlbauer, K., Roszko, M. K., and Wolfram, P. J.: xarray, https://doi.org/10.5281/zenodo.8153447, 2023.

IOC, SCOR, and IAPSO: The International thermodynamic equation of seawater–2010: calculation and use of thermodynamic properties.[includes corrections up to 31st October 2015]., Intergovernmental Oceanographic Com mission, Manuals and Guides, 56, 220, http://teos-10.org/pubs/TEOS-10_Manual.pdf, 2015.

https://doi.org/10.5194/egusphere-2023-2404
Preprint. Discussion started: 19 October 2023

Josey, S. A., Grist, J. P., Mecking, J. V., Moat, B. I., and Schulz, E.: A clearer view of Southern Ocean air–sea interaction using surface heat flux asymmetry, Philosophical Transactions of the Royal Society A: Mathematical, Physical and Engineering Sciences, 381, 20220 067, https://doi.org/10.1098/rsta.2022.0067, 2023.

Klocker, A., Naveira Garabato, A. C., Roquet, F., De Lavergne, C., and Rintoul, S. R.: Generation of the Internal Pycnocline in the Subpolar Southern Ocean by Wintertime Sea Ice Melting, Journal of Geophysical Research: Oceans, 128, e2022JC019 113, https://doi.org/10.1029/2022JC019113, 2023.

Kostianoy, A. G., Ginzburg, A. I., Frankignoulle, M., and Delille, B.: Fronts in the Southern Indian Ocean as inferred from satellite sea surface temperature data, Journal of Marine Systems, 45, 55–73, https://doi.org/10.1016/j.jmarsys.2003.09.004, 2004.

Lascaratos, A. and Nittis, K.: A high-resolution three-dimensional numerical study of intermediate water formation in the Levantine Sea, Journal of Geophysical Research: Oceans, 103, 18 497–18 511, https://doi.org/10.1029/98JC01196, 1998.

Lenn, Y.-D. and Chereskin, T. K.: Observations of Ekman Currents in the Southern Ocean, Journal of Physical Oceanography, 39, 768–779, https://doi.org/10.1175/2008JPO3943.1, 2009.

Li, Q. and Lee, S.: A Mechanism of Mixed Layer Formation in the Indo–Western Pacific Southern Ocean: Preconditioning by an Eddy-Driven Jet-Scale Overturning Circulation, Journal of Physical Oceanography, 47, 2755–2772, https://doi.org/10.1175/JPO-D-17-0006.1, 2017.

McDougall, T. J. and Barker, P. M.: Getting started with TEOS-10 and the Gibbs Seawater (GSW) Oceanographic Toolbox, SCOR/IAPSO WG127, 2011.

Mölder, F., Jablonski, K., Letcher, B., Hall, M., Tomkins-Tinch, C., Sochat, V., Forster, J., Lee, S., Twardziok, S., Kanitz, A., Wilm, A., Holtgrewe, M., Rahmann, S., Nahnsen, S., and Köster, J.: Sustainable data analysis with Snakemake [version 1; peer review: 1 approved, 1 approved with reservations], F1000Research, 10, https://doi.org/10.12688/f1000research.29032.1, 2021.

Naveira Garabato, A. C., Jullion, L., Stevens, D. P., Heywood, K. J., and King, B. A.: Variability of Subantarctic Mode Water and Antarctic Intermediate Water in the Drake Passage during the Late-Twentieth and Early-Twenty-First Centuries, Journal of Climate, 22, 3661–3688, https://doi.org/10.1175/2009JCLI2621.1, 2009.

Nycander, J., Hieronymus, M., and Roquet, F.: The nonlinear equation of state of sea water and the global water mass distribution: Global Water Mass Distribution, Geophysical Research Letters, 42, 7714–7721, https://doi.org/10.1002/2015GL065525, 2015.

Orsi, A. H., Whitworth, T., and Nowlin, W. D.: On the meridional extent and fronts of the Antarctic Circumpolar Current, Deep Sea Research Part I: Oceanographic Research Papers, 42, 641–673, https://doi.org/10.1016/0967-0637(95)00021-W, 1995.

Park, Y., Park, T., Kim, T., Lee, S., Hong, C., Lee, J., Rio, M., Pujol, M., Ballarotta, M., Durand, I., and Provost, C.: Observations of the Antarctic Circumpolar Current Over the Udintsev Fracture Zone, the Narrowest Choke Point in the Southern Ocean, Journal of Geophysical Research: Oceans, 124, 4511–4528, https://doi.org/10.1029/2019JC015024, 2019.

Pauthenet, E., Roquet, F., Madec, G., and Nerini, D.: A Linear Decomposition of the Southern Ocean Thermohaline Structure, Journal of Physical Oceanography, 47, 29–47, https://doi.org/10.1175/JPO-D-16-0083.1, 2017.

Pellichero, V., Sallée, J.-B., Chapman, C. C., and Downes, S. M.: The southern ocean meridional overturning in the sea-ice sector is driven by freshwater fluxes, Nature Communications, 9, 1789, https://doi.org/10.1038/s41467-018-04101-2, 2018.

Pollard, R., Lucas, M., and Read, J.: Physical controls on biogeochemical zonation in the Southern Ocean, Deep Sea Research Part II: Topical Studies in Oceanography, 49, 3289–3305, https://doi.org/10.1016/S0967-0645(02)00084-X, 2002.

Qiu, B. and Kelly, K. A.: Upper-Ocean Heat Balance in the Kuroshio Extension Region, Journal of Physical Oceanography, 23, 2027–2041, https://doi.org/10.1175/1520-0485(1993)023<2027:UOHBIT>2.0.CO;2, 1993.

https://doi.org/10.5194/egusphere-2023-2404
Preprint. Discussion started: 19 October 2023

Rintoul, S. R.: The global influence of localized dynamics in the Southern Ocean, Nature, 558, 209–218, https://doi.org/10.1038/s41586-018-0182-3, 2018.

Rintoul, S. R. and England, M. H.: Ekman Transport Dominates Local Air–Sea Fluxes in Driving Variability of Subantarctic Mode Water, Journal of Physical Oceanography, 32, 1308–1321, https://doi.org/10.1175/1520-0485(2002)032<1308:ETDLAS>2.0.CO;2, 2002.

Roach, C. J., Phillips, H. E., Bindoff, N. L., and Rintoul, S. R.: Detecting and Characterizing Ekman Currents in the Southern Ocean, Journal of Physical Oceanography, 45, 1205–1223, https://doi.org/10.1175/JPO-D-14-0115.1, 2015.

Roemmich, D., Church, J., Gilson, J., Monselesan, D., Sutton, P., and Wijffels, S.: Unabated planetary warming and its ocean structure since 2006, Nature Climate Change, 5, 240–245, https://doi.org/10.1038/nclimate2513, 2015.

Roquet, F., Madec, G., Brodeau, L., and Nycander, J.: Defining a Simplified Yet "Realistic" Equation of State for Seawater, Journal of Physical Oceanography, 45, 2564–2579, https://doi.org/10.1175/JPO-D-15-0080.1, 2015.

Roquet, F., Ferreira, D., Caneill, R., Schlesinger, D., and Madec, G.: Unique thermal expansion properties of water key to the formation of sea ice on Earth, Science Advances, 8, https://doi.org/10.1126/sciadv.abq0793, 2022.

Rossow, W. B. and Schiffer, R. A.: Advances in Understanding Clouds from ISCCP, Bulletin of the American Meteorological Society, 80, 2261–2287, https://doi.org/10.1175/1520-0477(1999)080<2261:AIUCFI>2.0.CO;2, 1999.

Sabine, C. L., Feely, R. A., Gruber, N., Key, R. M., Lee, K., Bullister, J. L., Wanninkhof, R., Wong, C. S., Wallace, D. W. R., Tilbrook, B., Millero, F. J., Peng, T.-H., Kozyr, A., Ono, T., and Rios, A. F.: The Oceanic Sink for Anthropogenic CO_2, Science, 305, 367–371, https://doi.org/10.1126/science.1097403, 2004.

Sallée, J.-B., Wienders, N., Speer, K., and Morrow, R.: Formation of subantarctic mode water in the southeastern Indian Ocean, Ocean Dynamics, 56, 525–542, https://doi.org/10.1007/s10236-005-0054-x, 2006.

Sallée, J.-B., Morrow, R., and Speer, K.: Eddy heat diffusion and Subantarctic Mode Water formation, Geophysical Research Letters, 35, L05 607, https://doi.org/10.1029/2007GL032827, 2008.

Schanze, J. J. and Schmitt, R. W.: Estimates of Cabbeling in the Global Ocean, Journal of Physical Oceanography, 43, 698–705, https://doi.org/10.1175/JPO-D-12-0119.1, 2013.

Schiffer, R. A. and Rossow, W. B.: The International Satellite Cloud Climatology Project (ISCCP): The first project of the World Climate Research Programme, Bull. Amer. Meteorol. Soc., 64, 779–784, 1983.

Schmidtko, S., Johnson, G. C., and Lyman, J. M.: MIMOC: A global monthly isopycnal upper-ocean climatology with mixed layers: MIMOC, Journal of Geophysical Research: Oceans, 118, 1658–1672, https://doi.org/10.1002/jgrc.20122, 2013.

Sloyan, B. M. and Rintoul, S. R.: Circulation, Renewal, and Modification of Antarctic Mode and Intermediate Water*, Journal of Physical Oceanography, 31, 1005–1030, https://doi.org/10.1175/1520-0485(2001)031<1005:CRAMOA>2.0.CO;2, 2001.

Sloyan, B. M., Talley, L. D., Chereskin, T. K., Fine, R., and Holte, J.: Antarctic Intermediate Water and Subantarctic Mode Water Formation in the Southeast Pacific: The Role of Turbulent Mixing, Journal of Physical Oceanography, 40, 1558–1574, https://doi.org/10.1175/2010JPO4114.1, 2010.

Small, R. J., DuVivier, A. K., Whitt, D. B., Long, M. C., Grooms, I., and Large, W. G.: On the control of subantarctic stratification by the ocean circulation, Climate Dynamics, 56, 299–327, https://doi.org/10.1007/s00382-020-05473-2, 2021.

Song, X.: Explaining the Zonal Asymmetry in the Air-Sea Net Heat Flux Climatology Over the Antarctic Circumpolar Current, Journal of Geophysical Research: Oceans, 125, e2020JC016 215, https://doi.org/10.1029/2020JC016215, 2020.

Speer, K., Rintoul, S. R., and Sloyan, B.: The Diabatic Deacon Cell, Journal of Physical Oceanography, 30, 3212–3222, https://doi.org/10.1175/1520-0485(2000)030<3212:TDDC>2.0.CO;2, 2000.

https://doi.org/10.5194/egusphere-2023-2404
Preprint. Discussion started: 19 October 2023

Sterl, M. F. and De Jong, M. F.: Restratification Structure and Processes in the Irminger Sea, Journal of Geophysical Research: Oceans, 127, e2022JC019 126, https://doi.org/10.1029/2022JC019126, 2022.

Swart, S., Gille, S. T., Delille, B., Josey, S., Mazloff, M., Newman, L., Thompson, A. F., Thomson, J., Ward, B., Du Plessis, M. D., Kent, E. C., Girton, J., Gregor, L., Heil, P., Hyder, P., Pezzi, L. P., De Souza, R. B., Tamsitt, V., Weller, R. A., and Zappa, C. J.: Constraining Southern Ocean Air-Sea-Ice Fluxes Through Enhanced Observations, Frontiers in Marine Science, 6, 421, https://doi.org/10.3389/fmars.2019.00421, 2019.

Tamsitt, V., Talley, L. D., Mazloff, M. R., and Cerovečki, I.: Zonal Variations in the Southern Ocean Heat Budget, Journal of Climate, 29, 6563–6579, https://doi.org/10.1175/JCLI-D-15-0630.1, 2016.

Virtanen, P., Gommers, R., Oliphant, T. E., Haberland, M., Reddy, T., Cournapeau, D., Burovski, E., Peterson, P., Weckesser, W., Bright, J., van der Walt, S. J., Brett, M., Wilson, J., Millman, K. J., Mayorov, N., Nelson, A. R. J., Jones, E., Kern, R., Larson, E., Carey, C. J., Polat, İ., Feng, Y., Moore, E. W., VanderPlas, J., Laxalde, D., Perktold, J., Cimrman, R., Henriksen, I., Quintero, E. A., Harris, C. R., Archibald, A. M., Ribeiro, A. H., Pedregosa, F., van Mulbregt, P., and SciPy 1.0 Contributors: SciPy 1.0: Fundamental Algorithms for Scientific Computing in Python, Nature Methods, 17, 261–272, https://doi.org/10.1038/s41592-019-0686-2, 2020.

Wang, J., Mazloff, M. R., and Gille, S. T.: Pathways of the Agulhas waters poleward of 29°S, Journal of Geophysical Research: Oceans, 119, 4234–4250, https://doi.org/10.1002/2014JC010049, 2014.

Yang, J.: The Seasonal Variability of the Arctic Ocean Ekman Transport and Its Role in the Mixed Layer Heat and Salt Fluxes, Journal of Climate, 19, 5366–5387, https://doi.org/10.1175/JCLI3892.1, 2006.

Yu, L. and Weller, R. A.: Objectively Analyzed Air–Sea Heat Fluxes for the Global Ice-Free Oceans (1981–2005), Bulletin of the American Meteorological Society, 88, 527–540, https://doi.org/10.1175/BAMS-88-4-527, 2007.

Zahariev, K. and Garrett, C.: An Apparent Surface Buoyancy Flux Associated with the Nonlinearity of the Equation of State, Journal of Physical Oceanography, 27, 362–368, https://doi.org/10.1175/1520-0485(1997)027<0362:AASBFA>2.0.CO;2, 1997.

Paper III

Temperature versus salinity: distribution of stratification control in the global ocean

Romain Caneill[1] and Fabien Roquet[1]

[1]Department of Marine Sciences, University of Gothenburg, Gothenburg, Sweden

Correspondence: Romain Caneill (romain.caneill@gu.se)

Abstract. The ocean stratification is controlled by temperature in subtropical regions (alpha oceans), by salinity in polar regions (beta oceans), and by both in the transition zones. The polar transition zone (PTZ) is located in between subtropical alpha and polar beta oceans. The PTZ exists in the North Pacific, North Atlantic, and Southern Ocean, despite different circulations and oceanic properties between them. Deep winter mixed layers (MLs) are found in the vicinity of the PTZ, which makes it a key component to link the surface and the ocean interior. The global climatological state and the variability from the climatology are not full described in previous studies studying control of stratification. Based on observational temperature – salinity profiles, we compute novel climatologies of the stratification below the ML, classifying the global oceans into alpha, beta, or transition zones. Using the profiles, we also computed a monthly product for every year between 2004 – 2021, allowing for the study of interannual variability. On the climatological state, we describe accurately the PTZ between subtropical alpha ocean and polar beta ocean. Our study highlights the difference between each basin: the alpha ocean stops at $40°$N in the Pacific basin, but reaches $80°$N in the eastern part of North Atlantic. In both the North Atlantic and Southern Oceans, the PTZ is narrow, while in the east-north Pacific Ocean it spans 20 degrees of longitude. The SO Subantarctic and Polar Fronts are located at the shifts between the stratification regimes.

1 Introduction

Temperature and salinity vary differently with depth in the subtropics and in polar regions. Taking transect between Australia and Antarctica reveals two opposite regimes (Fig. 1). In the subtropical part, temperature and salinity both decrease with depth, while in the polar part, temperature and salinity increase with depth. In between the subtropical and polar regimes exists a narrow region where temperature decreases with depth, and salinity increases. As warm and fresh water is lighter than cold and salty water, stratification of the upper ocean is thus controlled by temperature in the subtropics and salinity in the polar regions (Pollard et al., 2002; Carmack, 2007). These two different types of stratification are called alpha (stabilised by temperature) and beta (stabilised by salinity) oceans, respectively (Carmack, 2007). In between these regions lies the polar transition zone (PTZ), where both temperature and salinity increase stratification (Caneill et al., 2022). Tropical oceans at the equator are also stratified by temperature and salinity (Clément et al., 2020). The transition from an alpha ocean in subtropical regions through a transition zone to a beta ocean in polar regions is a notable characteristic observed both in the Northern and Southern Hemisphere (Pollard et al., 2002; You, 2002; Carmack, 2007; Stewart and Haine, 2016).

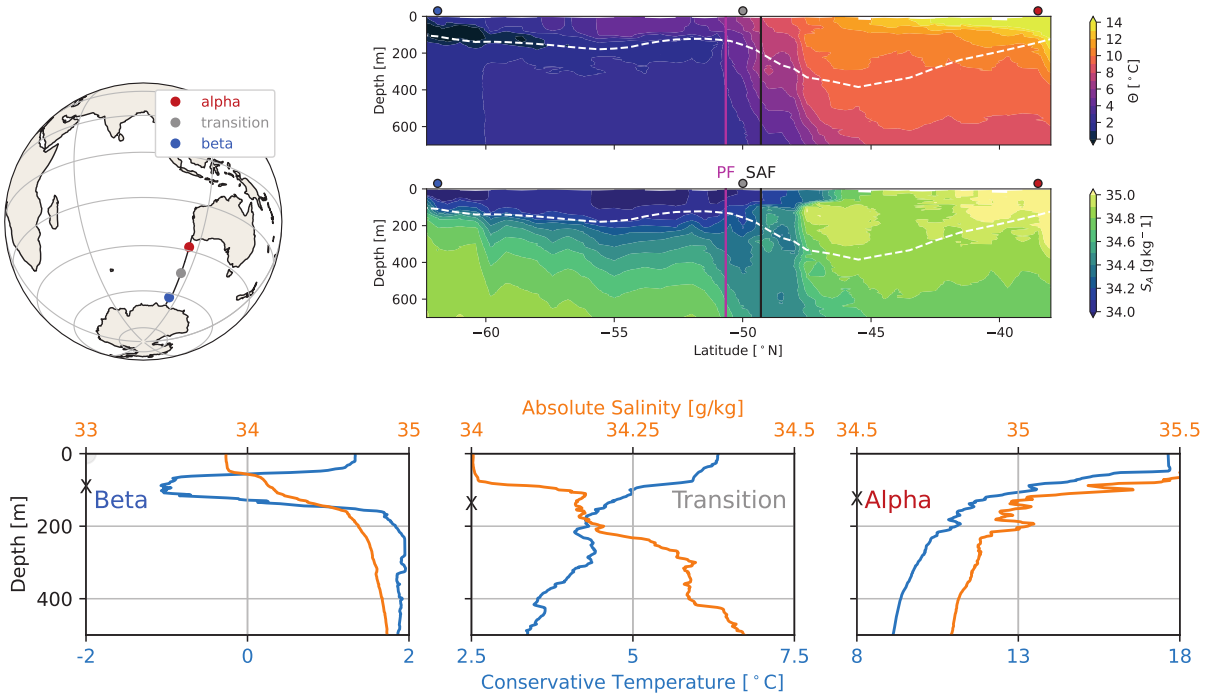

Figure 1. Temperature and salinity sections along the IO9S transect. Data are from the hydrographic cruise 09AR20120105 (CCHDO Hydrographic Data Office, 2023). The vertical lines mark the boundaries of, from north to south, alpha ocean, transition zone, and beta ocean. These boundaries are determined by the Subantarctic Front (SAF, black line) and the Polar Front (PF, purple line). The white and dashed line represents the climatological winter mixed layer depth (from (de Boyer Montégut, 2023)). The three bottom panels correspond to the three dots of the upper panels. The black crosses on the left vertical axes represent the climatological winter mixed layer depth.

The alpha – beta distinction reveals important implications. The halocline present in beta ocean is essential for sea-ice formation (Carmack, 2007). Simultaneously, the increase of temperature with depth maintains a heat reservoir, which can damp the formation of sea-ice, melt it, and contribute to deep convection events (Martinson et al., 1981; Pierce et al., 1995; Martin et al., 2013; Polyakov et al., 2013). Reduced sea-ice under warmer conditions lowers ocean albedo, increasing heat absorption and further amplify ocean warming (Curry et al., 1995; Perovich and Polashenski, 2012).

Winter mixed layers in temperature-stabilised regions are generally deeper than in salinity-stabilised ones, allowing beta ocean to re-stratify faster in summer (Carmack, 2007). Double diffusive effect arise in alpha and beta ocean, but not transition zone where both temperature and salinity stabilise the water column (Stern, 1960; Schmitt, 1994; You, 2002).

The existence of the polar transition zone in all subpolar oceans indicates that intrinsic properties of seawater could drive the alpha / beta distinction (Carmack, 2007). Roquet et al. (2022) showed that the existence of beta ocean is possible because

the thermal expansion coefficient becomes small in cold water. This makes the density of cold seawater almost insensitive to temperature. Moreover, polar regions undergo large surface freshwater input, which form the halocline. If the thermal expansion were larger, the halocline could not exist in winter due to heat loss driven convection (Roquet et al., 2022; Caneill et al., 2023, manuscript submitted to Ocean Science).

The characteristics of the PTZ vary however between the different basins. In the North Pacific Ocean, the PTZ is associated with a surface density maximum (Roden, 1970; Stewart and Haine, 2016; Johnson et al., 2012). This density maximum is however not found in the Southern Ocean (SO) PTZ: the density maximum is located close to the coast of Antarctica, in beta ocean.

In the SO, the transition from subtropical to polar waters is achieved by a succession of fronts part of the Antarctic Circumpolar Current (ACC). Three fronts have been historically defined based on thermohaline properties: from north to south the Subantarctic Front (SAF), the Polar Front (PF), and the Southern ACC front (SACCF). The Polar Frontal Zone (PFZ) is the zone of change between Antarctic and Subantarctic surface waters. The PFZ is a permanent feature in the SO (Emery, 1977), that exists by definition everywhere in the SO. Pollard et al. (2002) proposed to define the SAF and PF based on stratification, which directly relates to the concept of alpha and beta ocean: the SAF marks the boundary between alpha ocean and the PTZ, while the PF marks the boundary between the PTZ and the beta ocean. The boundary between regions of different thermohaline structure are thus used as definition for the fronts (Pauthenet et al., 2017; Thomas et al., 2021).

The position of the PF is associated with a strong ocean jet (e.g. Trathan et al., 1997). With more observations available (both in situ and from satellite) it became more common to consider that the ACC is made of multiple frontal filaments (Sokolov and Rintoul, 2009). Dynamic fronts are located at the position of strong jets and strong isopycnal slopes or sea surface height (SSH) gradient. Dynamic fronts can be transient, so a definition based on SSH gradient is more accurate than definitions following a SSH contour (Graham et al., 2012).

The control of stratification by temperature or salinity below the mixed layer (ML) usually varies depending on the season and location (Helber et al., 2012; Pellichero et al., 2017; DuVivier et al., 2018). The export of the ML properties to the interior happens when the ML is deepest and water escapes by lateral subduction (Sallée et al., 2010). The stratification control index (SCI) provides information on the relative effect of temperature and salinity on stratification, allowing to classify water masses in alpha, beta, or transition zone (Caneill et al., 2022; Roquet et al., 2022).

$$\mathrm{SCI} = \frac{N^2_\Theta - N^2_S}{N^2_\Theta + N^2_S} \tag{1}$$

$$N^2 = -\frac{g}{\rho_0}\frac{\partial \rho_\Theta}{\partial z} = N^2_\Theta + N^2_S \tag{2}$$

$$N^2_\Theta = g\alpha\frac{\partial \Theta}{\partial z} \tag{3}$$

$$N^2_S = -g\beta\frac{\partial S_A}{\partial z}\,. \tag{4}$$

It quantifies the relative effect of temperature and salinity on stratification, and is defined only for positive N^2. Based on the SCI, 3 regions are defined:

1. $SCI > 1$: alpha ocean where temperature (salinity) increases (decreases) stratification;

2. $-1 < SCI < 1$: transition zone where temperature (salinity) increases (increases) stratification;

3. $SCI < -1$: beta ocean where temperature (salinity) decreases (increases) stratification.

The SCI below the winter ML informs on the stratification properties of the permanent pycnocline that links the intermediate ocean with the surface. DuVivier et al. (2018) remarked that subsurface salinity maximums in the SO are misrepresented in Earth System Models, which in return lead to biases in mixed layer depth (MLD) compared to observations. Knowing whether temperature or salinity are stabilising the water column below the ML is of main importance to understand the exchange of properties (heat, salt, carbon, etc) between the surface and the interior.

Based on observational temperature – salinity profiles, we produce climatologies of the MLD and SCI for the different seasons. Following Pollard et al. (2002) and Carmack (2007) we thus use the thermohaline stratification to describe both the global oceans and the Southern Ocean. The description of the winter SCI provides a picture of the ocean that is both novel and at the same time coherent with previous descriptions. The paper is organised as follows: we first describe the EN.4.2.2 database and the methods we used to produce the MLD and SCI climatologies. Then, we present the results of the mean climatological state along with the seasonal variations for both the global ocean before focusing on convective regions in the SO and Irminger Sea. Finally, we provide more detailed analysis in the SO, and finish with discussion and conclusions.

2 Material and Methods

This study uses a database of profiles of temperature and salinity to compute the MLD and SCI for each individual profiles. Interpolation is then done to create both a gridded product, and a gridded monthly climatology.

2.1 EN4

The profiles are taken from the EN.4.2.2 (Good et al., 2013) ensemble members using Gouretski and Cheng (2020) MBT, and Gouretski and Reseghetti (2010) XBT corrections. Data from 2004 to 2021 are used. 2004 is the beginning of the ARGO era in the Southern Ocean, so we chose this lower limit to exclude years with too few measurements.

Data from EN4 have been filtered to remove badly flagged profiles. The profiles have been individually smoothed and re-sampled vertically following this algorithm, similar to (Johnson et al., 2002):

1. interpolate linearly along an evenly spaced grid with a resolution of 1 m, going from 0 to 2000 m;

2. smooth by applying the convolution with a hanning window (= a positive half sinus) with a window length of 20 m

3. interpolate linearly to a lower resolution vertical grid: every 5 m from 0 to 100 m, then every 10 m up to 350 m, then every 25 m up to 500 m, and then every 50 m to 2000 m.

Fig. A1 in Appendix A presents a profile before and after smoothing. Small scale variations are removed, while keeping the global shape of the temperature profile.

2.2 Methods

2.2.1 MLD and SCI

We compute the MLD using a density threshold criteria of $0.03\,\mathrm{kg\,m^{-3}}$ (de Boyer Montégut, 2004; Sallée et al., 2021).

The SCI is computed between 10 and 30 m under the ML.

2.3 Interpolation on a regular grid

The gridding of the variables extracted from the profiles (MLD or SCI) is done using a radial basis function (RBF) interpolation. The class *scipy.interpolate.RBFInterpolator* from the Python *scipy* library is used.

To account for the anisotropy between the longitude and latitude scale factors, the latitude is transformed by a Mercator projection, using the following formula:

$$\varphi' = \ln\Big(\tan\Big(\frac{\varphi}{2}\frac{\pi}{180} + \frac{\pi}{4}\Big)\Big) \cdot \frac{180}{\pi} \tag{5}$$

This will virtually increase the difference of latitude between 2 points located in polar regions. To achieve isotropy, 2 points separated by the same geographical distance (i.e. measured in meter) along longitude or latitude should get the same distance (Eq. (6) in a following paragraph). The difference of longitude is larger than the difference of latitude due to the spherical shape of the Earth. The Mercator projection increases the difference of transformed latitude to exactly reach the same difference of longitude (measured in degrees). The Mercator projection is not defined at the poles, however the South Pole is located on land, and the Arctic region north of 85N is not included in our study.

Longitude and latitude become isotropic with the Mercator projection, and the radius of effect (in meter) of each measurement point will decrease as $sin(\varphi)$. Thus, this will also take into account the decrease of the Rossby radius of deformation with latitude.

The distance to every measurement point is computed around each grid point:

$$d_i^2 = \left[\frac{\Delta\lambda}{L_\lambda}\right]^2 - \left[\frac{\Delta\varphi'}{L_{\varphi'}}\right]^2 - \left[\frac{\Delta t}{L_t}\right]^2 \tag{6}$$

with $\Delta\lambda$ the difference of longitude between the grid point and the measurement point (modulo 360, accounting thus for periodic condition), $\Delta\varphi'$ the difference of Mecator latitude, and Δt the number of days of difference (modulo 365.25 if producing the climatology). The three L express the decorrelation scales for longitude, Mercator latitude and time. The three decorrelation scales have been chosen as: $L_\lambda = L_{\varphi'} = 3.3°$, and $L_t = 45\,\mathrm{d}$, similar to the coefficient used to produce the MIMOC climatology (Schmidtko et al., 2013).

The 300 closest points are selected for the RBF interpolation. If less than 50 points are located in a sphere with distance $d = 1$ around the grid point, the grid point is masked and no interpolation is done (distance of 1 corresponds to e.g. $\Delta\lambda = L_\lambda$ or $\Delta t = L_t$). While this is not a big issue for the climatology, we acknowledge that it filters out some of grid point in e.g. the Southern Ocean or Arctic Ocean. However, it seems honest to mask grid points with not enough observation in its neighbourhood. The

choice of 50 points is somehow arbitrary, more work should be needed to provide an estimate of the minimum number of profiles needed.

The interpolation kernel uses a Gaussian function, the weighting function is:

$$w_i = \exp\left(-d_i^2 \epsilon^2\right) \tag{7}$$

ϵ is a shape parameter that changes whether the gaussian is flat or spiked. A large ϵ produces a spiky interpolation, as only the very close points will have a non-negligible distance. On the opposite, a small ϵ leads to a very smooth field. $\epsilon = 0.5$ is chosen as a good fit between smoothing and not only keeping the very large scale.

The covariance matrix between all the measurement points is defined as:

$$E_{ij}^0 = \exp\left(-d_{ij}^2 \epsilon^2\right) \tag{8}$$

using the distance between all points. A constant noise-signal ratio is added to $\mathbf{E^0}$, i.e. $\mathbf{E} = \mathbf{E^0} + \lambda \mathbf{I}$.

The interpolation at a point x is given by

$$s(x) = \mathbf{\Phi}(x) \cdot \boldsymbol{\omega} \tag{9}$$

where $\Phi_i(x) = \exp\left(-d_{xi}^2 \epsilon^2\right)$, and $\boldsymbol{\omega}$ is the solution of

$$\mathbf{E} \cdot \boldsymbol{\omega} = \mathbf{\Psi} \tag{10}$$

with $\mathbf{\Psi}$ the vector of measured properties. The final formula is then:

$$s(x) = \mathbf{\Phi} \cdot \mathbf{E}^{-1} \cdot \mathbf{\Psi} \tag{11}$$

By using either the time in Julian days, or in days of year, it is possible to use the same method to produce climatological fields or the monthly field of a certain year. While the interpolation method allows estimating variance (and thus error) associated with the computation, it highly depends on *a priori* estimates of the variance of the measures, which value is not known. Instead, we compute monthly products for years 2004 – 2021, and estimate the monthly standard deviation of MLD and SCI at each point, using the 17 years of the product. Due to the criteria of using strictly more than 50 points close by, some data points are not used for the monthly product, but only used in the climatology.

A regular longitude – latitude grid with a resolution of 1 degree is used for the mapping to produce monthly products.

During the interpolation, grid points are masked if they have less than 50 points in a circle of radius 1. Fortunately, this threshold does not affect the major part of the ocean, except for polar regions, especially the Arctic Ocean (Fig. 2). Some hotspots of measurement are visible, e.g. the Kerguelen Plateau (69E, 49S), in the Southern Ocean where seals are tagged with CTD sensors.

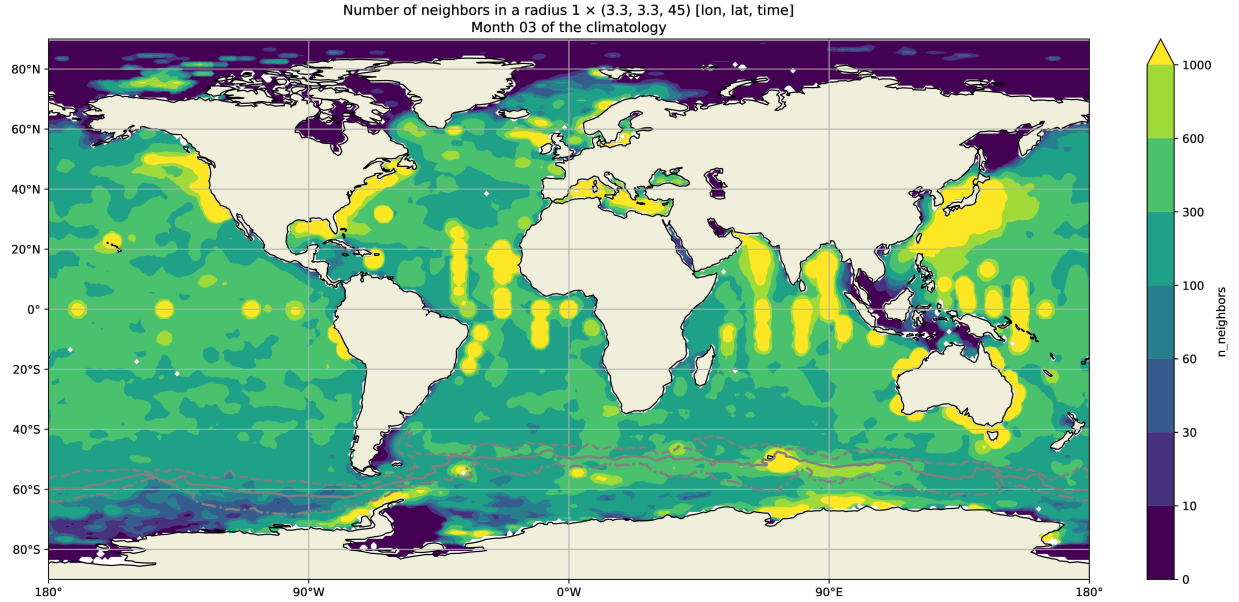

Figure 2. Number of profiles in a circle of distance 1 of each grid point for the month March. All years are taken into account. The distance is measured by Eq. (6) and is unitless.

3 Results

3.1 MLD climatology

In winter, the MLD is deep only in a few regions: the Labrador Sea, the Irminger and Nordic Seas, along the coast of Antarctica and in the Deep Mixing Band (DMB) north of the ACC (Fig. 3). These regions are also the regions where the climatological state is not precise due to large interannual variations (Fig. 4). In the North Pacific Ocean, a maximum of MLD is found around 40N. This is the location of the transition between subtropical and subpolar water (Roden, 1970). The SO DMB is present north of the SAF, and other regions in the SO exhibit ML deeper than their neighbourhood. Such a slightly deeper pool is visible south of the Kerguelen Islands. A narrow band of MLD of about 200 m is present in the South Atlantic Ocean, north of the ACC.

Deep winter mixed layers are found just north of the SAF in the DMB, ranging from 200 to 400 m (Fig. **??**) (Dong et al., 2007; DuVivier et al., 2018). Some deep ML regions are contained within the PFZ, south of New Zealand around 175E, 57S, and in the south-east Pacific basin where some PFZ pools MLD can exceed 200 m. The mixed layer is overall shallower in the Atlantic basin in the SAF compared with the Indian and Pacific basins. From 180E to 210E in the SAZ. the ML are getting shallower, before deepening again and be deeper than 300 m before the Drake Passage. Within the PFZ, the mixed layer is

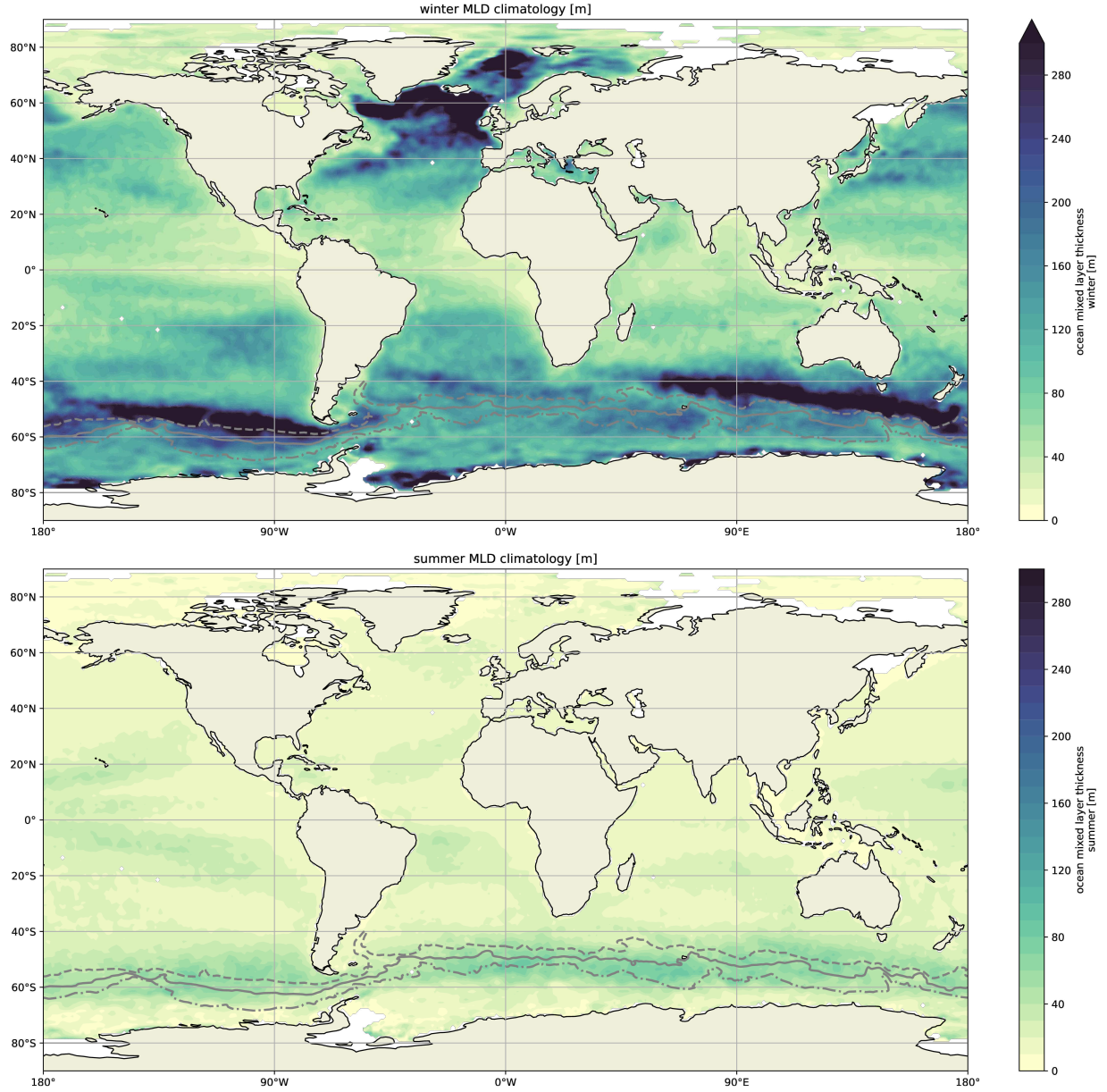

Figure 3. Climatologies of winter (deepest) and summer (shallowest) MLD. In the SO, the 3 gray lines represent from north to south the SAF, the PF, and the SACCF.

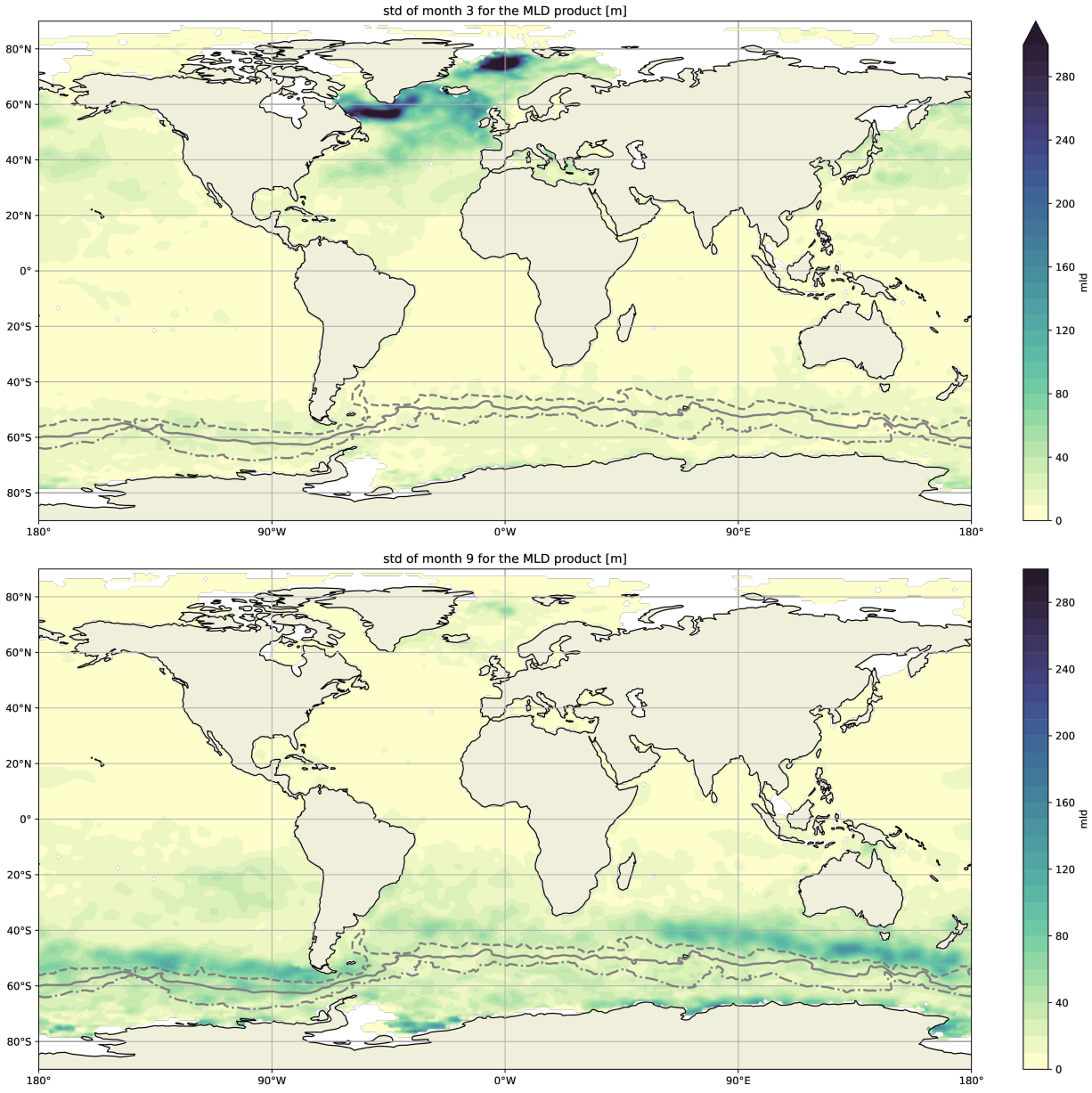

Figure 4. Standard deviation of monthly MLD for 2004 – 2021 period in March and September.

overall shallower, and is about 150 m deep. Apart from the major deep pool within the PFZ, some regions have slightly deeper MLs, e.g. south of the Kerguelen islands in the Indian Ocean, and north of the SAACF at about 90E.

In summer, the deepest ML worldwide are found within the ACC. The centre of the subtropical gyres have ML of about 20-30 m while being less than 10 m at their borders.

In summer, the ML is shallower everywhere. A major difference with the winter one, is that the ACC region presents the deepest ML, that are about 60 m deep, while the SAZ and SACCZ MLs are about 25 m deep.

In winter (March in the Northern Hemisphere, September in the Southern Hemisphere), the largest interannual variability occurs in regions of deep ML. In the North Atlantic, large interannual variability exists in the Labrador Sea, the Irminger Sea, and the Nordic Seas. However, scaling the standard deviation by the average presents a more uniform picture. The standard deviation is equal to about half of the mean MLD (Fig. B1 in Appendix). These regions of large interannual variability in the MLD are intrinsically misrepresented in a climatological state.

The DMB in the SO, with winter MLs on average deeper than 250 m, also exhibits interannual variability. The SO is overall poorly sampled due to its remote location, and part of the interannual variability that we see could arise from a sampling of water masses not representatives of the surrounding neighbourhood. To highlight the interannual variability, we compare our monthly product with time series of MLD from each profile at a distance 1 from the point (85.5E, 42.5S), located in the DMB north of the Kerguelen Plateau (Fig. 5). The median MLD in this circle is deeper than 500 m in the winter of 2014, and is 230 m in the winter of 2017. These 2 winters are the 2 extrema present in the time series, and both correspond to months with a fair amount of data. In months with little or no data (e.g. winter 2005 or summer 2008), the monthly product is computed using points located at a greater distance, which explains why in winter 2005 our product shows a maximum ML of 250 m while the median peaks at 450 m. The monthly climatology uses all points available for every year and thus smnoothes the extreme events. Plotting all the MLD measurements as function of day of year allows for a direct comparison with the climatology (Fig. 5). Our climatology is in good agreement with the individual points, with a maximum MLD of almost 400 m in August and September.

The Irminger Sea in the North Atlantic Ocean is one of the places where deep convection occurs in winter. Deep convection does not occur every year (Fig. 6). The winter 2014-2015 presents strong convection with MLD reaching 1000 m. Opposite, the MLD can be as shallow as 200 m in other winters. On a climatological state, the MLD follows a strong seasonal cycle, with winter MLD of about 400 m and summer MLD of 40 m (Fig. 6(d)).

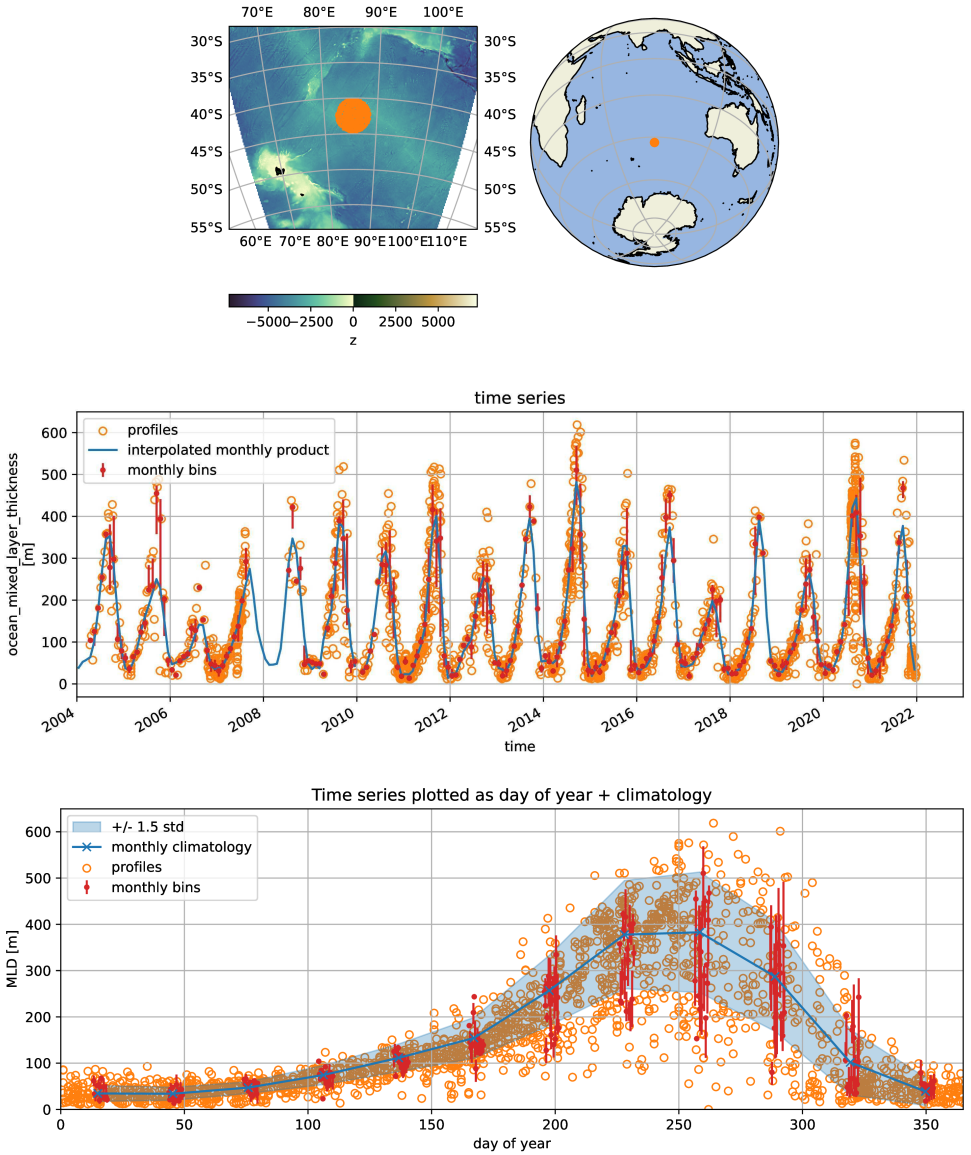

Figure 5. Time series of the MLD north of the Kerguelen Plateau, in the deep mixing band of the SO. The bathymetry and location of the profiles are shown in the upper row, the middle row presents the time series of the profiles MLD, the median and quartiles of monthly binned profiles, and our monthly interpolated product. The ticks and vertical lines are plotted the 1st of January of the years. The bottom row present our monthly climatology. All profiles in a distance 1 of the point (85.5E, 42.5S) are used.

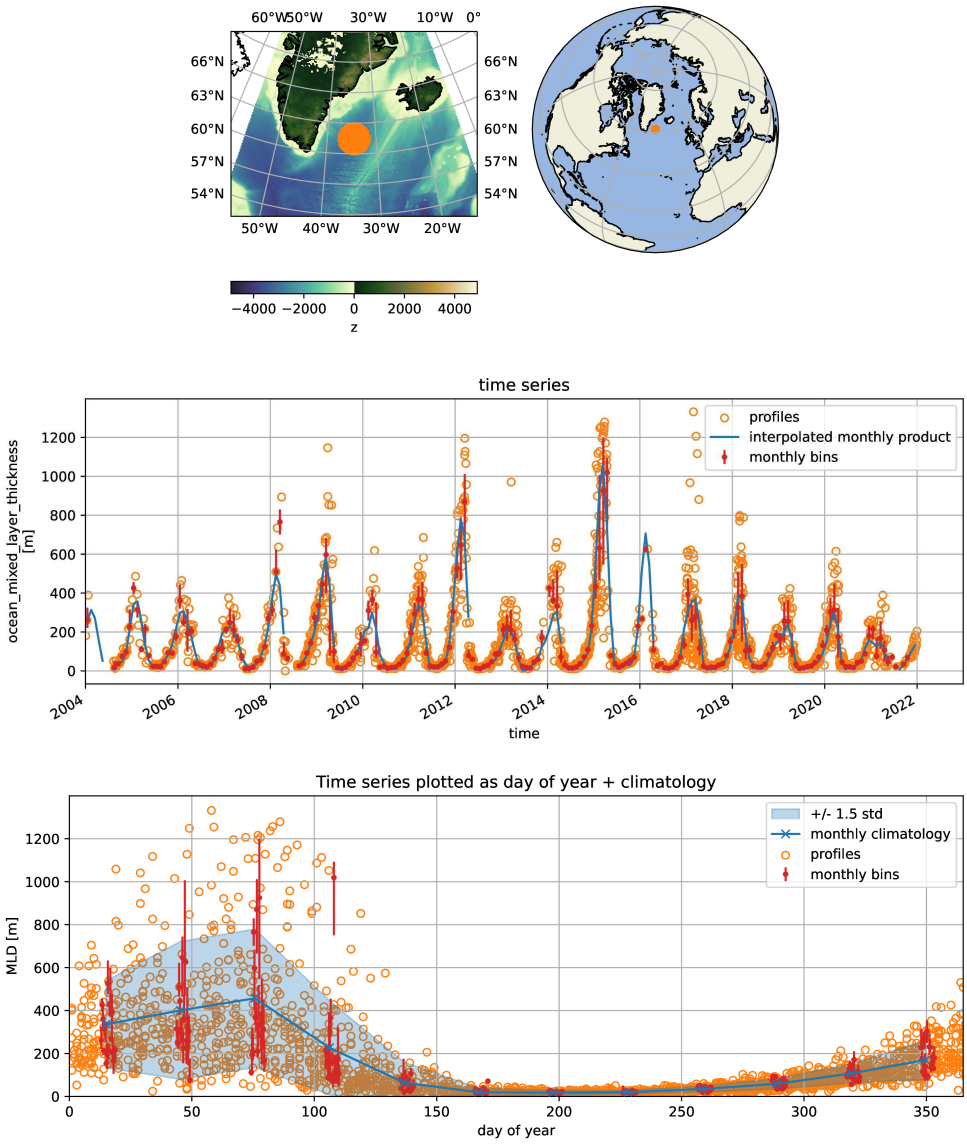

Figure 6. Time series of the MLD in the Irminger Sea. The bathymetry and location of the profiles are shown in the upper row, the middle row presents the time series of the profiles MLD, the median and quartiles of monthly binned profiles, and our monthly interpolated product. The ticks and vertical lines are plotted the 1st of January of the years. The bottom row present our monthly climatology. All profiles in a distance 1 of the point (325.5E, 61.5) are used.

3.2 SCI climatology

The SCI computed below the ML gives information on the stratifying agent. For $SCI > -1$ temperature decreases with depth and thus increases stratification, and for $SCI < 1$ salinity increases with depth, also increasing stratification. In winter, the majority of the ocean equatorward of the polar regions is classified as alpha ocean ($SCI > 1$) for mid-latitudes, and transition zone ($-1 < SCI < 1$) for tropical regions (Figs. 7 and 8). Evaporation is larger than precipitation in the subtropical gyres, so the surface salinity is larger than below the ML. Opposite, due to the large freshwater input from rain at the equator, the surface salinity is low and thus salinity stratifies in the tropical regions.

Beta ocean ($SCI < -1$) is found in the polar regions, south of 50-60S in the SO and north of 40-50N in the Pacific Ocean. In the North Atlantic Ocean, the alpha – beta separation does not follow a zonal pattern. Alpha ocean is present in the eastern part of the Atlantic Ocean north of 40N, and beta ocean is found in the western part. Using an idealised basin configuration of a numerical ocean model, Caneill et al. (2022) found a similar diagonal orientation of the transition zone. The southward advection by the subpolar gyre on the western part of the basin brings cold and fresh surface water, which creates the tongue of beta ocean along the coast of America.

The transition zone between subtropical (alpha) and polar (beta) water is generally narrow, except in the north-east Pacific Ocean, where the transition zone is 20 degrees of latitude wide (Figs. 7 and 8).

In the tropical ocean, the summer SCI is close to the winter SCI, where the MLD does not follow a strong annual cycle. The centre of the subtropical gyres are classified as alpha ocean in summer, but the SCI is smaller than in winter, indicating that salinity has a smaller destratifying effect in summer. The largest differences in SCI between summer and winter happen poleward of 40N or 40S. In summer, poleward of 40 degrees, the ocean is classified as transition zone. Indeed, the summer heat fluxes warm the upper layer of the ocean, thus temperature decreases with depth even in the polar regions. The SCI stays negative in the polar regions, indicating that despite relative warm water in the mixed layer, salinity remains the main stratifying agent. As pointed out by Roquet et al. (2022), the thermal expansion coefficient is small in cold water, reducing the impact of temperature on stratification. In summer, water in polar regions remains cold, so only very large gradients of temperature produce a similar stratification as the salinity gradient.

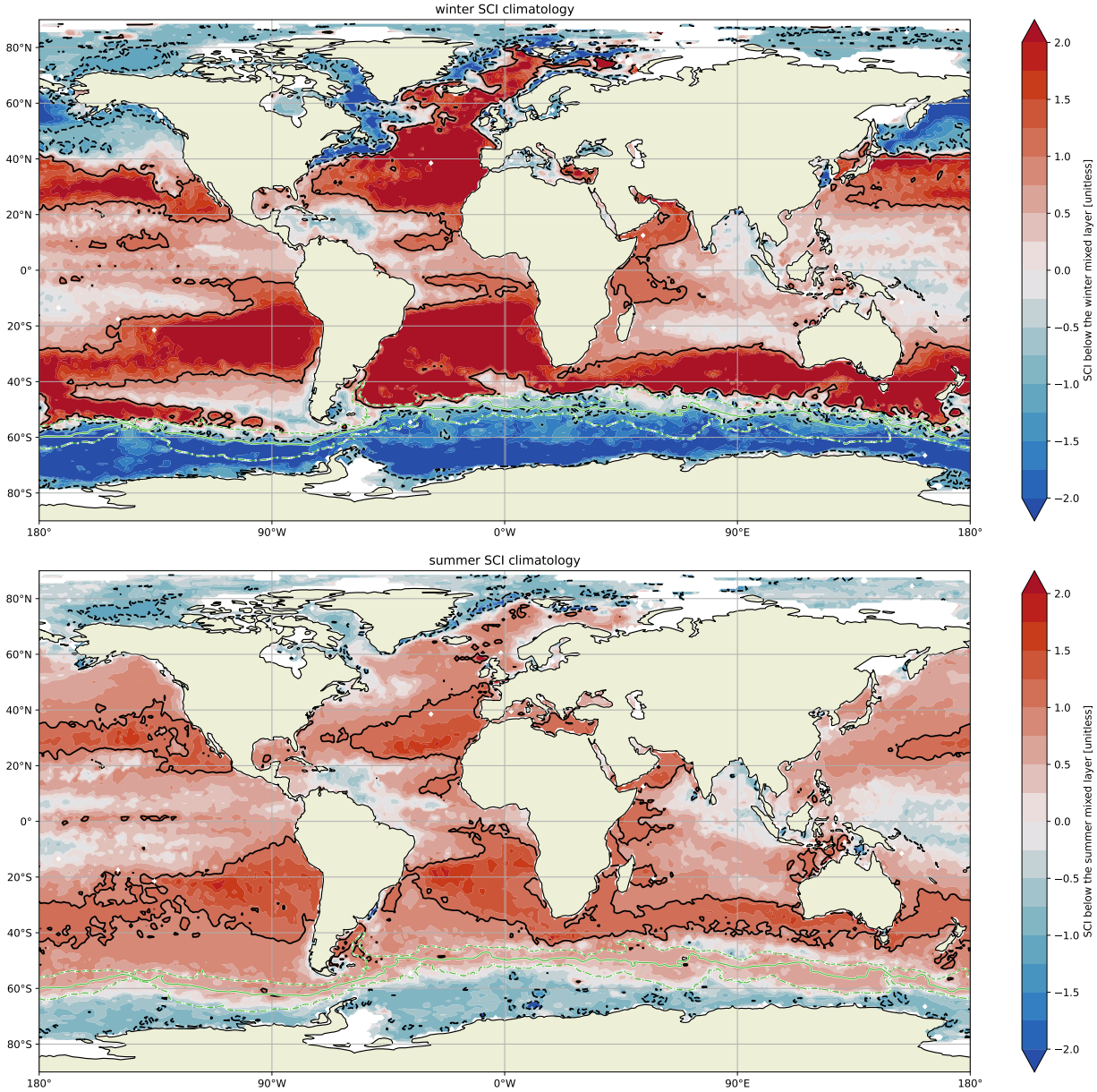

Figure 7. Climatologies of the SCI below the winter and summer ML. The white and green lines in the SO represent the 3 majors fronts of the ACC. The continuous black line is $SCI = 1$, the dashed black line is $SCI = -1$.

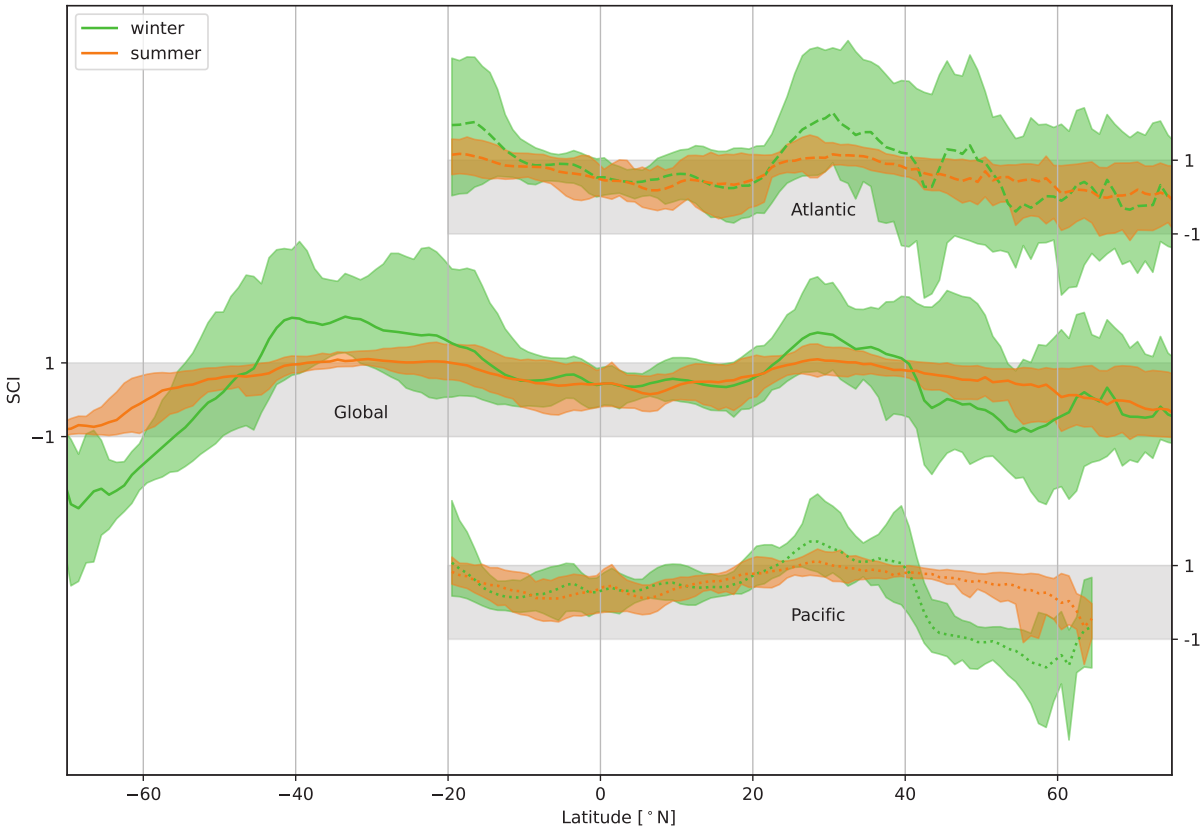

Figure 8. Zonal climatology of winter (green) and summer (orange) SCI below the mixed layer. The lines are the zonal means, and the shadings are the 10th and 90th percentiles. The middle lines are the global zonal means. The upper and lower lines, starting at 20°S, separate the Pacific basin, where the SCI is approximately zonally constant, from the Atlantic basin, where the SCI encounters large longitudinal variations. The Atlantic and Pacific zonal means have been shifted vertically for clarity, and they refer to their own axis on the right. The gray bands represent $-1 < SCI < 1$.

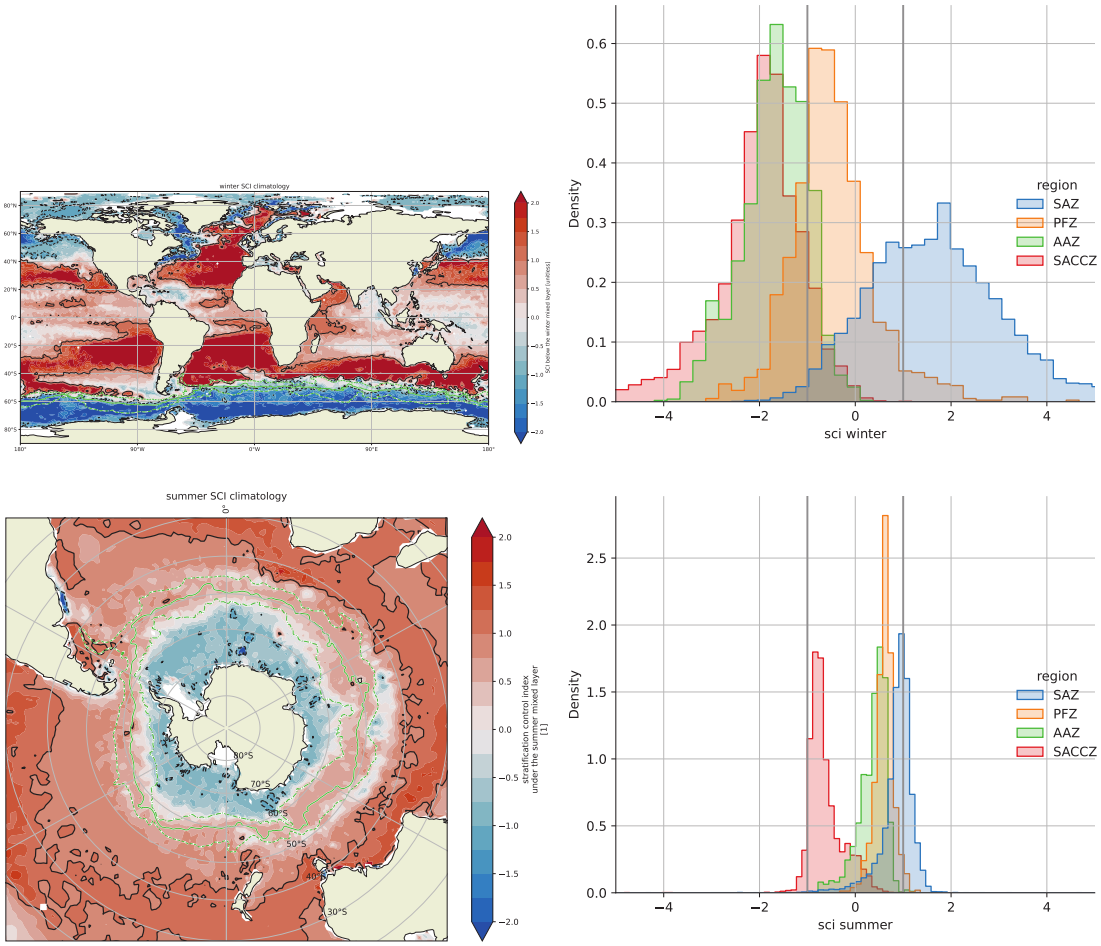

Figure 9. Climatology of the winter / summer SCI (left column), and histograms of the SCI per zone of the SO (right column).

In the Southern Ocean, there is an interesting connection between the SCI and the main frontal features. The position of winter $SCI = 1$ is located close to the SAF (Fig. 9). This is expected if we follow the Pollard et al. (2002) definition of the SAF as being the southern boundary of the region stratified by temperature and destabilized by salt. However, the $SCI = 1$ front is not a simple circumpolar closed line that monotonically turns around Antarctica. In the south-east Pacific, the $SCI = 1$ contour shifts westward and surrounds a transition zone tongue that seems to emanate from South-America. This layer is the surface expression of the Shallow Salinity Minimum Layer (SSMW), also called Eastern South Pacific Intermediate Water (Karstensen, 2004). The SSMW is a layer of minimum salinity, outcropping at about 45S in the south-east Pacific Ocean, and then subducting to about 200 m. It is a minimum salinity because of the combination of Ekman transport of freshwater

precipitation, and a slow geostrophic velocity within the ML, creating a freshwater flux larger than the area surrounding it when integrated temporally (Karstensen, 2004). The SSMW is fresher than the AAIW that lies below it, and hence the region where SSMW surfaces must have $\mathrm{SCI} > -1$.

Two main transition zones tongues interlocking into alpha region are found: one in the Atlantic basin centred around (0E, 40S), and the other south of New-Zealand (around 175E, 47S). A difference between these 2 tongues is the sign of the SCI: the Atlantic one has $\mathrm{SCI} > 0$, so salinity contributes less than temperature to stratification, while the New-Zealand's one has $\mathrm{SCI} < 0$, so is mainly stratified by salt. The New-Zealand transition tongue is also associated with a ML shallower than the surrounding ocean, while the Atlantic Ocean one is not marked by a change of MLD. The mean dynamic topography (MDT) gives information on the mean surface geostrophic flow. Close to New-Zealand, there is a meander going northward and then back southward. This meander could bring slightly colder and fresher water in this region. The MDT gradient is smaller in this region, implying smaller geostrophic flow, and hence more time for water to gain freshwater from the precipitation, creating a surface layer fresher than the layer below.

In summer, temperature is the most important component of stratification ($\mathrm{SCI} > 0$), except in SACCZ where $-1 < \mathrm{SCI} < 0$. A small region of the SAZ in the Indian Ocean also has $\mathrm{SCI} > 0$.

3.3 Seasonality of the SCI

Using a gridded ARGO product, DuVivier et al. (2018) computed the type of stratification below the ML in the DMB of the SO. They found that the stratification follows a strong seasonality, moving from transition zone in spring, to beta ocean in some area in June, and finally alpha ocean in winter. The MLD reaches this salinity maximum, when $SCI < 1$ in the time series around the (85.5E, 42.5S) point (Fig. 10). Above the salinity maximum, as salinity contributes to increasing stratification, $SCI < 1$. When the ML passes below it, salinity decreases with depth and $SCI > 1$. The ML reaches below the salinity maximum in July, when SCI becomes larger than 1. The climatological MLD in July is 250 m in this point (Fig. 5), so below 250 m salinity decreases with depth and the ocean is classified as alpha. In June, $SCI < -1$ which indicates a temperature inversion in the water column, at a depth of 150 m (Fig. 5).

South of the PF, salinity is the stratifying agent and temperature destratifies below the winter ML. Around the point (65.5E, 53.5S) located to the west of the Kerguelen Plateau, the SCI is below 1 all year long for the majority of the profiles (Fig. 11). This indicates that salinity always increases with depth below the ML. $SCI < -1$ in August, September, and October when the ML is the deepest and has eroded the summer stratification. The winter temperature of the ML is colder than the water below, the defining feature of beta ocean.

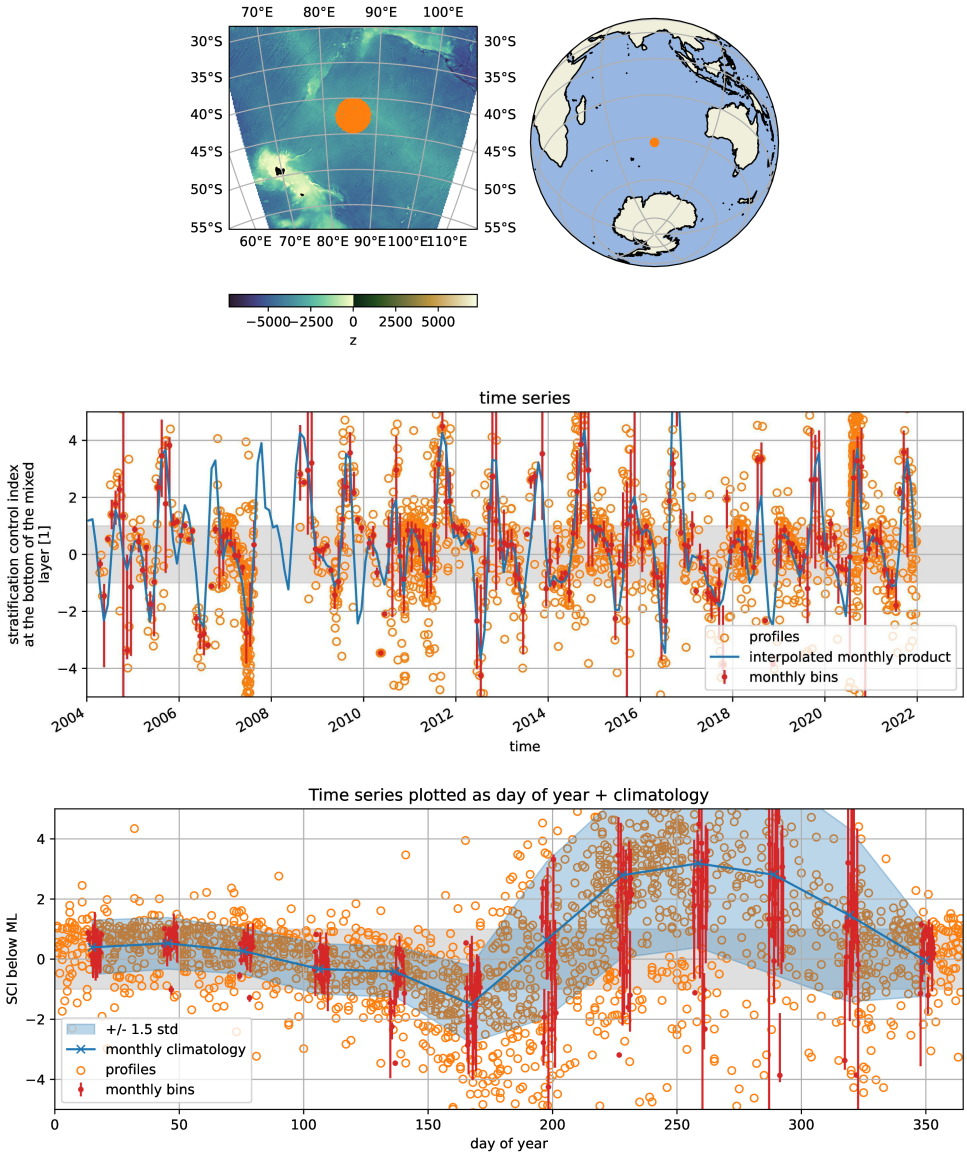

Figure 10. Time series of the SCI in the DMB, north of the Kerguelen Plateau. The location in alpha ocean in winter.

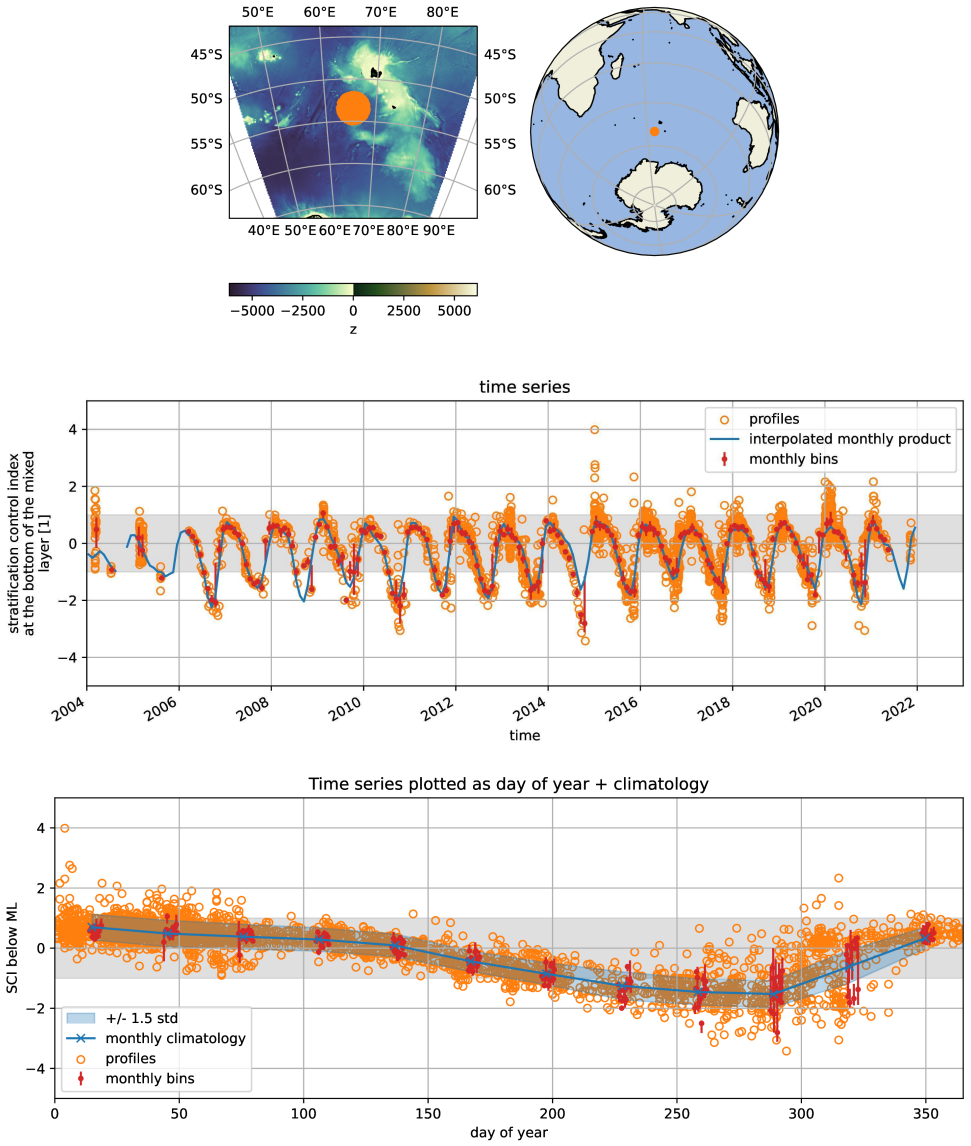

Figure 11. Time series of the SCI south-west of the Kerguelen Plateau. The location is in beta ocean in winter.

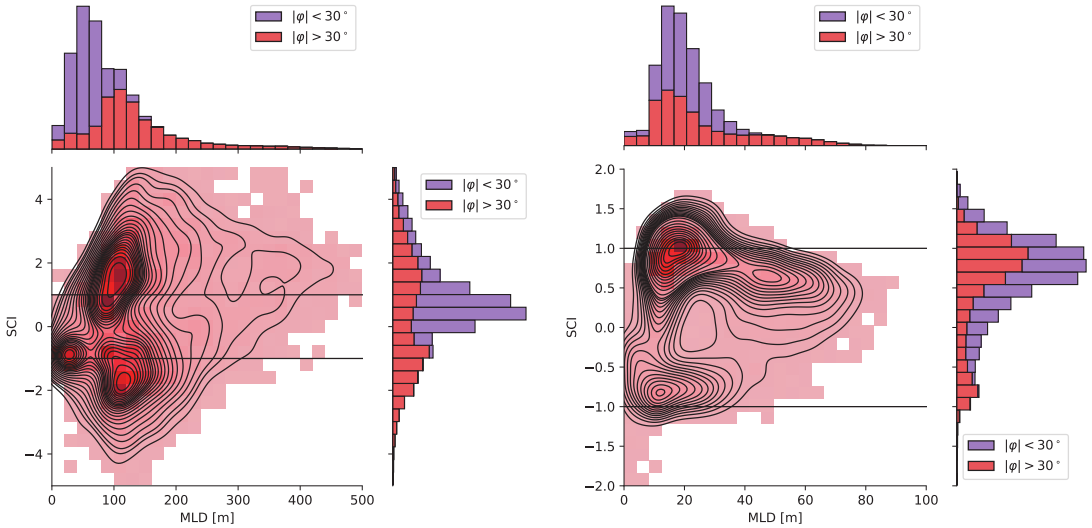

Figure 12. SCI versus MLD in winter (left) and summer (right). The centre figures represent a 2 dimensions histogram (colours), with a kernel density estimation (contour lines) superimposed. For the centre figures, only data with a latitude $|\varphi| > 30°$ are shown. The histograms on the sides are split into the tropical regions ($|\varphi| < 30°$) in purple, and the rest of the ocean ($|\varphi| > 30°$) in red. The upper histograms are for the MLD, and the histograms on the right are for the SCI. Data are taken from the $1°$ climatologies. Each data point is weighted by the area of its corresponding cell of the $1°$ grid.

3.4 On the link between the SCI and the MLD

Deep MLs occur more often in alpha oceans than in beta oceans or transition zones (Figs. 3 and 7). plotting the SCI versus the MLD (Fig. 12). MLs deeper than 250 m are mostly found in the alpha oceans (larger values of the two-dimensional histogram, Fig. 12). Deep MLs are also found in oceans classified as transition zones and are almost absent in beta oceans. Individual profiles in the beta oceans show deep MLs along the coast of Antarctica, but they represent a small area and are thus not seen in this figure.

Tropical regions (defined here with an absolute value of the latitude less than $30°$) are only plotted on the top and right histograms. They represent a large area with shallow MLs (less than 100 m) and are classified almost exclusively as transition zones.

For higher latitudes ($|\varphi| \geq 30°$), the ML distribution exhibits a peak at 120 m. The SCI distribution poleward of $30°$ is bimodal, centred around ± 1.5. The oceans thus encounter partial compensation between temperature and salinity more often than when temperature and salinity both stabilise. Poleward of $30°$, the shallowest MLs are found in regions where salinity dominates the stratification ($SCI < 0$), either in transition zones or beta oceans. Regions that encounter large density compensation (large $|SCI|$) do not present shallow ML.

In summer, MLs are shallow and the SCI is bimodal, both in tropical oceans and at higher latitudes. The majority of the ocean has a SCI around 1, representative of the summer thermocline. The majority of the oceans is located in a peak of $MLD = 20\,\mathrm{m}$ and $SCI = 1$.

4 Discussion and conclusions

In this work we computed monthly climatologies and monthly products for the years 2004 – 2021, for the mixed layer depth, and stratification control index below the ML, based on the EN4.2.2 profiles. After computing the MLD and SCI on individual profiles, we used a radial basis function interpolation to create the monthly products and climatologies. Despite its simple structure in two dimension, the SCI below the winter ML provide a comprehensive overview of the large scale oceanic circulation and main feature, as well as the regional discrepancies.

Region of deep and intermediate water formation are visible on the climatological state of the winter MLD (Fig. 3). In the Northern Hemisphere, MLs are deeper in the Atlantic Ocean than in the Pacific Ocean, the signature of the absence of deep water formation in the North Pacific. In the Atlantic Ocean, ML are deepest in the Labrador, Greenland, Island, and Norwegian Seas. The signature of the Gulf Stream and the Kuroshio Current can be followed by looking at the local maxima of MLD around 40N. In the SO, ML are deepest in the deep mixing band located north of the ACC, and close to the coast of Antarctica where deep water is formed in winter in coastal polynyas.

The regions of deepest MLD also present large interannual variability (Fig. 4). On average, the standard deviation of the MLD along years, for every month, is half of the climatological value. Part of this variation is certainly representative of the intrinsic interannual variability of the ocean, part could also come from spatial variability and unrepresentative sampling.

Time series of profiles from the DMB and Irminger Sea, two regions with deep ML in winter, both present large variability between years, and between profiles at the same date. In the Irminger Sea, convection occurs occasionally and was weak in the early 2000s before being more active in years 2015 – 2018 (Sterl and De Jong, 2022). Whether the climatological state should represent the years with or without convection may depend on the research question. In energetic regions, the mean state differs from snapshots states at meso- and submeso-scales. With a limited amount of observations, errors associated with individual profiles compared to mean state can be large. Future work needs to be done to assess the minimum number of profiles necessary to compute a representative mean state of a region.

As noted by Carmack (2007), polar regions are stratified by salinity, and subtropical to subpolar regions are stratified by temperature. The winter climatology of the SCI emphasizes this separation (Fig. 7). Alpha ocean reaches far north in the eastern side of the Atlantic Ocean, where MLD is deep in winter. In the Labrador Sea where MLD is also deep in winter, the ocean is classified as beta or transition zone. In the SO, the DMB is located in alpha ocean, except in the eastern Pacific Ocean where it is transition zone. Deep convection site close to Antarctica are located in beta ocean. Freshwater input at the surface of the ocean helps to build the polar halocline. Fluxes alone do not explain the alpha – beta distinction, cold water density variation is almost not sensitive to variation in temperature, so the strong winter heat loss is not able to destabilise the water column and the temperature inversion is maintained (Caneill et al., 2022; Roquet et al., 2022).

The main fronts of the ACC can be linked to the type of stratification (Pollard et al., 2002; Pauthenet et al., 2017). While in the Atlantic and Indian Oceans, the SAF and PF are closely related to the position of the winter $SCI = \pm 1$, in the eastern Pacific Ocean the SAF is located in the transition zone. The vision of dynamical fronts as circumpolar features is not representative of the reality, as jets are usually transient and a contour of SSH associated with a large SSH gradient at a time can correspond to a flat area somewhere else (Chapman et al., 2020). The meridional change of stratification is however a circumpolar feature, but cannot be directly linked to dynamical fronts.

MLD is commonly used to validate or compare climate models (e.g. Treguier et al., 2023). The SCI is a quantity easy to compute, but that still provides at a glance a global overview of the ocean state. Future work could be conducted to compare the SCI in ocean models with our newly produced climatology.

In conclusion, we computed new climatologies of MLD and SCI. The maps of the winter SCI provide an overview of the global ocean stratification. Polar regions appear to be the only places stratified by only salinity (beta ocean), as remarked by Carmack (2007) in precise locations. In the North Atlantic, the beta ocean goes down along the coast of America down to 40N, while the alpha ocean goes up to 80N on the eastern side of the Nordic Seas. In contrast, the transition between alpha and beta oceans is fairly zonal and centred around 40N in the North Pacific Ocean. The different zones of the SO defined by Pollard et al. (2002) stand out in the SCI maps. This study provides a global description of the ocean state.

Code and data availability. The code and data will be available uppon acceptation of the manuscript.

Appendix A: Comparison of raw and smoothed temperature profile

Appendix B: MLD mean and standard deviation

Author contributions. TEXT

Competing interests. TEXT

Disclaimer. TEXT

Acknowledgements. TEXT

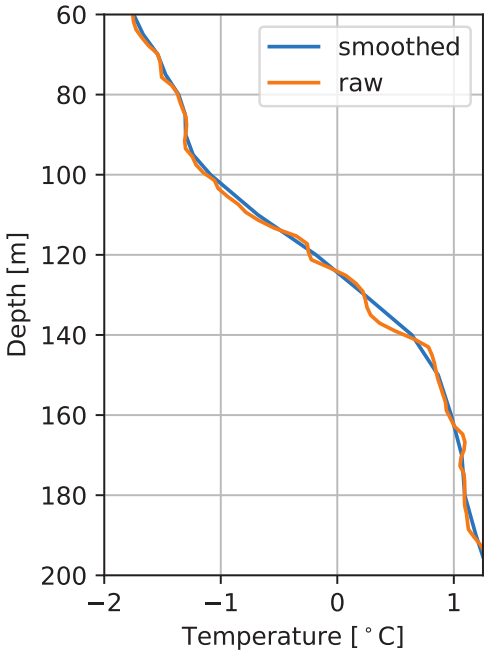

Figure A1. Comparison of raw and smoothed temperature profile.

References

Caneill, R., Roquet, F., Madec, G., and Nycander, J.: The Polar Transition from Alpha to Beta Regions Set by a Surface Buoyancy Flux Inversion, Journal of Physical Oceanography, 52, 1887–1902, https://doi.org/10.1175/JPO-D-21-0295.1, 2022.

Caneill, R., Roquet, F., and Nycander, J.: Southern Ocean deep mixing band emerges from a competition between winter buoyancy loss and upper stratification strength, EGUsphere, 2023, 1–29, https://doi.org/10.5194/egusphere-2023-2404, 2023.

Carmack, E. C.: The alpha/beta ocean distinction: A perspective on freshwater fluxes, convection, nutrients and productivity in high-latitude seas, Deep Sea Research Part II: Topical Studies in Oceanography, 54, 2578–2598, https://doi.org/10.1016/j.dsr2.2007.08.018, 2007.

CCHDO Hydrographic Data Office: CCHDO Hydrographic Data Archive, Version 2023-11-21, https://doi.org/10.6075/J0CCHAM8, in CCHDO Hydrographic Data Archive, 2023.

Chapman, C. C., Lea, M.-A., Meyer, A., Sallée, J.-B., and Hindell, M.: Defining Southern Ocean fronts and their influence on biological and physical processes in a changing climate, Nature Climate Change, 10, 209–219, https://doi.org/10.1038/s41558-020-0705-4, 2020.

Clément, L., McDonagh, E. L., Marzocchi, A., and Nurser, A. J. G.: Signature of Ocean Warming at the Mixed Layer Base, Geophysical Research Letters, 47, https://doi.org/10.1029/2019GL086269, 2020.

Curry, J. A., Schramm, J. L., and Ebert, E. E.: Sea Ice-Albedo Climate Feedback Mechanism, Journal of Climate, 8, 240–247, https://doi.org/10.1175/1520-0442(1995)008<0240:SIACFM>2.0.CO;2, 1995.

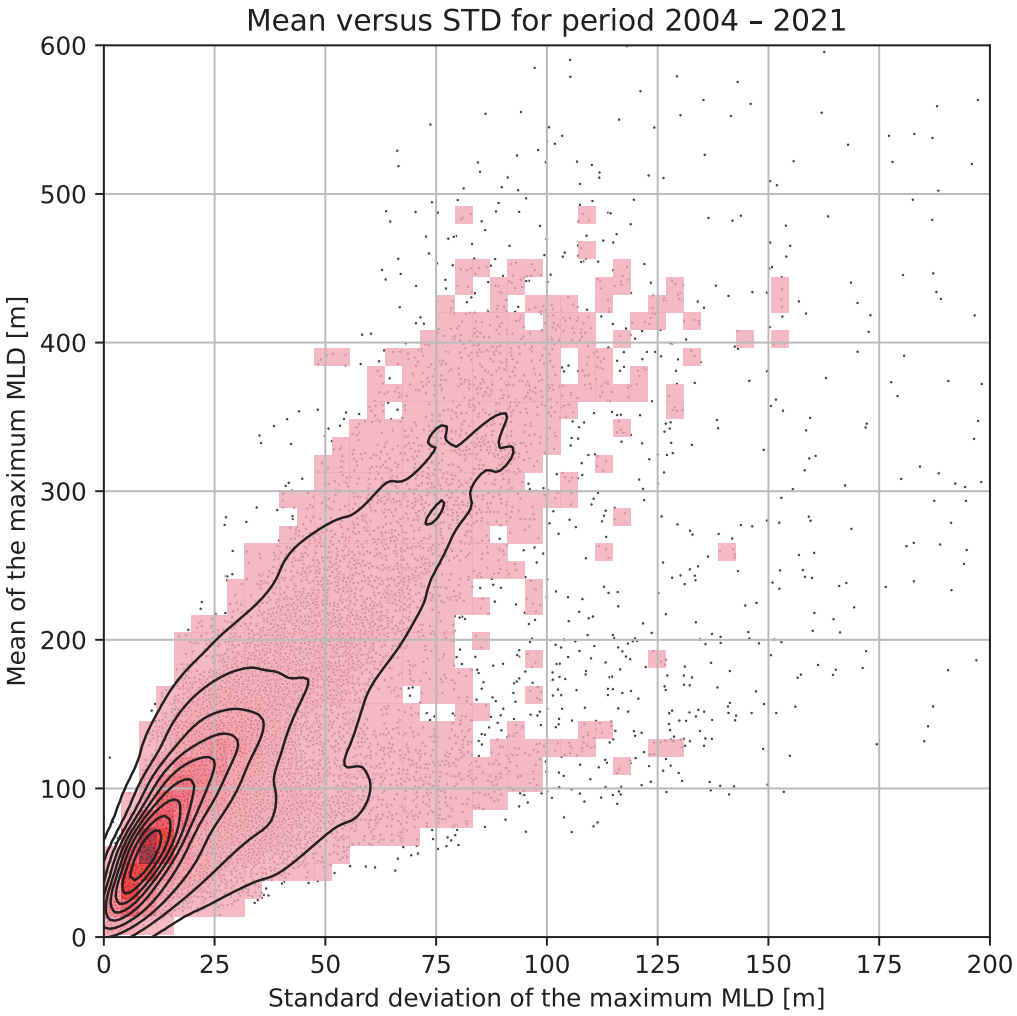

Figure B1. Mean of the MLD versus the standard deviation (for winter). The means are taken along years of the monthly product.

de Boyer Montégut, C.: Mixed layer depth over the global ocean: An examination of profile data and a profile-based climatology, Journal of Geophysical Research, 109, C12 003, https://doi.org/10.1029/2004JC002378, 2004.

de Boyer Montégut, C.: Mixed layer depth climatology computed with a density threshold criterion of 0.03kg/m3 from 10 m depth value, https://doi.org/10.17882/91774, 2023.

Dong, S., Gille, S. T., and Sprintall, J.: An Assessment of the Southern Ocean Mixed Layer Heat Budget, Journal of Climate, 20, 4425–4442, https://doi.org/10.1175/JCLI4259.1, 2007.

DuVivier, A. K., Large, W. G., and Small, R. J.: Argo Observations of the Deep Mixing Band in the Southern Ocean: A Salinity Modeling Challenge, Journal of Geophysical Research: Oceans, 123, 7599–7617, https://doi.org/10.1029/2018JC014275, 2018.

Emery, W. J.: Antarctic Polar Frontal Zone from Australia to the Drake Passage, Journal of Physical Oceanography, 7, 811–822, https://doi.org/10.1175/1520-0485(1977)007<0811:APFZFA>2.0.CO;2, 1977.

Good, S. A., Martin, M. J., and Rayner, N. A.: EN4: Quality controlled ocean temperature and salinity profiles and monthly objective analyses with uncertainty estimates: THE EN4 DATA SET, Journal of Geophysical Research: Oceans, 118, 6704–6716, https://doi.org/10.1002/2013JC009067, 2013.

Gouretski, V. and Cheng, L.: Correction for systematic errors in the global dataset of temperature profiles from mechanical bathythermographs, Journal of Atmospheric and Oceanic Technology, 37, 841–855, 2020.

Gouretski, V. and Reseghetti, F.: On depth and temperature biases in bathythermograph data: Development of a new correction scheme based on analysis of a global ocean database, Deep Sea Research Part I: Oceanographic Research Papers, 57, 812–833, 2010.

Graham, R. M., de Boer, A. M., Heywood, K. J., Chapman, M. R., and Stevens, D. P.: Southern Ocean fronts: Controlled by wind or topography?: SOUTHERN OCEAN FRONTS IN HIGEM, Journal of Geophysical Research: Oceans, 117, n/a–n/a, https://doi.org/10.1029/2012JC007887, 2012.

Helber, R. W., Kara, A. B., Richman, J. G., Carnes, M. R., Barron, C. N., Hurlburt, H. E., and Boyer, T.: Temperature versus salinity gradients below the ocean mixed layer: TEMPERATURE VERSUS SALINITY GRADIENTS, Journal of Geophysical Research: Oceans, 117, n/a–n/a, https://doi.org/10.1029/2011JC007382, 2012.

Johnson, G. C., Kunze, E., McTaggart, K. E., and Moore, D. W.: Temporal and Spatial Structure of the Equatorial Deep Jets in the Pacific Ocean*, Journal of Physical Oceanography, 32, 3396–3407, https://doi.org/10.1175/1520-0485(2002)032<3396:TASSOT>2.0.CO;2, 2002.

Johnson, G. C., Schmidtko, S., and Lyman, J. M.: Relative contributions of temperature and salinity to seasonal mixed layer density changes and horizontal density gradients: GLOBAL SEASONAL MIXED LAYER T AND S ROLES, Journal of Geophysical Research: Oceans, 117, n/a–n/a, https://doi.org/10.1029/2011JC007651, 2012.

Karstensen, J.: Formation of the South Pacific Shallow Salinity Minimum: A Southern Ocean Pathway to the Tropical Pacific, Journal of Physical Oceanography, 34, 2398–2412, https://doi.org/10.1175/JPO2634.1, 2004.

Martin, T., Park, W., and Latif, M.: Multi-centennial variability controlled by Southern Ocean convection in the Kiel Climate Model, Climate Dynamics, 40, 2005–2022, https://doi.org/10.1007/s00382-012-1586-7, 2013.

Martinson, D. G., Killworth, P. D., and Gordon, A. L.: A Convective Model for the Weddell Polynya, Journal of Physical Oceanography, 11, 466–488, https://doi.org/10.1175/1520-0485(1981)011<0466:ACMFTW>2.0.CO;2, 1981.

Pauthenet, E., Roquet, F., Madec, G., and Nerini, D.: A Linear Decomposition of the Southern Ocean Thermohaline Structure, Journal of Physical Oceanography, 47, 29–47, https://doi.org/10.1175/JPO-D-16-0083.1, 2017.

Pellichero, V., Sallée, J.-B., Schmidtko, S., Roquet, F., and Charrassin, J.-B.: The ocean mixed layer under Southern Ocean sea-ice: Seasonal cycle and forcing: OCEAN MIXED LAYER UNDER SOUTHERN SEA-ICE, Journal of Geophysical Research: Oceans, 122, 1608–1633, https://doi.org/10.1002/2016JC011970, 2017.

Perovich, D. K. and Polashenski, C.: Albedo evolution of seasonal Arctic sea ice, Geophysical Research Letters, 39, 2012GL051 432, https://doi.org/10.1029/2012GL051432, 2012.

Pierce, D. W., Barnett, T. P., and Mikolajewicz, U.: Competing Roles of Heat and Freshwater Flux in Forcing Thermohaline Oscillations, Journal of Physical Oceanography, 25, 2046–2064, https://doi.org/10.1175/1520-0485(1995)025<2046:CROHAF>2.0.CO;2, 1995.

Pollard, R., Lucas, M., and Read, J.: Physical controls on biogeochemical zonation in the Southern Ocean, Deep Sea Research Part II: Topical Studies in Oceanography, 49, 3289–3305, https://doi.org/10.1016/S0967-0645(02)00084-X, 2002.

Polyakov, I. V., Pnyushkov, A. V., Rember, R., Padman, L., Carmack, E. C., and Jackson, J. M.: Winter Convection Transports Atlantic Water Heat to the Surface Layer in the Eastern Arctic Ocean*, Journal of Physical Oceanography, 43, 2142–2155, https://doi.org/10.1175/JPO-D-12-0169.1, 2013.

Roden, G. I.: Aspects of the Mid-Pacific Transition Zone, Journal of Geophysical Research, 75, 1097–1109, https://doi.org/10.1029/JC075i006p01097, 1970.

Roquet, F., Ferreira, D., Caneill, R., Schlesinger, D., and Madec, G.: Unique thermal expansion properties of water key to the formation of sea ice on Earth, Science Advances, 8, https://doi.org/10.1126/sciadv.abq0793, 2022.

Sallée, J.-B., Speer, K., Rintoul, S., and Wijffels, S.: Southern Ocean Thermocline Ventilation, Journal of Physical Oceanography, 40, 509–529, https://doi.org/10.1175/2009JPO4291.1, 2010.

Sallée, J.-B., Pellichero, V., Akhoudas, C., Pauthenet, E., Vignes, L., Schmidtko, S., Garabato, A. N., Sutherland, P., and Kuusela, M.: Summertime increases in upper-ocean stratification and mixed-layer depth, Nature, 591, 592–598, https://doi.org/10.1038/s41586-021-03303-x, 2021.

Schmidtko, S., Johnson, G. C., and Lyman, J. M.: MIMOC: A global monthly isopycnal upper-ocean climatology with mixed layers: MIMOC, Journal of Geophysical Research: Oceans, 118, 1658–1672, https://doi.org/10.1002/jgrc.20122, 2013.

Schmitt, R. W.: Double Diffusion in Oceanography, Annual Review of Fluid Mechanics, 26, 255–285, https://doi.org/10.1146/annurev.fl.26.010194.001351, 1994.

Sokolov, S. and Rintoul, S. R.: Circumpolar structure and distribution of the Antarctic Circumpolar Current fronts: 1. Mean circumpolar paths, Journal of Geophysical Research, 114, C11 018, https://doi.org/10.1029/2008JC005108, 2009.

Sterl, M. F. and De Jong, M. F.: Restratification Structure and Processes in the Irminger Sea, Journal of Geophysical Research: Oceans, 127, e2022JC019 126, https://doi.org/10.1029/2022JC019126, 2022.

Stern, M. E.: The "Salt-Fountain" and Thermohaline Convection, Tellus, 12, 172–175, https://doi.org/10.3402/tellusa.v12i2.9378, 1960.

Stewart, K. D. and Haine, T. W. N.: Thermobaricity in the Transition Zones between Alpha and Beta Oceans, Journal of Physical Oceanography, 46, 1805–1821, https://doi.org/10.1175/JPO-D-16-0017.1, 2016.

Thomas, S. D. A., Jones, D. C., Faul, A., Mackie, E., and Pauthenet, E.: Defining Southern Ocean fronts using unsupervised classification, Ocean Science, 17, 1545–1562, https://doi.org/10.5194/os-17-1545-2021, 2021.

Trathan, P. N., Brandon, M. A., and Murphy, E. J.: Characterization of the Antarctic Polar Frontal Zone to the north of South Georgia in summer 1994, Journal of Geophysical Research: Oceans, 102, 10 483–10 497, https://doi.org/10.1029/97JC00381, 1997.

Treguier, A. M., de Boyer Montégut, C., Bozec, A., Chassignet, E. P., Fox-Kemper, B., McC. Hogg, A., Iovino, D., Kiss, A. E., Le Sommer, J., Li, Y., Lin, P., Lique, C., Liu, H., Serazin, G., Sidorenko, D., Wang, Q., Xu, X., and Yeager, S.: The mixed-layer depth in the

Ocean Model Intercomparison Project (OMIP): impact of resolving mesoscale eddies, Geoscientific Model Development, 16, 3849–3872, https://doi.org/10.5194/gmd-16-3849-2023, 2023.

You, Y.: A global ocean climatological atlas of the Turner angle: implications for double-diffusion and water-mass structure, Deep Sea Research Part I: Oceanographic Research Papers, 49, 2075–2093, https://doi.org/10.1016/S0967-0637(02)00099-7, 2002.

Paper IV

CLIMATOLOGY

Unique thermal expansion properties of water key to the formation of sea ice on Earth

Fabien Roquet[1]*, David Ferreira[2], Romain Caneill[1], Daniel Schlesinger[3]†, Gurvan Madec[4]

The formation of sea ice in polar regions is possible because a salinity gradient or halocline keeps the water column stable despite intense cooling. Here, we demonstrate that a unique water property is central to the maintenance of the polar halocline, namely, that the thermal expansion coefficient (TEC) of seawater increases by one order of magnitude between polar and tropical regions. Using a fully coupled climate model, it is shown that, even with excess precipitations, sea ice would not form at all if the near-freezing temperature TEC was not well below its ocean average value. The leading order dependence of the TEC on temperature is essential to the coexistence of the mid/low-latitude thermally stratified and the high-latitude sea ice–covered oceans that characterize our planet. A key implication is that nonlinearities of water properties have a first-order impact on the global climate of Earth and possibly exoplanets.

INTRODUCTION

Most of what makes the water molecule H_2O so unique can be traced back to its structure with the V-shaped arrangement of hydrogen atoms around the oxygen atom and its electronic structure with two lone pairs giving rise to a strong polarity (*1*). Because of its polarity, a water molecule can form hydrogen bonds with neighboring molecules, adding cohesion within the liquid and making the heat capacity, the latent heat of fusion and of evaporation, or the surface tension of liquid water all exceptionally large. These properties explain why water is so central to the climate system on Earth (*2*).

As the hydrogen and oxygen atoms form a 104.5° angle, almost equal to the 109.5° angle found in a regular tetrahedron (*3*), water molecules can form open crystal structures where each water molecule is at the center of a tetrahedron formed by the neighboring molecules. This is precisely why liquid water is denser than ice near the freezing point.

This is also the reason why the thermal expansion coefficient (TEC) of seawater drops considerably near the freezing point. Here, we will show that the strong dependence of the TEC on temperature has a profound and generally overlooked influence on the formation of sea ice on Earth, on the general organization of the upper ocean stratification, and on vertical exchanges between the surface and deep layers of the ocean.

The TEC of liquid water

The TEC measures the relative variation of density caused by a unit change of temperature

$$\alpha = -\frac{1}{\rho}\frac{\partial \rho}{\partial \Theta}\bigg|_{S,p} \quad (1)$$

where ρ is the mass density, Θ is the conservative temperature, S is the absolute salinity, and p is the pressure. Note that the exact definition of TEC varies depending on the standard used to define the temperature or salinity properties. Here, we use the thermodynamic equation of seawater TEOS-10 standard (*4*); however, we stress that our results are independent of the standard used.

In a simple liquid (e.g., liquid argon or nitrogen) (*5*, *6*), the TEC is most commonly positive, i.e., its density monotonously decreases when temperature increases. However, pure liquid water has the rare property that, at standard pressure, it does not reach the maximum density at the freezing point but at a temperature of 4°C. This means that the TEC for liquid water is negative at temperatures below 4°C.

The implications of this negative TEC are well known for the stratification of the so-called dimictic lakes (*7*, *8*). In these lakes, the bottom is filled with the densest 4°C water year long and isolated from surface waters both in winter and in summer. Note, however, that very deep lakes may have a bottom temperature substantially lower than 4°C as the temperature of maximum density decreases with pressure, effectively limiting the depth of full overturn (*9*). The 4°C maximum density property enables the formation of ice at the surface, as only a surface layer of limited depth needs to be cooled down to drive freezing. It is much harder to freeze entirely the lake over wintertime, thus providing a safe habitat for species living in the lake.

The situation is fundamentally different for the oceans, because salt substantially modifies the physical properties of water. Dissolving salt in water increases the TEC of the solution at the same time as it lowers its freezing point (Fig. 1B). The structure of the water solvent in NaCl aqueous solutions is known to be modified in a similar way to that of water under enhanced pressure (*10*). Increasing salinity by 1 g kg^{-1} induces a similar rise in the TEC value as a 100-dbar pressure increase (Fig. 1A). Negative TEC values are found only for salinities below 25 g kg^{-1}, making it extremely rare to encounter except near cold estuaries. Thus, the mechanism promoting the formation of ice in freshwater lakes does not operate in the ocean. However, sea ice is forming on large areas of the polar ocean, and this study explores whether this could be related to patterns of TEC variations in the upper ocean.

Stratification control in the ocean

Polar regions are generally associated with excess precipitation over evaporation, freshening the upper ocean and forming a permanent halocline (*11*, *12*). In turn, the permanent halocline limits thermally

[1]Department of Marine Sciences, University of Gothenburg, 40530 Gothenburg, Sweden. [2]Department of Meteorology, University of Reading, Reading RG66ET, UK. [3]Department of Environmental Science and Bolin Centre for Climate Research, Stockholm University, 106 91 Stockholm, Sweden. [4]LOCEAN, Sorbonne Universités, UPMC, Paris, France.
*Corresponding author. Email: fabien.roquet@gu.se
†Present address: Environment and Health Administration, SLB-analys, Stockholm 104 20, Sweden.

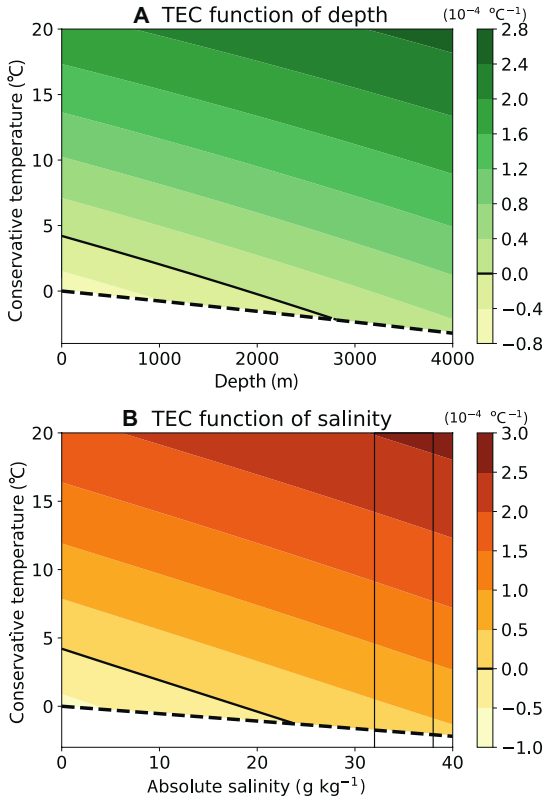

Fig. 1. Variation of the TEC with respect to temperature, salinity, and depth. (**A**) TEC function of temperature and depth for fresh water, i.e., at salinity $S = 0$ g kg^{-1}. Here, depth is taken proportional to pressure (1 m ≃ 1 dbar). (**B**) Variation of the TEC with respect to temperature and salinity at atmospheric pressure $p = 0$ dbar. The typical salinity range of seawater is indicated with light solid contours. The TEC decreases quasi-linearly with respect to temperature, pressure, and salinity. In both panels, the dashed line indicates the freezing point, while the solid line indicates where the TEC changes sign.

driven deep convection, thus promoting the formation of sea ice in polar regions. It has long been noted that sea ice formation occurs only in the presence of a halocline (*13*). It would seem natural to assume that the freshwater forcing alone explains why polar regions are stratified in salinity. However, the argument is somewhat incomplete and does not explain why the intense cooling is generally not able to wipe out the polar halocline.

The stratification is commonly quantified by the squared buoyancy frequency, $N^2 = -g\rho_z^{\Theta}/\rho$, where ρ^{Θ} is the potential density, g is the gravity acceleration, and the subscript z indicates the vertical derivative (*14*). The buoyancy frequency can be decomposed into the sum of temperature and salinity contributions

$$N^2 = N_{\Theta}^2 + N_S^2 \quad (2)$$

with $N_{\Theta}^2 = g\alpha\Theta_z$ and $N_S^2 = -g\beta S_z$. Here, $\beta = (\partial\rho/\partial S)\,|_{\Theta,p}/\rho$ defines the saline contraction coefficient, analogous to the TEC in Eq. 1 for salt.

Carmack (*13*) proposed to distinguish between the alpha ocean, where the upper ocean thermal stratification is stable ($N_{\Theta}^2 > 0$), and the beta ocean, where the haline stratification is stable ($N_S^2 > 0$). To avoid the ambiguity of this definition in regions where both thermal and haline stratifications are stable, we will define three regimes using the stratification control index (SCI) defined as $\mathrm{SCI} = (N_{\Theta}^2 - N_S^2)/N^2$: The alpha ocean is found where SCI > 1 immediately below the mixed layer, the beta ocean is where SCI < −1, while regions where −1 < SCI < 1 will be referred to as the transition zone. Alpha regions are associated with a thermocline, while beta regions feature a halocline. In the transition zone, both temperature and salinity contribute positively to the stratification.

Note that most of the ocean is either alpha or beta with a sharp transition, meaning that temperature and salinity stratifications are most often compensating each other (Fig. 2). For this reason, a large fraction of the global ocean is subject to double diffusion, either salt fingering (alpha) or diffusive (beta) (*15*), contributing to interior mixing. Figure 2C shows that the transition between the two regimes is generally found in the mid-latitudes, at a mean latitude of 50°N in both the Northern and Southern Hemispheres, although it can reach up to 80°N in the Nordic Seas. Note that an alternative definition for the separation between the three regimes has also been proposed on the basis of a statistical criterion (*16*).

The large TEC variations at the surface are dominated by changes in sea surface temperature (Fig. 2A). In the global ocean, the TEC varies from 0.3×10^{-4} °C^{-1} near the freezing temperature (≤0 ° C) to 3.5×10^{-4} °C^{-1} in tropical waters. In contrast, the saline contraction coefficient β varies by less than 10% in the ocean and can be considered constant to a good approximation. The temperature dependence of the TEC also induces the cabbeling or "densification upon mixing" effect in frontal regions (*17*, *18*). Note, however, that cabbeling is not a central focus of this work, as will be discussed more thoroughly in the last section.

A comparison between the global distributions of the TEC and SCI in the upper ocean indicates that beta regions correspond to relatively small TEC (Fig. 2). In this study, we investigate whether this correspondence is fortuitous or whether the decrease in TEC at low temperature is a key condition for the existence of beta regions in the ocean. This question cannot be addressed experimentally, as the equation of state (EOS) of seawater cannot be changed. The situation is, in this respect, analogous to the question of how a given bathymetric configuration constrains the observed circulation, which can only be investigated through theory and numerical simulations.

Forced ocean simulations (i.e., with imposed conditions at the surface boundary) have been performed in previous studies (*19*, *20*), which showed a large sensitivity of the global stratification distribution to changes in the TEC value, especially changes near the freezing point. However, the impact on sea ice was not realistic because forced simulations do not include atmospheric feedbacks. To avoid these unrealistic constraints, we use a fully coupled ocean–atmosphere–sea ice model with a simplified geometry (see Materials and Methods for details on the model configuration and sensitivity experiments). The nonlinear EOS implemented in the model will be replaced by a series of linear EOS with different TEC constant values, allowing us to investigate the sensitivity of the global climate to this water property.

RESULTS

The most marked changes observed when switching from a nonlinear to a linear EOS (at approximately constant global mean TEC) are

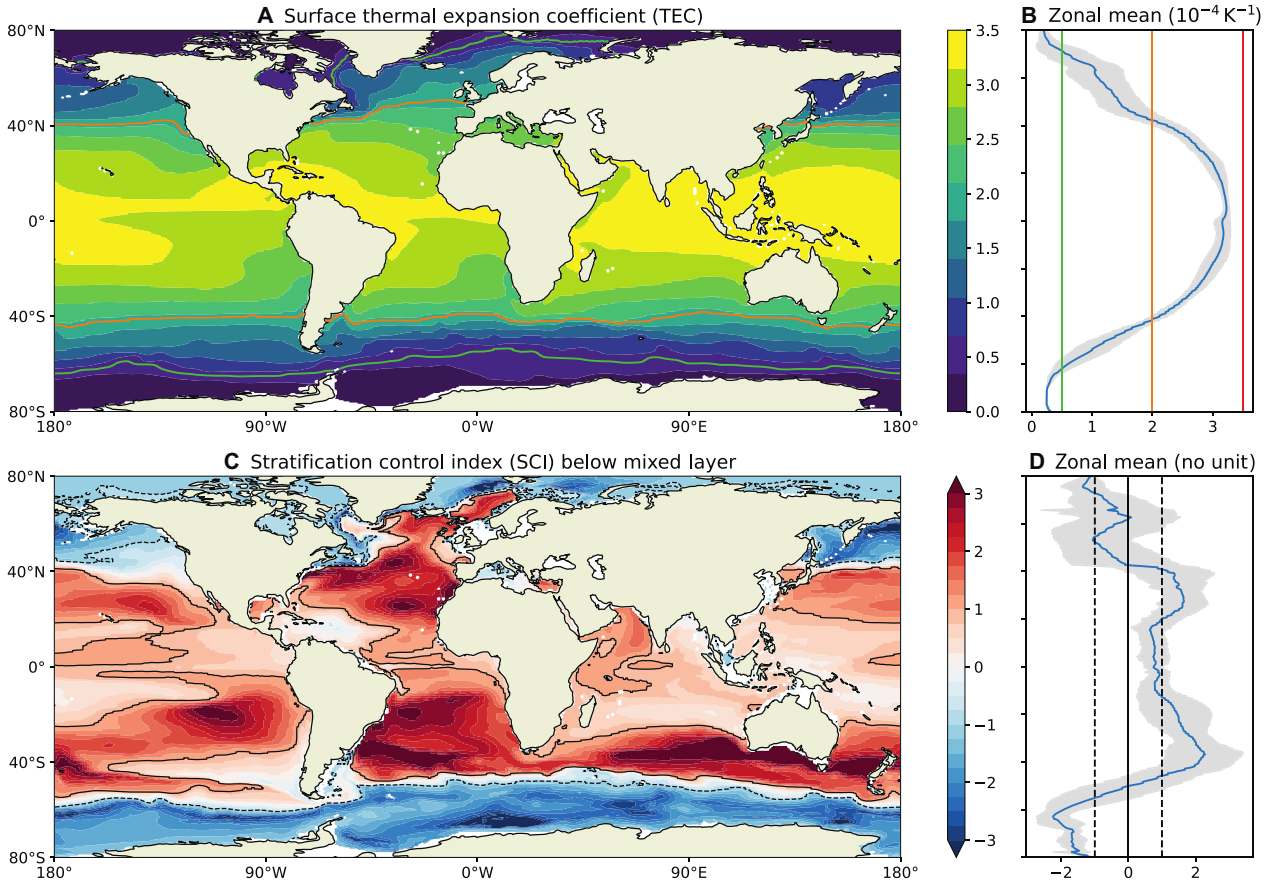

Fig. 2. Stratification control and surface TEC in the ocean. (**A**) Surface distribution of the TEC, showing a notable correlation with sea surface temperature. (**B**) Zonal-mean TEC showing an order of magnitude of var. (**C**) SCI (see core text for the definition). Blue, stratification dominated by salinity (beta regions); red, dominated by temperature (alpha regions). (**D**) Zonal-mean SCI. All figures are based on the Estimating the Circulation and Climate of the Ocean (ECCO) state estimate, version 4, release 4 (*66*). For each year, the SCI was computed on the layer found between 10 and 30 m below the mixed layer for the month of deepest mixed layer. The SCI distribution is obtained by averaging over the 21 years available in ECCO.

found in polar regions. While the control simulation Ctrl simulates a large ice pack in the Southern Hemisphere south of 60°S, the simulation Lin2.0 with a constant TEC value of 2.0×10^{-4} °C^{-1} is completely sea ice free (Fig. 3A; see also fig. S3). The sensitivity runs with linear EOS exhibit an abrupt regime transition between ice-free climates for large TEC and ice-covered poles for low TEC. The critical TEC value allowing the presence of sea ice is near 1.2×10^{-4} °C^{-1}. A constant value of about 0.8×10^{-4} °C^{-1} is required to produce the sea ice area found in Ctrl.

The surface and atmospheric responses to variations in TEC can be explained to a large extent by the changes in sea ice cover. A wider sea ice cover increases the planetary albedo, either directly or through changes in cloud cover, which not only tends to reduce the solar radiation absorbed at the surface (*21*) but also insulates the ocean from the atmosphere, allowing colder and drier conditions to develop in winter (*22*). The mean surface temperature increases rapidly (by about 2.5°C) with the disappearance of sea ice to stabilize just above 24°C in ice-free climates (Fig. 3B, blue).

Surface ocean forcings (fig. S5) are weakly affected by changes in TEC, with two notable exceptions. First, in polar regions and in the presence of sea ice, the strong divergence of fresh water from within the ice pack to its edge (due to equatorward spreading of ice) destabilizes the stratification and drives the formation of high-salinity bottom waters. In ice-free climates, the freshwater flux (due to net precipitation) stabilizes the stratification, but it is overcome by the destabilizing effect of the intense surface cooling that produces more widespread deep convection. Second, the surface heat flux is substantially modified in the mid-latitudes for the low-TEC run Lin0.5, reflecting fundamental differences in the structure of the overturning circulation with shallower overturning cells shifted equatorward (fig. S4). Changes in the Northern polar regions are less marked, probably because Ctrl had very little sea ice there to start with so surface fluxes are less likely to be modified.

Close inspection at zonal-mean temperature and salinity sections (Fig. 4) highlights the major impact that the value of TEC has on the ocean structure. For sufficiently high TEC values (2×10^{-4} to 3.5×10^{-4} °C^{-1}), the stratification in subtropical regions compares well with that of Ctrl (and the real ocean), with the characteristic W-shaped thermocline extending down to a similar depth of about 500 m. In the southern polar region, however, deep convection

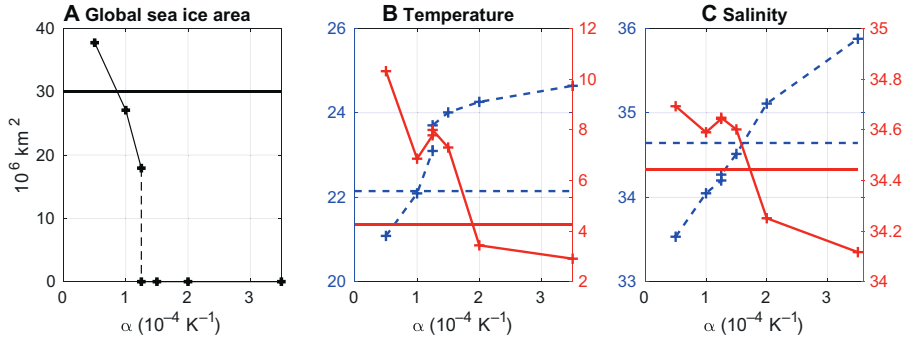

Fig. 3. Climate model sensitivity to different prescribed TECs. (**A**) Sea ice area, (**B**) sea surface temperature (0 to 40 m, blue) and bottom temperature (3000 to 4000 m, red), and (**C**) sea surface salinity (blue) and bottom salinity (red). Bottom values are averaged over the lowest kilometer (3000 to 4000 m), while surface values are averaged over the top 40 m. The horizontal lines denote the corresponding values in Ctrl.

becomes more vigorous at high TEC, and the stratification there nearly vanishes (Fig. 4, middle for Lin2.0). As a result, the southern polar surface becomes warmer/saltier and the bottom becomes cooler/fresher than in runs without convection. The spread of cold/fresh southern water masses results in lower bottom temperature globally (Fig. 3B, red) and a cooler global ocean, associated with a stronger deep overturning cell (fig. S4).

In contrast, at a low-TEC run (Lin0.5 in Fig. 4, C and F), deeper but weakly stratified thermoclines develop in both polar and subtropical regions. The abyssal ocean is filled with a warm water mass (10°C bottom temperature; Fig. 3B). This, as well as the absence of a subsurface salinity maximum in the subtropics, indicates the presence of salinity-driven convection in the subtropics. Overall, this run has weaker and less connected overturning cells, producing an essentially unventilated bottom ocean (fig. S4). The temperature contrast between surface and deep waters in the Southern Ocean is as large as 13°C, which is only possible due to the strong stabilizing effect of vertical salinity gradients.

The global mean sea surface salinity increases nearly linearly with the TEC (~1 g kg^{-1} for a unit 10^{-4} °C^{-1} of TEC; see Fig. 3C, blue). This is balanced by a freshening of the bottom ocean with increasing TEC, so as to satisfy global salt conservation in the ocean. The overall pattern of change is one of increasing contrast between the top and bottom of the ocean in both temperature and salinity (Fig. 3B). These temperature and salinity changes have opposite effects on the stabilization of the global stratification. As the temperature effect dominates (both the vertical temperature contrast and the impact of temperature on density increase with TEC), the top-to-bottom mean stratification strengthens for increasing values of TEC (Fig. 5).

The effect of the TEC on the stratification can be quantified by the SCI, which becomes systematically larger for higher values of TEC. In ice-free states, the thermal stratification N_T^2 is everywhere positive, indicating an inability to maintain cold waters near the surface while a salinity inversion ($N_S^2 < 0$, also seen in Ctrl) develops in the tropics and subtropics (corresponding to SCI > 1; Fig. 5C). In contrast, the low-TEC states have a marked temperature inversion in polar regions, as in Ctrl (see Fig. 4), but no salinity inversion in the subtropics, contrary to all the other simulations. The beta region (SCI < −1) in the low-TEC climates extends far into the subtropics up to 25° latitude, while the high-TEC climates do not exhibit beta regions at all.

It appears that the SCI in Ctrl closely matches at each latitude that the SCI value obtained in linear EOS simulations with the corresponding surface TEC. At high latitude where the TEC is low in Ctrl, the stratification resembles that of Lin0.5, while at low latitude, it resembles that of Lin2.0. This indicates that the TEC provides a strong constraint on the type of stratification that a particular location may experience. That is, the existence of distinct alpha and beta regions is primarily a consequence of the temperature dependence of the TEC of seawater.

Stratification below the sea ice

Our numerical experiments indicate the existence of a threshold in TEC above which sea ice cannot be sustained. The threshold value is between 1×10^{-4} and 1.5×10^{-4} °C^{-1} with a nonlinear transition, as a centennial oscillation between two unstable states is observed in Lin1.25 (see fig. S2). The quantitative prediction for the threshold value is likely model dependent and should be taken with caution. We argue, however, that the existence of such a threshold is expected and can be rationalized using the theoretical model of Martinson (*23*) for the stratification below sea ice.

The model considers a steady-state upper ocean and expresses the conservation of mass, salt, and heat. A central element is that, in the presence of sea ice, the surface layer is at the freezing point, which is the minimum possible temperature of seawater. This implies that the vertical gradient of temperature below sea ice is necessarily negative, $\partial_z\Theta \leq 0$.

To ensure static stability and a steady state, the total stratification N^2 must be positive, implying that the salinity stratification N_S^2 must be positive and large enough to compensate the temperature inversion or (see Eq. 2)

$$\beta\partial_z S \leq \alpha\partial_z\Theta \leq 0 \tag{3}$$

In the case of a freshwater lake ($\partial_z S = 0$), where $\alpha < 0$, the stability condition (Eq. 3) is satisfied unconditionally (recall, $\partial_z\Theta \leq 0$). In the saltwater ocean, however, the TEC is everywhere positive, so that $N_\Theta^2 \leq 0$ under the sea ice. There, the stratification must be salinity controlled, with $\partial_z S \leq 0$ (fresh water on top). This introduces an upper limit on the magnitude of the (negative) temperature gradient that can be maintained, which depends not only on the salinity gradient but also strongly on the TEC value.

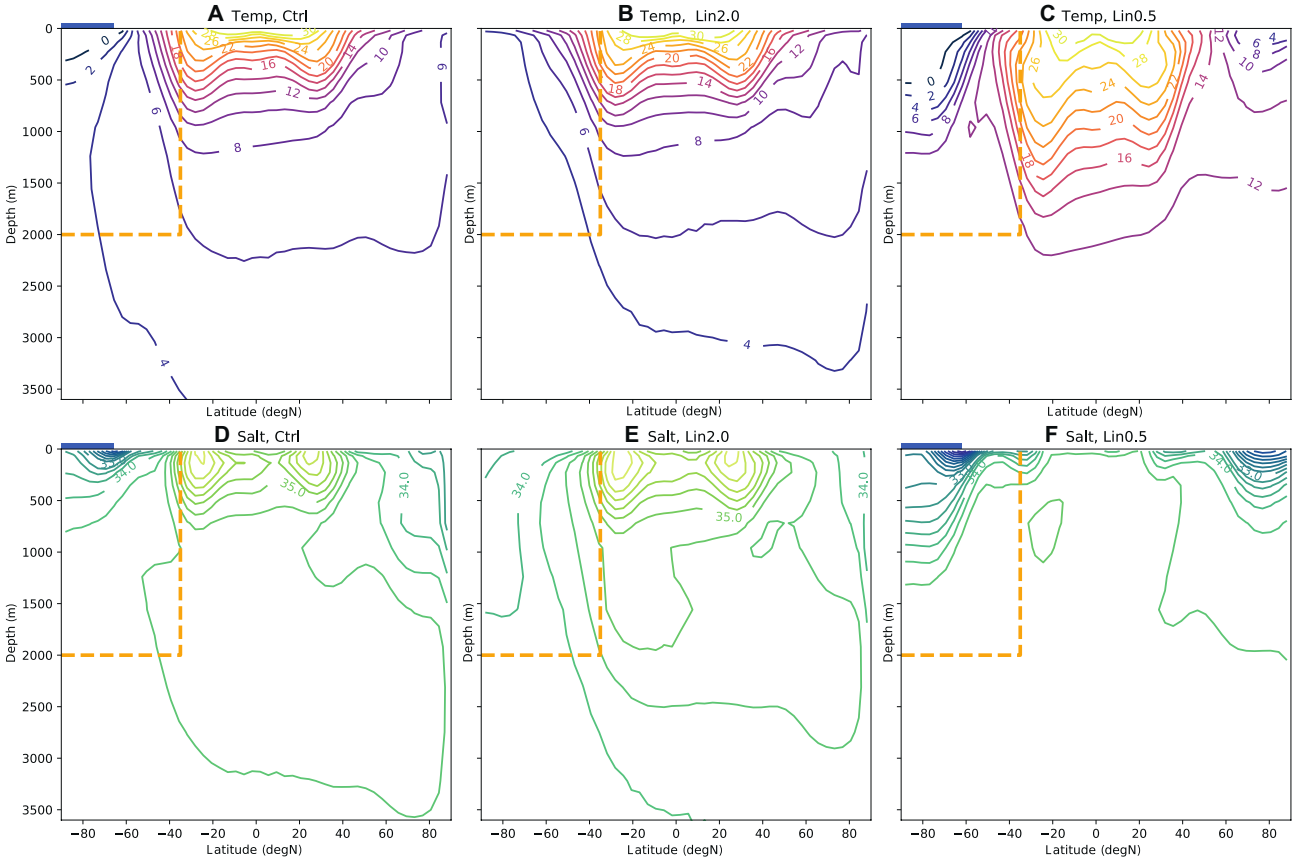

Fig. 4. Global modifications of the mean thermohaline stratification for different prescribed TECs. Zonally averaged sections of temperature (top) and salinity (bottom): (**A** to **D**) Ctrl, (**B** to **E**) Lin2.0, and (**C** to **F**) Lin0.5. Dashed orange lines in the top left corner denote the zonally reentrant section above the seal and south of the continents. Blue squares indicate the sea ice extent.

A critical value for the TEC can be obtained in the limit where the stratification would vanish

$$\alpha \leq \alpha_c = \frac{\beta \partial_z S}{\partial_z \Theta} \tag{4}$$

In a steady state, the gradient of salinity must be primarily controlled by the net rate of precipitation, which acts to stabilize the stratification. The surface cooling, which weakens the stability, may occur not only by air-sea/ice-sea interaction but also as a result of the ice melting needed to close the ice mass budget. Conservation of salt, mass, and heat requires compensating diffusive fluxes at the base of the mixed layer. Using simplified ice mass, heat, and salt budgets and assuming identical diffusivities for temperature and salinity, one finds an expression for the critical TEC α_c (see the Supplementary Materials for detailed derivations)

$$\alpha_c = \beta S_0 \frac{\rho_w c_p P}{Q + \rho_0 L_i A P} \tag{5}$$

where P is the net precipitation (defined as precipitation minus evaporation plus river runoff), Q is the net surface heat flux, and A is the sea ice fraction (see table S1 for definitions of constants). A stable state with sea ice can only be maintained for a TEC value smaller than α_c. In polar regions where precipitation dominates evaporation ($P > 0$) and the ocean loses heat to the ice/atmosphere ($Q > 0$), α_c is positive. Equation 5 shows that, as expected, larger heat loss reduces α_c and the range of stability. The role of net precipitation P is more complex, appearing both in the numerator and denominator of Eq. 5. Larger precipitation stabilizes the water column by lowering the surface salinity, which permits a larger α_c (numerator). Simultaneously, larger precipitation over ice must be balanced by melting at the ice base and hence larger latent heat loss, which reinforces the destabilizing effect of Q (denominator).

For realistic values of the parameters (table S1), a critical value of $\alpha_c \approx 0.9 \times 10^{-4}$ °C^{-1} is obtained. Despite strong simplifications, this estimate is consistent with the TEC values where the transition to an ice-free climate occurs in the coupled model (Fig. 3). The fact that the critical TEC value is well below the global mean TEC value confirms that the conditions to form sea ice in the open ocean could not be met in the current Earth climate if the TEC value was not dropping at low temperature. Furthermore, it demonstrates that this water property, through (Eq. 5), imposes a constraint on the Earth's climate state.

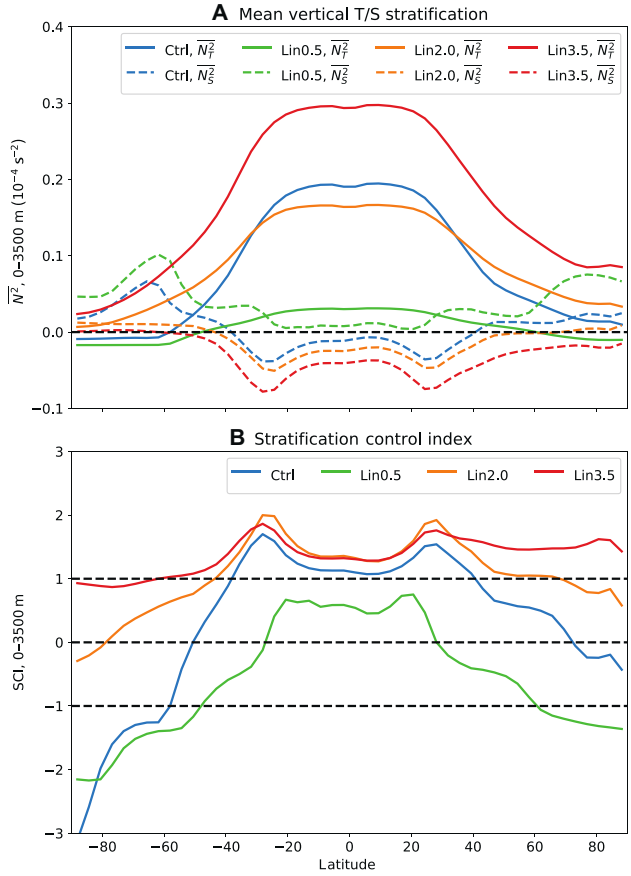

Fig. 5. Relative contributions of temperature and salinity on the stratification controlled by the TEC. (**A**) Zonally averaged haline (N_S^2) and thermal (N_Θ^2) buoyancy frequencies averaged from the surface to bottom, shown for the control run and the three sensitivity experiments. (**B**) SCI computed using vertically and zonally averaged buoyancy frequencies. The mean SCI of Ctrl compares well with that of Lin0.5 in polar regions, especially in the southern ice-covered domain, but is closer to that of Lin2.0 and Lin3.5 in subtropical regions. These variations in SCI are consistent with changes in surface TEC in Ctrl related to sea surface temperature changes.

DISCUSSION

Here, we have shown that the temperature dependence of the TEC is key to favoring the formation of a beta ocean (stratified by salinity) and largely controls the sea ice extent using a range of coupled ocean-atmosphere simulations. It was further shown that, even if a net freshwater flux in polar regions is necessary to form a halocline, it is not enough to maintain the beta stratification stable in the presence of intense surface cooling except maybe in geographically limited cold estuarine regions. Sea ice formation has long been noted to require beta ocean conditions to occur away from shallow areas (*13*, *24*). The idea that a reduction of the TEC in the cold high latitudes could promote sea ice formation was even suggested (*13*, *20*, *25*), and it is demonstrated here.

The transition from alpha to beta stratification is not caused by cabbeling, contrary to previous suggestions (*13*). Cabbeling, also known as densification upon mixing, generates a convergence across the frontal boundaries as isopycnal mixing in the interior acts to densify seawater (*26*, *27*). Rates of cabbeling depend on how fast the TEC varies with temperature; however, they also require a combination of eddy stirring and molecular diffusion to generate the convergence. That cabbeling may increase the abruptness of the transition from alpha to beta cannot be entirely discarded here; however, our results based on linear EOS simulations (thus entirely free of cabbeling by construct) show that cabbeling is not necessary for the existence of these transitions (Fig. 5).

This is consistent with recent numerical experiments showing that the transition zone in polar regions is set by an inversion of the mean surface buoyancy flux, linked to the drop in polar TEC value at low temperature (*28*) rather than cabbeling. This temperature dependence of the TEC should also imply a weaker and more indirect role of the wind forcing on the position of fronts than previously hypothesized (*29*). The position of the transition zone can, however, be influenced by changes in the strength of the halocline, which can be driven by hydrological changes (*30*), ice shelf melting (*31*), or wind anomalies (*32*). This points toward a subtle, nonlinear interplay between heat and freshwater surface fluxes in controlling the meridional structure of the upper ocean stratification.

The idea that the TEC might have a global influence on the climate is, of course, not entirely new although not always explicitly acknowledged. Experiments using global atmosphere/ocean general circulation models can be found in the literature, where the global mean salinity (*33*, *34*) or the global mean temperature (*35*) of the simulated ocean is artificially modified, indirectly modifying the thermohaline range of water masses and, consequently, the way the TEC varies with temperature. Our simulations show that increased TEC values in the polar region, as may be found in warmer climates, are associated with colder and fresher deep water properties (Fig. 3). The ventilation is expected to be stronger in warm climates than in cold climates, as the polar halocline necessitates temperature near the freezing point to be maintained (*36*). This, in turn, may induce an anticorrelation between the global mean temperature and the carbon storage in the deep ocean, further amplifying climate changes. This mechanism has been suggested to explain the transition to the Pleistocene cycle of ice ages, 2.7 million years ago (*37*). This may also explain why salinity forcing seems to dominate during the Last Glacial Maximum, simply because it was in a colder state (*38*).

The large sensitivity of the global ocean structure and sea ice formation to the TEC highlighted here has strong implications for how the ocean may respond to a climate change. If the position of the polar transition zone is controlled by the value of the TEC, itself mostly a function of the sea surface temperature, migrations of the transition zone between alpha and beta regions should be largely driven by the surface heat fluxes. This appears consistent with the current "atlantification" of the Eurasian Arctic basin, caused by a warming of the Atlantic inflows and producing a northward migration of the transition zone and a concurrent shrinking of the sea ice extent (*39*). On the other hand, the idea of an increased ventilation in a warmer climate (*35*, *36*) somewhat contradicts the common inference that global warming may induce a slowdown and even possibly a collapse of the Atlantic Meridional Overturning Circulation (*40*). The competing effects of freshening and warming in shifting the stratification control, particularly in the Nordic Seas (*41*, *42*), need to be better understood to predict how polar climate changes affect the ventilation and overturning rates.

Our simulation with a uniform TEC corresponding to the present-day global ocean value ($\alpha = 2.0 \times 10^{-4}$ °C^{-1}) is warmer than the

control simulation by about 2°C and is totally ice free. Depending on estimates of the climate sensitivity (*43*), a decrease in atmospheric CO_2 by a factor of about 2 to 5 would be necessary to form sea ice with this uniform TEC (see the Supplementary Materials). All things equal (concentration of CO_2 and other greenhouse gas, solar constant, continental distribution, etc.), the unique variation of the water TEC greatly facilitates the growth of sea ice, with a cascading impact on global climate conditions. For example, by affecting the stratification and rates of transport of essential nutrients such as phosphate, variations of seawater's TEC constrain the ocean productivity (with feedbacks on the global carbon cycle), making it potentially relevant to habitability conditions in the presence of an ocean (*44*). These exoplanets that have attracted a lot of attention as salty (e.g., the presence of nutrient) oceans, in addition to being a favorable medium to harbor life, can significantly moderate climate response to changing astronomical parameters and therefore widen the habitable zone (*45*).

Our study highlights that estimates of habitable zone should avoid simplified linear EOS with constant TEC (*34*, *46*). As shown by our simulations, neglecting the unique thermal expansion properties of seawater may significantly overestimate the global mean temperature and therefore underestimate the possibilities of a descent into global glaciation with potential relevance to the transition toward and from snowball states (*47*, *48*). Also, salinity of oceans may vary markedly over time (*49*) and between planets (*50*), affecting the thermal sensitivity of the global ocean. Exploration of the full range of salinity and their climate impact will require to account for the full nonlinearity of the seawater EOS.

MATERIALS AND METHODS

Description of the climate model

Simulations are carried out with the MIT General Circulation Model (*51*), which solves for the three-dimensional circulation of atmosphere and ocean and includes sea ice and land surface processes. The atmospheric physics is of "intermediate" complexity based on SPEEDY (*52*) at low vertical resolution (further details in the Supplementary Materials). The configuration comprises two land-barrier masses defining a narrow Atlantic-like basin and a wide Pacific-like basin connecting to an unblocked Southern Ocean. Despite its simplified geometry, the configurations include many of the essential dynamics that shape Earth's climate system (e.g., hydrological cycle and storm tracks) (*53*). It also captures two key asymmetries: an asymmetry between the two northern basins with the absence of deep water formation in the Pacific Ocean (*54*) and a north-south asymmetry between wind-driven gyres in the north and a vigorous Southern Ocean circumpolar current.

The barrier to the west of the small basin (analogous to the American continent) is extended with a submarine ridge between 2000 and 4000 m in depth. This allows a northward propagation of bottom water produced in the south and a more realistic representation of the bottom meridional cell than in previous reported simulations (*54*). Furthermore, a maximum sea ice concentration of 90% is set in the model, and an ice thickness diffusion is applied to prevent the formation of ice caps that completely insulate the ocean from the atmosphere and ensure a more realistic production of bottom waters in ice-covered areas.

In its reference configuration, the coupled model uses the standard EOS-80 for salty water, with potential temperature and practical salinity as prognostic variables (*4*). However, following recent recommendations (*55*), we will nonetheless interpret them as conservative temperature (a quantity proportional to potential enthalpy with units of temperature) and absolute salinity (the grams of solute per kilogram of seawater), respectively. Note that quantitative discrepancies between thermodynamic standards are small (<1%) and are not susceptible to modify the conclusions here.

Design of the sensitivity experiments

To test the sensitivity of the climate to the TEC value, we implement a linear EOS approximation

$$\rho_{\mathrm{model}} = \rho_0(1 - \alpha_0\Theta + \beta_0 S) \tag{6}$$

where α_0, β_0, and ρ_0 are uniform globally. Having a linear EOS enables us to investigate the effect of the TEC value at different latitudes while keeping the analysis simple. We chose not to include a nonlinear term in the EOS, despite their potential impact on the global water mass distribution through cabbeling or thermobaricity effects (*19*), to better isolate the local impact of the TEC value on the surface buoyancy forcings and on the upper stratification.

We carry out the following experiments, which only differ by their EOS:

1) Ctrl: Control simulation with the nonlinear EOS-80; spin up of 9 thousand years (ka).

2) Lin2.0: Simulation with the linear EOS with $\alpha_0 = 2.0 \times 10^{-4}$ °C^{-1}. The simulation is initialized from the end state of Ctrl and then run for 7 ka.

3) Lin0.5, Lin1.0, Lin1.25 and Lin1.5, and Lin3.5: Simulations with linear EOS with $\alpha_0 = 0.5$, 1.0, 1.25, 1.5, and 3.5 in units of 10^{-4} °C^{-1}, respectively. These simulations are branched off from the end state of Lin2.0 and run for a minimum of 5 ka.

Note that the globally averaged TEC values in Ctrl (nonlinear EOS) and Lin2.0 (linear EOS) are very similar. The haline contraction coefficient is set to the constant $\beta_0 = 7.8 \times 10^{-4}$ (g/kg)$^{-1}$. The time series of the sea surface temperature and sea ice area are shown in figs. S1 and S2. Illustrations below use the past 50 years of each simulation.

SUPPLEMENTARY MATERIALS

Supplementary material for this article is available at https://science.org/doi/10.1126/sciadv.abq0793

REFERENCES AND NOTES

1. Y. Maréchal, *The hydrogen bond and the water molecule: The physics and chemistry of water, aqueous and bio media* (Elsevier, 2007).
2. D. L. Hartmann, *Global Physical Climatology* (Newnes, 2015), vol. 103.
3. D. Eisenberg, W. Kauzmann, *The Structure and Properties of Water* (Oxford Univ. Press on demand, 2005).
4. IOC and SCOR and IAPSO, The international thermodynamic equation of seawater – 2010: Calculation and use of thermodynamic properties., Intergovernmental Oceanographic Commission, Manuals and Guides No. 56, UNESCO (English) (2010), 196 p.
5. T. S. Ingebrigtsen, T. B. Schrøder, J. C. Dyre, What is a simple liquid? *Phys. Rev. X* **2**, 011011 (2012).
6. A. Van Itterbeek, O. Verbeke, Density of liquid nitrogen and argon as a function of pressure and temperature. *Physica* **26**, 931–938 (1960).
7. G. E. Hutchinson, H. Löffler, The thermal classification of lakes. *Proc. Natl. Acad. Sci. U.S.A.* **42**, 84–86 (1956).
8. W. M. Lewis Jr., A revised classification of lakes based on mixing. *Can. J. Fish. Aquat. Sci.* **40**, 1779–1787 (1983).

9. B. Boehrer, Thermobaric Stratification of Very Deep Lakes, in *Encyclopedia of Lakes and Reservoirs*, L. Bengtsson, R. W. Herschy, R. W. Fairbridge, Eds. (Encyclopedia of Earth Sciences Series, Springer Netherlands, 2012), pp. 800–801.
10. R. Mancinelli, A. Botti, F. Bruni, M. Ricci, A. Soper, Perturbation of water structure due to monovalent ions in solution. *Phys. Chem. Chem. Phys.* **9**, 2959–2967 (2007).
11. V. Pellichero, J.-B. Sallée, S. Schmidtko, F. Roquet, J.-B. Charrassin, The ocean mixed layer under southern ocean sea-ice: Seasonal cycle and forcing. *J. Geophys. Res. Oceans* **122**, 1608–1633 (2017).
12. E. C. Carmack, M. Yamamoto-Kawai, T. W. N. Haine, S. Bacon, B. A. Bluhm, C. Lique, H. Melling, I. V. Polyakov, F. Straneo, M. L. Timmermans, W. J. Williams, Freshwater and its role in the arctic marine system: Sources, disposition, storage, export, and physical and biogeochemical consequences in the arctic and global oceans. *J. Geophys. Res. Biogeosc.* **121**, 675–717 (2016).
13. E. C. Carmack, The alpha/beta ocean distinction: A perspective on freshwater fluxes, convection, nutrients and productivity in high-latitude seas. *Deep Sea Res. Part II Top. Stud. Oceanogr.* **54**, 2578–2598 (2007).
14. G. K. Vallis, *Atmospheric and oceanic fluid dynamics* (Cambridge Univ. Press, 2012).
15. R. W. Schmitt, Double diffusion in oceanography. *Annu. Rev. Fluid Mech.* **26**, 255–285 (1994).
16. K. D. Stewart, T. W. N. Haine, Thermobaricity in the transition zones between alpha and beta oceans. *J. Phys. Oceanogr.* **46**, 1805–1821 (2016).
17. T. J. McDougall, Thermobaricity, cabbeling, and water-mass conversion. *J. Geophys. Res. Oceans* **92** (C5), 5448–5464 (1987).
18. S. Groeskamp, R. P. Abernathey, A. Klocker, Water mass transformation by cabbeling and thermobaricity. *Geophys. Res. Lett.* **43**, 10835–10845 (2016).
19. J. Nycander, M. Hieronymus, F. Roquet, The nonlinear equation of state of sea water and the global water mass distribution. *Geophys. Res. Lett.* **42**, 7714–7721 (2015).
20. F. Roquet, G. Madec, L. Brodeau, J. Nycander, Defining a simplified yet "realistic" equation of state for seawater. *J. Phys. Oceanogr.* **45**, 2564–2579 (2015).
21. D. Rind, R. Healy, C. Parkinson, D. Martinson, The role of sea ice in $2\times CO_2$ climate model sensitivity. Part I: The total influence of sea ice thickness and extent. *J. Climate* **8**, 449–463 (1995).
22. S. Manabe, R. T. Wetherald, The effects of doubling the CO_2 concentration on the climate of a general circulation model. *J. Atmos. Sci.* **32**, 3–15 (1975).
23. D. G. Martinson, Evolution of the southern ocean winter mixed layer and sea ice: Open ocean deepwater formation and ventilation. *J. Geophys. Res. Oceans* **95**, 11641–11654 (1990).
24. N. P. Bulgakov, The role of convection in the mechanism of heat transfer of deep atlantic water, in *Deep Sea Res. and Oceanographic Abstracts* (1962), vol. 9, pp. 233–239.
25. C. Rooth, Hydrology and ocean circulation. *Prog. Oceanogr.* **11**, 131–149 (1982).
26. A. Klocker, T. J. McDougall, Influence of the nonlinear equation of state on global estimates of dianeutral advection and diffusion. *J. Phys. Oceanogr.* **40**, 1690–1709 (2010).
27. S. Groeskamp, R. P. Abernathey, A. Klocker, Water mass transformation by cabbeling and thermobaricity. *Geophys. Res. Lett.* **43**, 10835–10845 (2020).
28. R. Caneill, F. Roquet, G. Madec, J. Nycander, The polar transition from alpha to beta regions set by a surface buoyancy flux inversion. *J. Phys. Oceanogr.* **52**, 1887–1902 (2022).
29. J. R. Toggweiler, Shifting westerlies. *Science* **323**, 1434–1435 (2009).
30. P. J. Durack, S. E. Wijffels, R. J. Matear, Ocean salinities reveal strong global water cycle intensification during 1950 to 2000. *Science* **336**, 455–458 (2012).
31. E. Rignot, S. Jacobs, J. Mouginot, B. Scheuchl, Ice-shelf melting around antarctica. *Science* **341**, 266–270 (2013).
32. S. R. Rintoul, M. H. England, Ekman transport dominates local air-sea fluxes in driving variability of subantarctic mode water. *J. Phys. Oceanogr.* **32**, 1308–1321 (2002).
33. P. D. Williams, E. Guilyardi, G. Madec, S. Gualdi, E. Scoccimarro, The role of mean ocean salinity in climate. *Dyn. Atmospheres Oceans* **49**, 108–123 (2010).
34. J. Cullum, D. P. Stevens, M. M. Joshi, Importance of ocean salinity for climate and habitability. *Proc. Natl. Acad. Sci. U.S.A.* **113**, 4278–4283 (2016).
35. A. M. de Boer, D. M. Sigman, J. R. Toggweiler, J. L. Russell, Effect of global ocean temperature change on deep ocean ventilation. *Paleoceanography* **22**, PA2210 (2007).
36. M. Winton, The effect of cold climate upon north atlantic deep water formation in a simple ocean-atmosphere model. *J. Climate* **10**, 37–51 (1997).
37. D. M. Sigman, S. L. Jaccard, G. H. Haug, Polar ocean stratification in a cold climate. *Nature* **428**, 59–63 (2004).
38. J. F. Adkins, K. McIntyre, D. P. Schrag, The salinity, temperature, and δ18O of the glacial deep ocean. *Science* **298**, 1769–1773 (2002).
39. I. V. Polyakov, A. V. Pnyushkov, M. B. Alkire, I. M. Ashik, T. M. Baumann, E. C. Carmack, I. Goszczko, J. Guthrie, V. V. Ivanov, T. Kanzow, R. Krishfield, R. Kwok, A. Sundfjord, J. Morison, R. Rember, A. Yulin, Greater role for Atlantic inflows on sea-ice loss in the Eurasian Basin of the Arctic Ocean. *Science* **356**, 285–291 (2017).
40. W. Weijer, W. Cheng, S. S. Drijfhout, A. V. Fedorov, A. Hu, L. C. Jackson, W. Liu, E. L. McDonagh, J. V. Mecking, J. Zhang, Stability of the atlantic meridional overturning circulation: A review and synthesis. *J. Geophys. Res. Oceans* **124**, 5336–5375 (2019).
41. C. Lique, M. D. Thomas, Latitudinal shift of the Atlantic meridional overturning circulation source regions under a warming climate. *Nat. Clim. Chang.* **8**, 1013–1020 (2018).
42. M. S. Lozier, F. Li, S. Bacon, F. Bahr, A. S. Bower, S. A. Cunningham, M. F. de Jong, L. de Steur, B. de Young, J. Fischer, S. F. Gary, B. J. W. Greenan, N. P. Holliday, A. Houk, L. Houpert, M. E. Inall, W. E. Johns, H. L. Johnson, C. Johnson, J. Karstensen, G. Koman, I. A. le Bras, X. Lin, N. Mackay, D. P. Marshall, H. Mercier, M. Oltmanns, R. S. Pickart, A. L. Ramsey, D. Rayner, F. Straneo, V. Thierry, D. J. Torres, R. G. Williams, C. Wilson, J. Yang, I. Yashayaev, J. Zhao, A sea change in our view of overturning in the subpolar North Atlantic. *Science* **363**, 516–521 (2019).
43. M. D. Zelinka, T. A. Myers, D. T. McCoy, S. Po-Chedley, P. M. Caldwell, P. Ceppi, S. A. Klein, K. E. Taylor, Causes of higher climate sensitivity in CMIP6 models. *Geophys. Res. Lett.* **47**, e2019GL085782 (2020).
44. S. L. Olson, M. Jansen, D. S. Abbot, Oceanographic considerations for exoplanet life detection. *Astrophys. J.* **895**, 19 (2020).
45. D. Ferreira, J. Marshall, P. A. O'Gorman, S. Seager, Climate at high-obliquity. *Icarus* **243**, 236–248 (2014).
46. K. M. Soderlund, B. E. Schmidt, J. Wicht, D. D. Blankenship, Ocean-driven heating of europa's icy shell at low latitudes. *Nat. Geosci.* **7**, 16–19 (2014).
47. P. F. Hoffman, D. P. Schrag, The snowball Earth hypothesis: Testing the limits of global change. *Terra Nova* **14**, 129–155 (2002).
48. P. F. Hoffman, D. S. Abbot, Y. Ashkenazy, D. I. Benn, J. J. Brocks, P. A. Cohen, G. M. Cox, J. R. Creveling, Y. Donnadieu, D. H. Erwin, I. J. Fairchild, D. Ferreira, J. C. Goodman, G. P. Halverson, M. F. Jansen, G. le Hir, G. D. Love, F. A. Macdonald, A. C. Maloof, C. A. Partin, G. Ramstein, B. E. J. Rose, C. V. Rose, P. M. Sadler, E. Tziperman, A. Voigt, S. G. Warren, Snowball earth climate dynamics and cryogenian geology-geobiology. *Sci. Adv.* **3**, e1600983 (2017).
49. L. P. Knauth, Salinity history of the earth's early ocean. *Nature* **395**, 554–555 (1998).
50. S. N. Raymond, T. Quinn, J. I. Lunine, Making other earths: Dynamical simulations of terrestrial planet formation and water delivery. *Icarus* **168**, 1–17 (2004).
51. J. Marshall, A. Adcroft, C. Hill, L. Perelman, C. Heisey, A finite-volume, incompressible navier stokes model for studies of the ocean on parallel computers. *J. Geophys. Res. Oceans* **102**, 5753–5766 (1997).
52. F. Molteni, Atmospheric simulations using a GCM with simplified physical parametrizations. I: Model climatology and variability in multi-decadal experiments. *Climate Dynam.* **20**, 175–191 (2003).
53. D. Ferreira, J. Marshall, J.-M. Campin, Localization of deep water formation: Role of atmospheric moisture transport and geometrical constraints on ocean circulation. *J. Climate* **23**, 1456–1476 (2010).
54. D. Ferreira, P. Cessi, H. K. Coxall, A. de Boer, H. A. Dijkstra, S. S. Drijfhout, T. Eldevik, N. Harnik, J. F. McManus, D. P. Marshall, J. Nilsson, F. Roquet, T. Schneider, R. C. Wills, Atlantic-pacific asymmetry in deep water formation. *Annu. Rev. Earth Planet. Sci.* **46**, 327–352 (2018).
55. T. J. McDougall, P. M. Barker, R. M. Holmes, R. Pawlowicz, S. M. Griffies, P. J. Durack, The interpretation of temperature and salinity variables in numerical ocean model output and the calculation of heat fluxes and heat content. *Geosci. Model Dev.* **14**, 6445–6466 (2021).
56. J. Marshall, C. Hill, L. Perelman, A. Adcroft, Hydrostatic, quasi-hydrostatic, and nonhydrostatic ocean modeling. *J. Geophys. Res. Oceans* **102**, 5733–5752 (1997).
57. J. Marshall, A. Adcroft, J.-M. Campin, C. Hill, A. White, Atmosphere-ocean modeling exploiting fluid isomorphisms. *Mon. Wea. Rev.* **132**, 2882–2894 (2004).
58. A. Adcroft, J.-M. Campin, Re-scaled height coordinates for accurate representation of free-surface flows in ocean circulation models. *Ocean Model.* **7**, 269–284 (2004).
59. A. Adcroft, J. Campin, C. Hill, J. Marshall, Implementation of an atmosphere-ocean general circulation model on the expanded spherical cube. *Mon. Wea. Rev.* **132**, 2845–2863 (2004).
60. J.-M. Campin, J. Marshall, D. Ferreira, Sea ice-ocean coupling using a rescaled vertical coordinate *z*. *Ocean Model.* **24**, 1–14 (2008).
61. P. R. Gent, J. C. McWilliams, Isopycnal mixing in ocean circulation models. *J. Phys. Oceanogr.* **20**, 150–155 (1990).
62. M. H. Redi, Oceanic isopycnal mixing by coordinate rotation. *J. Phys. Oceanogr.* **12**, 1154–1158 (1982).
63. B. A. Klinger, J. Marshall, U. Send, Representation of convective plumes by vertical adjustment. *J. Geophys. Res. Oceans* **101**, 18175–18182 (1996).
64. M. Winton, A reformulated three-layer sea ice model. *J. Atmos. Oceanic Tech.* **17**, 525–531 (2000).

65. G. Myhre, E. J. Highwood, K. P. Shine, F. Stordal, New estimates of radiative forcing due to well mixed greenhouse gases. *Geophys. Res. Lett.* **25**, 2715–2718 (1998).
66. G. Forget, J. M. Campin, P. Heimbach, C. N. Hill, R. M. Ponte, C. Wunsch, ECCO version 4: An integrated framework for non-linear inverse modeling and global ocean state estimation. *Geosci. Model Dev.* **8**, 3071–3104 (2015).

Acknowledgments
Funding: No funding was required for this work. **Author contributions:** F.R. initiated the project. D.F. performed numerical runs and helped with their analysis. R.C. carried out analysis of the Estimating the Circulation and Climate of the Ocean (ECCO) product. D.S. contributed with his expertise in chemical physics of water. G.M. provided important inputs in interpreting the results. F.R. wrote the initial draft. All authors contributed to the final manuscript. **Competing interests:** The authors declare that they have no competing interests. **Data and materials availability:** All data needed to evaluate the conclusions in the paper are present in the paper and/or the Supplementary Materials. Model data supporting the results reported here are openly available from the University of Reading Research Data Archive at https://doi.org/10.17864/1947.000394.

Submitted 16 March 2022
Accepted 23 September 2022
Published 16 November 2022
10.1126/sciadv.abq0793